THÈSE DE DOCTORAT

Préparée à l'Université de Lille par

Kanika SOOD

En vue de l'obtention du grade de Docteur en Énergétique, Thermique et Combustion

Ecole Doctorale : Sciences de la Matière, du Rayonnement et de l'Environnement

Combustion des nouveaux biocarburants : étude de la formation des Hydrocarbures Aromatiques Polycycliques Oxygénés (HAPOs) et les petites particules de suie (<10 nm)

Combustion of new biofuels: study of the formation of Oxygenated Polycyclic Aromatic Hydrocarbons (OPAHs) and small soot particles (<10 nm)

Soutenue publiquement le 19 Décembre 2023 devant la Commission d'Examen

Composition du Jury:

Christine ROUSSELLE	Professeure, Laboratoire INSA-PRISME, Université d'Orléans	**Rapporteure**
Andrea COMANDINI	Chargé de Recherche CNRS, HDR, ICARE-INSIS, UPR 3021	**Rapporteur**
Pierre A. GLAUDE	Directeur de Recherche CNRS, LRGP, Université de Lorraine	**Président du Jury/Examinateur**
Véronique DIAS	Maîtresse de Recherche, HDR, IMMC, Université de Louvain (BE)	**Examinatrice**
Laurent GAGNEPAIN	Coordinateur Scientifique, Ingénieur ADEME	**Membre invité**
Sylvie GOSSELIN	Ingénieur d'études, Laboratoire PC2A, Université de Lille	**Membre invitée**
Laurent GASNOT	Professeur, Laboratoire PC2A, Université de Lille	**Directeur**
Luc-Sy TRAN	Chargé de Recherche CNRS, Laboratoire PC2A, Université de Lille	**Co-encadrant**

Acknowledgements

I am deeply grateful for the opportunity to conduct this thesis at the Physico-Chemistry of Combustion Processes and the Atmosphere laboratory (PC2A-UMR 8522) at the University of Lille. This research was made possible through funding from l'ADEME and la Région Hauts de France, to whom I extend my sincerest appreciation.

I extend my deepest gratitude to my thesis directors, M. Laurent Gasnot and M. Luc-Sy Tran, for their invaluable guidance, unwavering support, and significant contributions throughout my thesis journey. Their scientific rigor, empathy, expertise, enthusiasm, and accessibility have been instrumental in shaping this endeavor. The autonomy they provided me with has facilitated substantial progress and personal growth. I sincerely appreciate Ms. Sylvie Gosselin for her exceptional contributions to the GC experiments, as well as her involvement in technical and strategic aspects. Her tireless efforts in ensuring the smooth functioning of the lab are truly commendable. The substantial effort involved in planning, anticipating and procuring necessary materials for executing experiments, often goes unnoticed. In addition to their mentorship, I am grateful to my supervisors and Sylvie for their proactive approach in planning and ensuring all necessary materials are gathered beforehand to conduct experiments. I truly cannot express enough gratitude for all that they have done for me.

I extend my heartfelt appreciation to my committee members, Ms. Christine Rousselle, Professor at INSA-PRISME, University of Orléans and M. Andrea Comandini, CNRS Research Scientist at ICARE-INSIS for their valuable feedback, and scholarly input, which have enriched the content and rigor of this dissertation. I would like to extend my gratitude to M. Pierre Alexandre Glaude, CNRS Research Director at the LRGP-University of Lorraine for accepting the role of the President/Examiner of the jury and to Ms. Véronique Dias, Researcher at the IMMC-Catholic University of Louvain, for honoring me by accepting the role of an Examiner. Furthermore, I am thankful to M. Laurent Gagnepain, Scientific Coordinator at l'ADEME and Ms. Sylvie Gosselin, Engineer at PC2A, University of Lille for their participation in the thesis jury.

A heartfelt appreciation goes to Ms. Pascale Desgroux and M. Alessandro Faccinetto. Your availability, expertise, and support, both scientifically and morally, have been of immeasurable assistance to me throughout these years and will continue to be invaluable for my future endeavors. I extend sincere thanks to M. Abderrahman El Bakali and M. Xavier Mercier for their generosity and invaluable scientific insights. I express my deepest gratitude to M. Kevin Van Geem, Professor at University of Ghent for their invaluable collaboration. I express my gratitude to M. Benjamin Hanoune, PC2A Laboratory Director for his availability and generosity throughout this dissertation. I extend my sincere gratitude to all the staff of the PC2A laboratory, with a special mention to Valerie Vilain, Pascal Demaux, Sébastien Batut, Etienne Arpin, and Olivier Hombert. I want to emphasize that without your support and presence, this work would not have been possible. I sincerely thank all the Post-Doctoral Students, Doctoral Students, and interns of PC2A, both past and present, for their camaraderie and the unforgettable moments we've shared during my tenure in the laboratory with a special mention to Quan, Dorra, Thomas, Nesrine B, Nesrine S, Juan, Jessy, Marwa, Doha, and Mohammad. Heartfelt appreciation goes to Romain and Léo for their genuine sincerity and dedicated efforts.

I extend my deepest gratitude to my family and for their steadfast support, trust, and encouragement throughout my journey. I am especially thankful to my sister Anika for her unwavering presence, despite the distance, her infectious joy, and countless trips to Lille during the most challenging times. To my mother, I am profoundly grateful for instilling in me the resilience to face difficulties with dignity, hope, and a smile, and for always believing in my abilities. Your sacrifices to provide opportunities for both Anika and me are deeply appreciated, and it is your efforts, immeasurable by any scale, that have equipped me to pen down this manuscript. Lastly, I express my heartfelt thanks to Aman for his unwavering presence by my side through the highs and lows, for his encouragement, support, and invaluable guidance. Without you, reaching the finish line would not have been possible.

In the memory of my dad, Late M. Arvind Kumar and my granny, Late Ms. Sharda Sood …

Abstract

Biofuels and other chemicals derived from biomass are now recognized as integral components of a sustainable energy mix, holding the promise to bolster our society's energy security. Despite the considerable interest presented by biofuels, their combustion processes may exacerbate the formation of Oxygenated Polycyclic Aromatic Hydrocarbons (OPAHs), potentially influencing the characteristics of soot. This thesis focuses firstly on identifying and quantifying oxygenated aromatics generated during the combustion of a lignin-based biofuel under flame conditions. Laminar premixed flames of anisole (a surrogate for lignin-based biofuels) and blends of hydrocarbon fuels using advanced Gas Chromatography (GC) were investigated. Employing a sample enrichment technique and various chromatographic analyses, including 1D GC-MS, 1D GC-SPT-FID, and 2D GC-MS, facilitated the identification of approximately 100 different oxygenated aromatics. These findings shed light on the fuel decomposition pathways leading to OPAH formation. Furthermore, the thesis presents a detailed experimental database illustrating the evolution of mole fraction concerning flame height for various oxygenated and non-oxygenated aromatics. A comparison to other biofuels such as 2,5-DMF and ethanol was also performed and it revealed significant differences in the formation of intermediate species and pollutants, including OPAHs, due to distinct molecular structures. The study also investigates the characteristics of soot particles, revealing particles smaller than 10 nm using LII and SMPS. It was observed that at a constant equivalence ratio, the presence of anisole increased the number of small soot particles formed in these flames. These particles are referred to as primary soot particles due to their small size. Additionally, it was noted that the soot inception processes began at an early flame height in the anisole flames compared to the reference flame without anisole. Moreover, soot growth processes were observed to be very limited in these flames. At a higher equivalence ratio of 1.90, anisole produced more soot than DMF under similar conditions. Although the growth processes were limited, they occurred at a faster pace in the anisole flame compared to the DMF flame. In addition to measuring oxygenated aromatics and soot particles, temperature profiles were determined in this work using an experimental protocol that was validated for laminar premixed flames by comparison with other techniques such as LIF-NO. Our findings demonstrated that employing the extrapolation method, which utilizes four thermocouples of varying diameters, facilitated straightforward calibration of radiative losses.

Key words: biofuels, OPAHs, PAHs, aromatics, combustion, premixed flames, anisole, kinetics, gas chromatography.

Résumé

Les biocarburants et autres composés dérivés de la biomasse sont désormais reconnus comme des éléments essentiels pour un mix énergétique durable, susceptibles de renforcer la sécurité et viabilité énergétique de notre société. Malgré l'intérêt considérable que présentent les biocarburants, leurs processus de combustion peuvent cependant contribuer à une formation significative d'hydrocarbures aromatiques polycycliques oxygénés (OPAH), influençant potentiellement les caractéristiques et propriétés des particules de suies susceptibles d'être formées. Cette thèse se concentre d'abord sur l'identification et la quantification des aromatiques oxygénés générés lors de la combustion d'un biocarburant à base de lignine dans des conditions de flamme. La structure de flammes laminaires prémélangées atmosphériques d'anisole (un substitut des biocarburants à base de lignine) et d'hydrocarbures ont été étudiées en utilisant un parc de plusieurs chromatographes en phase gazeuse (GC) complémentaires permettant une analyse détaillée des milieux réactionnels. L'utilisation de techniques d'enrichissement d'échantillons couplées aux analyses chromatographiques, notamment GC-MS 1D, GC-SPT-FID 1D et GC-MS 2D, a permis l'identification d'environ 100 composés aromatiques oxygénés différents. Ces résultats mettent en évidence les voies privilégiées de décomposition du carburant conduisant à la formation des OPAH. De plus, le travail réalisé a permis d'établir une base de données expérimentales détaillées illustrant l'évolution de la fraction molaire d'un grand nombre de composés aromatiques, oxygénés ou non, en fonction de la position dans les flammes. Une comparaison avec d'autres biocarburants tels que le 2,5-DMF et l'éthanol a également été réalisée et a révélé, en raison de structures moléculaires distinctes, des différences significatives dans la formation des espèces chimiques intermédiaires et des polluants, y compris les OPAH. L'étude s'est également focalisée sur la caractérisation des particules de suie formées lors de la combustion de ces biocarburants. La mise en œuvre des techniques LII et SMPS a ainsi permis de révéler la présence de particules inférieures à 10 nm. Il a également été observé qu'à richesse constante, la présence d'anisole augmentait le nombre de petites particules de suie formées dans ces flammes. Ces particules sont appelées particules primaires de suie en raison de leur petite taille. De plus, il a été noté que les processus d'apparition de suie commençaient à une hauteur de flamme précoce dans les flammes d'anisole par rapport à une flamme de référence sans anisole. Les processus de croissance des suies se sont d'ailleurs révélés très limités dans ces flammes. Pour une richesse plus élevée de 1,90, l'anisole produit de plus importantes quantités de suie que le DMF dans des conditions similaires. Bien que les processus de croissance aient été limités du fait des conditions opératoires, ils se sont malgré tout produits à un rythme plus rapide dans la flamme d'anisole que dans la flamme de DMF. En complément de la mesure des aromatiques oxygénés et des particules de suie, les profils de température ont été déterminés à l'aide d'un protocole original utilisant quatre thermocouples de différents diamètres afin de pouvoir corriger les mesures des pertes radiatives. Le protocole a été validé par comparaison avec d'autres techniques telles que la thermométrie LIF-NO.

Mot clés : Biocarburants, HAPOs, HAPs, aromatiques, combustion, flammes prémélangées, anisole, cinétique, chromatographie en phase gazeuse.

Table of contents

Introduction

The essence of energy in our society is constantly growing to ensure the quality of life and smoothly run other elements of the world's economy [1,2]. Energy production is, and remains, the main challenge of today's societies. Since the industrial revolution in the 19th century, until today, energy mainly comes from fossil fuel resources i.e., coal, oil, and natural gas (non-renewable resources). Over the years, a surging boost in the global energy demand has led to a continuous increase in the consumption of these resources. Furthermore, this consumption is not stagnant and in fact is relentlessly increasing as we continue to burn more each year to keep up with the increasing energy demand. This inflation in energy consumption and dominance of fossil fuels has not only led to environmental deterioration and climate change, remarkably due to the endless CO_2 emissions and global alteration of the composition of our atmosphere, but is also a reminder of the fragility and unsustainability of our current energy system [3]. Ample pollutants like carbon monoxide (CO), nitrous oxides (NO_x), sulfur dioxide (SO_2), Polycyclic Aromatic Hydrocarbons (PAHs) and soot particles produced in real combustion processes severely affect human health by damaging the cardiovascular system, weakening the immune system and impairing lung functioning [4]. Despite such unfavorable effects, global energy production from the combustion of fossil fuels continues to account for over 80% of the total energy produced across the world [3].

The intercontinental recognition of these issues has led to a series of international agreements aiming at limiting greenhouse emissions and decarbonizing the energy system. To do so, research interests have switched to the development of hybrid, all-electric or fuel cell technologies to electrify land-based transport within the next few decades and completely phase out the Internal Combustion Engine Vehicles (ICEVs). Although the hybrid, all-Electric Vehicles (EVs) fully fit into our current needs, the increased prices for the minerals (e.g., copper, lithium, nickel, manganese, cobalt, graphite, rare earth metals etc.) needed to manufacture batteries pose additional challenges. In addition, electric grids still need to get much cleaner before the electric vehicles are truly emissions free. Moreover, the amount of minerals needed to manufacture a conventional car and an electric car are nearly ~34 kg/vehicle and ~207 kg/vehicle respectively, i.e., a typical electric car requires six times the mineral inputs of a conventional car [5]. These minerals are mined by the mining industry that uses energy from fossil fuels and contributes to approximately 8% of the global carbon footprint [6,7].

Though electric vehicles represent a maturing technology suitable for passenger or light-duty vehicles in the long-run, as the range and mass of the vehicles increase, electrification becomes increasingly difficult. Despite often being grouped together shipping, aviation and haulage each presents unique challenges for decarbonization [8]. Regulations and aircraft designs imply that the aviation sector is dependent on jet fuels for the foreseeable future, with liquid fuels being deemed as the most suitable option due to the scales required. Heavy-duty transportation has constraints on cargo space and payload which means fuels with high energy density are necessary for economic operation [8]. Because of the time needed to reduce and phase out the current infrastructure and replace it with zero-carbon energy system on a large-scale for the heavy-duty transportation system, the transition, if at all technically, economically, and socially feasible, is still challenging to achieve within the next 40 years [9]. This means that for the present and the next 40 years, fossil fuel resources are still likely to provide for a large portion of the global energy demand, despite the significant progress made in alternative energy systems such as fuel cells and battery-based electrification.

Though the transition to decarbonize the current energy system is happening, it is certainly not fast enough for the renewables and nuclear to keep up with the growing energy demand. Particularly for the transport sector, the introduction of biofuels is considered as a promising and cost-effective approach at the current stage for realizing a decarbonized energy system [10,11]. Biofuels are considered as a vital part of sustainable energy portfolio, where they promise to contribute to our society's energy security [12] especially in sectors where electrification is not yet feasible. Transport fuels are now subjected to blending mandates with alternative fuels to achieve ambitious emission targets in several countries. In this context, biofuels present the short-term option and their demand is likely to remain in the long-run to fulfil such mandates as they are identical to the petroleum-based fuels that they are designed to replace making them compatible with today's engines and other infrastructure [11]. Substitute fossil fuels mandates are incentivizing investments in the production of biofuels at large scales. Liquid biofuels can facilitate the transition towards a more sustainable transportation sector by curbing carbon emissions while maintaining most of the current vehicle fleet. Over recent years, various oxygenated fuels have received increasing interests as alternative engine fuels, not only due to their potential in improving engine combustion and emission performance [13,14] but also due to their renewable and environmentally-friendly nature which may provide a pathway towards a carbon-neutral energy system [15].

Recent research and development undoubtedly present a sign of progress towards providing a sustainable energy system for transportation. However, the road towards the widespread implementation of oxygenated biofuels needs to address several issues such as the availability of feedstocks, large-scale production techniques, as well as a fundamental understanding of their combustion and emission characteristics which are closely related to their end-use in practical combustion devices. The first-generation biofuels present some skepticism to scientists concerning the sourcing of feedstocks and the impact it may have on the biodiversity because of the competition with food crops which sets limits in their large-scale production. Ongoing debates have shifted focus onto biofuels that are derived from the lignocellulosic feedstock, i.e., the biofuels of the 'second generation' [16,17]. Advanced biofuels, also referred to as 2nd generation biofuels, are carbon-based fuels that are produced by innovative processes via lignocellulosic materials (abundant nonfood materials) for which commercial utilization is still under development. Currently, their production is not cost effective because several technical barriers need to be overcome before their potential can be realized [17,18].

Most of the currently proposed biofuels contain one or more oxygen atoms in their chemical structure (in the form of alcohol, ester, or ether functionality), and are commonly referred to as "oxygenated biofuels". It is well-known that in most cases, oxygenated biofuels generally present a smaller sooting tendency as compared to their structurally-analogous hydrocarbons; the reason being in most cases their lower tendencies to form soot precursors [19]. The presence of oxygen alone in the chemical structure of biofuels leads to the formation of more CO_2 and CO, thereby removing the carbon atoms from the system which would otherwise participate in soot formation [19,20]. The presence of the oxygen atoms in the structure of biofuels is likely to modify the formation of aromatic species, especially oxygenated aromatics, that may profoundly modify the properties of the formed soot particles [21]. Soot particles generated from the combustion of biofuels differ from particles from the combustion of conventional fossil fuels as they consist of higher amounts of oxygenates [21], altered nanostructure [22] and are potentially more toxic. Recent studies have shown that the combustion of oxygenated biofuels produces fewer large soot particles, and therefore a lower mass concentration of the particulate matter than that resulting from the combustion of conventional petroleum fuels [23,24]. Impressive soot reduction characteristics strongly support the use of biofuels. However, the number concentration of sub-10 nm soot particles is also strongly enhanced (see Figure 1) [23,25]. The underlying reasoning so far behind the increased number concentration of small soot particles during the combustion of oxygenated biofuels is not clear. A greater number of small soot particles present a disadvantage of not being trapped by the particulate filters currently in use. The use of biofuel blended with commercial fuel like diesel reduces the total mass concentration of particulate matter in agreement with literature data [19,25] but also significantly increase the number concentration of sub-10 nm particles [23].

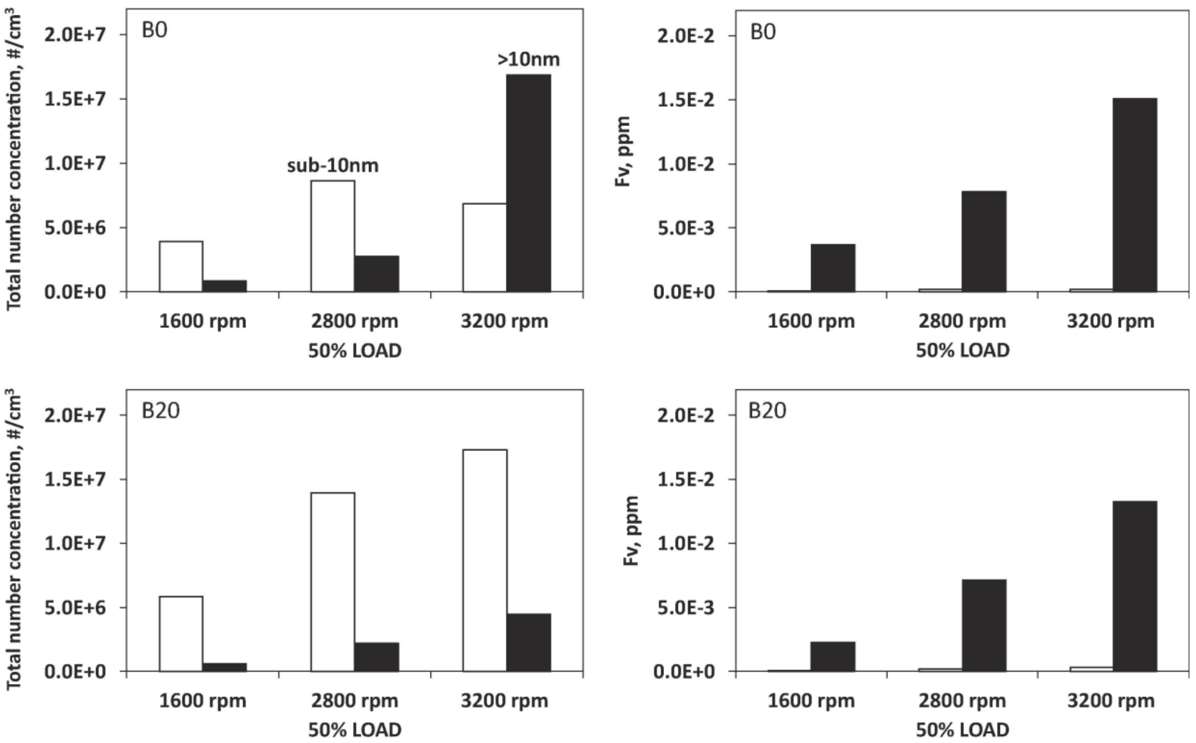

Figure 1 : Particle total number concentration (on the left) and soot volume fraction (on the right) of sub-10 nm (white bars) and larger soot particles (black bars) retrieved from particle size distributions reported for diesel fuel (B0) and 20% v/v rapeseed methyl-ester and diesel fuel blend (B20) measured at the exhaust of a diesel engine by Sirignano et al. [23].

In addition to soot particles, oxygenated aromatics constitute a large family of undesirable pollutants from combustion processes. These species must play a very critical role in the combustion of biofuels, however, fundamental studies to investigate their formation especially in flame conditions are very scarce in the literature. Some studies have illustrated the acute challenges associated with the experimental identification of oxygenated aromatics and their isomers [26], whereas this information is somewhat crucial for decoding their formation kinetics [26]. To achieve safe integration of biofuels into the energy landscape, fundamental laboratory scale studies on Oxygenated Polycyclic Aromatic Hydrocarbons (OPAHs) emissions and the size of soot particles during the combustion of biofuel doped fuel blends are essential. Figure 2 illustrates a pictorial representation of the underlying context behind this study. In this context, the current study aims to contribute to a better understanding of the discussed phenomena. This PhD research project was funded by ADEME and la Region Hauts-de-France and has two main objectives. The first and the main part was to study the flame structure of lignin-based biofuel doped blends i.e. anisole doped hydrocarbon fuel blend, with a special focus on the oxygenated aromatics. Ethanol and dimethyl furan doped blends were also studied for comparison. This thesis is essentially focused on obtaining a detailed experimental database of species profiles in premixed flames at atmospheric pressure to characterize the combustion of lignocellulosic biofuels. This involves precisely identifying and quantifying the maximum number of new oxygenated aromatics and other pollutants using advanced 1-D and 2-D Gas Chromatography (GC) setups equipped with a trap accessory. To complete the experimental study, flame temperature profiles are also measured using thermocouple-based thermometry. The second part concerns the characterization of the small soot particles that are formed in these same biofuel doped blends using the Laser Induced Incandescence (LII) and the Scanning Mobility Particle Sizer (SMPS) experimental techniques.

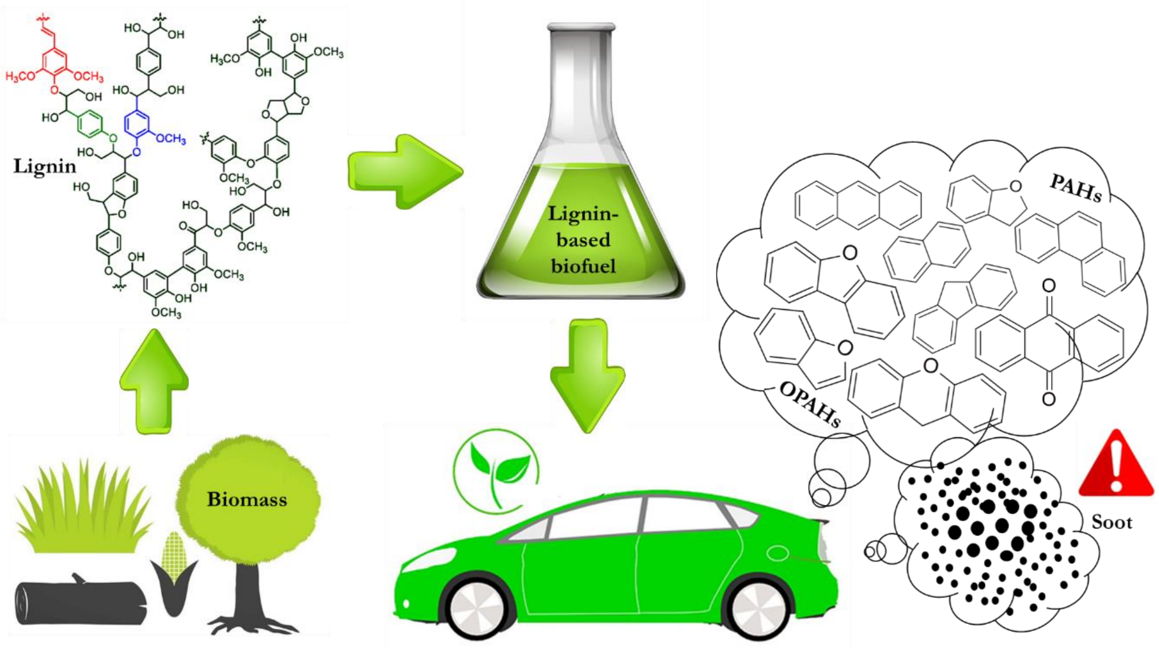

Figure 2 : A pictorial representation of the context of this study together with two-fold objective focusing on the OPAHs and the small soot particles that can be formed during the combustion of lignin-based biofuels.

This thesis report consists of **6 Chapters** followed by a general conclusion and potential perspectives. **Chapter 1** presents a brief background and a summary of the existing studies that have previously focused on the experimental detection of OPAHs during the combustion of biofuels in real combustion systems as well as in laboratory-scale reactors. Soot formation studies from the combustion of lignocellulosic biofuels are also listed in the same chapter. **Chapter 2 and Chapter 3** detail the experimental setup of the flame burner together with the analysis techniques used and special details concerning the new developments and the methodology adopted to measure the temperature of the flames, respectively. **Chapter 4** presents the qualitative as well as quantitative results concerning experimental observation of oxygenated aromatics in biofuel-doped flames along with their dependence on the biofuel amount and the equivalence ratio. Later, **Chapter 5** presents a comparison study of species' profiles produced from different biofuel-doped flames to study the dependence of the formation of aromatics and other pollutants on the structure of the biofuel. Finally, **Chapter**

6 presents some results on the characterization of the soot particles formed in these flames in terms of the soot volume fraction and the particle size distributions.

Chapter 1. Combustion of biofuels and its influence on the formation of aromatics and soot: State of the art

This chapter presents a prevalent context and a brief summary of the studies focusing on the influence of the oxygenated additives on the formation of aromatics and soot in a combustion environment. Section 1.1 presents a concise literature review on the formation of OPAHs from oxygenated biofuels. This discussion is divided into two parts. The first part is devoted to listing existing studies where researchers experimentally detected OPAHs during the combustion of solid and liquid biomass-derived fuels in real-combustion systems (engines and in-house stoves). These studies further motivated researchers to carry out fundamental studies in laboratory-scale flames and reactors to analyze these species qualitatively and quantitatively. These fundamental studies constitute the second part of this section. Later, Section 1.2 presents a brief literature review on the soot formation behavior of biofuels, with special attention devoted to lignocellulosic biofuels. Section 1.1 and Section 1.2 altogether underline the inadequacy of our current understanding about the combustion of oxygenated biofuels, especially the ones that are lignin-based in terms of their tendency to produce oxygenated aromatics and soot. Thereupon, Section 1.3 presents the why and wherefore behind the choice of our biofuel for the current study followed by a summary of its existing studies in the literature. The chapter is subsequently concluded with a small discussion on the limitations in our current understanding and provides a preliminary scope of this thesis (Section 1.4).

1.1. Literature review: OPAHs and associated PAHs from biofuels

Following PAHs (Polycyclic Aromatic Hydrocarbons), scientific interest for OPAHs (Oxygenated Polycyclic Aromatic Hydrocarbons) has increased in the past decade because of their persistence in the environment and concern over potential toxicity [27]. They consist of one or more oxygen atoms attached to an aromatic ring structure that may also contain other chemical functional groups. Their formation can be derived from petrogenic and pyrogenic sources, and via chemical or photo-oxidation of the PAHs [27]. In addition, they are expected to be largely formed during the thermal conversion of lignin [28]. Ongoing research has also described several processes of incomplete biodegradation leading to the production of OPAHs [29–32]. Determinations of individual and mixed OPAH toxicities are active areas of research.

There is increasing evidence that OPAHs are more toxic than their parent PAH analogs [27,33–37]. It has also been reported that OPAHs are more persistent in the environment as opposed to other organic compounds [27,31,32]. Over the past decade, researchers have recognized that it is of great importance to understand their emission characteristics and formation mechanisms especially during the combustion of biomass, which is a promising renewable source of energy in the near-future. Table 1. 1 presents a list of the most representative studies where OPAHs (and PAHs) associated with Particulate Matter (PM) produced during the combustion of biomass in real combustion systems were experimentally detected and quantified.

Table 1. 1 : A summary of the most representative experimental studies devoted to the detection of particulate and gas phase OPAHs produced during the combustion of biomass/biofuels in real combustion systems like engines and in-house stoves.

Reference	**Experimentally detected OPAHs**	**Biofuel**	**Combustor type**	**Analysis technique***
Shen et al., 2011 [38]	9-Fluorenone, 9,10-Anthraquinone, Benz[a]anthracene-7,12-dione, Benzanthrone	Crop residues and coal	Cooking stove	GC-MS
Vicente et al., 2015 [39]	9-Fluorenone, 9,10-Anthraquinone, 1-Indanone, 1,4-Naphthaquinone, 1,2-Acenaphthylenequinone, 1,8-Naphthalic anhydride, 2-Methylanthracene-9,10-dione, Benzo[a]fluorenone, 7H-Benz[d,e] anthracene-7-one, Naphthacene-5,12-dione, 6H-Benzo[c,d]pyrene-6-one	Biomass	Cooking stove	GC-MS
Nyström et al., 2016 [40]	9,10-Anthraquinone, Cyclopenta[def]phenanthren-4-one, 7H-Benz[de]anthracen-7-one, Benz[a]anthracene-7,12-dione	Rapeseed methyl ester biodiesel	Engine	GC-MS
Guan et al., 2017 [21]	9-Fluorenone, 9,10-Anthraquinone, Benz[a]anthracene-7,12-dione, Benzanthrone, 1-Naphthaldehyde, 1,4-Naphthoquinone	Waste cooking oil biodiesel and ethanol	Engine	GC-MS
Ahmed et al., 2018 [41]	Anthraquinone, Cyclopenta[def]phenanthren-4-one, Benzanthrone, Benz[a]anthracene-7,12-dione	Ethanol	Engine	GC-MS
Li et al., 2018 [42]	9,10-Anthraquinone, 9-Fluorenone, Benzanthrone, Benz[a]anthracene-7,12-dione, 1,4-Naphthoquinone, 1-Naphthaldehyde	Waste cooking oil biodiesel	Engine	GC-MS
Lara et al., 2023 [43]	9-Fluorenone, 9,10-Anthraquinone	Biodiesel (78% soybean+28 % palm)	Engine	GC-MS

In 2011, Shen et al. [38] studied the combustion of indoor solid fuels (crop residues and coal) under simulated kitchen conditions and reported the presence of several OPAHs with 9-fluorenone being the most abundant species. They also observed that in comparison to parent PAHs, OPAHs presented a higher tendency to be adsorbed on particulate matter (PM), especially fine PM. High affinities of OPAHs to fine particles were also reported earlier in other studies [44,45]. Later, in 2015, Vicente et al. [39] carried out combustion experiments in a manually operated batch stove (burning wood logs) and an automatic pellet stove. They also analyzed the PM samples from the exhaust flue gas via Gas Chromatography-Mass Spectrometry (GC-MS) to quantify fifteen OPAHs. In 2016, Nyström et al. [40] studied the physical and chemical properties of exhaust particle emissions during an engine operation using standard diesel and biodiesel. They observed that the particulate mass concentration almost halved compared to when diesel was used and associated this decrease with a decrease in the average particle size. When shifting from diesel to biodiesel, the decrease in the particle mass and size was attributed to the presence of less PAHs but a relatively higher fraction of OPAHs by the authors.

In 2017, Guan et al. [21] characterized the soot particles (and associated particle-phase organic compounds) emitted from a diesel engine fueled with oxygenated fuel blends (Diesel-Biodiesel/DB and Diesel-Biodiesel-Ethanol/DBE). They used waste cooking oil biodiesel and reported that employing oxygenated fuel blends increased the total measured OPAHs emissions. They also observed that both the blends reduced the particle mass emission rate as well as the total number concentration of the soot particles. In addition, they reported that the geometric mobility diameter of the particles also decreased with an increase in the blended ratios of the oxygenated fuels, i.e., their size distribution curves moved towards smaller-sized bins.

The following year, Ahmed et al. [46], determined emission factors for OPAHs and PAHs from two different fuel flexible light duty vehicles using the GC-MS analysis. Three different gasoline/ethanol blends, commercially available in Sweden, i.e., gasoline E5, (with 5% v/v ethanol), E85 (with 85% v/v ethanol), and the winter time quality E70 (with 70% v/v ethanol), were tested. They reported higher average total OPAH emissions when driving vehicles with E85 compared to when operating with E5. The most abundant OPAH in almost all their samples was 9,10-anthraquinone. Later, Li et al. [42], compared PAH and OPAH emissions from a direct injection diesel engine fueled with conventional diesel, waste cooking oil biodiesel (B100), and their two blends (B20 and B50). Their results showed an increasing trend of OPAH emissions with added biodiesel. Almost all oxygenated derivatives were over their parent PAHs for the fuels with high biodiesel content (B50 and B100). They also observed that high molecular weight PAHs exhibited higher oxygenated derivative fractions than those of low molecular weight PAHs. An increase trend of the total OPAH emissions was observed with increasing engine load. In addition, they observed that adding biodiesel to diesel also led to increase in the total OPAH emissions as shown in Figure 1. 1.

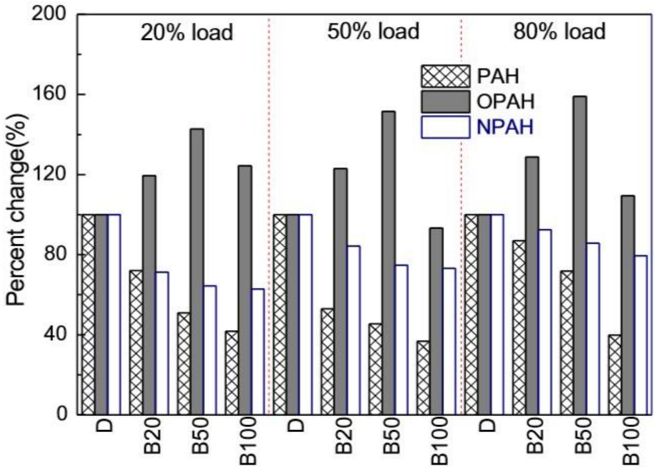

Figure 1. 1 : The percent change of total PAH, OPAH, and NPAH for the tested fuels at different loads reported by Li et al. [42].

In 2023, Lara et al. [43] performed a qualitative and quantitative analysis of PAHs and OPAHs present in different soot samples generated using a diesel engine bench powered by diesel and biodiesel fuels under different combustion conditions. The predominant compounds in all soot samples studied were fluorene, phenanthrene, fluoranthene, pyrene, 9-fluorenone and 9,10-anthraquinone. They also reported that the percentage of OPAHs with respect to the total PAHs was highest in the soot generated from a biofuel. The list of studies mentioned in Table 1. 1 present real combustion systems where OPAHs are emitted as pollutants. Most of the OPAHs reported in these studies seem to have the ketone functionality. Though these studies provide hints concerning the different OPAHs that one might expect to be formed during the combustion processes (or post-combustion phenomena) and their emission factors (in µg/km), other possibilities and OPAHs formation mechanisms are not clear. Besides, these studies also indicate that an increase in the amount of the biofuels used leads to an increase in the emission of OPAHs. Motivated by the diverse studies on OPAHs emissions from real combustors, researchers decided to investigate them in fundamental laboratory scale reactors. Table 1. 2 lists the main experimental studies carried out in fundamental laboratory-scale systems where OPAHs were also quantified during the combustion of biofuels.

Table 1. 2 : Summary of the main experimental laboratory-scale studies on the combustion of biofuels where OPAHs were detected and quantitatively analyzed. Studies for anisole have been highlighted in bold.

Reference	**Experimentally detected OPAHs**	**Biofuel**	**Combustor type**	**Analysis technique**
Therrien et al., 2010 [47]	Benzofuran, Dibenzofuran, 9,10-Anthracenedione 2-Naphthaldehyde	Ethanol	Premixed flame	GC-FID/MS
Nowakowska et al., 2014 [48]	**Benzofuran, Dibenzofuran**	**Anisole**	**Jet-stirred reactor**	**GC-FID/MS**
Pelucchi et al., 2018 [49]	**Benzofuran, Dibenzofuran**	**Anisole**	**Flow reactor**	**GC×GC-FID/TOF-MS**
Nowakowska et al., 2018 [50]	Benzofuran, Dibenzofuran, 2,3-Dihydrobenzofuran, 1-Indenol, Naphthol, 2-Methyl benzofuran, 2,2-Biphenyldiol	Guaiacol	Jet-stirred reactor	GC-FID/MS
Bierkandt et al., 2019 [51]	**Benzofuran**	**Anisole**	**Premixed flame**	**VUV-MBMS-PEPICO**
Yerrayya et al., 2019 [52]	Benzofuran, 2-Methyl benzofuran, Dihydrobenzofuran	Guaiacol	Micro-pyrolyzer	GC-MS
Yuan et al., 2019 [53]	**Benzofuran, Dibenzofuran**	**Anisole**	**Flow reactor**	**SVUV-PIMS**
Namysl et al., 2020 [54]	Benzofuran, Dibenzofuran	Benzaldehyde	Jet-stirred reactor	GC-MS
Kim et al., 2021 [55]	Benzofuran, Dibenzofuran, Dihydrobenzofuran	Ethyl phenol isomers	Flow reactor	GC-MS
Chen et al., 2022 [56]	**Benzofuran, Dibenzofuran**	**Anisole**	**Laminar counterflow flame**	**TOF-MBMS/GC-MS**

In 2010, Therrien et al. [47] investigated flat laminar premixed ethanol/ethylbenzene flames (with 0%, 25%, 50%, 75% and 90% ethanol) at atmospheric pressure. They stabilized all the flames at their visual soot onset thresholds, and kept similar temperature profiles for all flames. The temperature was controlled by adjusting the total cold gas velocity through the burner for each flame. By increasing the total cold gas velocity, the flame was pushed away from the burner surface and consequently, the heat loss to the burner reduced. This way, temperature profiles of all the flames were kept nearly-constant to prevent the temperature effects from governing the flame chemistry. They identified and quantified lighter species and several aromatics (OPAHs and PAHs) using the GC-MS system. Amongst OPAHs, they identified and quantified benzofuran, 2-naphthalenecarboxaldehyde, dibenzofuran, and 9,10-anthracenedione in the range of few ppm.

Later in 2014, Nowakowska et al. [48] studied anisole pyrolysis and stoichiometric oxidation in a Jet Stirred Reactor (JSR, 673–1173 K, residence time 2s, 800 Torr) coupled with Gas Chromatography–Flame Ionization Detector and Mass Spectrometry (GC-FID/MS). The main pyrolysis products were phenol, methane, carbon monoxide, benzene, and hydrogen. They detected and quantified benzofuran, dibenzofuran (OPAHs), naphthalene and acenaphthylene (PAHs) in the range of hundreds to thousands of ppm. They also proposed a detailed kinetic model (303 species, 1922 reactions) based on a combustion model for light aromatic compounds which they extended to anisole.

In 2018, Pelucchi et al. [49] presented experimental data obtained in a flow reactor coupled to two-dimensional GCs, and provided a kinetic mechanism for anisole pyrolysis. They used the Time-Of-Flight (TOF) MS to identify stable aromatics like benzofuran and other bicyclic aromatics with hydroxyl side chains. In the same year, Nowakowska et al. [50] investigated guaiacol (3-methoxyphenol) pyrolysis and oxidation in a JSR (623–923 K, residence time 2s, 800 torr) using the GC-FID/MS system. In their study, they also measured some OPAHs namely, 2,3-dihydrobenzofuran, 1-indenol, naphthol, 2-methyl benzofuran, and 2,2-biphenyldiol.

The following year in 2019, Bierkandt et al. [51], studied two laminar, premixed, fuel-rich anisole flames (30 torr) investigated by Molecular Beam Mass Spectrometry (MBMS) at two synchrotron sources where tunable vacuum-ultraviolet radiation enabled isomer-resolved photoionization. One flame with a stoichiometry of 1.2 was measured at the Advanced Light Source (ALS) in Berkeley, USA, while the other flame (ϕ = 1.6) was investigated at the Swiss Light Source (SLS) in Villigen, Switzerland. In both experiments, Synchrotron Vacuum-UltraViolet (SVUV) radiation provided soft ionization and a Molecular Beam Mass Spectrometry-Photoelectron Photoion Coincidence Spectroscopy (MBMS-PEPICO) setup was used for the identification and quantification of the combustion intermediates. In this study, they identified and estimated the absolute concentrations of OPAHs like benzofuran and acetyl naphthalenes as well as PAHs like naphthalene. They observed species with masses higher than guaiacol, but could not identify them because of the lack of known ionization energies. In the same year, Yerrayya et al. [52] focused on both experimental and theoretical analysis of fast pyrolysis of guaiacol in an analytical pyrolyzer coupled with the GC-MS in the temperature range of 723–923 K. They determined the relative concentrations for 3 OPAHs, namely, benzofuran, 2-methyl benzofuran, and dihydrobenzofuran at different temperatures in their study. Yuan et al. [53] studied anisole pyrolysis in a flow reactor using SVUV PhotoIonization Mass Spectrometry (PIMS) where they detected and quantified benzofuran and dibenzofuran.

Later, in 2020, Namsyl et al. [54] reported an experimental and modeling study of benzaldehyde oxidation in a JSR coupled with GCs. They identified 48 compounds including benzofuran and dibenzofuran. In 2021, Kim et al. [55] also measured three different benzofurans in flow reactor measurements of 2- and 3-ethyl phenol isomers. Later, in 2022, TOF-MBMS and GC were used by Chen et al. [56] to investigate a laminar counterflow diffusion-flame of anisole under oxy-fuel conditions and reported about forty stable species, including benzofuran and dibenzofuran.

In 2023, Wang et al. [57] comprehensively investigated the thermochemistry of OPAH species and other relevant radicals via quantum-chemical calculations. Temperature-dependent enthalpy of formation, entropy, and heat capacity were determined for several OPAHs. These thermodynamic properties are crucial for the development for kinetic mechanism. This study is not listed in Table 1. 2 as it only lists laboratory-scale experimental studies.

1.2. Literature review: soot from biofuels

Soot formation is a rather complicated process in itself as it involves various chemical and physical processes many of which are still not well understood. Aromatic species are considered as important soot precursors i.e., molecular gas-phase species that serve as the molecular building blocks of soot particles and play an important role in soot particle inception and mass/size growth [58]. Though knowledge gaps still exist, it is now generally accepted that soot formation proceeds from fuel molecules to particles via three broad lumped steps; (1) formation of gas-phase soot precursors, (2) formation of nanoparticles in the condensed phase, (3) surface growth and particle-particle coagulation [59–69]. Figure 1. 2 presents a schematic of the soot formation in flames reported in a detailed review by Martin et al. [66].

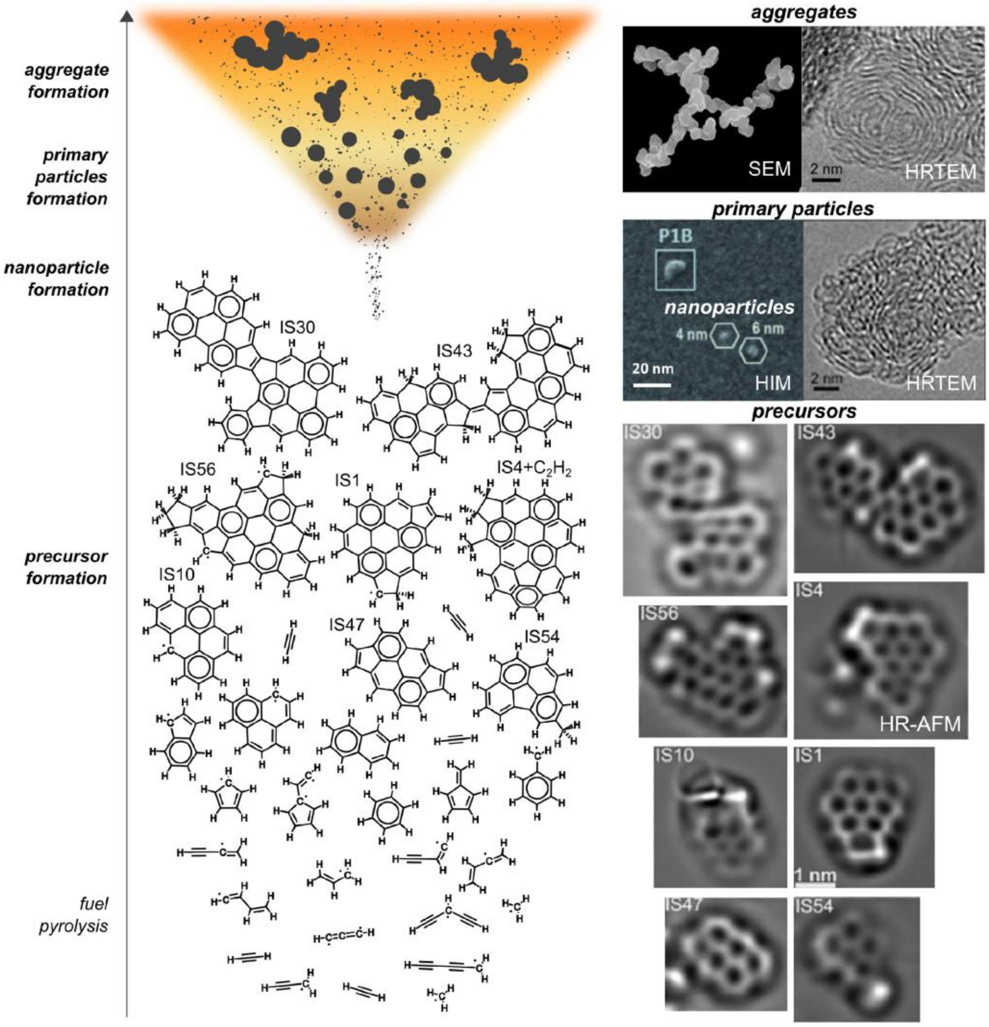

Figure 1. 2 : Schematic of carbonaceous particulate formation in flames [66].

The first step involves the decomposition of the parent fuel to form gas-phase smaller hydrocarbon molecules, radicals, and soot precursors such as PAHs. The second step is the transition process from the gas-phase precursors to condensed-phase carbonaceous nanoparticles. This complex gas-to-condensed-phase transition is termed as "*particle inception*" or "*soot inception*" and is the least well understood steps of soot formation [58,66]. Different inception pathways proposed in the literature have their own limitations and a universal explanation for different conditions does not exist yet [66]. After inception, the newly-formed incipient soot particles (size of 2-3 nm) eventually grow up in mass/size through interactions between gas-phase species and soot particles. Together with surface growth, particle-particle coagulation also takes place to form fractal-like soot aggregates. Faultless description of these processes is not yet attained which is why they are all very challenging to model. The overall soot formation process remains an everlasting unsolved problem in the combustion field as the complex processes involved render it difficult to isolate the different events. To address this issue, several fundamental studies in well-controlled laboratory-scale flames and reactors have been reported in literature to uncouple the convoluted factors involved. Many detailed reviews have been written to summarize these studies such as, by Richter and Howard in 2000 [69], Frenklach in 2002 [59], McEnally et al. in 2006 [61], D'Anna in 2009 [62], Hansen et al. in 2009 [70], Li and Fei Qi in 2010 [71], Wang in 2011 [63], Desgroux et al. in 2013 [64], Kittelson and Kraft in 2014 [68], Michelsen in 2017 [65], Wang and Chung in 2019 [72], Frenklach and Mebel in 2020 [60], Martin et al. in 2022 [66], as well as a recent glossary about soot nomenclature by Michelsen et al. in 2020 [58].

Furthermore, since recent research interests have shifted to the combustion of biofuels, fundamental studies to evaluate the sooting behavior of biofuels are also reported, where a general soot reduction trend is observed on the addition of oxygenated biofuels [19,73–80]. The dependence of oxygenated fuels' soot-reducing potential on the type of functional groups, the carbon skeletons of the base fuels and the flame configurations has been a subject of interest for numerous experimental and numerical studies investigating neat as well as blended 1st generation biofuels (ethanol, methanol, dimethyl ether (DME), dimethoxymethane (DMM), biodiesel etc.) [19]. Studies report that even with the same oxygen content, structurally-different oxygenated biofuels can have different soot reduction effectiveness [19,81–84]. Increase in the concentrations of O, OH and HCO radicals from the introduction of oxygenates may influence the soot formation process. Most often, the justification relies on their different tendencies to form soot precursors. High concentrations of O and OH radicals may promote the oxidation of carbon atoms, which would reduce the amount of carbon that produces soot precursors thereby inhibiting the soot nucleation process [19,20].

While there are numerous studies on the sooting behavior of the 1st generation biofuels during combustion processes [19], those for lignocellulosic biofuels (from the 2nd generation) are rather limited in this aspect. Research on soot formation from these biofuels is considerably recent. These biofuels have cyclic structures and aromatic rings in their molecular structure, and thus possess a relatively higher ability to form soot. This section is devoted to reviewing the recent existing studies in the literature concerning soot formation behavior of these biofuels. Table 1. 3 presents a recapitulation of three types of main experimental laboratory-scale studies carried out in this decade, where the authors focused on neat furanic (dimethyl furan, DMF and methyl furan, MF) and lignin-based biofuels as well as their blends. The table lists three different types of studies:

- Studies on the soot formation and the sooting tendencies of these biofuels.
- Studies focusing on the morphology and the nanostructure of soot particles from the combustion of these biofuels.
- Studies on particle size distributions (PSDs) from the combustion of these biofuels.

It must be noted that studies focusing on the measurement of soot precursors formed during the combustion of these biofuels have not been listed in the table but have been cited in the text when relevant.

Table 1. 3 : Summary of the main experimental laboratory-scale studies concerning the effects of furanic (in normal font) and lignin-based (in bold) oxygenated fuels on soot particle formation, morphology and nanostructure, and soot particle size distributions.

Reference	Biofuels	Base fuels	Apparatus	Analysis method*
Studies focusing on soot formation and sooting tendencies				
Cheng et al., 2014 [85]	DMF	-	Flow reactor	SVUV-PIMS; simulation
Sirignano et al., 2015 [86]	DMF, MF, Furan	Ethylene	Counterflow flame	LII and LIF
Alexandrino et al., 2015 [87]	DMF	-	Flow reactor	GC, FTIR; simulation
Viteri et al., 2016 [88]	MF	-	Flow reactor	GC–MS
Conturso et al., 2016 [89]	DMF, MF, Furan	Ethylene	Premixed flame	LII and LIF
Alexandrino et al., 2016 [90]	DMF	-	Flow reactor	GC, ex-situ soot collection
Liu et al., 2018 [91]	n-Butanol, DMF	Diesel	Co-flow flame	LII and LIF; simulation
Alexandrino et al., 2018 [92]	MF	-	Flow reactor	GC and ex-situ soot collection; simulation
Xiong et al., 2019 [93]	**Anisole**	**n-Heptane**	**Counterflow flame**	**LOSA**
Etz et al., 2021 [94]	**1-Phenylethanol, 2-Phenylethanol**	**-**	**Flow reactor**	**GC–MS; simulation**
Wang et al., 2021 [95]	**Anisole, Benzyl alcohol**	**n-Heptane**	**Co-flow flame**	**LII and LOSA**
Kim et al., 2021 [55]	**2-Ethylphenol, 3-Ethylphenol**	**-**	**Flow reactor**	**GC–MS; simulation**
Cruz et al., 2023 [96]	**Anisole**	**Gasoline surrogate**	**Co-flow flame**	**LII and LOSA**
Studies focusing on the morphology and the nanostructure of soot particles				
Gogoi et al., 2015 [97]	DMF	Diesel	Wick-fed burner flame	FTIR, XRD, Raman, TGA
Russo et al., 2016 [98]	DMF	Ethylene	Premixed flame	FTIR, Raman and UV–vis
Peña et al., 2018 [99]	DMF	Gasoline	Laminar diffusion flame	TEM, XRD, FTIR, EA, Raman spectra
Alexandrino et al., 2019 [100]	DMF, MF	-	Flow Reactor	TEM, XRD, Raman spectra
Jiang et al., 2020 [101]	DMF	n-Heptane	Co-flow flame	TEM, XRD, Raman spectra
Jiang et al., 2020 [102]	DMF	Iso-octane	Co-flow flame	HRTEM, XRD, Raman spectra
Chu et al., 2020 [103]	Ethanol, DMF	Iso-octane, n-Heptane	Co-flow flame	SEM, TGA
Zhang et al., 2022 [104]	**Anisole**	**n-Heptane**	**Laminar diffusion flame**	**TEM**
Studies focusing on the soot particle size distributions				
Conturso et al., 2017 [105]	DMF	Ethylene	Premixed flame	DMA
Xiong et al., 2018 [106]	**Veratrole, Anisole**	**n-Heptane**	**Co-flow flame**	**LII**
Zhang et al., 2022 [104]	**Anisole**	**n-Heptane**	**Laminar diffusion flame**	**TEM**

** LII: Laser Induced Incandescence; LIF: Laser Induced Fluorescence; GC-MS: Gas Chromatography Mass Spectrometry; FTIR: Fourier Transform Infrared Spectroscopy; TEM: Transmission Electron Spectroscopy; HR-TEM: High Resolution Transmission Electron Microscopy; SEM: Scanning Electron Microscopy; TGA: Thermogravimetric Analysis; DMA: Differential Mobility Analyzer; XRD: X-ray Diffraction; EA: Elemental Analysis; UV-vis: Ultraviolet visible spectroscopy; LOSA: Line of Sight Attenuation; SVUV-PIMS: Synchrotron Vacuum Ultraviolet Photoionization Mass Spectrometry*

It can be seen that only a few laboratory-scale studies have focused on the blending effects of furans (cellulose/hemicellulose derived biofuels) on soot formation in flames. Studies show that the effects of DMF on soot formation, either promoting or inhibiting, are sensitive to flame configurations. While DMF addition to ethylene reduced soot formation in premixed flames [89,105], it exhibited a promoting effect on PAH/soot formation in counterflow flames [86]. A possible explanation could be related to the different flame conditions, which changed the DMF consumption pathways thus affecting the efficacity of soot precursors formation. Different combustion conditions can change the effectiveness of important channels and might invert the particle production tendency of furanic fuels. Kinetic analyses revealed that under pyrolytic or fuel-rich conditions, the ring-opening to produce cyclopentadiene and phenol were favored, thereby resulting in enhanced PAH and soot formation [87]. Whereas under oxidative conditions (as in premixed flames), the addition of OH to produce acetylene, the acetyl radical and acetaldehyde become the primary consumption pathway for DMF, thereby hindering the formation of soot precursors and leading to reduced sooting propensity [89,105]. While the detailed consumption pathways may vary with the chemical kinetic mechanism, a consensus has been reached that the most important consumption channel for DMF is H-abstraction to yield the resonance-stabilized 5-methyl-2-furanylmethyl radical, which then forms phenol (C_6H_5OH) and cyclopentadiene (cC_5H_6) that are known to be important PAH precursors. Besides, DMF flame could produce higher amounts of cyclopentadienyl radicals (cC_5H_5) than MF, thereby leading to enhanced formation of naphthalene ($C_{10}H_8$). Liu et al. [91] and Conturso et al. [89] studied the effect of DMF blends on soot formation in flames where they reported a notable reduction in soot concentration with DMF addition. Conturso et al. [105] later also performed PSD measurements in flames and showed that DMF could significantly reduce the amount and thus the total mass of particles.

As demonstrated in Table 1. 3, there are only very few recent studies on soot formation from the combustion of lignin-based biofuels. Recently, Xiong et al. [93,106] studied the blending effects of anisole on soot formation in both laminar co-flow and counterflow flames of n-heptane. The results showed that anisole was more sooting than n-heptane, but less sooting than toluene. Later, Wang et al. [95] also reported similar observations and showed that the promotion effect of benzyl alcohol is stronger than that of anisole. They showed that with blending ratio of 20%, the soot volume fraction (f_v) in anisole/n-heptane and benzyl alcohol/n-heptane flames was approximately three times and five times more than that for n-heptane flames respectively. Recently, Cruz et al. [96] studied laminar co-flow diffusion flame of anisole and gasoline surrogate blend and suggested that the presence of anisole noticeably increased f_v by a factor of 1.6-1.8 depending on the flame height. They attributed this observation to the increased formation of aromatics in the presence of anisole. Yuan et al. [53] showed that anisole tended to produce cyclopentadienyl radicals (cC_5H_5), which are responsible for the production of aromatic products such as benzene, toluene, styrene and naphthalene. Given the special oxygenated aromatic structure of anisole, more fundamental soot studies are necessary to understand its soot formation behavior. Apart from anisole, recent studies by Etz et al. [94] and Kim et al. [55] focused on the pairs of 1-phenylethanol/2-phenylethanol and 2-ethylphenol/3-ethylphenol (isomers). The objective was to comprehend how the difference in the alcohol functional group could alter the reaction pathways and their sooting tendencies. The authors reported that the sooting tendency of 2-phenylethanol was higher than 1-phenylethanol, as the oxygen attached in the former is eliminated during the early decomposition process, leading to the formation of the benzyl radical. In comparison, the consumption of 1-phenylethanol produced more oxygenated products. On the other hand, 2-ethylphenol presented a lower sooting tendency than 3-ethylphenol, since the *ortho* position in 2-ethylphenol supports increased resonance stabilization of the radical intermediates and therefore produces more oxygenated products than 3-ethylphenol.

Though the summary of the fundamental studies listed in Table 1. 3 provides a preliminary understanding of the soot formation behavior of furanic- and lignin-based biofuels, it also highlights the exigency for more laboratory-scale investigations. It seems that these biofuels present contradicting results with respect to the configuration in which they are investigated as the fuel consumption pathways might differ. This is why one should be forethoughtful in projecting their results and trends obtained from one laboratory-scale configuration to another directly. It is thus necessary to study their blending effects on soot formation over a range of laboratory-scale configurations for a complete and profound understanding of their soot formation and growth behavior. It can be seen that in the case of lignin-based biofuels, only six studies in the past four years have focused on the soot formation. That said, though the sooting tendencies are being evaluated in these studies, there are no studies so far concerning the size of the soot particles. The size of the soot particles and the overall particle count are important parameters to investigate because of their negative health impacts. However, so far, no studies have been carried out on sub-10 nm or ultrafine particles that are produced from these kinds of biofuels. Measuring particles down to 10 nm (sub-23 nm) is also problematic and definitely requires improved methodologies and advanced measurement equipment.

1.3. Choice of the biofuel

To study oxygenated aromatics and the soot formation behavior of advanced biofuels at a fundamental level, we chose to study anisole (2nd generation biofuel and lignin-based biofuel) doped premixed flames at atmospheric pressure. Anisole is an essential component in biomass pyrolysis [107] and is commonly used as an effortless model compound to imitate the behavior of pyrolysis of lignocellulosic biomass [108,109]. Lignin is one of the main components of biomass, taking about 10–30% of its weight [110,111]. Its structure contains a large portion of aromatic rings with oxygen functionalities such as the hydroxyl and methoxy groups. Biofuels produced from lignin via different processes are referred to as “lignin-based biofuels” [112]. The simplest model compound that can be employed to investigate lignin-based biofuels is indeed anisole. The ether linkage in anisole is one of the most common functional groups found in these fuels. It can eventually lay the foundation for studies of larger aryl ethers. Until recent years, anisole has also been recognized as a worthy advanced biofuel candidate owing to its suitable properties. It improves the stability and storability of gasoline [113]. Gschwend et al. [114] reported that anisole is not more toxic than gasoline. It has bolstered its claim as a bio-based anti-knock fuel primarily due to its high Research Octane Number (RON = 120) [115] and octane sensitivity [116], and is now considered as a promising spark ignition fuel component. Besides, on account of its weak O-CH_3 bond (see Figure 1. 3), it is an exemplary and ideal precursor to produce phenoxy and cyclopentadienyl radicals [117,118]. These radicals are important intermediates and act as vital precursors of oxygenated and non-oxygenated polycyclic aromatic hydrocarbons [118]. Thus, anisole as a biofuel seemed suitable to investigate the formation of aromatics and then soot.

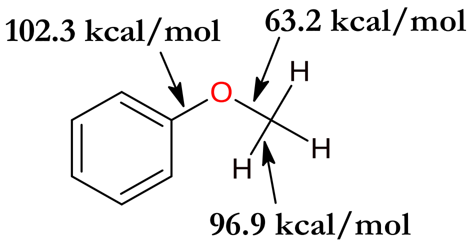

Figure 1. 3 : Structure of anisole and the bond dissociation energies [48].

Bibliography on anisole combustion

Anisole combustion has been a subject of interest for numerous fundamental investigations since recent years. Table 1. 4 presents a recapitulation of the main experimental laboratory-scale studies devoted to characterize its combustion behavior. The ignition delay time and laminar flame velocity measurements are generally used to characterize the combustion of a given fuel.

Table 1. 4 : A recapitulation of the different types of experimental laboratory-scale studies performed to characterize the combustion behavior and kinetics of anisole decomposition. Here, the subscript “$_i$” and “$_c$” are used for initial gas parameters and parameters after compression respectively, and ϕ represents the equivalence ratio.

Reference	**Apparatus**	**Experimental Conditions**
Measurement of ignition delay times		
Herzler et al., 2017 [119]	Shock tube	T_c= 770–1600 K; P_c= 10, 20, 40 bar; ϕ = 0.5
Büttgen et al., 2020 [120]	Shock tube	T_c = 900–1315 K; P_c= 10, 20, 40 bar; ϕ = 0.5, 1
Büttgen et al., 2020 [120]	Rapid compression machine	T_c= 750–900 K; P_c= 10, 20, 40 bar; ϕ = 0.5, 1, 2
Mergulhão et al. 2020 [121]	Rapid compression machine	T_c = 684 K, P_c = 20 bar, ϕ = 1 (anisole blend)
Measurement of laminar flame velocity		
Wu et al., 2017 [122]	Bunsen burner	T_i = 423 K, P_i = 1 bar, ϕ = 0.6–1.3
Wagnon et al., 2018 [123]	Premixed flame	T_i = 358 K; P_i = 1 bar; ϕ = 0.6–1.2
Zare et al., 2019 [124]	Constant volume bomb	T_i = 460–575 K; P_i = 1 bar; ϕ = 0.8–1.4
Zare et al., 2019 [124]	Constant volume bomb	T_i = 460–575 K; P_i = 0.5–3 bar; ϕ = 1
Studies devoted to investigate kinetics (pyrolysis, oxidation, etc.)		
Lin and Lin., 1986 [117]	Shock tube	T = 1000–1580 K; P = 0.4–0.9 bar; $\phi = \infty$
Zabeti et al., 2017 [125]	Shock tube	T = 1425, 1530 K; P = 1.62, 1.48 bar; $\phi = \infty$
Arends et al., 1993 [126]	Tubular reactor	T = 793–1020 K; P = 1 bar; $\phi = \infty$
Pecullan et al., 1997 [127]	Tubular reactor	T = 999–1003 K; P = 1 bar; $\phi = \infty$, 1.05, 0.62, 1.71
Platonov et al., 2001 [128]	Tubular reactor	T = 1023–1173 K; $\phi = \infty$
Friderichsen et al., 2001 [129]	Tubular reactor	T = 873–1373 K; P = 1 bar; $\phi = \infty$
Scheer et al., 2010 [130]	Tubular reactor	T = 1473-1573K; P = 1 bar; $\phi = \infty$
Pelucchi et al., 2018 [49]	Tubular reactor	T = 525–675 K; P = 1 bar; $\phi = \infty$
Yuan et al., 2019 [53]	Tubular reactor	T = 850–1160 K; P = 0,04, 1 bar; $\phi = \infty$
Mackie et al., 1989 [131]	Jet stirred reactor	T = 850–1000 K; P = 0.015–0.12 atm; $\phi = \infty$
Nowakowska et al., 2014 [48]	Jet stirred reactor	T = 673–1173 K; P = 1 bar; $\phi = \infty$,1
Chen et al., 2021 [26]	Jet stirred reactor	T = 700-1050 K, P = 0.921 bar, ϕ = 0.4
Bierkandt et al., 2019 [51]	Premixed flame	P = 0.04 bar; ϕ = 1.2,1.6
Zhang et al., 2021 [132]	Premixed flame	P = 1 bar; ϕ = 2.3 (anisole blend)
Chen et al., 2022 [56]	Counterflow diffusion flame	P = 1 bar

Büttgen et al. [120] reported the first experimental determination of ignition delay times for anisole in a Rapid Compression Machine (RCM), covering a wide range of temperatures, pressures and equivalence ratios. They also performed shock tube experiments to extend the range of investigated temperatures and demonstrated an Arrhenius behavior under all their studied conditions with significantly higher slopes in the RCM than in the shock tube.

Mergulhão et al. [121] also measured ignition delay times in the RCM (T = 684 K, P = 20 bar, ϕ = 1) for anisole/iso-octane blend (40/60) and showed a significant inhibiting effect of the added anisole on the alkane reactivity. Laminar flame velocities measurements for anisole were performed using either a constant volume bomb, flat flame or bunsen burners. The first flame velocity measurements for anisole were published in 2017 by Wu et al. [122] where they used OH chemiluminescence and reported flame speeds of 68.8, 65.6, and 58.1 cm/s for neat anisole, 4-methylanisole and toluene respectively (T = 423 K, ϕ = 1.06). Later, Wagnon et al. [123] used a premixed laminar flame with the heat flux method and Zare et al. [124] used the constant volume bomb method to measure the flame velocity of neat anisole. Studies quoted in Table 1. 4 were performed at atmospheric pressure; the study from Zare et al. [124] being an exception where the pressure and the temperature ranged from 0.5 to 3 bar and 358 to 575 K respectively.

In addition to ignition delay time and flame speed measurements, some studies were reported to study the kinetic behavior of anisole at atmospheric pressure. In 1983, Schlosberg et al. [133] performed anisole pyrolysis in small batch autoclaves and reported phenol, methane and CO as the major products using MS analysis. Later, using GC, Klein and co-workers [134,135] reported the formation of carbon monoxide, o-cresol, phenol, and benzene as major end products from anisole pyrolysis. Two other studies of anisole pyrolysis were performed using shock tube. Lin and Lin [117] studied CO formation via laser resonance-absorption and deduced rate constants for the related reactions from their measurements (Reaction 1. 1 and Reaction 1. 2).

$C_6H_5OCH_3$ (+M) = C_6H_5O + CH_3 (+M) *Reaction 1. 1*

This reaction of anisole decomposition to produce the phenoxy and the methyl radical is significantly favored by the very low bond dissociation energy of the C-O bond connected to the methyl group (63.2 kcal/mol [48]).

C_6H_5O = C_5H_5 + CO *Reaction 1. 2*

Zabeti et al. [125] studied anisole pyrolysis using mass spectrometry to follow the time evolution of the mole fractions of anisole+cresol, CO+C_2H_4, and benzene.

Anisole pyrolysis was most frequently investigated using flow reactors, with six studies in tubular reactors and about three in JSRs. In 1993, Arends et al. [126], studied the gas-phase decomposition of anisole in 10-fold excess of hydrogen in an atmospheric pressure tubular reactor, quantifying methane and phenol as the major products and proposing a rate constant for Reaction 1. 3. This pathway is particularly favored due to the low bond dissociation energy of the broken C-H bond (89 kcal/mol) to produce a neutral CO.

$C_6H_5CO = C_6H_5 + CO$ *Reaction 1. 3*

In 2010, Scheer et al. [130] studied the thermal decomposition of anisole and deuterated anisole to investigate formation of aromatics using a tubular reactor using a combination of photoionization and TOF-MS at 1473-1573K. They concluded that cyclopentadienyl radical decomposes to propargyl radical and acetylene. They proposed that the major pathway for the formation of benzene goes via methylcyclopentadiene (methyl recombination with cyclopentadienyl). Platonov et al. [128] studied homogenous pyrolysis of anisole using GC and found that increasing the temperature decreased the formation of phenolic compounds and increased the formation of PAHs. Friderichsen et al. [129] used both a flow reactor and a hyperthermal nozzle, with TOF-MS and Fourier Transform InfraRed (FTIR) spectroscopy. By identifying free radicals and other reaction intermediates, they demonstrated the importance of phenoxy and cyclopentadienyl radicals in the formation of naphthalene. More recently, Pelucchi et al. [49] reported some stable products during anisole pyrolysis like benzofuran and other bicyclic aromatics with hydroxyl side chains.

Later, Yuan et al. [53] achieved the most comprehensive speciation together with the previously reported stable products, important radicals, i.e., the phenoxy, cyclopentadienyl and methyl radicals using the SVUV-PIMS (at the National Synchrotron Radiation Laboratory in Hefei, China). Amongst tubular reactor studies, the study by Pecullan et al. [127] in 1997 was the first to investigate both pyrolysis and oxidation of anisole. Their experiments demonstrated anisole thermal decomposition near 1000 K mainly proceed through Reaction 1. 2. Using GC, same major products, i.e., phenol, cresols, methylcyclopentadiene, and CO, were quantified. They determined that the reaction intermediates were virtually independent of equivalence ratio.

Concerning studies in a JSR, in 1989, Mackie et al. [131] used a perfectly stirred reactor and worked at pressure significantly below 1 atm. They used the GC and concluded that CO, phenol, and cresols are the most important products from anisole pyrolysis. More recently, the pyrolysis and oxidation of anisole were studied in JSRs again using GC for product quantification by Nowakowska et al. [48] where they pinned down on the formation of carbon monoxide, cyclopentadiene, benzene, phenol, and cresol as the major end products during pyrolysis and oxidation.

Apart from these studies, two recent studies focused on the quantification of products in anisole flames. Bierkandt et al. [51] quantified more than 60 species in a premixed laminar flame using the PIMS (at the Advanced Light Source in Berkeley, USA, and at the Swiss Light Source in Villigen, Switzerland) with photoelectron spectroscopy. They found that, besides CO and H_2, CH_3 radical, CH_4, C_2H_2, C_2H_4, C_2H_6, CH_2O, cC_5H_5 radical, cyclopentadiene, benzene, phenol, and benzaldehyde were some of the key intermediates produced in greater amounts (10^3-10^4 ppm), and the phenoxy radical was present in the range of hundreds of ppm.

In 2021, Chen et al. [26] studied anisole oxidation in a JSR. They sampled the reaction products in-situ by MB-TOF-MS using synchrotron radiation as a photon ionization source and identified nearly 40 sum formula for OPAHs experimentally. Then, they used a computational thermodynamic approach to deduce the possible isomers corresponding to the raw formulas by determining their Gibbs free energies. In 2021, Zhang et al. [132], studied the chemical effects of anisole and toluene on PAH formation in n-heptane laminar premixed flames using LIF. They showed that toluene was much more effective at promoting PAH formation than anisole where the latter contributes to PAH formation via styrene and indene reaction networks.

Later, in 2022, MB-TOF-MS and GC were used by Chen et al. [56] to investigate a laminar counterflow diffusion-flame of anisole under oxy-fuel conditions and reported about forty stable species, including naphthalene and dibenzofuran. In parallel with ignition delay times measurements in the RCM for an anisole/iso-octane blend, Mergulhão et al. [121] also followed the time evolution of reactants and several products, including, benzene, toluene and benzaldehyde. They showed that, under those low-temperature conditions, anisole mainly reacted via H-atom abstraction on its methyl group to form the anisyl radical ($C_6H_5OCH_2$), which then adds to oxygen and forms cyclohexadienone or phenol, and for the major part to a non-cyclic C_5 species.

$C_6H_5OCH_3 + OH = C_6H_5OCH_2 + H_2O$ *Reaction 1. 4*

The summary of studies listed in Table 1. 4 shows that there are so far only three studies dedicated to the investigation of species formation from anisole in flame conditions. These studies analyzed only a few OPAHs like benzofuran and dibenzofuran (see Table 1. 2). It is noteworthy that more studies in flame configurations are necessary to characterize the combustion chemistry of anisole with special attention to OPAHs.

The combustion behavior of prototypical fuel mixtures (base fuel+biofuel), including intermediate species formation and potential chemical interactions amongst the fuel components in fuel blends are necessary to understand as the current regulations impose biofuels blending mandates. In this thesis, we addressed the premixed flame combustion of **iso-octane** (as the base fuel) and its blends with oxygenated biofuel. Generally speaking, iso-octane (RON = 100) is the simplest surrogate for gasoline [136]. It is also a significant component in primary reference fuels to assess the octane number and knocking tendency under Spark Ignition (SI) or Homogeneous Charge Compression Ignition (HCCI) conditions [137,138] and is commonly used as a representative branched alkane in jet fuel surrogates [139,140].

Together with anisole-doped iso-octane blends, two more biofuel blends, i.e., **ethanol** and **DMF** doped with iso-octane were also investigated as a part of this thesis. DMF is a 2nd generation biofuel cellulose/hemicellulose-based biofuel that has received increasing attention [141–146] because of the breakthrough advances in its industrial production [141,146–149] and a recognition of its suitable fuel properties such as high energy density, low heat of vaporization, and strong anti-knock performances for engine applications, as summarized in a recent review [150]. Ethanol, a widely adopted biofuel, is already commercially utilized, and several studies have been reported to consolidate its combustion characteristics, kinetics and its impact on soot formation [11,19,78,151–157]. The idea was to compare a foreseeable potential biofuel like anisole with other popular existing and forthcoming biofuels that are comparatively more well-researched.

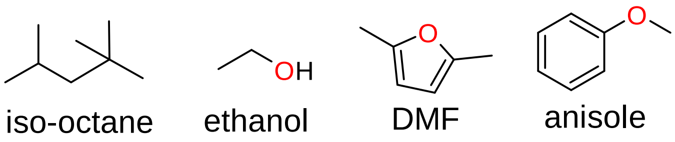

Figure 1. 4 : Structures of the different biofuels and iso-octane (gasoline surrogate) whose blends are studied in this work.

1.4. Limitations in current understanding and the scope of this thesis

The combustion of oxygenated biofuels has been found to influence aromatics especially OPAHs and soot emissions. As discussed in this chapter, though the importance of studying OPAHs has been recognized by the researchers, studies focusing on their identification and quantification using fundamental laboratory-scale studies are still very scarce in the literature. Although some OPAHs have been experimentally detected in the literature, it is worth mentioning that the species analyzed are rather limited to mainly benzofuran and dibenzofuran. There are several numerical studies that highlight the importance of studying OPAHs and seek for more experimental evidences [26,158]. It is worth mentioning that though researchers are putting in the requisite efforts, OPAHs are indeed very challenging species to study. PAHs are usually present in few ppm and it is expected that OPAHs would be present in even lower concentrations as compared to PAHs which is why experimentally, it is very challenging even to detect and investigate them. Sometimes, since analytical standards for many of these species are not available, their identification in unknown samples is also ambiguous as there is no reference for comparison in the database. Certainly, more strategic, and advanced investigations are necessary to overcome these challenges and detect OPAHs in combustion systems as it is an inevitable step towards adopting biofuels as alternative renewables.

This thesis aims at pushing these boundaries by providing experimental evidences about the various OPAHs that are formed during the combustion of a component model of lignin-based biofuels, i.e., anisole. Together with identification of the oxygenated aromatics, their absolute concentrations' determination is also performed to comprehend the amount of each of these species produced. This kind of knowledge is significant to understand the main pathways involved in the fuel decomposition. In addition to identifying and quantifying oxygenated aromatics, non-oxygenated aromatics and the associated PAHs have also been studied. To gain deeper insights concerning different conditions, the dependence of aromatics' formation on the biofuel amount and the equivalence ratio have been investigated. To understand the effect of chemical structure differences, comparative studies on aromatics formation from anisole, DMF (a furanic biofuel) and ethanol (a commercial-scale biofuel) are also performed.

Finally, the soot particles formed in these flames are also characterized by investigating the soot volume fraction and the particle size distributions. As discussed previously, laboratory-studies [11,80,105,157,159] and investigations on real combustion systems [25,160–162] suggest an increase in the number concentration and generally a nonlinear effect on the particulate emission during the combustion of biofuels. Soot nanoparticles (a few nanometers) do not contribute to the total mass concentration of the emitted particulate matter due to their very low sizes, however, these particles play a particularly important role in health as they can penetrate deeper than larger particles into the respiratory system. Also, the difficulty in measuring these small particles, especially the sub-10 nm class, makes them often being overlooked. In this study, attempts are made to study the soot volume fraction and size distributions of the very small soot particles (<10 nm) that are formed during the combustion of biofuel blended iso-octane flames.

Chapter 2. Experimental setup and measurement techniques

In the previous chapter, the limitations in the literature that will be addressed in this thesis are documented. In this chapter, the analytical tools and methodology implemented to address those limitations are discussed. The experimental approach and design adopted for this study can be broadly categorized into two parts as the purpose of this thesis is twofold. A global overview of the experimental setup used in this work has been presented in Figure 2. 1.

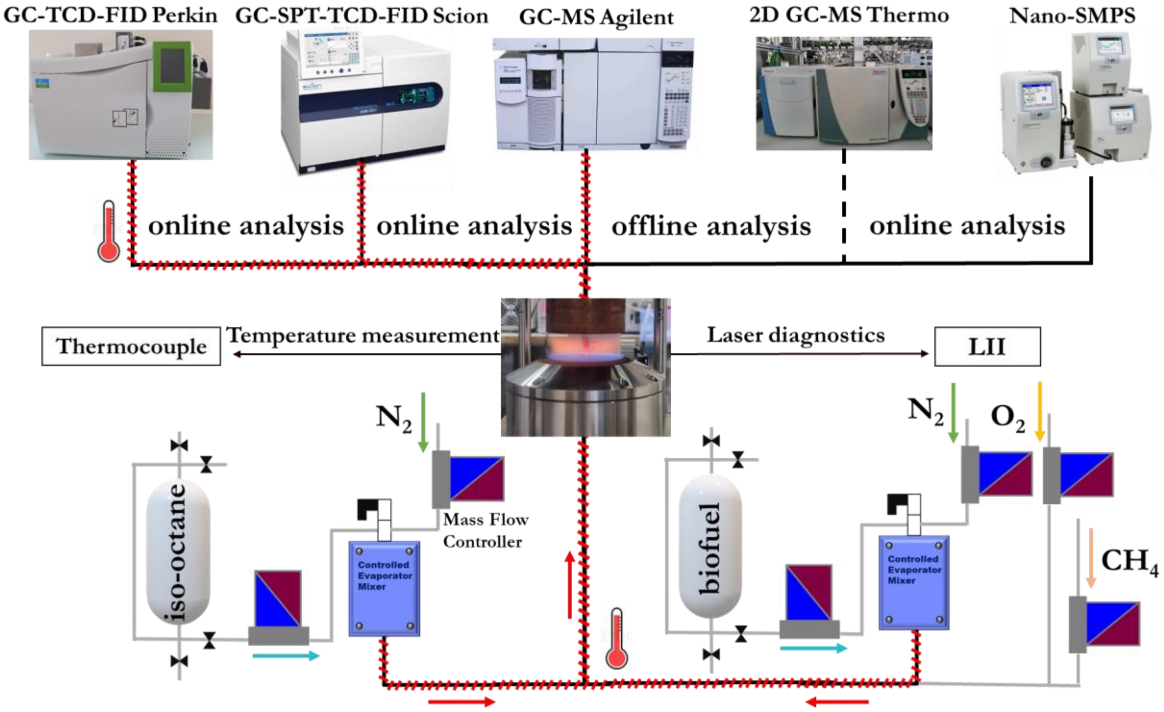

Figure 2. 1 : A schematic representation of the global experimental setup used in this work. Here, GC: Gas Chromatograph, TCD: Thermal Conductivity Detector, FID: Flame Ionization Detector, MS: Mass Spectrometry, SPT: Sample Pre-concentration Trap, SMPS: Scanning Mobility Particle Sizer. LII: Laser Induced Incandescence. Short forms often used in the text to refer to GC-TCD-FID Perkin and to GC-SPT-TCD-FID Scion are "GC Perkin" and "GC Scion" respectively.

The first and foremost part of the study was to investigate the gaseous phase of the 1-D flat laminar premixed flames stabilized on the McKenna burner at atmospheric pressure with aromatic species, particular oxygenated ones being the center of attention using advanced GCs. In order to stabilize premixed flames using liquid fuels, vaporization setups were built to vaporize the liquid fuels. For analysis, both 1-D and 2-D GC setups combined with the preconcentration step were employed to detect a broad range of bulk as well as trace level species in flames. By using the front-line trap technology in GC Scion (GC-SPT-TCD-FID Scion in Figure 2. 1) to concentrate our samples prior to injection, we could analyze OPAHs and PAHs present in very low concentrations which would otherwise not be detected with direct injection onto the usual chromatographic system. Both online and offline GC setups are explored in order to accomplish our goals.

At the beginning of this thesis, we began by installing online GC setups to analyze all types of species simultaneously. To do so, a new sampling system was purpose-built and assembled to perform online sampling from the flame and a significant time span was dedicated altogether to the overall development and optimization of the GC systems and the sampling procedures. In addition to online analysis, offline GC-MS (1-D and 2-D) systems were also used to carry out the identification of species. These GC-MS setups were not equipped with the trap accessory. With the intention of achieving exhaustive identification of aromatics, a homemade trap system was built to pre-concentrate the samples from the flame followed by collection in a vial together with a low boiling solvent (acetone in our case). These samples were afterwards injected into the GC-MS systems using an injection syringe. The same chromatographic column and similar GC methods were used to compare the chromatograms obtained from the 1-D GC Scion (with the trap accessory via online sampling) and the 1-D GC-MS (homemade trap via offline sampling) systems to ensure the same order of elution for the species. Together with independent identification from the 1-D GC-MS, this way we could also identify the compounds corresponding to the unknown peaks observed in the 1-D GC Scion system. Once identified, the species were calibrated whenever pure commercial products were available to deduce their absolute concentrations.

The second part of the study was to gain insights into the particle phase or the soot formed in such flames (carried out in collaboration with Dr. Pascale Desgroux and Dr. Alessandro Faccinetto). To do so, Laser Induced Incandescence (LII) technique and a new generation Scanning Mobility Particle Sizer (nano-SMPS) were used to characterize the soot particles formed in the flames, and to obtain soot volume fractions and particle size distributions. LII is an in-situ technique that involves heating the soot particles using a high-power pulsed laser to temperatures that are high enough such that the soot emits measurable quasi-blackbody radiation which is then recorded to deduce the soot volume fraction. LII is particularly sensitive and highly selective for soot particles as they have the ability to absorb strongly and can be heated to temperatures of ~4000 K before their sublimation [163]. The LII measurements were complemented with online particle size distributions (PSDs) measurements from the nano-SMPS. These measurements require extractive sampling and delivery to the measurement device. Dilution techniques are also employed in an attempt to avoid the interaction of particles in the sampling lines. In the subsequent sections, each of the setups have been described individually with a narrative of the different techniques employed in this work.

2.1. Premixed flames stabilized at atmospheric pressure

This section is devoted to the description of the liquid fuel system that was used to vaporize the liquid fuels as well as the burner configuration used to stabilize our flames. Additionally, the operating flame conditions have also been listed in this section.

2.1.1. Liquid fuel vaporization setup

The reference fuel (iso-octane) and the chosen biofuels (anisole, DMF, ethanol) are liquids at atmospheric temperature and pressure. Thus, two distinct liquid fuel vaporization setups were used. The first system (to vaporize isooctane) was built previously during the thesis work of C. Betrancourt [164] and upgraded by Tran et al. [142,165] whereas the second system (to vaporize the biofuel) was built as a part of this thesis. Figure 2. 2 presents a schematic representation of the two setups. Each of these setups is composed of 3 units:

- A mini “CORI-FLOW” Mass Flow Controller, also abbreviated as MFC, (Bronkhorst) to control and measure the flowrate of the liquid fuel.
- A Mass Flow Controller (Bronkhorst) to control and measure the flowrate of N_2, CH_4 and O_2.
- A Controlled Evaporation Mixer (CEM, Bronkhorst) chamber equipped with a heater which allows vaporization of the liquid fuel and promotes sufficient mixing between the fuel vapors and the carrier gas in the mixing chamber.

The gas MFC used in the setup were calibrated with the DryCal standard for volumetric flow calibrations. The mini “CORI-FLOW” meter works on the principle of the Coriolis effect, i.e., a moving object is deviated from its linear trajectory when it is observed from a rotating frame of reference. It consists of a single tube to which an oscillatory motion is applied. When a liquid flows through this tube, forces begin to act on it, causing the entire loop to twist by an amount that is directly and linearly proportional to the mass flow rate of the liquid. The main advantage of this MFC is that the flowrate measurement is independent of the nature of the liquids and thus does not need re-calibration if the liquid fuel is changed. The mini “CORI-FLOW” is connected upstream to the tank in which the liquid fuel is stocked. This tank is pressurized at 4 bars with helium. Helium is chosen in comparison to nitrogen as its Henry’s constant is higher than that of nitrogen. This constant is inversely proportional to the amount of the gas entering the solution (representing its solubility) which implies that it has lower solubility and thus eliminates the phenomenon of the formation of bubbles to ensure constant flow rate. High pressure is maintained in the tank to ensure the flow of the liquid through the mini "CORI-FLOW" until the control valve in the CEM unit. The necessary flow rate is controlled to the setpoint value via this control valve which is an integral part of the system. Thereafter, the pressurized liquid fuel enters the mixing chamber through an orifice whose size is of the order of 200 µm. The liquid fuel is then nebulized in the mixing chamber and is subsequently led to the evaporator/heat exchanger in order to achieve complete vaporization. This justifies the abbreviation of CEM, i.e., Control-Evaporation-Mixing, which are the three fundamental functions of this liquid delivery module. The complete system also incorporates a readout and a control unit including power supply to operate the CEM-system. The flow rates and the temperature of the heat exchanger can be controlled via this control unit.

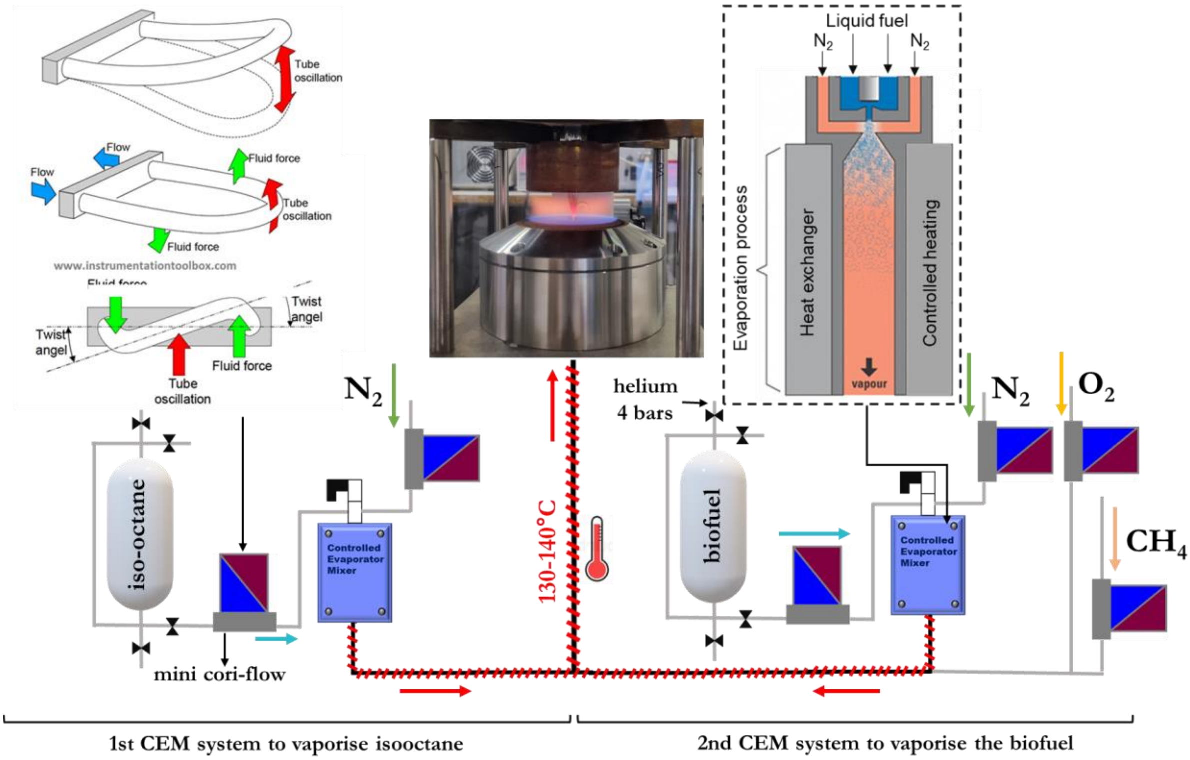

Figure 2. 2 : Schematic representation of the two CEM systems used to vaporize the liquid fuels.

The choice of an optimum temperature to achieve efficient vaporization in the CEM is a crucial step for flame stabilization. The temperature chosen is determined as a function of the flow rate of the liquid fuel and the carrier gas. By calculating the partial pressure exerted by the liquid fuel in the fuel/carrier gas mixture, the appropriate temperature to vaporize the fuel can be deduced by referring to its phase diagram. This value of temperature can also be verified using the software FLUIDAT [166] proposed by Bronkhorst for the same purpose. This software can calculate the dew point temperature of a biphasic mixture, considering the pressure inside the mixing chamber, flow rates, the physiochemical properties, and the characteristics of the CEM system. The CEM technology allowed us to rapidly generate a stable and homogenous flow of the liquid fuel vapors at a suitable temperature in a short span of time. After some calculations and a series of flame stability tests, the temperatures chosen to vaporize iso-octane, anisole, ethanol and DMF were 45°C, 77°C, 77°C and 40°C respectively.

Ultimately, the liquid fuel vapors with nitrogen are mixed with oxygen and methane and are fed to the burner. The fuel line is heated at high temperature (130-140°C) from the CEM output until the burner to prevent any condensation that might occur.

2.1.2. The McKenna flat flame burner

In this thesis, target fuels have been investigated in laminar premixed flames at atmospheric pressure. A premixed flame is produced when the fuel and the oxidant are mixed in a homogenized way prior to the passage of the reaction zone. Laminar premixed flames allow us: to work on a 1-D medium, which facilitates the monitoring of changes in the species' concentration; to overcome the interactions between the chemical processes involved and the mechanical aspect of fluids due to the laminar regime; and therefore, to directly comprehend the kinetics of combustion. They are a realistic medium of choice for the development and fine-tuning of complex combustion kinetic mechanisms. Usually they operate at steady state, and the conditions can be easily varied. Also, spatially-resolved probe-sampling in the large-area flat premixed flame is relatively easy and less susceptible to errors due to the probe intrusion. In such flames, reaction pathways can also be identified by measuring the concentrations of the species as a function of the flame height. These flames are widely used as a benchmark flame configuration for not only investigating the combustion chemistry but also soot formation processes. They are relatively simple configurations as compared to non-premixed flames because of their stoichiometry which is well-controlled and varies very slightly within a given flame [61].

All the premixed flames in this study have been stabilized using a commercial McKenna burner (manufactured by Holthius and Associates, presented in Figure 2. 3) at atmospheric pressure. McKenna burners have been widely used for many years to produce flat premixed flames (reference in the scientific community of combustion) and are employed in many laboratories around the world. It consists of a central bronze porous plug (60 mm in diameter). This bronze porous has the role of creating a uniform profile of the gas velocity over the entire burner surface thereby producing a flat flame. The central porous zone is surrounded by another co-annular porous used for the nitrogen shroud, which makes it possible to avoid the air entrainment responsible for the formation of a peripheral or an external diffusion flame. A new burner was bought and assembled in the laboratory for this project. The temperature of the burner was constantly maintained at 60°C using a cryostat for all flames. To stabilize fuel-rich flames, a stainless-steel disc, also known as the stagnation plate (6 cm in diameter and 3 cm thick) was surmounted at 21 mm with respect to the burner surface in order to stabilize the flame away from the burner surface, and was pierced at its center to provide access for the quartz nozzle. An additional metallic grid was placed directly on the stagnation plate, to avoid peripherical flame ignition.

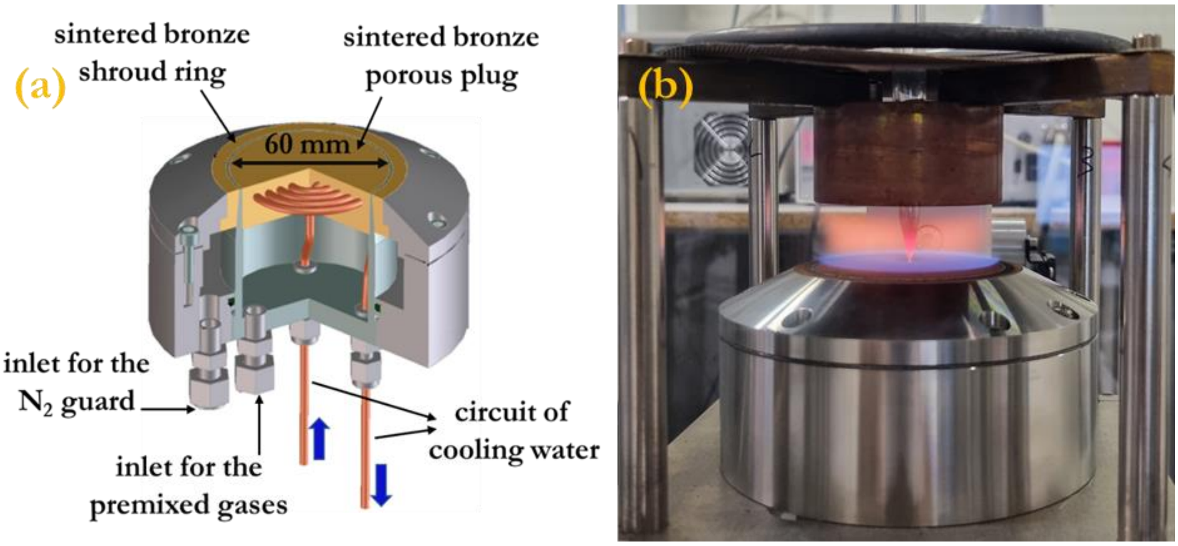

Figure 2. 3 : (a) A schematic diagram of the McKenna burner used to stabilize the laminar premixed flames , extracted from [167] ; (b) a real view of the burner, stagnation plate and the nozzle assembly.

2.1.3. Operating flame conditions

In this thesis, seven flames at atmospheric pressure were studied to analyze the effect of the presence of three biofuels in premixed flames. Special focus was dedicated to the study of anisole: four out of the seven flames contained anisole. There was one DMF flame, and one ethanol flame whereas one isooctane/methane flame without any biofuel served as a reference flame. For all the seven flames, the total flow and dilution were always kept constant. Our choice of operating conditions is influenced by the practical considerations like flame stability and a good spatial resolution. Also, we were mindful of having similar or related conditions in order to carry out some comparisons between the different flames. The different operating flame conditions have been summarized in Table 2. 1. The percentage of the biofuel mentioned in the table correspond to its mole fraction in the overall fuel. The range of equivalence ratios chosen here (1.70, 1.82, and 1,90) represent slightly sooting conditions so that not only aromatics but also small soot particles could be characterized. The C/O ratio represents the amount of carbon present in the fuel with respect to the amount of oxygen present as the oxidizer as well as in the fuel (oxygen atom in the structure of the fuel).

Table 2. 1 : Summary of the operating flame conditions investigated in this thesis where L_n/min=normal liters per minute.

Flame	Biofuel (%)	Gaseous flow rates (L_n/min)						Equivalence ratio	C/O
		Biofuel	C_8H_{18}	CH_4	O_2	N_2	Total		
F1	-	-	0.18	0.925	2.25	6.50	9.85	1.82	0.52
F2	Anisole (10)	0.102	0.15	0.766	2.338	6.50	9.85	1.82	0.55
F3	Anisole (15)	0.147	0.13	0.696	2.377	6.50	9.85	1.82	0.57
F4	Anisole (10)	0.097	0.14	0.729	2.387	6.50	9.85	1.70	0.52
F5	Anisole (10)	0.105	0.15	0.788	2.308	6.50	9.85	1.90	0.58
F6	Ethanol (10)	0.112	0.164	0.843	2.236	6.50	9.85	1.82	0.52
F7	DMF (10)	0.106	0.156	0.801	2.291	6.50	9.85	1.90	0.57

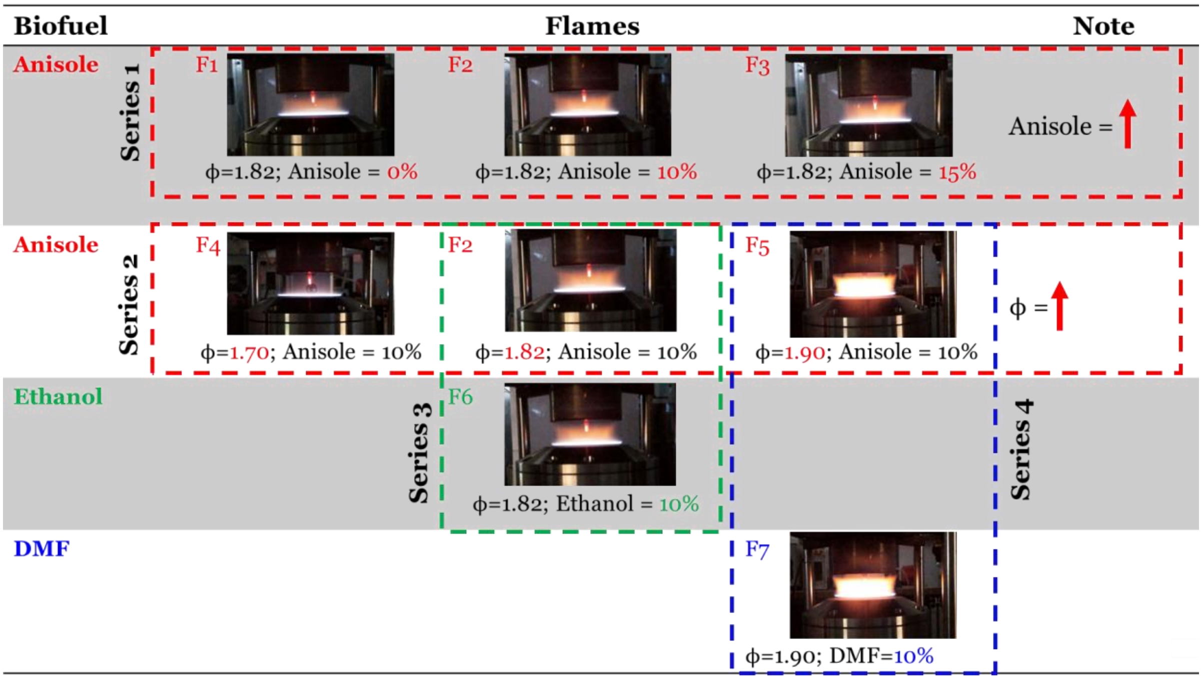

Figure 2. 4 : A summary of the different flames investigated in this work along with the depiction of the different series for comparison where ϕ represents the equivalence ratio.

2.2. Measurement of gaseous species using gas chromatography

This section describes the sampling system and the different 1-D and 2-D gas chromatograph (GC) systems, with and without the trap accessory that were employed to analyze the species formed in the flames. All kinds of species were analyzed using the systems described in the subsequent sections with special attention devoted to OPAHs and PAHs.

2.2.1. The sampling system

Though, probe sampling approaches are intrusive and may disturb the flame thermally and aerodynamically, they are necessary for GC and SMPS measurements. Nonetheless, to minimize this perturbation, the choice of the microprobe material and its orifice size are important. We chose a quartz microprobe for this study because of its low thermal conductivity (to reduce thermal losses), its low coefficient of expansion (allows the probe to keep the same geometry at any point in the flame) and its chemical inertness (respects the representativeness of the gaseous sample). In addition to the material and the size of the orifice, the needle-like shape of the probe also plays a role in limiting disturbances.

In order to assess the effect of the orifice size on the flame structure and choose an appropriate probe, mole fraction profile measurements were performed using three quartz microprobes with different orifice sizes (350, 250, 190 µm) using a test methane flame. The summary of the flame conditions for the test flame is presented in Table 2. 2. This flame is stabilized very far from the burner surface (5-7 mm above the burner), which increased the spatial resolution thus facilitating our test. Our sampling system mainly consisted of a microprobe, a heated sampling line, a vacuum pump, and a pressure gauge. Samples from the flame gases were sampled by a quartz nozzle connected to the heated sampling line via a short PFA-Teflon tube (~30 cm). Species mole fraction profiles were measured at the centerline of the flame as a function of the height above the burner (HAB). Gas samples were injected into the first GC (PerkinElmer Clarus 580, refer to Figure 2. 1). The details of this GC are available in the next section. The burner could be precisely vertically displaced (manually) with respect to the microprobe to effectuate the sampling process at different HAB. The relative error in the position of the probe is ~0.1-0.2 mm.

Figure 2. 5 presents two exemplary mole fraction profiles i.e., methane (reactant) and ethane (intermediate species) measured for the methane test flame using three nozzles with different orifice sizes. We compared also the experimentally obtained mole fractions with the initial theoretical mole fraction of reactants. The figure shows that we recovered the theoretical initial mole fraction value of the reactant using the nozzle with the smallest orifice size i.e., 190 µm. Also, it was observed that the lowest orifice size led to minimum intermediate species' amount close to the burner and that the perturbation close to the burner surface increased as the size of the orifice increased. It is worth mentioning that besides perturbing the flame close to the burner surface, the size of the nozzle orifice also affects the shape of the stable

intermediate species. As shown in the figure, the nozzle with an orifice size of 350 µm leads to broader mole fraction profiles whereas the nozzle with the least orifice size of 190 µm led to narrow profiles. Note that the test flame was a sooting flame to ensure if there were any clogging problems. It was observed that none of the probes posed clogged orifice issues during the flame measurements. Thus, since the nozzle with the least orifice size (i.e., 190 µm) posed minimum flame perturbations amongst the three nozzles, it became our undisputed choice for eventual flame measurements. All the flame measurements in this work were carried out using this quartz nozzle (190 µm orifice, 0.9 mm tip, 24° opening angle along 14 mm length, then 7 mm outer diameter along 50 mm length).

Table 2. 2 : Summary of the methane flame conditions used to test the three nozzles with different orifice sizes; L_n: normal liters per minute.

Equivalence ratio	*Total gas flow rate (L_n/min)*	*Mole fraction CH_4*	*Mole fraction O_2*	*Mole fraction N_2*
1.82	12.003	0.183	0.202	0.614

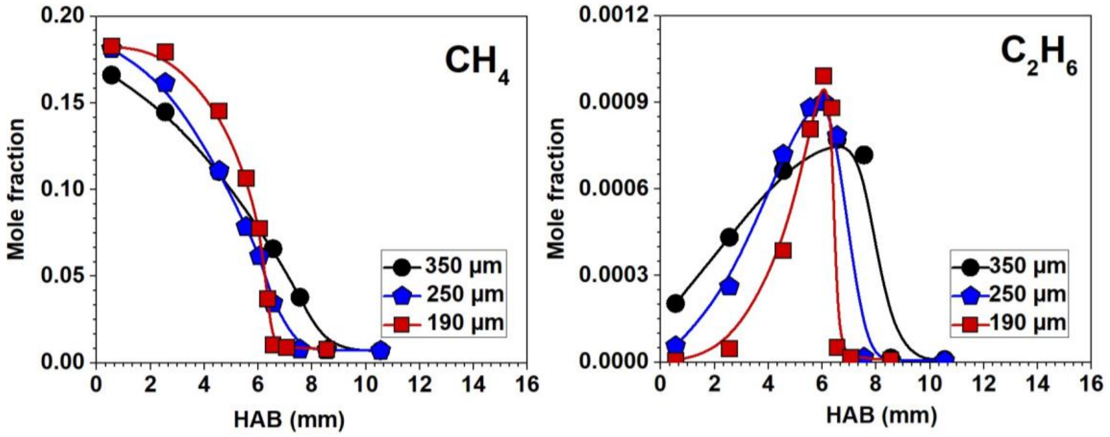

Figure 2. 5 : Evolution of the mole fraction for methane and ethane determined in the test methane flame ϕ=1.82, obtained using three nozzles with different orifice sizes.

It must be noted that the temperature of the entire sampling system, from the microprobe to the sampling loop was controlled with heating devices (using heating cables and thermocouples). An optimal temperature value for the sampling line is necessary to determine to be sure that the species of interest existed in gas phase and do not condense to their liquid phase during their transport. To determine the temperature at which the sampling line must be heated for flame measurements in this study, we investigated the temperature dependent vapor pressures for some expected two to three-ring aromatics (aromatics up to a molar mass ~200 g/mol). Figure 2. 6 presents the temperature dependent vapor pressure curves for some selected aromatics from the literature [168–174]. The data from the figure indicates that a temperature of 130-140°C was sufficient to avoid any major condensation problems in the line for such species. Thus, for all flame measurements performed during this thesis, the sampling line was always heated to nearly 140°C to avoid condensation problems.

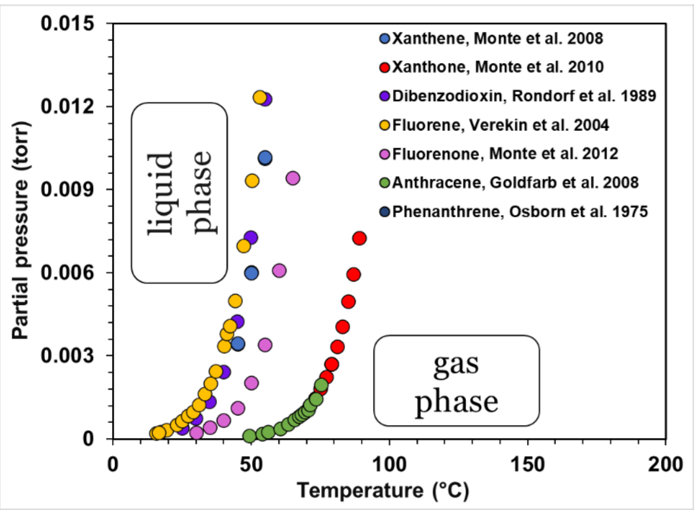

Figure 2. 6 : A collective temperature-dependent vapor pressure evolution diagram for some selected aromatics (molar mass < 200 g/mol) expected as combustion products from anisole to estimate and fix the temperature of the sampling line intending to avoid condensation during online sampling.

2.2.2. GC-TCD-FID Perkin for small species

The first GC-TCD-FID Perkin device (Perkin Elmer Clarus 580; short form "GC Perkin") consists of two channels in a parallel architecture with two detectors, a Thermal Conductivity Detector (TCD) and a Flame Ionization Detector (FID). A 10-port sampling and switching rotary valve equipped with two injection loops enables to simultaneously inject the gaseous samples into the two channels. Figure 2. 7 shows the configuration of the device during an analysis process.

The first channel is dedicated to the analysis of permanent gases like O_2, H_2 and N_2. It comprises of the Hayesep Q column (1/16" 2m × 1 mm, Restek), the Molecular Sieve (1/16" 2m × 1 mm, Restek) column using argon as the carrier gas and a TCD.

The second channel is exclusively devoted to analyze several lighter hydrocarbons (saturated and unsaturated), small oxygenated species (like aldehydes, ketones, and ethers) as well as some of the monoaromatics (like benzene, toluene, cresols etc.). It comprises of a capillary Rt-Q Bond column (30 m × 0.25 mm × 0.008 mm, 100% divinylbenzene, Restek) using helium as the carrier gas and a FID equipped with a Methanizer.

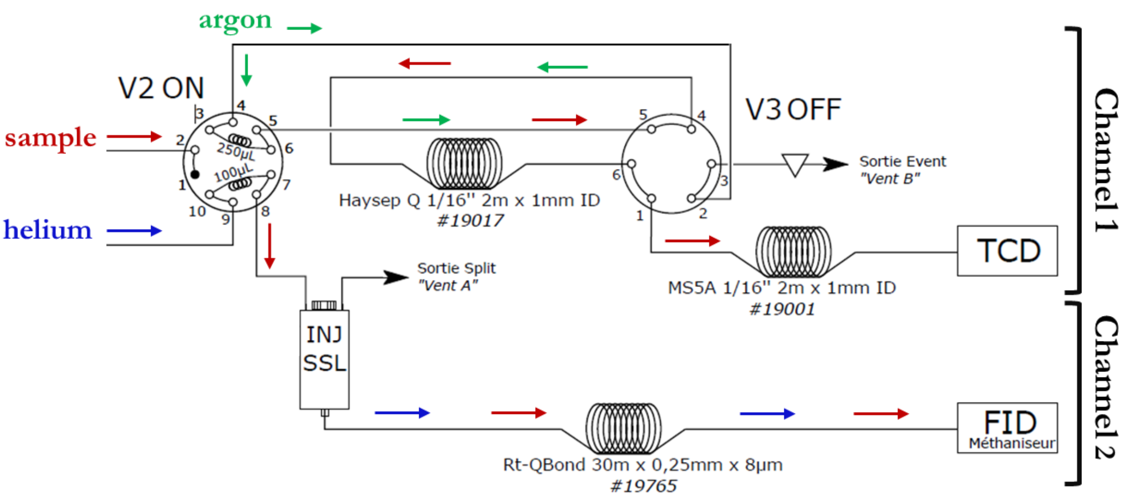

Figure 2. 7 : Schematic representation of analysis via two channels in 1D GC-FID Perkin.

The FID is a sensitive detector with a large dynamic range and a quantification limit of about 1 ppm (in conventional GC configuration without enhanced sampling system). Aliphatic hydrocarbons generally possess proportional response factors with respect to the number of carbon atoms in their molecule. However, a regular FID would in fact show reduced response for oxygenated hydrocarbons like HCHO and no response to species like CO and CO_2. These issues were resolved in GC Perkin as it is equipped with a methanizer. A methanizer is composed of a bed of nickel powder catalyst which reduces these species to corresponding hydrocarbons in the presence of hydrogen at about 380°C, which in turn are measured by the FID. Thus, the special FID detector and methanizer assembly presents a high detection sensitivity to detect oxygenated hydrocarbons.

Other than the sensitivity issues, the quality of resolution of the peaks is also affected by the split ratio. The split ratio describes the amount of gas that will split through the different parts of the injection. This ratio can range anywhere between 5:1 to 500:1, and can be fixed prior to analysis as per an individual application and requirement. The higher the ratio, the lower is the amount of the sample that enters the column as compared to what passes out through the split vent. For example, a split ratio of 25:1 means that one part of the sample goes onto the column while 25 parts exit out the split vent. We chose to analyze the lighter hydrocarbons and oxygenates ($<C_3$) that were more abundant in flames via the split mode (25:1) while other intermediates ($>C_3$) in smaller quantities were investigated via the splitless mode to obtain satisfactory results in terms of resolution and sensitivity. This setup was optimized during the thesis work of L. Giarracca [175] and later upgraded by Tran et al. [142,165].

In order to quantify major species (like CH_4, CO, CO_2, O_2, H_2, N_2) and lighter hydrocarbons (like C_2-C_3 saturated and unsaturated species), the usual calibration procedure was implemented to determine their sensitivity factors (also known as the response factor or the calibration factor) by using commercial gas bottles consisting of standard mixtures of known concentrations. Figure 2. 8 shows an example of the calibration curve obtained using this procedure for acetylene as an example. This method relies on Equation 2. 1 which shows how the mole fraction x_i of a particular species can be expressed as a function of its peak area A_i and the total injection pressure, P_T.

$$x_i = \frac{p_i}{P_T} = \frac{A_i}{\alpha_i . P_T} \qquad \text{Equation 2. 1}$$

x_i: mole fraction of species

p_i: partial pressure of the species

P_T: total pressure of the gaseous sample injected

A_i: area of the peak corresponding to the species

α_i: sensitivity factor or response factor or calibration factor

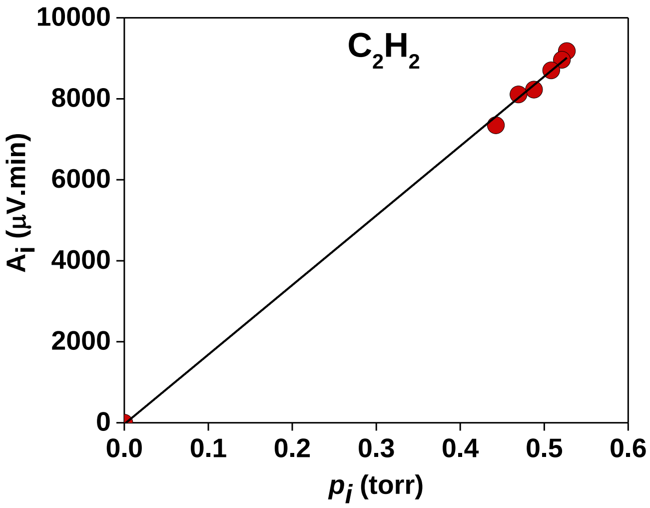

Figure 2. 8 : An example of a calibration curve for acetylene obtained via GC-FID Perkin using the commercial standard mixture bottles where A_i is the integrated area of the peak in µV.min and p_i represents the partial pressure in torr.

In addition to using the method of standard mixtures for calibration, certain species which cannot be calibrated directly have been calibrated using the carbon number method. In this method, we can determine the contribution per carbon atom by analyzing the response coefficients of other compounds calibrated using the commercial bottles and then apply this contribution per carbon atom to predict the calibration coefficient for other species based on the number of carbon atoms present in it.

2.2.3. GC-SPT-TCD-FID Scion for aromatic species

A second GC, i.e., the GC-SPT-TCD-FID Scion 456 equipped with the SPT (Sample Pre-concentration Trap) system (short name "GC Scion"), was used besides GC Perkin. With an initiation from Prof. El Bakali and the Scion Instruments company, GC Scion was custom-built and personalized to meet our requirements explicitly. The primary motivation behind using this instrument was to analyze heavier aromatics which could not be investigated by GC Perkin. GC Scion was used to investigate the flame structure for the first time in this thesis and a significant amount of time was attributed to optimization of the best operating GC conditions. It has a specific design as shown in Figure 2. 9. Unlike other conventional GC's, it consists of three channels in parallel architecture with three detectors for the separation of complex mixtures as present in flames. The three different channels serve different purposes each of which are described here. In this thesis, the channel 3 (for aromatics) was extensively explored, while other two channels (1 and 2) were used only to quantify C_4 species and to recheck some species already measured by GC Perkin.

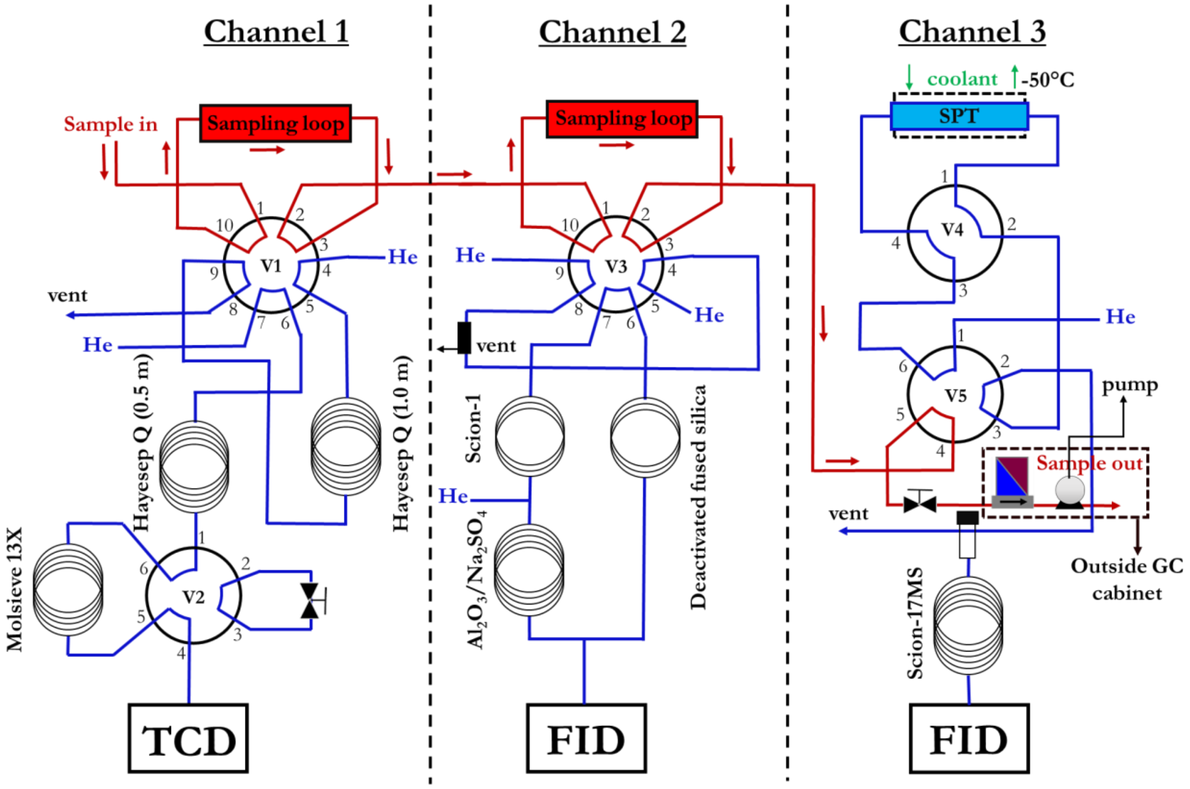

Figure 2. 9 : Schematic presentation of the 3 channels in parallel architecture in GC-SPT-FID Scion.

The front channel (Channel 1, Figure 2. 9) or the permanent gases analyzer channel was principally used for the simultaneous determination of oxygen, nitrogen, CO, and CO_2. The sample was injected by means of a gas sampling valve onto a series of Hayesep columns. The fraction containing oxygen, nitrogen, CO, and methane was flushed onto a Molecular Sieve column and parked. CO_2 and C_2 isomers were eluted to the TCD, bypassing the Molecular Sieve column. After the elution of these species, the Molecular Sieve column was set to flow again giving the separation of oxygen, nitrogen CO and methane. These species were already measured by GC Perkin and were rechecked using this channel.

The middle channel (Channel 2, Figure 2. 9) or the light hydrocarbon analyzer channel was used in this work to measure the C4 isomers that could not be separated well using GC Perkin. This channel is also capable of analyzing a range of low boiling hydrocarbons (C_1-C_5) and was thus also used to recheck some of these species already measured by GC Perkin. However, a full exploration for this channel 2 was not performed because GC Perkin was used for this range of species. GC Scion consists of a SCION-1 (12.5 m × 0.32 mm × 1.2 μm) pre-column and the Alumina/Na_2SO_4 analytical column. The sample was injected onto the pre-column. The components having a boiling point of below C_6 are transferred onto Alumina/Na_2SO_4 (50 m × 0.53 mm × 10 μm) column. The highly selective Alumina/Na_2SO_4 column separates all individual isomers from the light hydrocarbon fraction. The fraction with higher boiling point i.e., C_6 species and higher was back flushed from the pre-column to the FID. The light hydrocarbon analyzer channel was set for the determination of the hydrocarbon isomers down to 0.001%. The first peak to appear is the grouped peak with C6 and higher species via the backflush. After that, the lighter hydrocarbons were eluted following the normal separation on the Alumina/Na_2SO_4 column. The backflush can be set to match the required application. Alternatively, if deemed necessary the instrument can be set to do a C5+ backflush.

GC-FID Perkin had already been thoroughly studied and optimized during previous thesis' carried out at our laboratory [175] and was thus the foundation and our primary reference to compare the new results with GC-SPT-FID Scion as it was being used for the very first time in this thesis. Figure 2. 10 presents an example of selected mole fraction profiles of CO and ethane (C_2H_6) determined using the two GCs for the same flame. As seen in the figure, the profiles obtained are in excellent agreement between the two GCs. Note that direct calibration using commercial calibration bottles was performed for these species in both GCs.

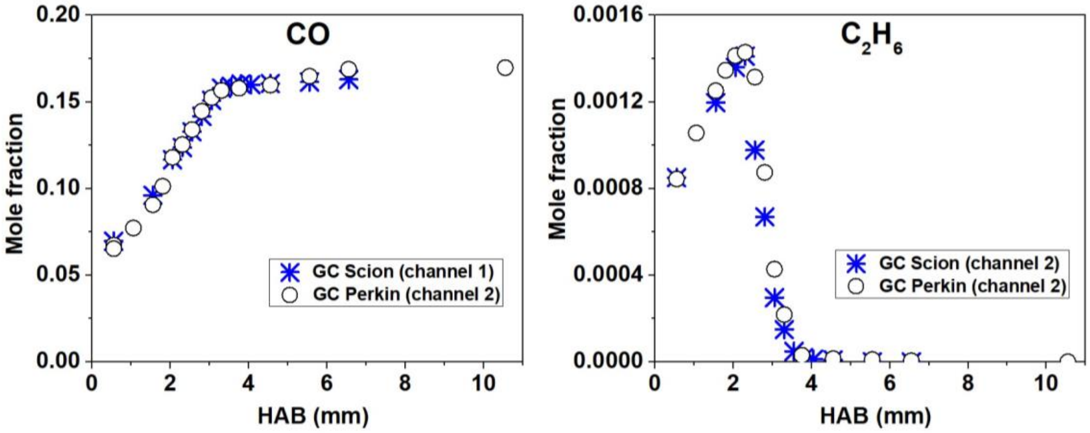

Figure 2. 10 : An example of a comparison of the mole fraction profiles for CO and C_2H_6 in flame F2 (10% anisole, 1.82) obtained using GC Perkin and GC Scion.

The rear channel (Channel 3, Figure 2. 9) is a special channel as it is integrated with the SPT and allows measurements of aromatic species. SPT is a sample enrichment device. As the aromatics, PAHs and OPAHs are present in concentrations that are too low to be correctly determined by a regular GC detector, this system can be used to enrich the sample. The trap is connected to a pump to suck the sample through the trap and to an MFC to control and measure the sample flow rate. The entire process can be categorized in four steps and is illustrated in Figure 2. 11.

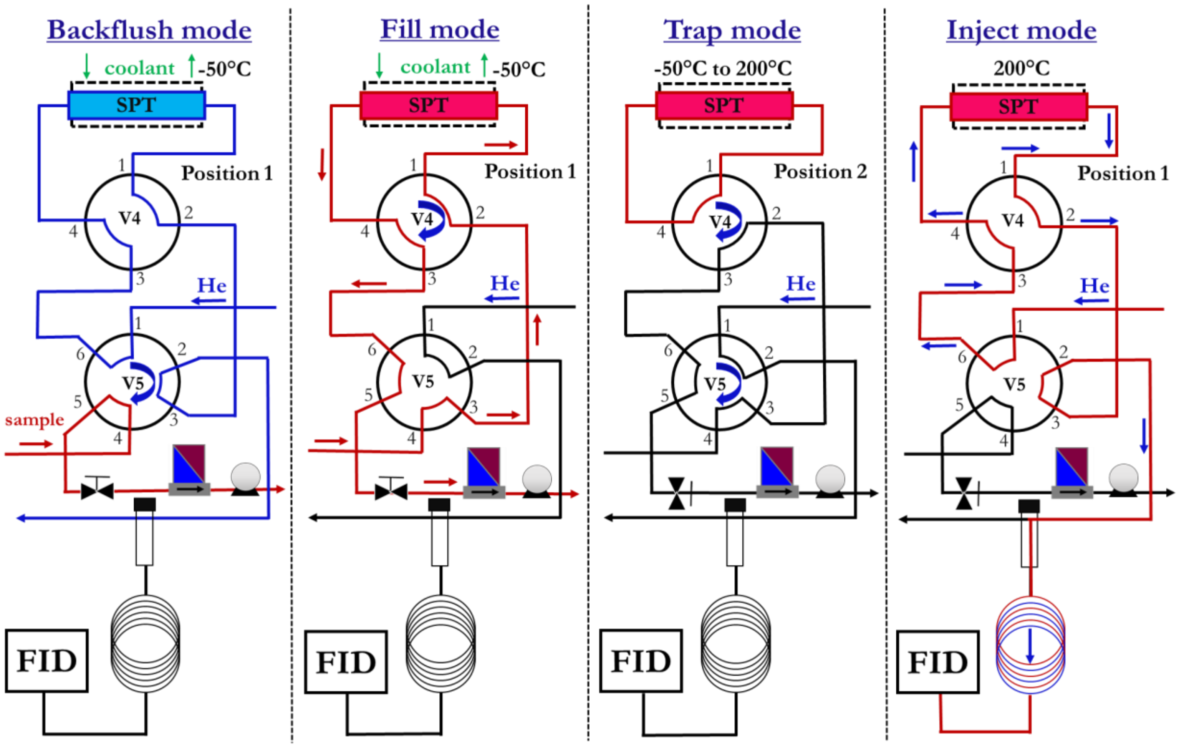

Figure 2. 11 : Illustration of the different steps involved during the trap and desorb processes in the SPT channel [also referred to as Channel 3 in Figure 2. 9].

This concentrating system operates on the idea of cryofocusing–thermodesorption which is a common and a very powerful technique to perform low level determinations. The first step is the “backflush” mode where the SPT is flushed with helium. During this step, the carrier gas flushes the SPT with any unwanted components through the split vent. Then, the second step is where valve ‘V5’ rotates and connects the sample coming from the sampling line to the SPT. This is the “fill” mode where the analytes pass through the SPT. The SPT is composed of an inert adsorptive glass beads surface on which the analytes present in the gaseous flame sample are preconcentrated at a specific adsorption temperature (-50°C) using a coolant (liquid N_2). The trap is subjected to -50°C for a duration of about six minutes during which the analytes are adsorbed in the trap. The duration of six minutes (fill mode) was fixed for the flame measurements conducted eventually. After this step, valve ‘V4’ rotates in order to isolate the trap. This is the “trap” mode where the SPT gets detached from the remaining system and is subjected to a very high heating rate (about 8°C/s). In a span of about 30 seconds, the temperature of the SPT rises from -50°C to 200°C. Through subsequent rapid heating of the adsorptive material in the trap to a desorption temperature of 200°C, the steady state is instantaneously shifted towards desorption (thermodesorption), consequently remobilizing the trapped analytes. Consequently, valves ‘V4’ and ‘V5’ rotate again to connect the SPT to the column. This is the “inject mode” where the formerly trapped analytes are flushed in the opposite direction to sampling flow, onto the chromatographic column (SCION-17MS; 30 m × 0.32 mm × 0.25 µm, 50% phenyl methylpolysiloxane) with helium as the carrier gas for separation and detected with the FID detector. This procedure is a reproducible procedure and was kept constant for all calibrations and flame measurements.

With the support of the exceptional trap technology in the rear channel, PAHs and OPAHs present in very low concentrations (detection limit~1 ppb) could be identified and quantified in this thesis. However, analysis of aromatics is indeed a complicated process especially when we may have oxygenated and non-oxygenated aromatics with their respective isomers as analytes. Thus, in this study, we used the SCION-17MS column with 50% phenyl methylpolysiloxane as the stationary phase as it a suitable candidate when it comes to analyzing aromatics and covers the broadest selectivity range possible for the same. An example of the chromatogram with identified compounds obtained using the rear SPT channel has been presented in Figure 2. 12. Several peaks were identified but some of the peaks could not be identified because of reasons discussed in Chapter 4 in Section 4.1.2.

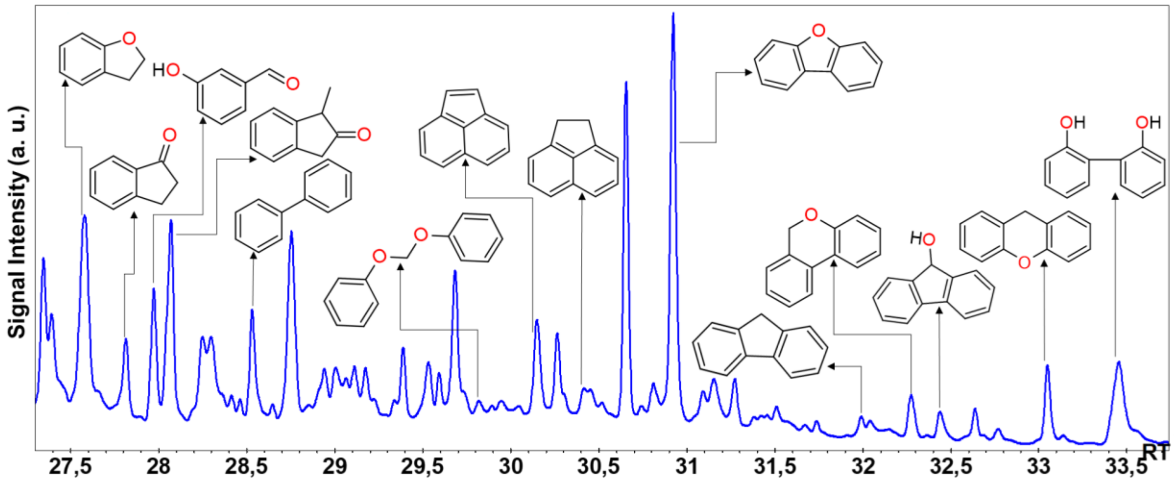

Figure 2. 12 : An example of the chromatogram obtained using the rear SPT channel in GC-SPT-FID Scion in Flame F2 (10% anisole, ϕ=1.82) at an HAB of 1 mm.

2.2.3.1 Calibration of PAHs/OPAHs

Since most of the PAHs and OPAHs are solids at room temperature, another calibration method was implemented whose principle relies on knowledge of the injected mole fraction of the respective species. In this method, the species of interest (PAH or OPAH) is put in a cell that is electronically regulated in temperature (accuracy better than 0.1°C).

A flow of carrier gas (nitrogen) is then introduced into the cell so as to transport the vapor phase of the species to the analysis system. This flow must ideally be slow enough to assure complete saturation of the gas phase so that the vapor pressure of the transported species indeed corresponds to its saturation vapor pressure at that particular temperature of the cell. In order to define the ideal range of flow rate of nitrogen that could be sent into the standard cell, Wartel et al. [176] performed a study where they measured the Laser Induced Fluorescence (LIF) intensity of the vapor phase of pyrene issued from the cell carried by the nitrogen flow for different flow rates. They observed that the measured fluorescence signal decreases when the nitrogen flow becomes greater than a certain value which was determined around 10 mL/min. They attributed this decrease in the signal intensity to the residence time of the nitrogen inside the cell which now becomes too short to enable its saturation by the pyrene vapors. They also reported another set of measurements in a range of flow rates between 1 and 10 mL/min and showed that, within this flow range, the fluorescence signal remains constant irrespective of the nitrogen flow rate, indicating that the vapor pressure of pyrene carried by the nitrogen now does indeed correspond to its saturated vapor pressure at that temperature. Thus, we chose not to use more than 10 mL/min of nitrogen in the cell.

Figure 2. 13 presents the experimental setup used. Nitrogen is used as a carrier gas as well as for the dilution. The principle of the method relies on the Clausius Clapeyron equation. The set of equations related to this concept have been described here. Under any conditions, the initial mole fraction, $x_{i,0}$ of any species is defined as the ratio of its partial pressure in the cell $p_{i,0}$ to the total pressure inside the line using Equation 2. 2.

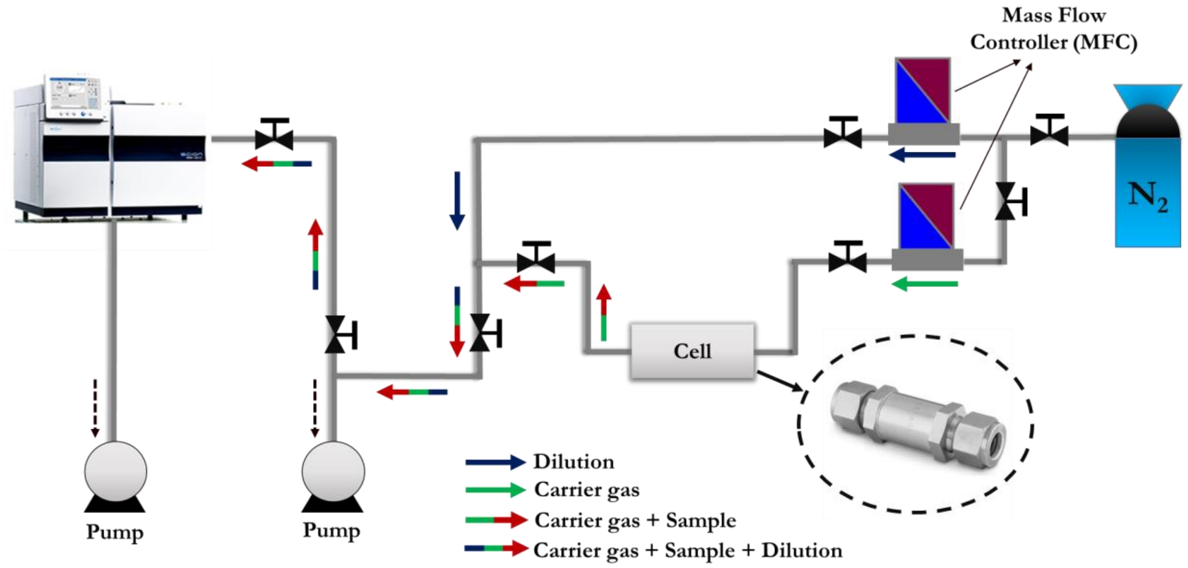

Figure 2. 13 : Schematic representation of the experimental setup used to calibrate OPAHs/PAHs.

$$x_{i,0} = \frac{p_{i,0}}{P_{total}} \qquad \textit{Equation 2. 2}$$

The partial pressure exerted by the substance in the cell at a particular temperature can be determined via the Antoine equation (Equation 2. 3), where A, B and C are the Antoine constants. The Antoine equation is derived from the Clausius-Clapeyron relation and expresses the dependence of the vapor pressure on the temperature for pure substances.

$$Ln\, P = A - \frac{B}{T + C} \qquad \textit{Equation 2. 3}$$

The concentration of the species can then be modified through the dilution line ($D_{dilution}$). Flow rates of the carrier gas can be varied to generate different concentrations while adjusting the flow rate of the dilution line. The mole fraction of the species that is being injected in the GC can be determined by the Equation 2. 4.

$$x_i = x_{i,0} \cdot \left(\frac{D_{carrier\ gas}}{D_{carrier\ gas} + D_{dilution}} \right) \qquad \textit{Equation 2. 4}$$

Substituting the expression for $X_{i,0}$ from Equation 2. 2 in Equation 2. 4, we can simplify the expression to obtain Equation 2. 5.

$$x_i = \frac{p_{i,0}}{P_{total}} \cdot \left(\frac{D_{carrier\ gas}}{D_{carrier\ gas} + D_{dilution}} \right) \qquad \text{Equation 2. 5}$$

By using Equation 2. 5, we can determine the mole fraction of the substance that is injected in the GC by knowing the total injection pressure, dilution, and the partial pressure. The value of the partial pressure exerted by the species in the cell can be derived from the Antoine equation and its corresponding vapor pressure curve. As seen in Equation 2. 3, this pressure value will apparently depend on the temperature of the cell. For most of the OPAHs and PAHs, it is necessary to heat the cell to generate sufficient vapor pressure to perform our measurements. On the other hand, for PAHs such as naphthalene, which has a much higher vapor pressure, we set up an ice bath around the cell containing naphthalene to maintain its temperature at 0°C in order to limit its vapor pressure to produce mole fractions of similar orders of magnitude as those expected in our flames. By varying the dilution, we can perform different successive injections with known mole fractions to obtain a linear fit that corresponds to the calibration curve.

An example of the vapor pressure curve for dibenzofuran deduced from the data reported in the literature [177–179] is presented in Figure 2. 14 (a). To inject different mole fractions of dibenzofuran, we heated the cell to 46°C to obtain comparable peak areas as were observed in chromatograms with flame injections. Consequently, using Equation 2. 5 and varying dilutions, we could vary the mole fractions injected and obtained the calibration coefficient or the response factor for dibenzofuran using the rear SPT channel in GC-SPT-FID Scion as presented in Figure 2. 14 (b). Similar procedure was repeated to perform calibration for other OPAHs and PAHs.

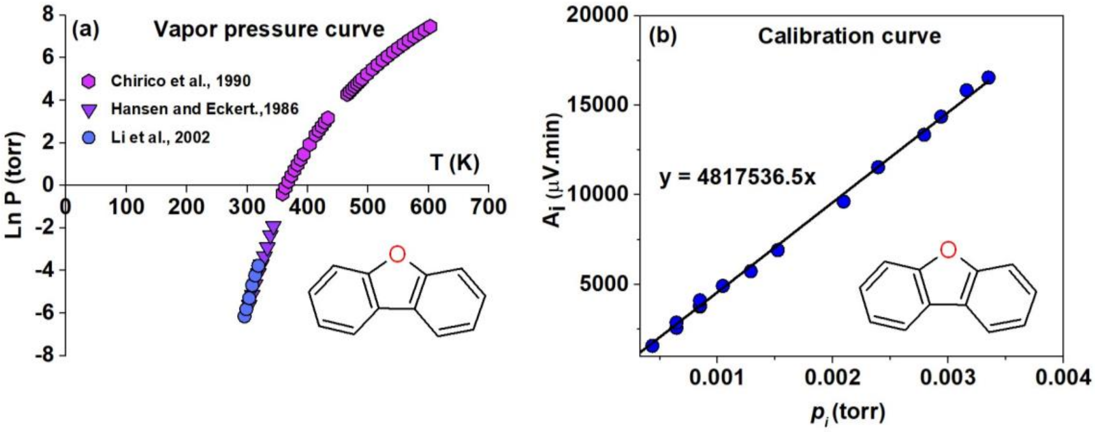

Figure 2. 14 : An exemplary OPAH; dibenzofuran (a) Vapor pressure curve and (b) Calibration curve.

2.2.4. Uncertainties related to GC quantitative results

Amongst several factors, the quality of the data strongly depends on the accuracy of the measurements. Therefore, uncertainties associated with the experimental results are important to determine in order to obtain a reliable dataset with quantification. This is why online GC measurements to deduce the mole fraction profiles were repeated at least twice to verify the repeatability and the reproducibility of the results. It was always ascertained that the mole fraction profiles were characterized with a very good reproducibility (<5%).

Apart from fairly good repeatability, there are other aspects to consider as well. If we review all the elements constituting the experimental device, it is undoubtable that the potential sources of uncertainty are numerous. For instance, the accuracy of the composition of the gas mixture sent to the burner is directly related to the accuracy of the mass flow controllers used in the system (±0.5% per MFC, thus 0.5 × 6 = ±3%). Besides this, the calibration of the chemical species also constitutes important error sources, for instance, the accuracy of the composition of the commercially available standard mixtures (±0.5% for CO, CO_2; ±2-4% for C_2-C_6), stability of the detectors between the period of calibration and the period of measurements, the accuracy of the pressure sensors used to measure the injection pressure (±0.25%), estimation of the response factor using the Effective Carbon Number (ECN) method when standard bottles were not available (±10%) and so on. The ECN method is not straightforward for oxygenated species especially the ones including more than one oxygen atom. The accuracy of the ECN method itself could go up to ±10% [150]. The signal-to-noise ratio in the chromatograms is also an important parameter that needs to be evaluated in uncertainty estimations as the noise of the baseline influences the integrated peak area. This error increases as the signal to noise ratio reduces. For instance, uncertainty could be nearly ±2% for species with concentrations in thousands of ppm, nearly ±4-8% for species with concentrations in hundreds of ppm, and about ±12-17% for species with a few tens of ppm. Other source of errors related to the analysis temporal resolution of GC signal may also be implicated.

Moreover, calibration of PAHs and OPAHs using the distinct setup already described requires precise knowledge of the vapor pressure at a given temperature. The vapor pressure values were either taken directly from the literature or were calculated using the Antoine constants given in the literature. Thus, errors associated with the determination of these parameters in the literature is a surplus source of error in our calibration. For example, Hansen and Eckert [177] and Li et al. [179] reported that the errors associated with their experimental determination of the vapor pressure data for dibenzofuran was nearly ±5% and ±4%

respectively. Stability of the temperature of the cell containing the PAH/OPAH also matters. The accuracy of the K-type thermocouple used to record the real-time temperature of the cell is nearly ±1%. The uncertainty in the flow rate from two mass flow controllers of calibration system (±0.5% × 2 = ±1%) also needs to be considered.

Overall, it was estimated that there is <15% uncertainty associated with the major species like the fuel and major end products, <25% for abundant intermediates (until C_6), and <55% for minor species (<10 ppm) quantified using GC Perkin. For the PAHs and OPAHs (by GC Scion) calibrated directly, additional errors from the calibration setup are a surplus. For PAHs and OPAHs whose response factors were predicted, the uncertainty associated with the estimation increases the overall uncertainty as well. Although each quantified species is associated with an individual absolute uncertainty value, it is safe to assume that this uncertainty is similar for all the flames measured during this thesis and therefore, a relative comparison of trends between the flames can be performed with significantly higher precision. As mentioned previously, following our two-fold repetition for all flame measurements, the repeatability was determined to be <5%.

2.2.5. GC-MS for the identification of species

Online 1-D GC-MS system was also used to identify certain abundant intermediates. Offline Gas Chromatography Mass Spectrometry, GC-MS (1-D and 2-D) systems were used to carry out the identification of species in low concentrations. Since the GC-MS setups do not have the trap accessory, a homemade trap system was built to preconcentrate the samples. To make a homemade trap, the sampling line from the flame was connected to the inlet of a cold borosilicate glass trap which was immersed inside a Dewar flask filled with liquid nitrogen whereas the outlet was connected to a vacuum pump. Apart from withstanding very low temperatures, high quality borosilicate glass has high resistance to chemicals and temperature changes which makes it a suitable candidate for our application. The gaseous sample from the flame passes through the sampling line and consequently flows down the wall of the trap and condenses at the bottom of the trap as liquid nitrogen surrounds the trap.

The pressure inside the trap was constantly regulated. After about 40-45 minutes, the cold borosilicate glass trap was disconnected from the sampling line and the pump and was then removed from the Dewar flask. A schematic representation of the cold trap placed in the Dewar flask has been presented in Figure 2. 15 (a) and a real view of the sample collected at the bottom of the trap after the Dewar flask with liquid nitrogen is removed is shown in Figure 2. 15 (b). After sample collection, acetone was added to dissolve the condensate in the trap to form a solution which was then collected in a vial. Next off, this solution was injected using a thin injection syringe (1 μL) and analyzed using the GC-MS systems. It must be noted that this procedure was carried out at different HABs as different types of aromatics could be present in different amounts at a given HAB. Thus, to perform a thorough and extensive identification of the species in flames, at least two or more HABs were selected to prepare samples via the manual trap system.

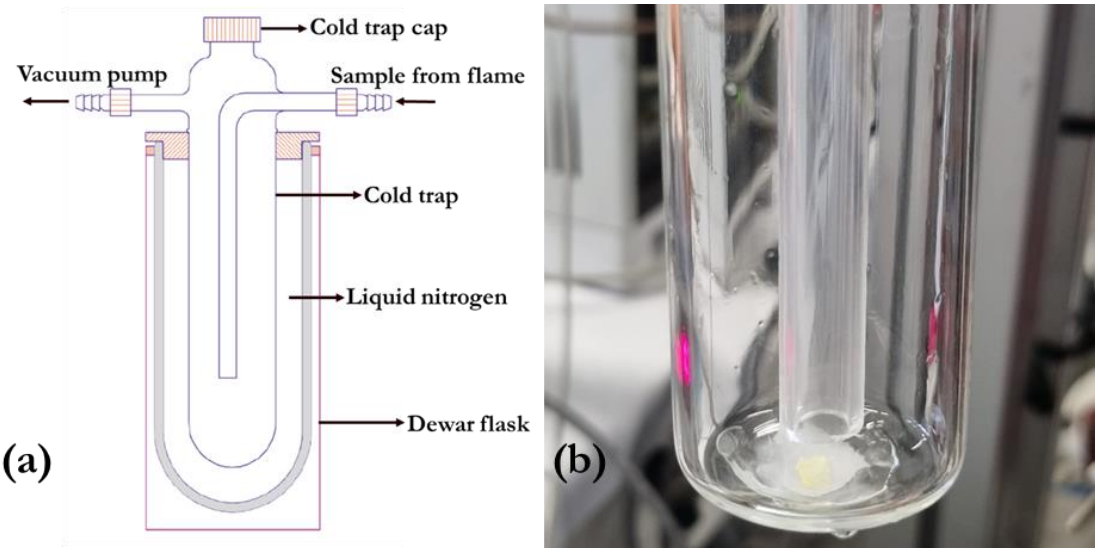

Figure 2. 15 : (a) A schematic representation of the cold trap placed in the Dewar flask; (b) A real view of the sample collected on the bottom of the cold trap after sampling from flame F3 (15% anisole, ϕ=1.82) at an HAB of 1 mm.

2.2.5.1 1-D GC-MS Agilent

A third GC, 1-D GC equipped with a mass spectrometer as a detector (MS) with an electron ionization source at 70 eV (GC: Agilent Technologies 7890A and MS: Agilent Technologies 5975C), was used. The use of 70 eV facilitates the comparison of the generated spectra with library spectra from the 2011 version of the NIST-USA mass spectral database. Analyses were performed online (for small aromatics) as well as offline using a homemade liquid nitrogen trap system (for heavier aromatics). Two different columns, the Rt-Q Bond and the SCION-17MS were alternatively used, one at a given time to identify lighter oxygenates and aromatic species, respectively. The chromatographic column is connected to the mass spectrometer via a transfer device.

The ion source of the mass spectrometer contains a tungsten or a rhenium filament which emits a stream of thermionic electrons when subjected to a very high temperature under vacuum. Thereafter, these electrons are accelerated in a potential field to achieve a standardized energy of 70 eV. After segregation along the column, molecules undergo ionization under the influence of these highly energetic electrons which generate large fluctuations in their local electric fields thus producing radical cations from neutral analytes (electron impact ionization). High vacuum is ensured in the ion source to minimize reactions between the ions formed and other ions or radicals. The high vacuum is chiefly necessary in the *whole* instrument to ensure the ion transfer from the source to the quadrupole analyzer to the detector, as it increases the mean free path of the ions up. At higher pressure, the ions would interact with air molecules at the exit of the ion source, scatter and never reach the analyzer or the detector. The radical cations once formed typically undergo post ionization dissociation or rearrangement reactions to achieve a more stable state. These fragments and the molecular ions are then separated according to their mass to charge ratio (m/z) to generate a mass spectrum. Electron impact mass spectra are highly structured and constitute a "fingerprint" of the analyte for comparison with spectra of already studied compounds. In our case, the mass spectra of the analyzed species are compared to those of the NIST spectral library for identification (Figure 2. 16). Variable split injections were performed to achieve the desired separation and identification.

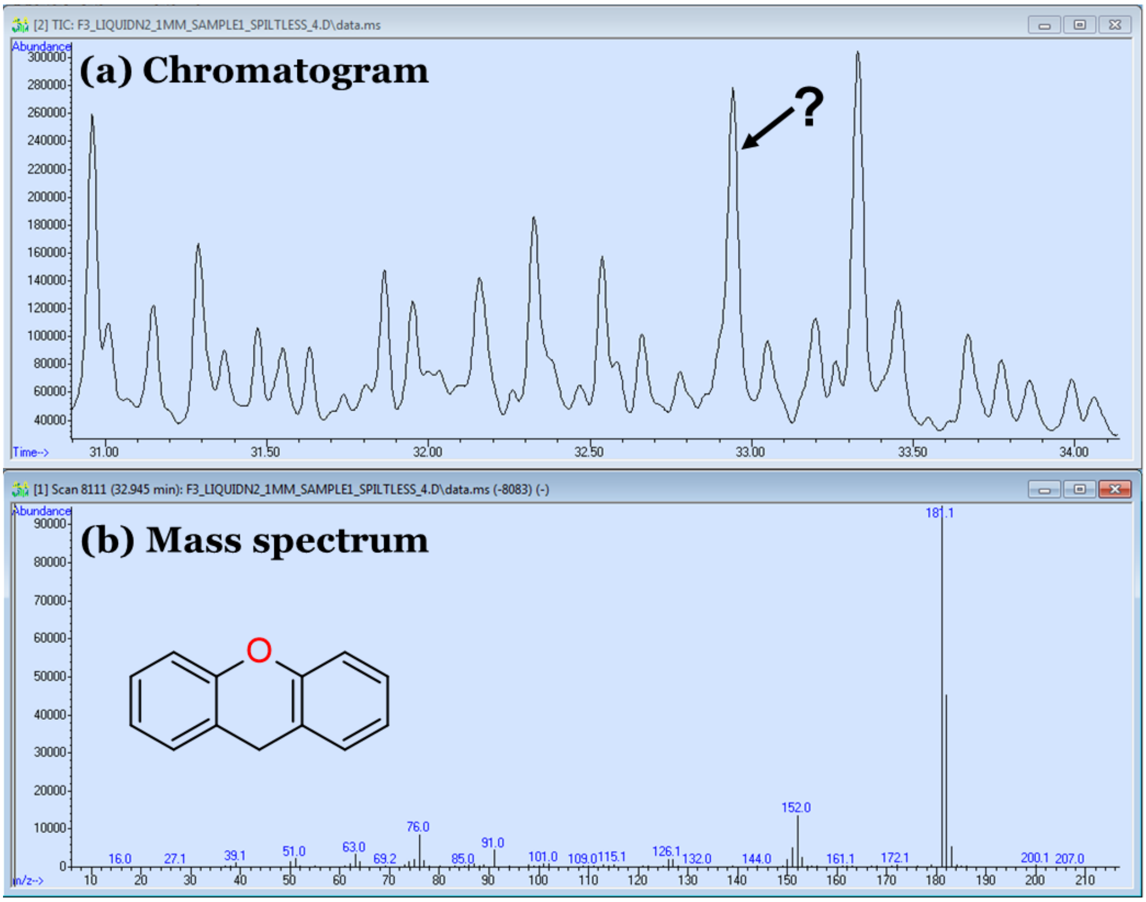

Figure 2. 16 : A zoomed example of the (a) 1-D GC-MS chromatogram for the liquid injection performed using the sample prepared from flame F3 (15% anisole, ϕ=1.82) at an HAB of 1 mm and (b) a mass spectrum for the peak in question at a retention time of 32.945 minutes from the NIST database.

2.2.5.2 2-D GC-MS Thermo Fischer Scientific

Because of the complexity of the chemical composition of the samples containing OPAHs/PAHs from the flames, we thoroughly rechecked the identification using another analytical apparatus. After having analyzed the samples obtained via our homemade trap using 1-D GC setups at our facility, we set out to perform analysis with the 2-D GC-MS in Ghent by transferring our sample vials in an ice box to transport them. A fourth GC: 2-D GC-MS (Thermo Scientific D Trace GC Ultra, with Quadrupole Mass Analyzer and electron ionization at 70 eV) is used in this work at Laboratory for Chemical Technology in collaboration with the team of Prof. K. M. Van GEEM at University of Ghent [180]. We really acknowledge this invaluable collaboration and express gratitude to the research participants involved.

Comprehensive two-dimensional GC (2D-GC or GC × GC) provides an additional dimension to conventional chromatographic separation thus greatly improving the resolution that can be attained, particularly for samples comprising of overwhelmingly unresolved complex mixtures. In this method, each analyte in the sample is subjected to two different separations attained using two GC columns, typically a nonpolar column connected to a more polar column in series via a modulator. The latter is a two-jet cryogenic modulator that spatially compresses and reinjects a portion of the first GC column eluent into the second GC column. In this way, all compounds are subjected to two different separations. Modulation time (6 seconds in this study) being a few seconds is not enough to transfer a full peak but more reasonably slices of it as presented in Figure 2. 17.

The 2-D GC-MS in Ghent employed: a non-polar column (DB-5MS; 30 m × 0.25 mm × 0.25 μm, 5% phenyl-methylpolysiloxane, Agilent) and a polar column (DB-17MS; 2 m × 0.25 mm × 0.25 μm, 50% phenyl-methylpolysiloxane, Agilent) in the same oven using helium as the carrier gas. Figure 2. 18 presents an example of the obtained 2D chromatogram. Using this setup, we confirmed several aromatics that were already seen in our 1-D GC-MS system, and also observed some new species.

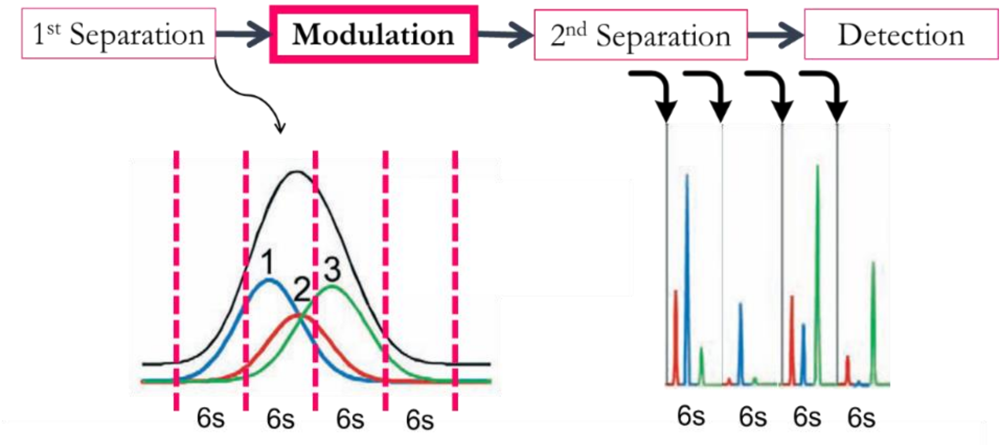

Figure 2. 17 : Depiction of the fundamental principle behind the functioning of a 2-D GC.

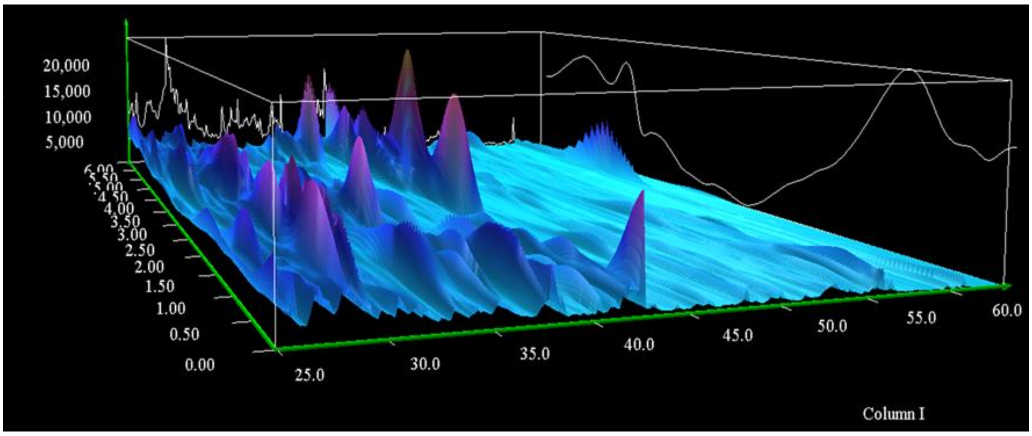

Figure 2. 18 : A 3D view of an example of the chromatogram obtained via the 2-D GC at LCT (Laboratory for Chemical Technology), University of Ghent for flame F5 (10% anisole, ϕ=1.90) at an HAB of 1 mm.

2.3. Measurement of soot particles

This section is devoted to the description of the tools and methodology adopted to perform soot particle measurements. Two techniques namely, the Laser Induced Incandescence (LII) and the Scanning Mobility Particle Sizer (SMPS) were used to measure the soot volume fraction and the particle size distribution respectively. The first part of this section is dedicated to fundamentals of LII and the setup used whereas the second part deals with the essentials of SMPS and the overall system used.

2.3.1. Soot volume fraction determination using Laser Induced Incandescence (LII)

The Laser induced incandescence (LII) technique is a powerful laser diagnostic for the study of soot formation. Due to its potential, it has been used to measure soot volume fraction in many applications in fundamental and applied combustion experiments, such as laminar and turbulent flames, exhausts of automobiles and aero engines [64,65,181–186]. In addition, LII models and techniques have been elaborated to retrieve physicochemical soot properties as the absorption soot properties [187–189] and particles size distribution notably with the time-resolved LII signals. This section is composed of two subsections. The first subsection is devoted to the fundamentals behind LII whereas the second subsection details the experimental setup and approach used to retrieve the axial profiles of soot distribution in this thesis.

2.3.1.1 Fundamentals of LII

The laser-induced incandescence (LII) technique is an optical method used to measure the soot volume fraction in flames with high precision and excellent sensitivity (ppt levels). Its principle is based on the prior heating of soot particles by laser radiation.

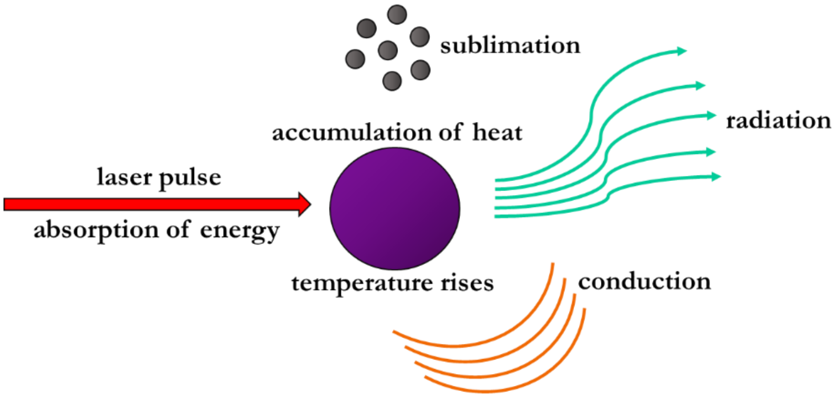

Figure 2. 19 : Illustration of the main processes occurring during the interaction between the laser pulse and soot.

Under the effect of a laser pulse, the internal energy of the soot particles increases as they accumulate heat via the absorption process. These heated soot particles acquire temperatures close to the sublimation temperature of graphite carbon (~3940 K at atmospheric pressure) and will consequently cool down by three competitive routes: conduction towards the external environment, sublimation, and thermal radiation. Figure 2. 19 presents the various processes involved following the absorption of the laser energy by the primary soot particles. Incandescence corresponds to the thermal radiation emitted during the cooling phase of the primary soot particles that constitute soot aggregates. The determination of the quantity of soot particles results from the analysis of this thermal emission. The LII signal, which characterizes this phenomenon of thermal radiation, is expressed based on Planck's law (law of thermal emission of the black body) in which various parameters such as the number of heated particles emitting photons, their respective geometries and optical properties are taken into consideration. The monochromatic emittance of a blackbody at a temperature T integrated over the emission spectral range $\Delta\lambda_{em}$ is given by Equation 2. 6.

$$M(\Delta\lambda_{em}, T) = \int_{\lambda_1}^{\lambda_2} \frac{2\pi hc^2}{\lambda_{em}^5} \left[exp\left(\frac{hc}{\lambda_{em} k_b T}\right) - 1\right]^{-1} d\lambda_{em}$$

Equation 2. 6

$M(\Delta\lambda_{em}, T)$: Emittance W/m^2

$\Delta\lambda_{em}$: Emission spectral range ($\Delta\lambda_{em} = \lambda_2 - \lambda_1$)

T: Temperature of the black body (K)

h: Planck's constant (6.62×10^{-34} Js)

k_b: Boltzmann constant (1.38×10^{-23} J/K)

c: Speed of light (3×10^8 m/s)

A black body is an ideal absorber and emitter of energy. However, soot particles behave like gray bodies, i.e., they do not re-emit all the energy absorbed. Thus, an emissivity term, $\varepsilon(\lambda)$ needs to be introduced to account for this deviation from the Planck's Law (for a black body which re-emits all the absorbed flux) for a gray body-type emitter (body re-emitting only part of the absorbed flux). The power emitted by a single spherical particle of diameter $r_p(t)$ over its emission range $\Delta\lambda_{em}$ can be expressed at any instant t during the cooling process via Equation 2. 7 [190]:

$$P_{LII}(t, \Delta\lambda_{em}) = \int_{\lambda_1}^{\lambda_2} \frac{2\pi hc^2}{\lambda_{em}^5} \left[exp\left(\frac{h.c}{\lambda_{em} k_b T_p(t)}\right) - 1\right]^{-1} 4\pi r_p^2(t)\varepsilon(\lambda) d\lambda_{em}$$

Equation 2. 7

If we apply the Kirchhoff hypothesis to our case, which states that the particles are in thermodynamic equilibrium with the electromagnetic radiation, the absorption efficiency $Q_{abs}(\lambda)$, can be considered equivalent to its emissivity $\varepsilon(\lambda)$ [191].

$$Q_{abs}(\lambda) = 8\pi r_p(t) \frac{E(m)}{\lambda_{abs}} = 8\pi r_p(t) \frac{E(m)}{\lambda_{em}} = \varepsilon(\lambda)$$

Equation 2. 8

The term $E(m)$ in this expression, referring to the absorption function of the soot particles, is a quantity dependent on the refractive index of the soot and is representative of their morphology and maturity. This term is also a function of the absorption wavelength.

Typically, $E(m)$ may vary from 0.21 to 0.40 at 1064 nm depending on the soot maturity [189,192–198]. Thus, the LII signal, $S_{LII}\left(\Delta\lambda_{em}, T_p(t)\right)$ which corresponds to the flux of incandescence photons emitted isotropically from all the primary soot particles, N_p (cm^{-3}) considered as spherical can be expressed by Equation 2. 9. N_p here represents the number of primary soot particles and not the number of aggregates.

$$S_{LII}\left(\Delta\lambda_{em}, T_p(t)\right) = \int_{\lambda_1}^{\lambda_2} 64E(m)\frac{\pi^3 hc^2}{\lambda_{em}^6}\left[exp\left(\frac{hc}{\lambda_{em}k_b T_p(t)}\right) - 1\right]^{-1} N_p r_p^3(t) d\lambda_{em}$$

Equation 2. 9

Equation 2. 10 expresses the term soot volume fraction f_v, as a product of the number of primary soot particles and the volume occupied by those particles.

$$f_v = N_p \frac{4\pi r_p^3}{3}$$

Equation 2. 10

By incorporating Equation 2. 10 in Equation 2. 9, we obtain the final Equation 2. 11 which shows that the LII signal is reliant on numerous parameters such as the soot volume fraction f_v, the soot refractive index $E(m)$, the detection wavelength λ_{em} and the temperature of the soot particles T_p. This temperature depends on the absorbed laser energy. At higher laser energies, the soot particles may reach their sublimation temperatures and loose mass thereby leading to a reduction in their diameters which contributes to a loss of signal intensity. The modeling of the time dependent thermal response of the primary particles to the laser energy (incandescence signals) thus requires precise knowledge of these parameters as well as their variations in the flames. Through modeling, it is possible to evaluate the diameter of the particles being analyzed [187,199].

$$S_{LII}\left(\Delta\lambda_{em}, T_p(t)\right) = \int_{\lambda_1}^{\lambda_2} 48E(m)\frac{\pi^2 hc^2}{\lambda_{em}^6}\left[exp\left(\frac{hc}{\lambda_{em}k_b T_p^{max}(t)}\right) - 1\right]^{-1} f_v d\lambda_{em}$$

Equation 2. 11

$$S_{LII}\left(\Delta\lambda_{em}, T_p(t)\right) = 48E(m)\frac{\pi^2 hc^2}{\lambda_{em}^6}\left[exp\left(\frac{hc}{\lambda_{em}k_b T_p^{max}(t)}\right) - 1\right]^{-1} f_v \Delta\lambda_{em}$$

Equation 2. 12

In this thesis, the intensity of LII signals (temporal peak) enable us to deduce the relative quantity of soot produced and therefore allows the determination of the volume fraction profiles (in relative intensity) as a function of the HAB.

2.3.1.2 LII experimental setup

LII experiments were performed in collaboration and the entire experimental system shown in Figure 2. 20 was developed, built, assembled, and made operational by Dr. Pascale Desgroux. The LII experiments were performed by using a 1064 nm laser excitation wavelength generated by a Nd:YAG laser (Quantel Brilliant) at 10 Hz with a FWHM pulse duration of 5 ns. This wavelength is used to avoid any spectral interferences with PAHs absorption transitions [64,200]. The laser beam has a gaussian distribution. To heat all the primary soot particles uniformly in the measured volume, measurements were carried out with the same top-hat laser beam energy distribution profile (and therefore same laser energy) at all HABs. The fairly top-hat laser energy distribution allowed to heat the primary soot particles with nearly the same energy along the burner axis. To do this, the initial laser beam was transformed into a laser sheet using two different cylindrical lenses: a diverging lens of focal length f_1 = -40 mm and a converging lens of focal length f_2 = 200 mm. Then, a section of this sheet was selected using a rectangular slit and was imaged at the center of the burner using another lens with focal length f_3 = 300 mm. This way we ensured heating all the primary soot particles uniformly. In this configuration, the laser energy can be varied using an optical attenuator and monitored with a power meter.

The LII signal or transmitted laser radiation from the soot in the flame is collected simultaneously using narrow bandpass filters centered at 532 nm and was recorded by an oscilloscope. It should be noted that to determine the axial profiles of the volume fraction, the background signal from the flame was subtracted from the measured LII signal. The image characterizing the flame's own emission due to its luminosity is recorded simply by cutting the laser beam.

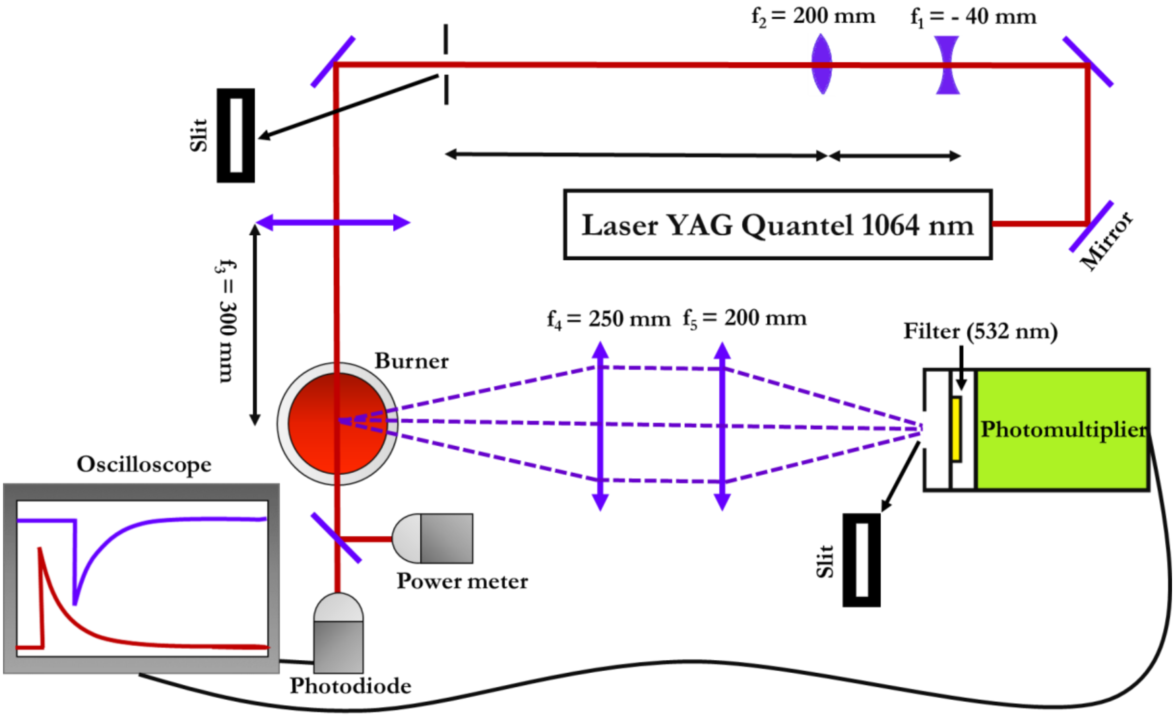

Figure 2. 20 : Schematic representation of the experimental setup used for LII.

2.3.1.3 Methodology and calibration

Description of Fluence curves and E(m) determination

LII fluence curves represent the dependence of the LII signal on the fluence i.e., the laser energy per unit area of cross section. They present the variation of the absorption efficiency of the particles (or their ability to be heated) with respect to the laser energy. An example of fluence curve for flame F5 is presented in Figure 2. 21. This fluence curve was obtained by recording the value at the temporal peak of the incandescence signal (HAB=16 mm). It can be seen that the LII signal starts to appear at lower fluences (0.10 J/cm^2) which marks its onset (threshold) and then increases as the energy of the laser is increased followed by a bend around 0.54 J/cm^2 which marks the highest LII signal obtained with respect to laser energy. At high laser fluences, particle temperatures reach a maximum close to their sublimation temperature. Understanding the fluence curves is central to demonstrate the critical choice of the appropriate fluence to carry out quantitative LII measurements. It is necessary to determine the optimal laser energy, to obtain the most intense signal while avoiding sublimation of the particles and minimizing the impact of the fluctuations of the laser. As seen in the figure, an energy density of 0.54 J/cm^2 seemed as the most suitable for the acquisition of the axial soot distribution profiles.

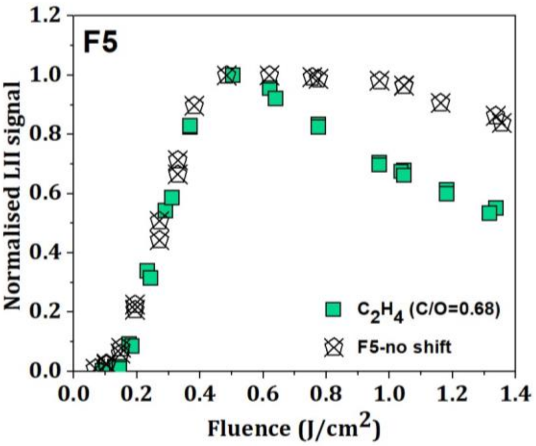

Figure 2. 21 : Evolution of the normalized LII signal with respect to the laser fluence for flame F5 and the reference ethylene flame.

To obtain the absolute value of the soot volume fraction via the LII signals, it is primordial to determine the soot absorption function $E(m)$. It is worth mentioning that curves shifting to lower fluences signify that the absorption efficiency of the soot particles is high whereas curves shifting to higher fluences indicate that the soot particles absorb the laser energy less efficiently [201]. This implies that the characteristics of the LII fluence curves can indicate the variation of the physiochemical properties of the soot particles and can allow us to retrieve information on the soot absorption function $E(m)$. Figure 2. 21 presents the fluence curves for flame F5 and a reference ethylene flame for which the $E(m)$ is already known [202]. It can be seen that the gradient of the two fluence curves exactly coincide with each other which reflects that soot particles in these flames absorb the laser energy in a similar way and thus possess similar optical properties [202]. Assuming that the maximum temperature attained by these particles would be similar, it is reasonable to infer that their soot absorption functions $E(m)$ would be equal. This way, we could determine the $E(m)$ for flame F5. It is noteworthy that the fluence curve for some flames may not possess the same gradient as the reference flame as their soot particles might not absorb in an identical way. In these cases, the variable on the abscissa can be transformed to take the difference into account and estimate the value of $E(m)$. The details concerning this methodology is discussed in Chapter 6.

Methodology to determine the soot volume fraction profiles

The soot volume fraction profiles for the flames were determined using a reference C_2H_4 flame for which the $E(m)$ and the soot volume fraction ($f_{v\,(C_2H_4)}$) were already determined via the CRDS (Cavity Ring Down Spectroscopy) technique by Dr. Pascale Desgroux. The profiles were calibrated using this reference flame (at HAB=16mm). Equation 2. 11 can be expressed for the reference flame (C_2H_4) and the flame in question (x) to give two equations. Dividing these two equations and further simplification would lead to Equation 2. 13 under a hypothesis that the maximum temperature acquired by the soot particles on being heated is similar in the two flames.

$$f_{v(x)} = \frac{\mathrm{S_{LII}}\left(\Delta\lambda_{\mathrm{em}}, T_p^{max}\right)_x}{\mathrm{S_{LII}}\left(\Delta\lambda_{\mathrm{em}}, T_p^{max}\right)_{C_2H_4}} \frac{E(m)_{C_2H_4}}{E(m)_x} \times f_{v\,(C_2H_4)} \qquad \textit{Equation 2. 13}$$

To deduce the absolute soot volume fraction using Equation 2. 13, one also needs to estimate the parameter $E(m)_x$. The soot absorption function or $E(m)_x$ was estimated using the methodology explained in the previous subsection and in Chapter 6. In this equation, $f_{v\,(C_2H_4)}$ is already known and the ratio $\mathrm{S_{LII}}\left(\Delta\lambda_{\mathrm{em}}, T_p^{max}\right)_x / \mathrm{S_{LII}}\left(\Delta\lambda_{\mathrm{em}}, T_p^{max}\right)_{C_2H_4}$ was deduced by performing alternate measurements in the two flames. This way all the unknowns in Equation 2. 13 could be determined in order to calculate the soot volume fraction. The overall uncertainty associated with the soot volume fraction measurements is estimated to be around ±20%.

2.3.2. Particle size distribution measurements by scanning mobility particle sizing

In the context of flame studies, several investigators have widely demonstrated the utility of Scanning Mobility Particle Sizer (SMPS) devices in recent years by measuring the size of soot particles, particularly in premixed flames [203–210]. The SMPS technology allows to measure the particle concentration as a function of a quantity, called the electrical mobility, that represents the ability of a particle suspended in a gas to traverse an electric field and it is fundamentally related to the particle size (monomer or aggregate). The notion of the electrical mobility diameter (D_p) can be considered equivalent to the size of soot particles when subjected to certain assumptions on their density and morphology (discussed later in Chapter 6). Here, the soot particles are charged and size-selected according to their electrical mobility in the carrier gas and subsequently counted. This technique yields the electric mobility diameter, which is the diameter of a sphere that would balance the electric force with the drag force on a charged particle in an electric field

2.3.2.1 SMPS setup

Commercial SMPS are generally limited to d_m > 10 nm. The SMPS used for this thesis is additionally equipped with a nano-enhancer module, which permits the measurement of very small particles down to $d_m \approx 1.5$ nm. The actual SMPS device (TSI, Inc.) is composed of different elements each of which has a specific role to play. It consists of a 3088 neutralizer, a

1 nm 3086 differential mobility analyzer (DMA), a 3082 electrostatic classifier, a 3757 nano-enhancer and a 3750-condensation particle counter (CPC). The experimental setup used for the measurement of the PSDs is presented in Figure 2. 22. It consists of two parts, the sampling system and the actual SMPS device.

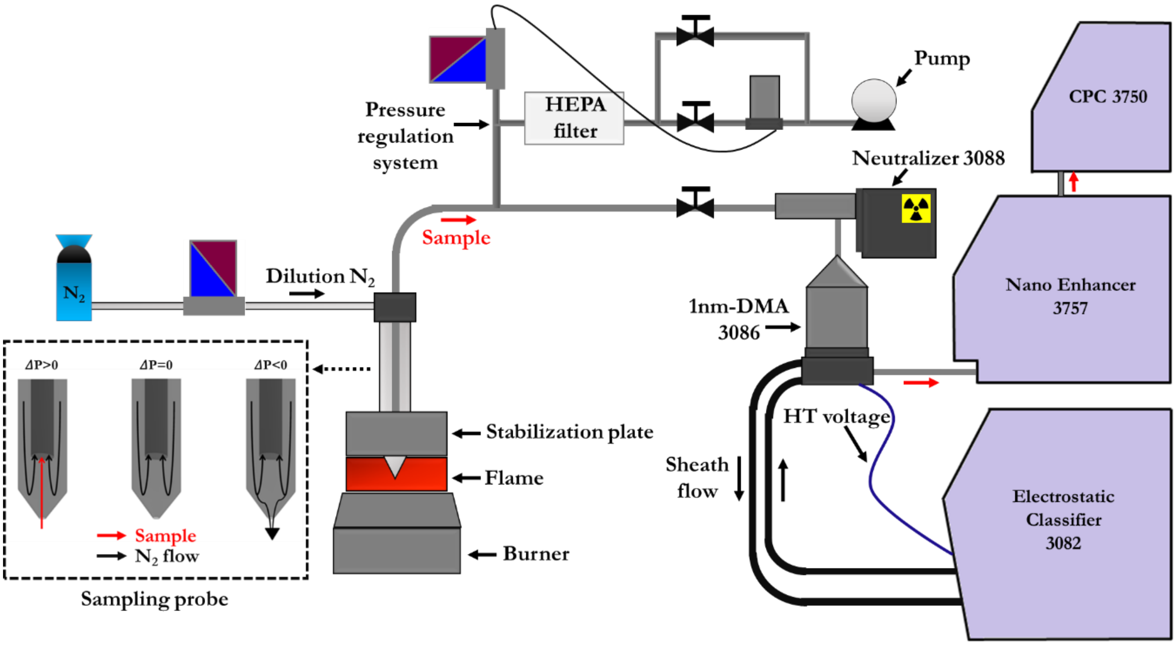

Figure 2. 22 : Experimental setup of the sampling system and the SMPS device used for PSDs.

In order to sample soot from the flame, a special probe sampling system featuring high dilution ratio to quench post sampling chemical reactions and avoid coagulation and aggregation of the particles, was used.

The sampling probe, made of two co-annular tubes is coupled downstream to an automatic pressure regulation system for stabilizing the pressure in the sampling line. The outer quartz tube has an orifice size of about 180-200 µm. The probe was fixed and introduced axially in the perforated stabilization plate. A dilution flow (nitrogen 5 L_n/min) enters the probe via the side port and flows between the two quartz tubes up to the probe tip. On applying a controlled pressure difference between the flame pressure i.e., atmospheric pressure and the pressure in the line, the sample from the flame enters the probe via its orifice. The sample entering the probe is immediately diluted at the probe tip by the cold nitrogen dilution flow, and both are pumped across the inner tube. The larger the differential pressure, the more efficient the extraction of soot from the flame (soot and gas concentration in the sampling line increase). Such sampling procedure was adopted to prevent particle coagulation and to quench chemical reactions, thus preventing particle mass growth within the sampling line. However, low dilution typically results in unwanted phenomena like post-sampling particle coagulation that bias the readings by shifting d_m to higher values. The chosen differential pressure to perform the sampling is a compromise between sufficient signal to noise ratio and avoiding coagulation of the particles as well as saturation of the neutralizer ($<10^7$ #/cm^3), nano-enhancer and CPC ($<3\times10^5$ #/cm^3).

The size distribution and concentration accuracy are dependent on the knowledge of the charge distribution of the incoming aerosol. The stream of soot particles sampled from the flame is first sent to the neutralizer that uses bipolar diffusion charging to obtain a known steady-state charge distribution of the aerosol. The radiation ionizes the molecules of the air and the formed ions are attracted to the soot particles and thus attribute them with positive or negative unit or multiple charges as a function of their respective diameters. This way the charges get redistributed in order to obtain a predictable charge distribution. This step is critical to collecting reliable particle size data when using an electrical mobility-based sizing instrument. The aerosol flow rate in the SMPS system was set at 2.5 L/min so that the residence time of the latter in the neutralizer was sufficient to effectively impose a known charge distribution.

The flow of aerosol at the outlet of the neutralizer is directed onto the column of the 1nm-DMA 3086. The DMA column consists of a cylinder, the walls of which are grounded, and a charged central rod which is subjected to a variable voltage delivered by the electrostatic classifier 3082. This makes it possible to create an electrostatic field in the space between the walls and the rod which is used to select the particles according to their electric mobility when they pass through the column. Physically, this field deflects the particles from their trajectory depending on the voltage applied to the central electrode. Particles that possess an electrical mobility smaller than the targeted one are discharged on the central electrode while particles that possess an electrical mobility greater than that targeted are evacuated with the sheath flux. Only the particles with well-defined electrical mobility exit through the output slit to be counted by the CPC. Thus, by crossing the DMA column, the soot particles which have a narrow range of electric mobility (monodisperse) are filtered from the mixture of particles having different mobilities (polydisperse).

From the electrostatic classifier 3082, a particle-free sheath flow with a flow rate of about 25 L/min is sent to the DMA column. The 1:10 sample/sheath flows ratio ensures laminar flow conditions in the column. The latter undergoes several stages of filtration in order to be reprocessed. This flow circulates in a loop in the column of the DMA. The flow of aerosol entering the CPC particle counter is 2.5 L/min. This flow is split again to supply the sample stream. The sheath flow filtered beforehand is mixed with gaseous butanol in the saturation chamber maintained at 39°C. This stream is then mixed with the sample stream and cooled at the condenser to a temperature of 14°C. This rapid temperature drop creates conditions necessary for butanol vapors to condense on droplets coming from the nano-enhancer 3757 to increase droplet size up to a few micrometers that are counted individually via optical counting based on light scattering. This counting is ensured by means of a laser diode and a photodetector which counts the pulses of scattered light. The ultrafine CPC is sensitive to particles as small as 2.5 nm.

Soot particles smaller than 3 nm are difficult to detect by the regular CPCs that use 1-butanol as working fluid [211]. This is why the nano-enhancer module is used to increase the detection threshold down to around 1.5 nm. For our system, the 3757 nano-enhancer uses diethylene glycol (DEG) as a working fluid to activate the smallest particles. DEG has a higher surface tension and a lower vapor pressure than 1-butanol which promote particle size growth while avoiding parasitic homogeneous nucleation processes [212,213] that may bias the results of particle counting. In the nano-enhancer, the aerosol flow (2.5 L/min) is distributed to feed the sample flow. The sheath flow previously filtered is mixed with DEG in the saturation chamber maintained at 70°C. This stream is then mixed with the sample stream and cooled to a temperature of 10°C. Thus, the DEG vapors become supersaturated and condense on the particles to form micro-droplets before entering the CPC 3750 where these are counted.

Overall, the nano-SMPS allows the measurement of soot particles with sizes between 1.5 to 50 nm. This device also has excellent specificities for measuring soot smaller than 3 nm. It is therefore perfectly suited for the study of our flames and in particular for the measurement of very small soot particles. The evolution of the number and size of the soot particles is followed real-time at several HABs to deduce the particle size distributions (PSDs).

2.3.2.2 Data treatment methods

In order to attain deeper insights in connection with the PSDs derived experimentally from the SMPS device, mathematical functions were used to fit the PSD data in order to identify monomodal or bimodal distributions. To do so and determine the adjustment parameters associated with these fits, the procedure proposed by Commodo et al. [206] was followed. It is well known that the lognormal distribution function usually provides a good fit for the PSD and has widely been used for the soot particles [203,214]. The measured PSDs were therefore fit with 1-2 log-normal functions, depending on the HAB, using the OriginLab software and the onset of the bimodality of the PSD was estimated from the subsequent analysis of these fits. It was sometimes observed at higher HABs that the double log-normal is the best fitting function and a single log-normal function is no more representative of what was experimentally obtained. At lower HAB, one lognormal function was sufficient to fit the PSD while two lognormal functions were required to fit the PSDs at higher HABs indicating the presence of two modes. The resulting parameters from the fit procedure such as the mean diameter, area and log standard deviation corresponding to Mode-1 and Mode-2 log-normal distributions were plotted respectively as a function of the HAB to study the evolution of the two modes. Figure 2. 23 shows the normalized PSDs, $\frac{dN}{dlogD_p}$, where N is the number density measured by the SMPS and D_p is the particle diameter, as a function of N at several HABs for flame F5. The number particle concentration here is presented on the y-axis as $\frac{dN}{dlogD_p}$ in the log-scale and the mobility diameter (nm) is presented on the x-axis in the log scale. The $\frac{dN}{dlogD_p}$ concentration is the normalized concentration. dN is the number of particles in a given range (total concentration) and $dlogD_p$ represents the difference in the log of the channel width. $dlogD_p$ is calculated by subtracting the log of the lower bin boundary from the log of the upper boundary for each channel i.e. normalizing with respect to the bin width. The concentration is then divided by the bin width, giving a normalized concentration value that is independent of the bin width. Presentation of the particle number concentration in this way enables us to compare our PSDs with other PSDs from other instruments with different resolutions.

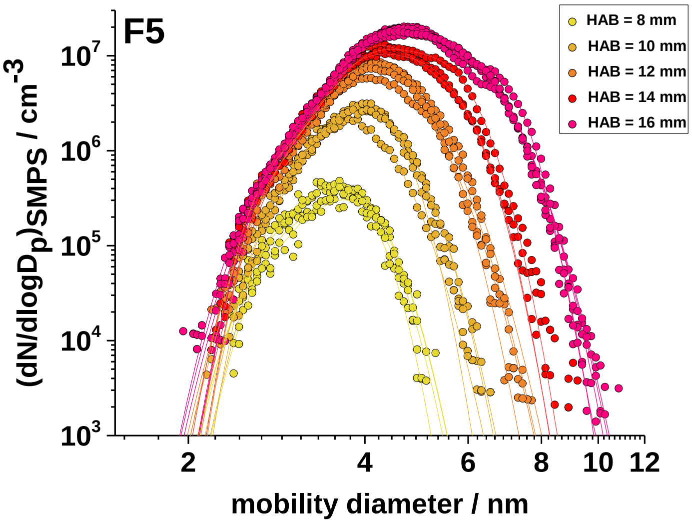

Figure 2. 23 : Particle size distribution (PSD) obtained for flame F5 (10% anisole, ϕ=1.9) at different HABs; Multiple acquisitions were recorded at each HAB. The solid lines here represent the cumulative fits performed using log-normal fitting.

2.4. Conclusion

In this chapter, the different techniques and the approaches that were adopted to study the role of some specific biofuels (anisole, DMF and ethanol) are presented. The idea was to characterize the flame structure with primary focus on the oxygenated aromatics together with a study of soot particles. In order to achieve this goal, seven flames were stabilized to be investigated using an experimental approach. The flame structure study was performed by using different, but complementary GC setups described in this chapter. The mole fraction profiles of the stable chemical species in the flames were obtained by gas chromatography analysis. LII was used to measure the soot volume fraction profiles and the SMPS was used for the determination of the PSDs. In addition to the measurement of gaseous and particulate species, the temperature profiles were measured and the method implemented is presented in Chapter 3. Main qualitative and quantitative GC results are presented in Chapter 4 and Chapter 5. Results on the characterization of the soot particles are presented in Chapter 6.

Chapter 3. Measurement of temperature

Accurate temperature measurements are critical when dealing with the subject of kinetics in flames [215]. The measured temperature profiles are necessitated to perform numerical simulations in order to develop and validate chemical kinetic models. These measurements are typically performed using optical techniques or thermocouple-based thermometry. The former presents the benefit of being non-intrusive, consequently ensuring local measurements without perturbing the flame whereas the latter despite being intrusive, particularizes much less expensive equipment and comes across as a much simpler technique to implement. In spite of what preceded, the high sensitivity of the non-intrusive laser diagnostics to interferences like beam steering can lead to high uncertainties [216,217]. Thus, even though employing thermocouples necessarily disturbs the flat flame as the wire junction needs to be physically placed at the point of temperature measurement, they are still extensively used in combustion to perform temperature measurements in many laboratories because of their simplicity in terms of installation, low cost, and robustness [218]. In this work, thermocouple-based thermometry is used to perform temperature measurements and LIF-NO thermometry is used to compare with our experimental approach.

3.1. Thermocouple based measurements

A fine-wire thermocouple consists of two wires of dissimilar metals or alloys welded at one end to form a junction. When this fused junction is heated, a measurable temperature-dependent voltage is induced at the open end which can be correlated to the temperature of the junction. Since their first applications, it is known that thermocouples are reliable in relating the induced voltage to their own temperature (i.e. that of the junction). However, it is important to take into consideration that the temperature being measured here is the temperature of the welded junction and this value does not necessarily correspond to the real temperature of the surrounding gases in which the junction is immersed. In the common situation of a thermocouple surrounded by a hot gaseous environment, the wires and the junction are at a temperature lower than that of the gas because of different kind of losses. The obtained data might be significantly under-estimated in an amount that depends on the flame and the thermocouple (in particular, its size). Consequently, quantitative interpretation of thermocouple-based measurements in high-temperature environments is hampered by the need to account for the important heat transfer mechanisms associated with the wire and the junction to compensate for these energy losses. The following text lists the different types of energy losses that might occur.

Firstly, there are potential losses by conduction. The temperature of the bead junction can be affected by the conduction of heat to the adjacent wires which may induce an underestimation of the temperature. This phenomenon can be avoided by positioning the thermocouple in the same horizontal plane as the heat flow or can also be discarded by design, usually by setting a certain length of the wires [219]. In addition to conduction losses, catalytic reactions are likely to occur at the junction. While platinum and its alloys are generally selected for the thermocouple wires as they do not alter under oxidative atmospheres (such as in flames), such materials can still act as catalysts for exothermic chemical reactions at the bead surface, for instance the OH radical recombination which is especially prone to occur in a premixed flames [220]. Such an effect can lead to over-estimation of the measured temperature by prompting extra energy transfers and can be prevented by protecting the thermocouple with specific non-catalytic material coatings [220] .

Whilst conduction and catalytic losses can be limited, radiation losses remain the most important sources of error during temperature measurement of hot gases. The inherent radiative losses in high temperature media cannot be avoided by design and potentially lead to underestimation of the flame temperature by several hundred degrees [221]. In 1981, Attya et al. [222] reported that at a temperature of 1400°C, radiation losses as high as 250°C could occur during temperature measurements in a kerosene spray flame using a 0.30 mm diameter thermocouple. Conduction losses are negligible for fine-wire thermocouples and thus radiation loss corrections present the most difficult challenge to deduce accurate measurement of gas temperatures. This correction is a complex problem that is difficult to quantify and is complicated by uncertainties in variables such as the local convective heat transfer coefficient, the bead size, its shape, and its emissivity. Therefore, different experimental solutions have been developed to minimize the radiative exchange between thermocouples and their surroundings, for instance, the use of shielded thermocouples whose use is mostly recommended for global temperature measurements as a fine resolution in space and time cannot be achieved [223]. The most widespread approach to address the problem of radiation correction is using bare bead thermocouples together with a correct estimation of the radiation bias to determine the true local temperature. Several methods have been reported in the literature to estimate these losses [224,225]. In 2017, Lemaire et al. [226] performed a comparative study of the different methods, namely the Electrical Compensation (EC), the Reduced Radiative Error (RRE), the Multi-EleMent method (MET) and the Extrapolation method to determine the radiation losses that occur in thermocouple-based temperature measurements. They made a comprehensive study on the implementation of these methods together with a breakdown of their sensitivities and accuracies and highlighted the underlying sources of uncertainties. The EC method allows to estimate the true gas temperature by correcting measurements from the contribution of radiative losses estimated via vacuum experiments. The RRE method is based on a steady state heat transfer model allowing the estimation of radiation errors by using two thermocouples having different diameters. The extrapolation method is relatively straightforward to implement as it only requires knowing the diameter of the two (or more) thermocouples selected to perform the temperature measurements [226].

This study seeks to implement a simple experimental methodology, without the level of sacrifice to spatial and temporal resolution that is inherent in this kind of temperature measurements combined with the extrapolation method as a correction method to retrieve the actual flame temperature. The extrapolation correction method is one of the oldest documented methods in modern combustion science [227], however, structured studies intending to validate its use are scarce in the literature [228–230]. It is based on the principle that the radiation losses are proportional to the size of the thermocouple, i.e., the thinner the thermocouple the lower the radiative losses. To put it in another way, this method relies on the statement that a zero-dimension thermocouple is supposed to experience no radiation losses at its surface thus providing the real value of temperature. Recently, Elias et al. [231] reported a methodology to correct for fine wire thermocouple losses in a methane laminar diffusion flame where they showed that there exists a linear correlation between the radiation losses and the size of the thermocouple by implementing four thermocouples of different sizes (0.20, 0.35, 0.42 and 0.50 mm). Thereafter, they compared their corrected temperature profiles with those obtained by OH and NO Laser Induced Fluorescence (LIF) thermometry to validate their measurements. Their results seemed to suggest that the actual flame temperature could be retrieved by making use of the linear extrapolation to zero diameter. In this study, we employed a similar approach as Elias et al. [231]. However, presuming beforehand whether the anticipated linear extrapolation findings are universal and would be applicable to premixed flames irrespective of the different flame conditions and that no other factors apart from the diameter of the thermocouple could influence such radiative losses was questionable. Thus, to arrive at a judgement by reasoning, we conducted a separate unbiased study where we used four thermocouples of different sizes to estimate the radiative losses via the extrapolation method in different flames and widened the domain of validation for this method.

3.1.1. Experimental setup

For this work, 4 beaded type S thermocouples (TC S.A., Pt-Pt/10%Rh) were used. These thermocouples are characterized with different wire diameters of 0.20, 0.35, 0.42 and 0.50 mm (supplier data) and bead diameters of 0.62, 1.01, 1.15 and 1.27 mm respectively, which were determined experimentally using a micrometer (sensitivity of 5 µm). To limit conduction losses in accordance with the recommendations stipulated in the literature [220,230], the four thermocouples possessed a wire length-to-diameter ratio higher than 300 and were sheathed with Alsint ceramic insulation which is the best high temperature ceramic material (temperature limit 1700°C). Usually, surface treatment is carried out on the junction of the thermocouples using a hot mixture of yttrium and beryllium oxides in HCl solution. However, it should be noted that no surface treatment was applied to any of the four thermocouples in order to keep the diameter of the junction bead at a minimum size and to minimize flame disturbance as well as the detection delay [229]. To measure the temperature, a motorized remote-controlled system enabling an automatic, easy, and reproducible insertion of the thermocouple in the flame was used. This system was operated using a LabVIEW code explicitly written for these experiments. The thermocouples were radially inserted into the centerline of the flame at various HABs as shown in Figure 3. 1 using this motorized positioning system and the temperature values were recorded in real-time.

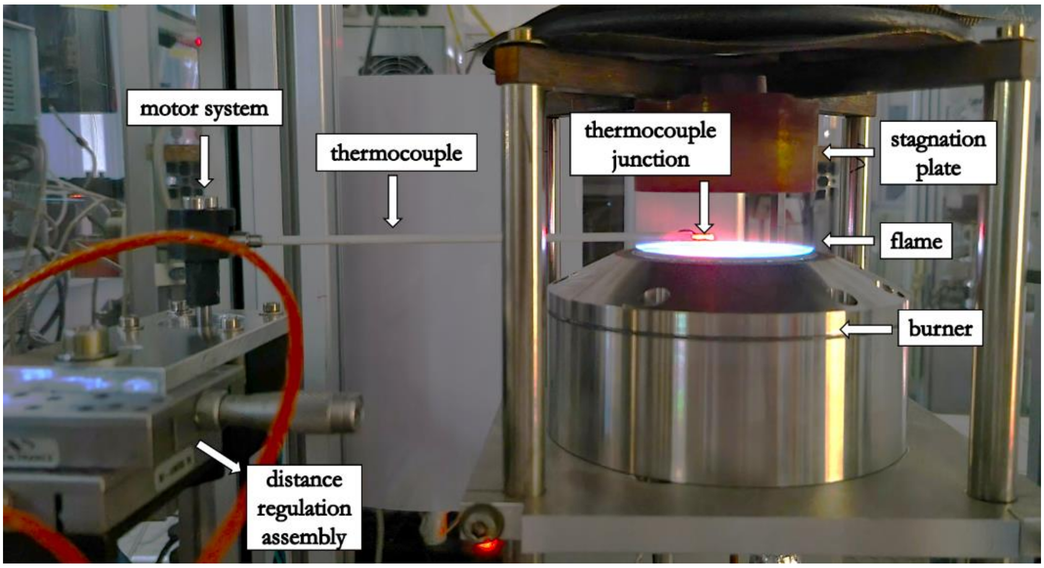

Figure 3. 1 : View of the thermocouple radially inserted using the motor assembly (on the left) in the flame (on the right) to record the temperature as a function of its residence time.

The parameters controlling the displacement of the thermocouple from its initial position outside the flame to reach the point of measurement in the flame (in the same plane) were experimentally controlled to enable repetitious insertion and minimize the perturbations using LabVIEW code. The length of the thermocouple was nearly 10 cm and its residence time in the flame (acquisition time) to record the temperature was set to 90 seconds. After 90 seconds in the flame, the thermocouple would revert back to its initial position outside the flame automatically.

3.1.2. Characterization of the temporal evolution of the measured temperature

The temperature measurement was carried out by following the temporal evolution of the temperature value as a function of the insertion time in the flame. An example of the evolution of the temperature measured by the thermocouple as a function of the acquisition time at any given HAB is presented in Figure 3. 2 (a). As can be seen in this figure, a rapid increase in the measured temperature was observed as the thermocouple was inserted in the flame. This rise time was estimated to be less than 5 seconds and it was followed by a stable value of the measured temperature when thermal equilibrium is reached (t→∞). The highest temperature value recorded during the measurement, which usually corresponded to the constant temperature value (flat plateau), was noted as the measured value (T_M). The total residence time of the thermocouple in the flame was fixed to nearly 90 seconds to ensure that the thermocouple stayed in the flame long enough to acquire a stable temperature value during the temporal evolution of the temperature indicating a stable temperature value of the medium at a given HAB.

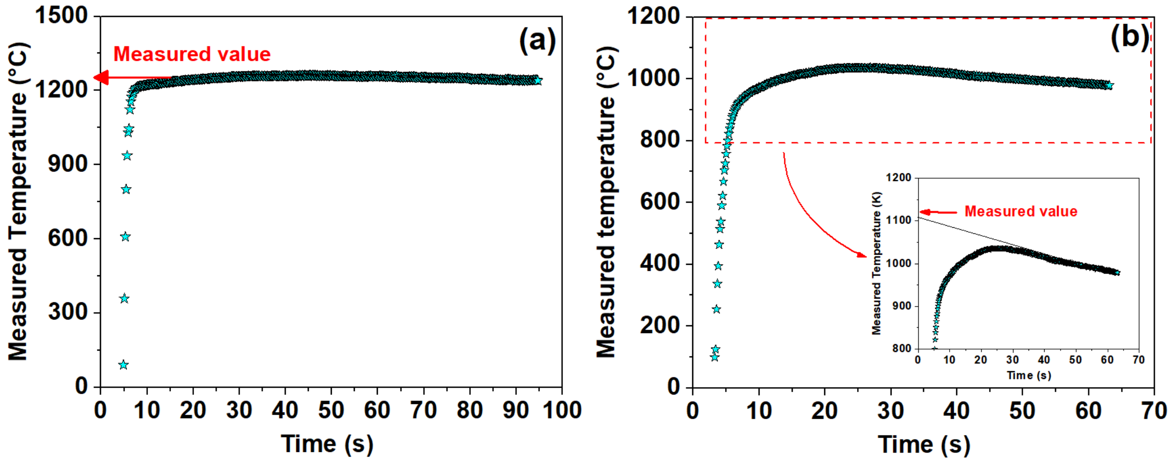

Figure 3. 2 : Examples of the evolution of the measured temperature during an acquisition with respect to the residence time of the thermocouple in the flame T(t); where plot (a) and plot (b) present acquisitions at lower and higher HABs respectively.

However, it is worth mentioning that soot deposition on the thermocouples during these measurements was sometimes non-negligible especially at higher heights as we were investigating fuel-rich flame conditions. Soot deposition on the thermocouple is a familiar issue when employing thermocouples to measure the temperature of the flames. The absence of soot deposits at lower HABs was confirmed by the rapid attainment of a stable temperature threshold value as illustrated in Figure 3. 2 (a). On the contrary, at higher HABs, when the thermocouple was radially inserted in a flame, in a span of few seconds soot particles were deposited on the thermocouple. This was also reflected in the rapid and the continuous decrease of T(t) (real-time temperature measured as a function of time by the thermocouple) as soot deposits accumulated on the surface of the thermocouple (see Figure 3. 2 (b)).

In addition to the radiation losses, soot deposition on the thermocouple leads to further underestimation of the actual flame temperature in sooting flames. In 1997, Mc Enally et al. [227] showed that the errors in temperature measurements due to soot deposition via rapid thermocouple insertion method depend linearly on the soot volume fraction. They estimated the error caused by the soot deposition on the temperature and rectified it by extrapolating the temporal temperature evolution back to the insertion time. The method they proposed has been validated for relatively mild soot depositions corresponding to soot volume fraction lower than 50 ppm, which is far above the soot volume fraction measured in these flames. The maximum soot volume fraction present in our flames is < 200 ppt. As illustrated in Figure 3. 2 (b), we used the same procedure as Mc Enally et al. [227] to compensate for the soot deposition effect and determine the measured temperature value. This way, temperature measurements were carried out for five flames using four different thermocouples (at various HABs) to obtain four temperature profiles per each flame at all HABs. Soot deposition corrections were performed when necessary especially at higher HABs (zones of the flame where the amount of soot is highest).

3.1.3. Correction of radiative losses using the extrapolation method

The correction of the radiative losses by means of the extrapolation method is based on the principle that the radiative losses depend on the emitting surface of the thermocouples. So, the thinner the thermocouple, the lower the radiative losses. Actual flame temperatures can be determined by extrapolation of the measurements to $d = 0$, $T_0 = T\ (d \rightarrow 0)$ where T is measured at the same HAB with different thermocouples. At any given HAB, four temperature values were measured using the four thermocouples. These temperature values, recorded at the same HAB were then plotted as a function of the diameter of the thermocouple wire as shown in Figure 3. 3. To study the radiation losses explicitly, higher HABs have been specially chosen as the most desirable as the temperature in the burnt gas is not likely to be affected by the aerodynamic disturbances.

As the independent variable, the thermocouple wire diameter is used instead of the bead diameter to express the nature the thermocouple junction. It should be noted that sometimes the diameter of the thermocouple beads have been chosen for this purpose in the literature [232,233]. We also tested this possibility but it turned out to be much less consistent than with wire diameters. To explain this divergence, we found very few arguments in the literature. Corrections by the bead diameter are valid for beads that are approximately spherical and much larger than the diameter of the thermocouple wire [232]. In our case, the surface area of the bead would be considered smaller as compared to the surface area of the wires. Thus, it is expected that the thermocouple wires would be heated quickly and that the presence of the bead would only induce a minor disturbance in the temperature measurement at the junction [232]. Although difficult to verify, this explanation is valid in our case, as the corrections made and the temperatures determined by considering the diameter of the wires do show an excellent agreement with the temperatures obtained by LIF thermometry discussed subsequently. Figure 3. 3 demonstrates an example for the case of flame F3 (15% anisole, ϕ=1.82) of how the measured temperature at a given HAB is susceptible to decrease as the thickness of the thermocouple wires increases due to radiation losses. By extrapolating this trend to d → 0 as shown in Figure 3. 3, it is possible to determine a radiative losses-corrected temperature value. This way, real temperature values at these specific HABs can be retrieved from intercepts of the fits.

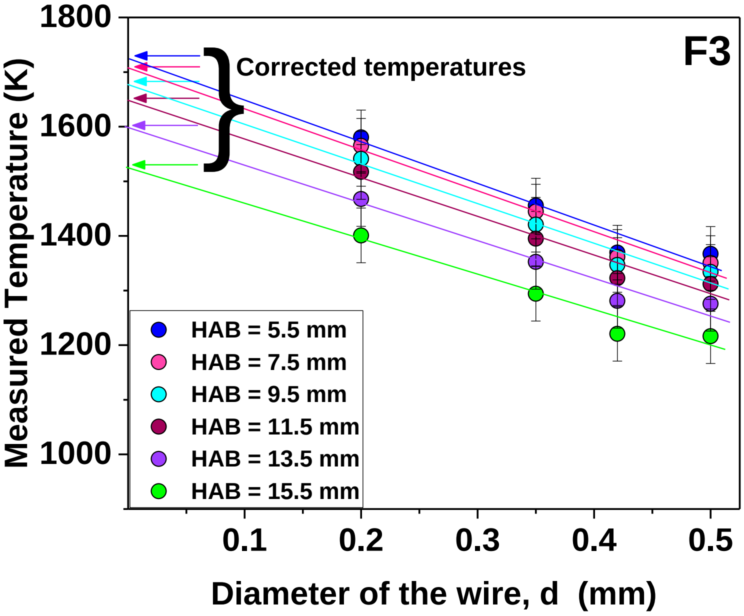

Figure 3. 3 : Temperature recorded via each of the 4 thermocouples v/s their respective sizes at higher HAB with a linear fit extrapolation to obtain the temperature at zero wire diameter $T_{corrected} = T_{measured\,(d \to 0)}$ *for flame F3 (15% anisole,* ϕ*=1.82).*

It is worth mentioning that certain studies in the literature reported the use of polynomial functions [229,234] whereas others opted for linear fits [218,230] for extrapolation. We tried extrapolating both ways, however, given the poor experimental agreement of the quadratic extrapolation with the LIF-NO temperature, we opted for a linear fitting. Agreement based on a comparison with LIF-NO (detailed later in the text) later justifies the use of this protocol for determining the temperatures in our flames.

From the values of the raw temperatures T(t→∞) shown in Figure 3. 3 as a function of the diameter of the thermocouples, it is possible to deduce a calibration curve for each of the four thermocouples making it possible to deduce the flame temperatures (T_0), corrected for radiative losses. These corrected temperatures obtained via extrapolation for each thermocouple from Figure 3. 3 can be plotted against the raw temperature values corresponding to the selected HAB to deduce correlations as reported in Figure 3. 4. This figure thus indicates a linear correlation between the measured temperatures (the independent variable) and the corrected temperatures (dependent variable) for radiative losses over the entire temperature range of our flame F3. Linear regressions can be used to fit these points to establish a relationship between the measured and the corrected temperature values for different wire diameters; i.e., $\boldsymbol{T_{corrected}} = \boldsymbol{a} \times (\boldsymbol{T_{measured}}) + \boldsymbol{b}$, where $\boldsymbol{a}$ and $\boldsymbol{b}$ are the deduced by linear fittings (see Figure 3. 4). This linear relationship can then be extended to rectify the entire measured temperature profile by compensating for the radiation losses. To evaluate the potential influence of experimental conditions, similar approach was applied to other flames as to deduce such expressions for the four thermocouples in five flames. Table 3. 1 summarizes the correction equations derived for the four thermocouples in each flame.

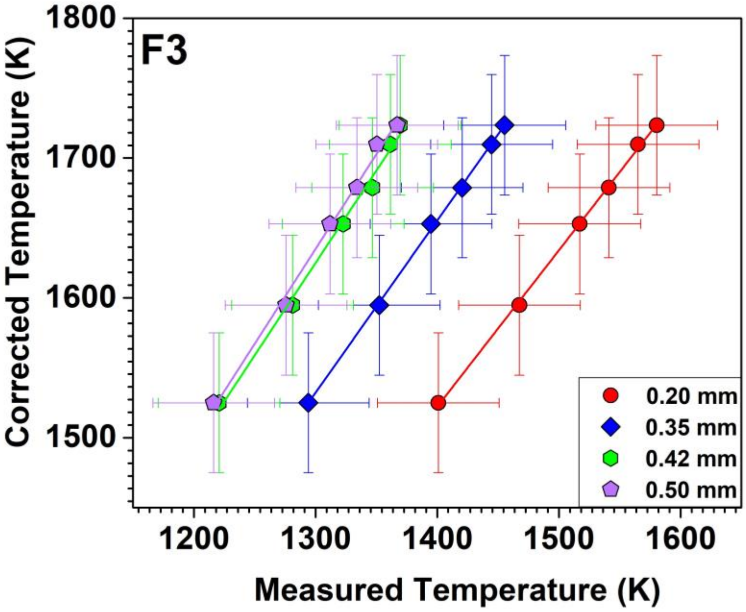

Figure 3. 4 : Corrected temperature as a function of the measured temperature for flame F3 (15% anisole, ϕ=1.82) deduced using Figure 3. 3.

Table 3. 1 : A summary of the correction relationships derived for the different thermocouples in the five flames where a and b are the slopes and the intercepts of the linear curves

Temperature correction relationship: $T_{corrected} = a \times (T_{measured}) + b$			
Thermocouple thickness (mm)	Flames	a	b
0.20	F1 (0% anisole, 1.82)	1.07±0.06	39.79±85.53
	F2 (10% anisole, 1.82)	1.07±0.02	22.93±28.33
	F3 (15% anisole, 1.82)	1.11±0.02	-45.84±24.13
	F4 (10% anisole, 1.70)	1.07±0.01	21.91±16.01
	F5 (10% anisole, 1.90)	1.08±0.02	7.62±42.18
0.35	F1 (0% anisole, 1.82)	1.23±0.14	-50.48±191.86
	F2 (10% anisole, 1.82)	1.28±0.03	-141.29±48.39
	F3 (15% anisole, 1.82)	1.23±0.02	-68.117±23.76
	F4 (10% anisole, 1.70)	1.11±0.04	91.13±59.70
	F5 (10% anisole, 1.90)	1.25±0.13	-115.47±176.27
0.42	F1 (0% anisole, 1.82)	1.23±0.14	29.40±194.53
	F2 (10% anisole, 1.82)	1.18±0.04	83.72±51.27
	F3 (15% anisole, 1.82)	1.32±0.05	-91.418±68.87
	F4 (10% anisole, 1.70)	1.23±0.03	7.95±32.78
	F5 (10% anisole, 1.90)	1.20±0.13	40.45±167.87
0.50	F1 (0% anisole, 1.82)	1.24±0.12	54.72±153.33
	F2 (10% anisole, 1.82)	1.28±0.05	-30.06±65.66
	F3 (15% anisole, 1.82)	1.36±0.05	-126.95±58.16
	F4 (10% anisole, 1.70)	1.18±0.04	94.81±44.51
	F5 (10% anisole, 1.90)	1.27±0.12	-27.49±147.59

Figure 3. 5 illustrates the correlation between the raw and the corrected temperatures for the thinnest (0.2 mm) as well as the thickest (0.50 mm) thermocouple used in five flames. It shows that the radiation losses are independent of the different flame conditions and depend only on the thermocouple wire thickness. To rephrase it, the relationship derived to correct for the radiation losses (for any given thermocouple) from any one of the flames can be applied to other flames as well to correct their measured temperature profiles (using the same given thermocouple). It was then clear that the linear relationships between the corrected and the measured temperature determined in different flames are in fact equivalent regardless of the different flames studied. Henceforth, for future temperature measurements, it will be sufficient to measure the temperature profile of a flame using only one thermocouple that can be corrected using the linear correction relationship already derived.

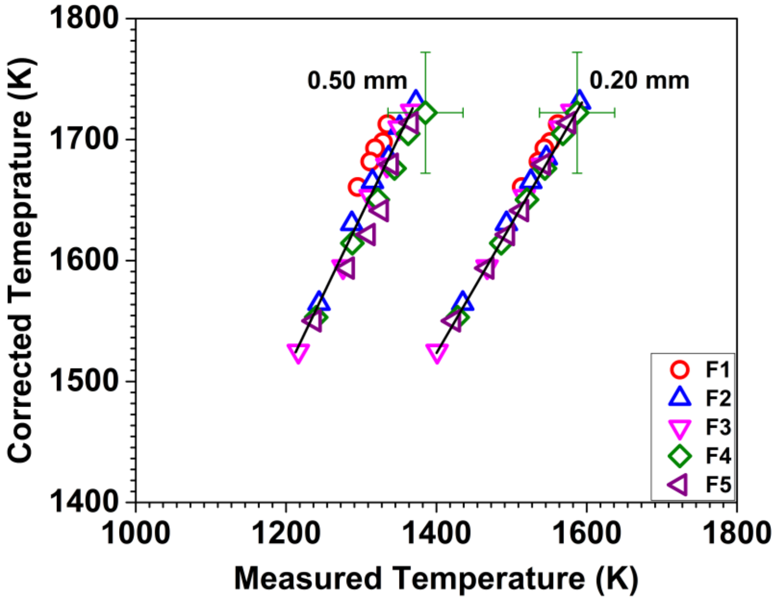

Figure 3. 5 : Correlation between the measured and the corrected temperatures derived from different flames (the error bars are only shown for one datapoint to avoid overloading the figure with numerous data points with error bars).

To determine the final temperature profiles and validate the extrapolation method, we used the measured temperature profiles for the flames together with the correction relationship derived for the thinnest thermocouple (0.2 mm) as presented in Table 3. 1. An example of the final temperature profile obtained for flame F3 is presented in Figure 3. 6. It is clear from Figure 3. 6 that radiation losses can lead to undervaluation of the actual flame temperatures by nearly 200-300 K.

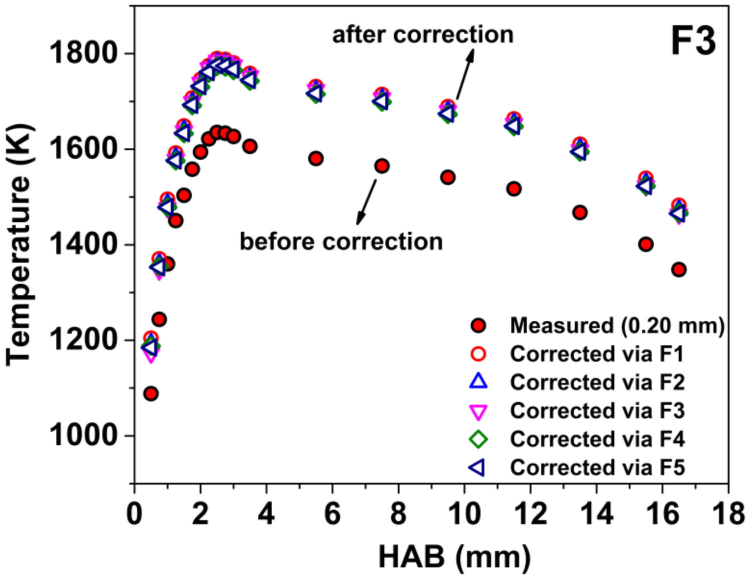

Figure 3. 6 : A comparison of the measured temperature profile using the thinnest thermocouple and the corrected temperature profiles obtained using the correction relationships from different flames for flame F3 (15% anisole, ϕ=1.82). "Corrected via F1" here signifies that the temperature correction was performed using the correction relationship derived in flame F1 and so on.

The relationships from different flames are equivalent. The choice of the thinnest (0.20 mm) thermocouple was made in order to limit the disturbance of the flame linked to its insertion, and to maximize the spatial resolution of the measurements. This thermocouple was also preferentially favored to restrict the influence of the radiative losses. Using this thermocouple, uncertainties on the temperature measurements are estimated to be around ±50 K.

3.1.4. Effect of the nozzle on the temperature profile

Temperature measurements were also performed in the presence of the nozzle used to sample the flame for GC measurements. During these measurements, the thermocouple junction was placed parallel to the burner surface right below the tip of the sampling quartz nozzle (as shown in Figure 3. 7 (a)) to account for the effect of the nozzle proximity on the temperature of the sampled gases and to get a better approximation of the axial temperature profile in its presence. The fixed distance between the nozzle and the thermocouple was ensured to be the same at all HABs in all flames (about 0.4 mm), and was regularly verified. This distance corresponds to the estimated position of the volume that was sampled by the probe. The measured temperature profiles in the presence of the nozzle were corrected by implementing the method discussed in section 3.1.3. Figure 3. 7 (b) presents a comparison of the temperature profile corrected for radiation losses for flame F1 (0% biofuel, ϕ=1.82) with and without the nozzle. As presented in the figure, the profile shifts towards the burnt gas zone in the presence of the probe. Meanwhile, the temperature in the burnt gases is similar with and without the probe. It is in fact even slightly warmer in the presence of the probe. Since the acquisitions were performed starting from the burner's surface to higher HABs, it is possible that the probe did not have the time to completely "cool" to the flame temperature before the next scan, after the highest temperatures were attained. This would be consistent with the temperatures at low HAB being lower with the probe than without it. However, the figure in general indicates that the presence of the probe produces a shift in the position of the gradient of the temperature profile.

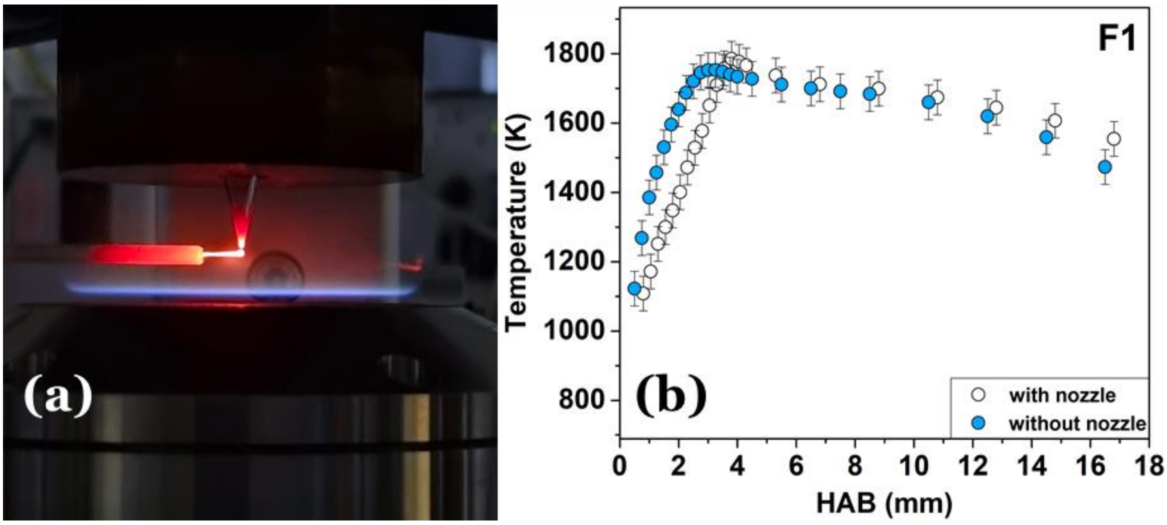

Figure 3. 7 : (a) View of the thermocouple placed at a distance of 0.4 mm below the probe (b) A comparison of the temperature profile obtained in the presence and the absence of the nozzle for flame F1 (0% biofuel, ϕ=1.82)

3.1.5. Comparison of the method used with other techniques

In order to examine the thermocouple-based method together with the extrapolation correction method used in this work, we compared the corrected temperature profiles with the data obtained from a non-intrusive thermometry technique i.e., LIF-NO thermometry. This experiment was performed for flame F1 as an example by Dr. Pascale Desgroux.

Laser Induced Fluorescence (LIF) is a non-intrusive optical method that involves excitation a molecule (as well as atoms) from the ground state to an excited electronic state using laser radiation absorption, along a given rovibronic transition, followed by subsequent analysis of the spontaneous radiation emission (fluorescence) emitted from the excited state. By collecting the fluorescence using a photomultiplier tube (PMT) or a camera, it is possible to relate the fluorescence signal to the ground state rotational population of the species, probed by the laser at the selected wavelength (i.e., along the given rovibronic transition). The principle of LIF-thermometry relies on probing multiple ground state rotational populations which are related to the Boltzmann population distribution [235]. In practice the temperature determination relies on the analysis of a laser excitation scan performed over a significant number of rovibronic transitions. The method, performed on NO species, is detailed in literature studies [230-232] and only few details are reported here. A small amount of N_2 (0.15%) was replaced by NO in the premixed mixture [236]. This small quantity does not perturb the chemical structure or the temperature of the flame and was considered sufficient to provide a good signal-to-noise ratio [236,237]. It must be noted that a spectrum acquisition requires 45 minutes. The laser (Quantel, TDL+ pumped with a seeded YAG Q-smart 850) was tuned over 225.65–225.73 nm to excite NO in the A-X (0,0) band. The laser energy was maintained at 40 µJ, which is within the linear LIF regime. The LIF signal was then collected in the A-X(0,2) band of NO using a spectrometer centered at 245 nm. Temperatures were determined by fitting synthetic LIF excitation spectra to the experimental spectra following a procedure previously detailed [238]. Uncertainties associated are estimated to be around ±100 K for the temperature measurements using this technique.

Figure 3. 8 presents a comparison of the corrected temperature profile obtained using the thermocouple method (without the nozzle) and LIF-NO for flame F1 (0% biofuel, ϕ=1.82).

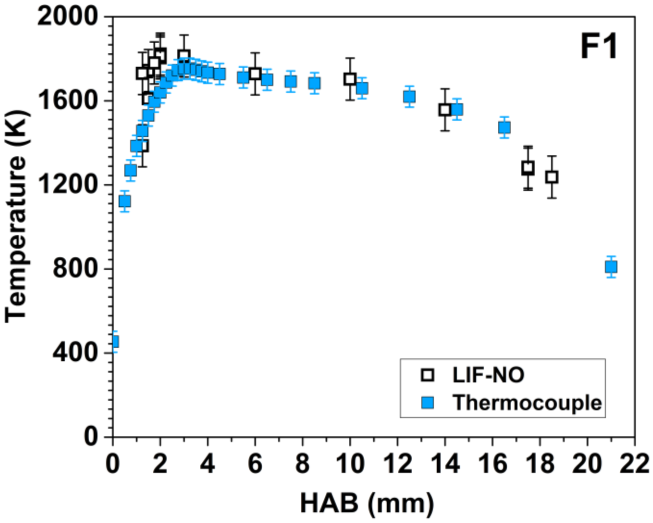

Figure 3. 8 : Comparison of the temperature profiles obtained from the thermocouple and the LIF-NO measurements for flame F1 (0% biofuel, ϕ=1.82).

The corrected temperature profile and the LIF thermometry data are in excellent agreement, between the two techniques where the gradient is low, certainly not perfect in the steep gradient region. Statistically, this means that the readings by the two techniques differ around the peak temperature. The gradient observed using LIF-NO is steeper than the gradient obtained using the thermocouple method. This difference can be attributed to the nature of the two techniques. The LIF technique is non-intrusive, with a vertical spatial resolution set to 0.2 mm. On the contrary, the thermocouple method is an intrusive method and thus despite using the thinnest thermocouple (0.20 mm wire thickness), it is beyond the bounds of possibility to completely restrain from flame perturbations. In an attempt to minimize such perturbations, we always performed corrections on the temperature profiles measured using the thinnest thermocouple to obtain the final temperature profiles for all flames.

To extend the validation of our extrapolation method for radiation loss corrections, we performed temperature measurements for three laminar premixed butane flames with different equivalence ratios (ϕ=1.60, 1.75 and 1.95) for which temperature measurements have already been reported in the literature using LIF-NO [205]. Out of these flames, two flames are much more sooting than our flames with soot volume fractions ranging up to 10 ppb as the dilution imposed in these flames is much lesser (55.4%) than our flames (65.9%). Thus, before proceeding to correct for the radiation losses, soot deposition corrections were also performed as discussed previously. Overall, two correction steps were applied to finally obtain the actual temperature profiles of the butane flames which were then compared to their LIF-NO and calculated temperature profiles from the literature [205]. The comparison is presented in Figure 3. 9.

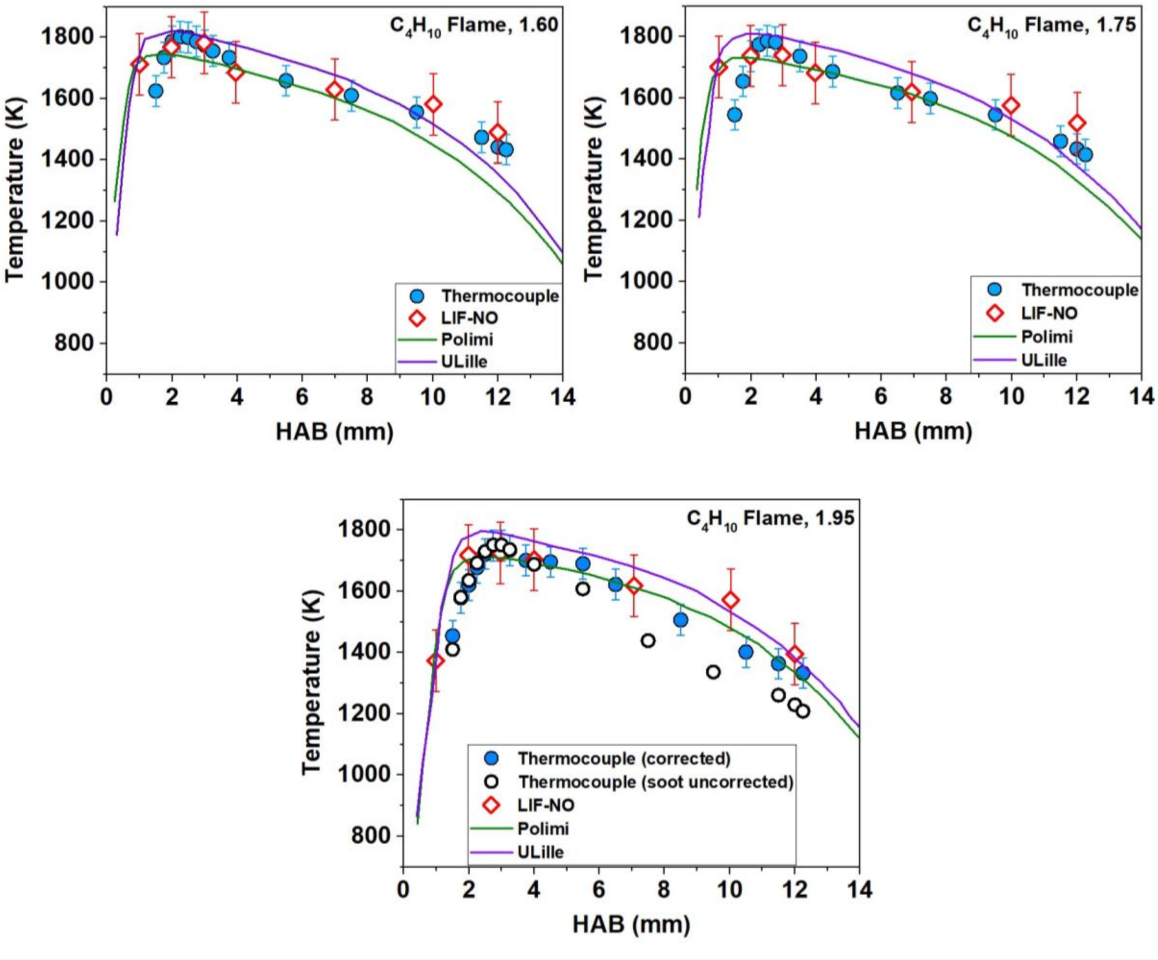

Figure 3. 9 : Comparison of the temperature profiles determined in three butane flames with three different equivalence ratios (1.60, 1.75 and 1.95) using the thermocouple method from this work and LIF-NO thermometry (and the calculated profile) from the literature [205]. An example of the temperature profile without soot correction is shown for the C_4H_{10}, 1.90 flame.

The authors also compared their experimentally determined temperature profiles to the simulated profiles using the Polimi and ULille models [205]. The comparison between our thermometry-based measurements and the LIF-NO measurements from the literature is not as easy in the gradient zone as there are very few numbers of points from the LIF-NO technique to define the gradient of the profile. Nevertheless, there is satisfactory agreement between the temperature profiles derived from the two techniques all along the flame HAB, which helps us widen the domain of validation for the extrapolation correction method used in this work.

3.2. Conclusion

Temperature measurement is essential when analyzing flame structure and chemical kinetics. In this study, we have used a thermocouple-based temperature measurement technique for which the extrapolation method is implemented for radiative losses corrections. We observed that the impact of radiative losses is clearly the dominant disturbance element in temperature measurements. These losses can lead to an underestimation of the temperature by a few hundred K, and it was noted that the difference between measured temperature and actual temperature increases progressively with thermocouple wire thickness, in accordance with the theory of radiative losses. In this work, the measured temperature is shown to be linearly correlated to the diameter of the thermocouple wires. By applying the extrapolation procedure for selected HABs characterized by different temperatures, linear relationships can be established for selected thermocouples that relate the measured temperature to the actual flame temperature corrected from the radiation losses. This method has one important practical consequence, as in principle measurements using one thermocouple are now sufficient for a reliable flame temperature measurement. Overall results demonstrate that the extrapolation method is a fast and efficient method to determine the flame temperature profiles with high accuracy, even in the presence of soot particles. This work demonstrates the capability of this thermocouple method to easily access accurate temperature measurements in harsh environments characterized by high temperature gradients. This method appears very simple to implement in comparison to other complex methods to estimate the radiation losses. A good agreement from the ccomparison with non-intrusive measurements like LIF-NO, both in the flame of study from this thesis, and in flames from the literature validates the use of the extrapolation method. This makes it a very powerful tool for accessing the temperature. This being so, these measurements and their respective comparisons demonstrate the efficiency of the quick measurement protocol using thermocouple for easily accessing temperatures even in sooting flames.

Chapter 4. Detection of oxygenated aromatics in anisole doped flames and a study of the influence of anisole on soot precursors

As mentioned in Chapter 1, some recent studies have considered the formation of oxygenated aromatics in combustion [26,56]. However, knowledge of the kinetics of these aromatics is still very limited as one of the issues that needs to be resolved is the lack of experimental evidence concerning their identification. As discussed earlier, identification of OPAHs in turn is a very challenging step. This chapter begins with a discussion focusing on experimentally detected oxygenated aromatics, including OPAHs, in anisole doped flames in this work. The first part of this chapter presents an overview on the number and the structure of these species, together with an analysis of the kinetic signature of their formation from anisole (Section 4.1). This section is followed by quantitative results on the evolution of their mole fractions and those of related non-oxygenated aromatics, including PAHs, with respect to the flame height in the form of a detailed comparison study (Sections 4.2 and 4.3). For quantification, though special focus is dedicated to the study of the oxygenated and associated non-oxygenated aromatics (important soot precursors), the discussion is also extended to smaller aliphatic soot precursors as these species also indicate the overall reactivity of the system and play an important role in the formation of the first aromatic ring or in the enlargement of aromatics.

Overall, this study consists of five different flames. Out of these five flames, two different series of measurements were studied independently. To demonstrate the effect of the change in the equivalence ratio, three flames comprising the first set of series are studied (Section 4.2), namely F4 (10% anisole, ϕ=1.70), F2 (10% anisole, ϕ=1.82), and F5 (10% anisole, ϕ=1.90), where the equivalence ratio is increasing, meanwhile the percentage of anisole in the total fuel mixture for the three flames is constant (10%). The second set of series also consists of three flames, namely F1 (0% anisole, ϕ=1.82), F2 (10% anisole, ϕ=1.82), and F3 (15% anisole, ϕ=1.82) where the equivalence ratio is fixed to a value of 1.82 while the amount of anisole is increasing (Section 4.3), which allows us to investigate the influence of added anisole amounts.

A total of nearly 140 species were experimentally identified in anisole flames. These species include reactants, final products, small intermediates, more than 80 oxygenated aromatics and more than 20 non-oxygenated aromatics. Overall, about 80 stable species have been quantified. Mole fraction profiles for some relevant species have been discussed in the subsequent sections, whereas peak mole fractions for all species are listed in Table A. 3 in the Appendices.

4.1. Detection of oxygenated aromatics in anisole doped flames

Species identification was performed in all flames using GC-MS systems and sampling procedures described in Chapter 2. However, flame F5 (conditions summarized in Table 4. 1) was chosen as the main flame in this step to present in this section. This flame has the best spatial resolution (far away from the burner's surface) and therefore it was relatively easier to sample from its reaction zone. This flame was stabilized at an equivalence ratio of 1.90 at atmospheric pressure and consisted of 10% of anisole in the total fuel mixture. Though both, oxygenated and non-oxygenated species were identified, this section is devoted to the discussion on oxygenated ones. Identified non-oxygenated aromatics are listed in the Table A. 2 in the Appendices.

Table 4. 1: Summary of the flame conditions studied (flame F5); L_n/min: normal liter per minute.

Flame	*Biofuel (%)*	*Gaseous flow rates (L_n/min)*						*Equivalence ratio*	*C/O*
		Biofuel	C_8H_{18}	CH_4	O_2	N_2	Total		
F5	Anisole (10)	0.105	0.15	0.788	2.308	6.50	9.85	**1.90**	0.58

4.1.1. Examples of the obtained chromatograms and mass spectra

One of the most powerful tools in the identification of unknown peaks is the comparison of the associated mass spectrum with those in a database of mass spectra acquired under the same conditions. Representative chromatograms and some examples of mass spectra obtained are shown in Figure 4. 1. The middle panel of this figure presents two chromatograms obtained via the GC-SPT-TCD-FID i.e., the GC Scion (on the left) and the 2D GC-MS (on the right). The columns used for these GC setups were specific to aromatic species. Though the chromatogram from GC Scion was very complex and consisted of about 120 peaks, it indicated that several aromatic species are certainly present in the anisole flame. Several peaks amongst these were identified by comparing the chromatogram with that obtained using the 1D GC-MS (by using the same column, temperature program, and column flow rate) and it was observed that almost 60% of these aromatics were oxygenated, which highlighted their significant co-formation along with classic aromatic species. Following the complexity of the GC Scion chromatogram, we chose to perform additional analyses using the 2D GC-MS as mentioned before. By using the 2D GC-MS, we could confirm the identification from 1D GC-MS as well as identify additional species besides the ones already identified from 1D GC-MS on account of its different separation mechanism. For example, dibenzofuran ($C_{12}H_8O$) and 2,2'-methylenediphenol ($C_{13}H_{12}O_2$) identified by 1D GC-MS were confirmed by 2D GC-MS.

The top and bottom panels of Figure 4. 1 show the mass spectra of these two species and four other selected oxygenated aromatics. The presence of the molecular ion peaks (base peak) and fragment peaks in these spectra are very consistent with the molecular mass and the fragmentation mechanism of the identified molecules.

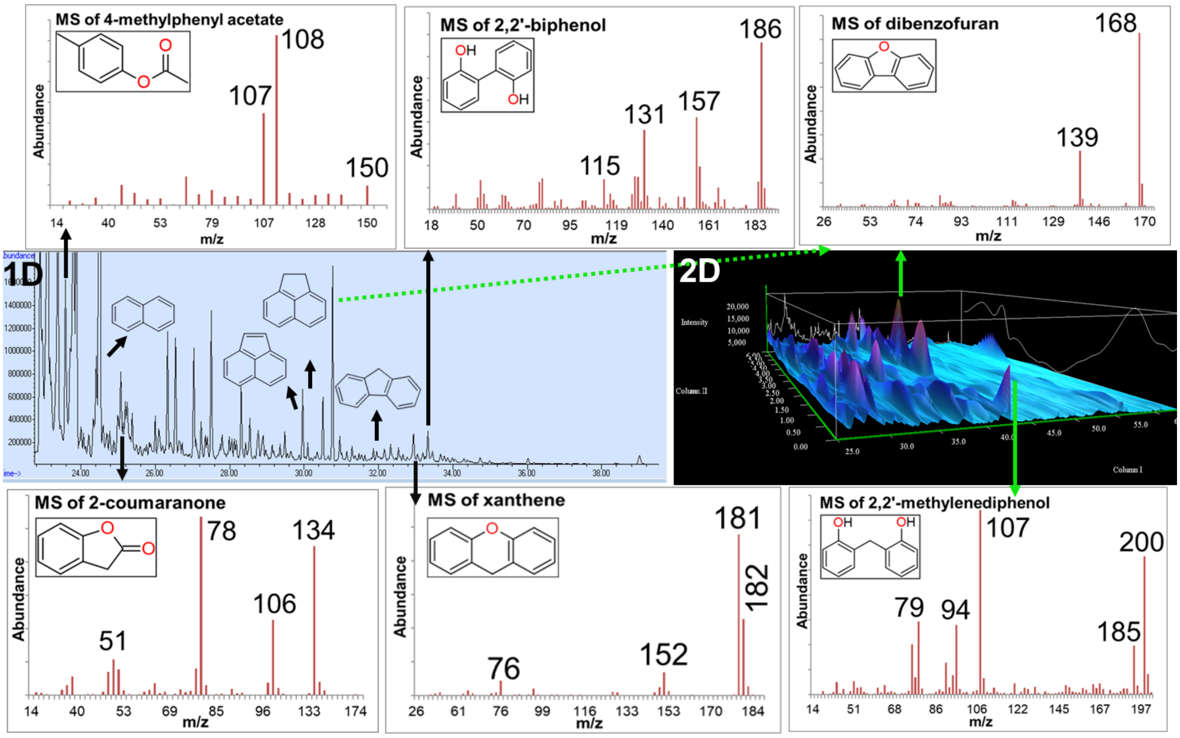

Figure 4. 1: Examples of chromatograms (middle panel) obtained by 1D GC-SPT-FID and 2D GC-MS in the doped anisole flame at HAB=1.5 mm. The nomenclature of some important species is given. Some mass spectra (MS, top and bottom panels) for the selected oxygenated aromatics obtained by GC-MS systems are presented.

An example of the anticipated fragmentation pattern for 4-methylphenyl acetate is shown in Figure 4. 2. The peak at m/z 150 corresponds to the mass of 4-methylphenyl acetate. This molecule can readily undergo the benzyl ester rearrangement by eliminating a ketene molecule in order to form this fragment ion at m/z 108 (see path 1). This phenolic molecular ion fragment may further preferably dissociate via the benzylic H-bond cleavage to produce another intense peak at m/z 107. This resonance stabilized benzyl ion may reversibly isomerize to the corresponding tropylium ion isomers m/z 107 (see path 2).

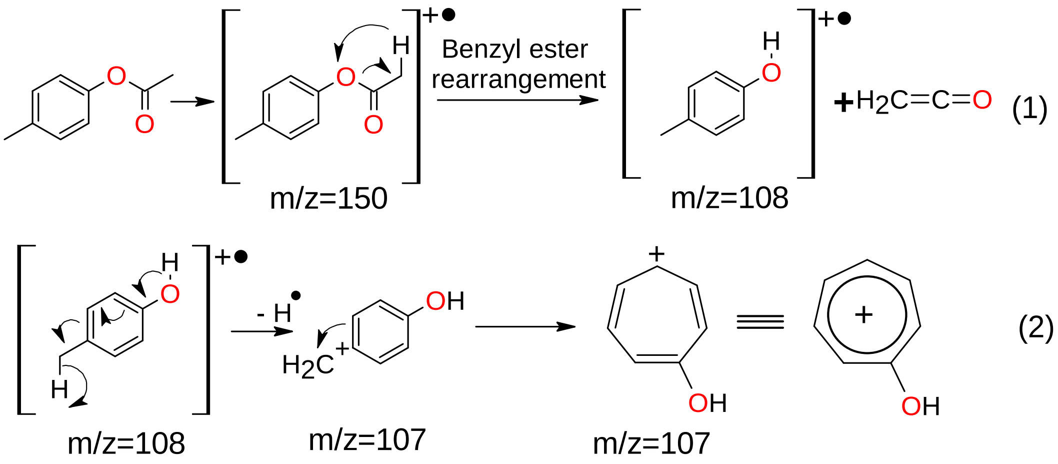

Figure 4. 2: Example of fragmentation rules used to explain the mass spectra of 4-methylphenyl. acetate.

4.1.2. Identified oxygenated aromatics

Based on the approach described above, about 84 oxygenated mono- and polyaromatics were identified. They are reported in Table 4. 2 and Figure 4. 3. While Table 4. 2 presents the different species by mass (with their corresponding chemical formula, common and IUPAC names and structures), Figure 4. 3 presents a pictorial representation of the identified species in accordance with the number of rings (and similar core structure placed close together) to provide another overview on the detected oxygenated aromatics.

Table 4. 2 : Identified oxygenated aromatics in the studied anisole flame together with their names and molar masses (M). [a] *Names in italic refer to the IUPAC nomenclature. M: Nominal mass.* [b]*: literature studies on anisole as fuel; Here: "✓": the identified molecule structure is reported in the cited references; "*": signal corresponding to this mass was detected, but the molecule structure was not experimentally identified (possible isomers were proposed based on theoretical calculations); "**": hydroxybenzaldehyde is mentioned but not specified which isomer; "-": not reported in the literature.*

Detected in the present flame					Detected in literature experiments[b]	
N°	M	Formula	Name[a]	Structure	Flames	Other reactors
1	94	C_6H_6O	*Phenol*	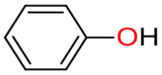	✓ [51,56]	✓ [26,48,49,53,127,131,239,240]
2	106	C_7H_6O	*Benzaldehyde*	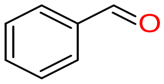	✓ [51,56]	✓ [26,48,49,53,131,239,240]
3	108	C_7H_8O	*Anisole*	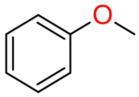	✓ [51,56]	✓ [26,48,49,53,131,239]
4	108	C_7H_8O	*o*-Cresol; *2-Methylphenol*	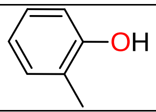	✓ [56]	✓ [26,48,49,123,131]
5	108	C_7H_8O	*m*-Cresol; *3-Methylphenol*	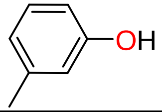	-	-
6	108	C_7H_8O	*p*-Cresol; *4-Methylphenol*	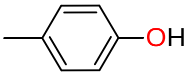	✓ [56]	✓ [26,48,49,123,131]
7	110	$C_6H_6O_2$	Hydroquinone; *Benzene-1,4-diol*	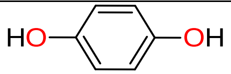	-	-
9	118	C_8H_6O	Benzofuran; *1-Benzofuran*	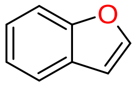	✓ [51,56]*	✓ [49,53,123,240]
11	120	C_8H_8O	2,3-Dihydrobenzofuran; *2,3-Dihydro-1-benzofuran*	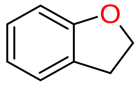	-	[26]*
13	122	$C_7H_6O_2$	Salicylaldehyde; *2-Hydroxybenzaldehyde*	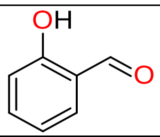	-	[26]*; [48]**
14	122	$C_7H_6O_2$	*m*-Formylphenol; *3-Hydroxybenzaldehyde*	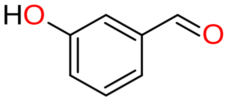	-	[26]*; [48]**
15	122	$C_7H_6O_2$	*4-Hydroxybenzaldehyde*	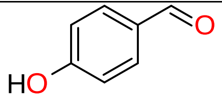	-	-
16	122	$C_7H_6O_2$	1,3-Benzodioxole; *2H-1,3-benzodioxole*	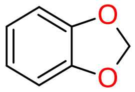	-	[26]*

17	122	$C_8H_{10}O$	2,6-Xylenol; *2,6-Dimethylphenol*	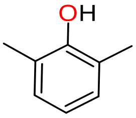	-	[26]*
18	122	$C_8H_{10}O$	*2,4-Dimethylphenol*	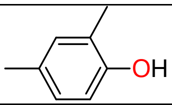	-	-
19	122	$C_8H_{10}O$	*2-Ethyl phenol*	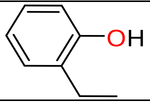	✓ [56]	✓[53]; [26]*
20	122	$C_8H_{10}O$	*3-Ethyl phenol*	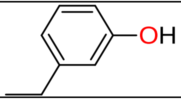	-	-
21	122	$C_8H_{10}O$	Ethyl phenyl ether; *Ethoxybenzene*	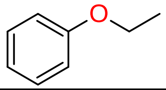	-	[26]*
22	122	$C_8H_{10}O$	*1-Methoxy-4-methylbenzene*	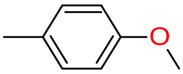	-	-
23	124	$C_7H_8O_2$	*m*-Guaiacol; *3-Methoxyphenol*	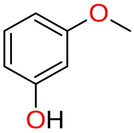	-	✓ [48]; [26]*
24	124	$C_7H_8O_2$	*o*-Guaiacol; *2-Methoxyphenol*	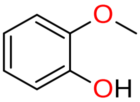	-	-
25	124	$C_7H_8O_2$	p-Guaiacol *4-Methoxyphenol*	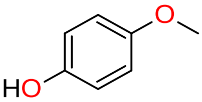	-	-
26	132	C_9H_8O	1-Indanone; *2,3-Dihydro-1H-inden-1-one*	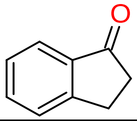	-	[26]*
27	132	C_9H_8O	2-Methyl benzofuran; *2-Methyl-1-benzofuran*	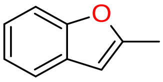	-	[26]*
28	132	C_9H_8O	*[(prop-2-yn-1-yl)oxy]benzene*	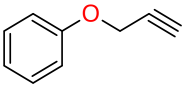	-	-
29	132	C_9H_8O	*1,3-Dihydro-2H-inden-2-one*	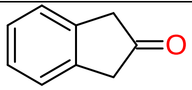	-	-
30	134	$C_8H_6O_2$	2-Coumaranone; *1-Benzofuran-2(3H)-one*	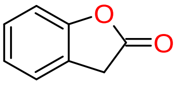	-	[26]*
31	134	$C_9H_{10}O$	*[(prop-2-en-1-yl)oxy] benzene*	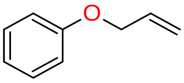	-	-
32	134	$C_9H_{10}O$	*4-(prop-2-en-1-yl) phenol*	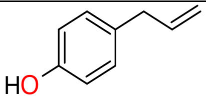	-	-
33	136	$C_8H_8O_2$	*5-Methyl-2H-1,3-benzodioxole*	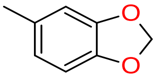	-	-

34	136	$C_8H_8O_2$	*Phenyl acetate*	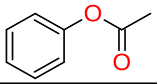	-	-
35	136	$C_9H_{12}O$	5-Ethyl *m*-cresol; *3-Ethyl-5-methylphenol*	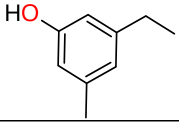	-	-
36	138	$C_8H_{10}O_2$	*3-Methoxy-2-methylphenol*	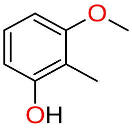	-	-
37	138	$C_8H_{10}O_2$	*3-Ethoxyphenol*	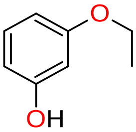	-	-
38	144	$C_{10}H_8O$	2-Vinyl benzofuran; *2-Ethenyl-1-benzofuran*	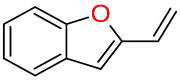	-	-
39	144	$C_{10}H_8O$	1-Naphthol; *Naphthalen-1-ol*	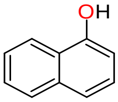	-	-
40	144	$C_{10}H_8O$	2-Naphthol; *Naphthalen-2-ol*	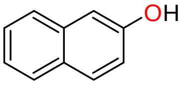	-	-
41	144	$C_{10}H_8O$	3-Phenylfuran	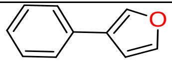	-	-
42	146	$C_{10}H_{10}O$	1-Methylindan-2-one; *1-Methyl-1,3-dihydro-2H-inden-2-one*	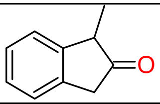	-	-
45	146	$C_{10}H_{10}O$	2-Ethyl benzofuran; *2-Ethyl-1-benzofuran*	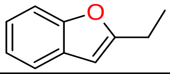	-	-
46	146	$C_{10}H_{10}O$	*1-methyl-4-[(prop-2-yn-1-yl)oxy] benzene*	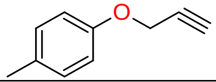	-	-
49	148	$C_{10}H_{12}O$	*2-(2-methylprop-2-en-1-yl) phenol*	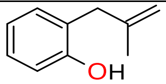	-	-
50	148	$C_{10}H_{12}O$	*4-(2-methylprop-2-en-1-yl) phenol*	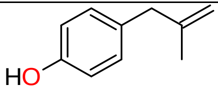	-	-
51	148	$C_{10}H_{12}O$	*[(2-methylprop-2-en-1-yl)oxy] benzene*	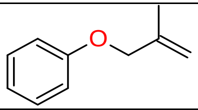	-	-
52	150	$C_9H_{10}O_2$	*p*-Acetoxy toluene; *4-Methylphenyl acetate*	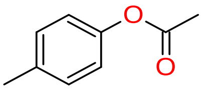	-	-
53	150	$C_9H_{10}O_2$	Phenyl propionate; *Phenyl propanoate*	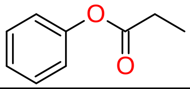	-	-
54	156	$C_{11}H_8O$	2-Naphthaldehyde; *Naphthalene-2-carbaldehyde*	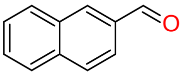	-	-
55	168	$C_{12}H_8O$	Dibenzofuran; *Dibenzo[b,d]furan*	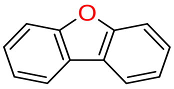	✓ [56]	✓[48,53,126] ; [26]*

56	168	$C_{12}H_8O$	*Acenaphthylen-1(2H)-one*	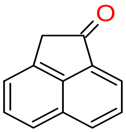	-	-
57	170	$C_{12}H_{10}O$	Diphenyl ether; *1,1'-Oxydibenzene*	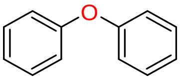	-	-
58	170	$C_{12}H_{10}O$	o-Hydroxybiphenyl; *[1,1'-Biphenyl]-2-ol*	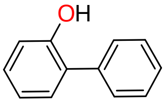	-	✓ [49]
59	180	$C_{13}H_8O$	9-Fluorenone; *9H-Fluoren-9-one*	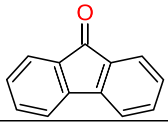	-	-
60	182	$C_{13}H_{10}O$	Xanthene; *9H-Xanthene*	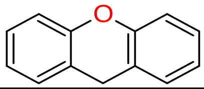	-	[26]*
61	182	$C_{13}H_{10}O$	9-Fluorenol; *9H-fluoren-9-ol*	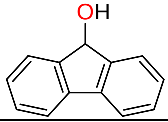	-	-
62	182	$C_{13}H_{10}O$	4-Methyldibenzofuran; 4-Methyldibenzo[*b*,*d*]furan	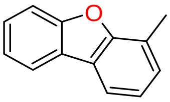	-	-
63	182	$C_{13}H_{10}O$	6*H*-Dibenzo[*b*,*d*]pyran	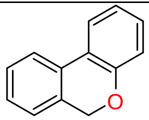	-	[26]*
64	184	$C_{12}H_8O_2$	Dibenzo-p-dioxin; *Oxanthrene*	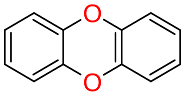	-	[26]*
65	184	$C_{12}H_8O_2$	2-Dibenzofuranol; *Dibenzo[b,d]furan-2-ol*	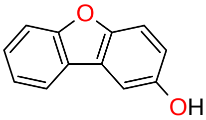	-	[26]*
66	184	$C_{13}H_{12}O$	Benzyl phenyl ether; *(Benzyloxy)benzene*	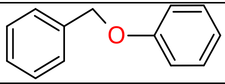	-	-
67	184	$C_{13}H_{12}O$	o-Benzylphenol; *2-Benzylphenol*	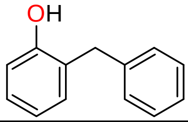	-	-
68	184	$C_{13}H_{12}O$	p-Benzylphenol; *4-Benzylphenol*	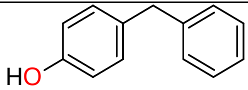	-	-
69	186	$C_{12}H_{10}O_2$	2,2′-Diphenol; *[1,1'-Biphenyl]-2,2'-diol*	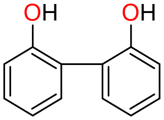	-	[126]
70	186	$C_{12}H_{10}O_2$	*[1,1'-biphenyl]-4,4'-diol*	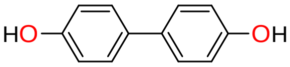	-	-
71	186	$C_{12}H_{10}O_2$	m-Phenoxy phenol; *3-Phenoxyphenol*	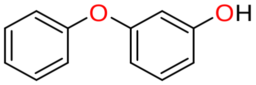	-	-

72	186	$C_{12}H_{10}O_2$	1-Naphthyl acetate; *Naphthalen-1-yl acetate*	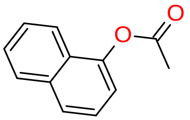	-	-
73	186	$C_{13}H_{14}O$	2-(2-Naphthyl)-2-propanol; *2-(Naphthalen-2-yl)propan-2-ol*	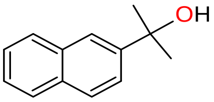	-	-
74	186	$C_{13}H_{14}O$	2,5,8-Trimethylnaphthalen-1-ol	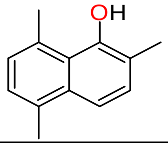	-	-
75	196	$C_{13}H_8O_2$	Xanthone; *9H-Xanthen-9-one*	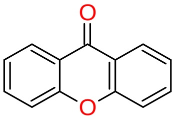	-	[26]*
76	200	$C_{13}H_{12}O_2$	Bis (2-hydroxyphenyl) methane; 2,2'-*Methylenediphenol*	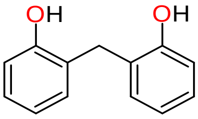	-	-
77	200	$C_{13}H_{12}O_2$	*2-[(4-Hydroxyphenyl)methyl] phenol*	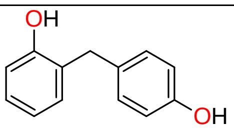	-	-
78	200	$C_{13}H_{12}O_2$	*4,4'-methylenediphenol*	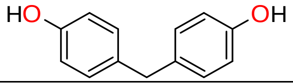	-	-
79	200	$C_{13}H_{12}O_2$	*1,1'-[methylenebis(oxy)]dibenzene*	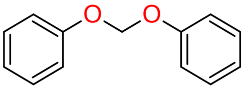	-	-
80	200	$C_{13}H_{12}O_2$	*1-methoxy-2-phenoxybenzene*	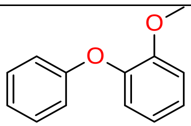	-	-
81	208	$C_{14}H_8O_2$	Anthraquinone; *Anthracene-9,10-dione*	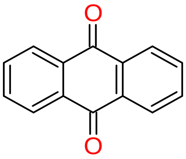	-	-
82	208	$C_{14}H_8O_2$	*Phenanthrene-9,10-dione*	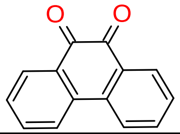	-	-
83	224	$C_{15}H_{12}O_2$	9-Fluorenyl acetate; *9H-Fluoren-9-yl acetate*	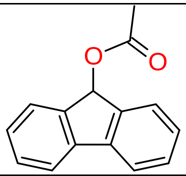	-	-

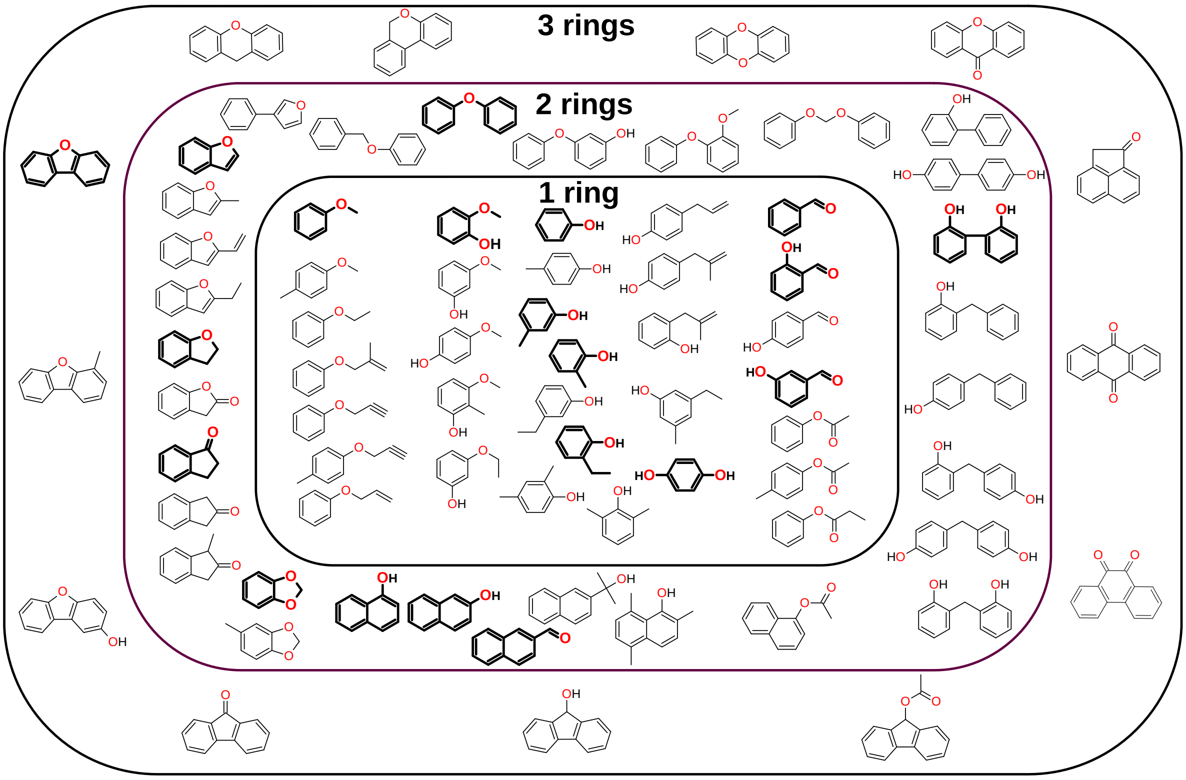

Figure 4. 3 : Identified OPAHs with one-, two-, and three-rings, respectively. For each category, somewhat similar core structures are placed close together. Species highlighted in bold font/bonds are those that are already considered in the current kinetic models in the literature (discussed in the following section, Section 4.1.3).

It is clear that an aromatic ether biofuel like anisole is giving rise to a whole new set of species during its decomposition in flames namely OPAHs. The identified oxygenated aromatics have molar masses ranging from 94 (phenol, C_6H_6O) to 224 (9-fluorenyl acetate, $C_{15}H_{12}O_2$) and contain in their structure one or two O-atoms. Though some aromatics containing three or four O-atoms were also proposed by the NIST database, we prefer not to solely rely on the numerical values for the match factors and in fact find pure analytes in order to confirm their identification in the future. Therefore, such species have not been presented in this thesis manuscript. Amongst the species listed previously, we distinguished between several different isomers such as C_7H_8O (mass 108, 4 isomers), $C_{10}H_8O$ (mass 144, 4 isomers), $C_{13}H_{10}O$ (mass 182, 4 isomers). Also, non-isomeric species with same molar masses could also be well distinguished and identified, such as 10 species at mass 122, 5 species at mass 184, 5 species at mass 186 and so on. Some species, for instance, 4-methyldibenzo[b,d]furan ($C_{13}H_{10}O$) and 2,5,8-trimethylnaphthalen-1-ol ($C_{13}H_{14}O$) were observed only using 2D GC-MS. Separating and identifying such complex compositions is already considered to be very challenging for different techniques [26,51,53]. Compared to the literature, more than half of the species detected in our study are reported for the first time for anisole combustion (see

Table 4. 2; last two columns to the right). Concretely, amongst the 85 oxygenated aromatics listed in Table 4. 2, 77 species (~91%) are reported for the first time as compared to the literature studies under the flame conditions, and 59-74 species (69-87%, depending on whether Ref [26] is taken into account or not) are reported for the first time as compared to the literature studies in other reactors. As presented in Table 4. 2, a significant percentage (~50%) of oxygenated one-ring aromatics were also reported by the literature studies, while this percentage is around ~30% and ~10% for two-ring and three-ring oxygenated aromatics, respectively.

It is worth mentioning that despite the potential of our GC systems, we still encountered some difficulties especially concerning the quantification of these species. Several identified species could not be quantified due to multiple reasons. For instance, amongst the three guaiacols (mass 124), peaks for o- and p-guaiacol were right before the intense peak of m-guaiacol which made it really difficult to distinguish between o- and p-guaiacols. As a consequence, the peaks for o- and p-guaiacols could not be integrated precisely at all HABs, thus making it impossible to trace their mole fraction evolution profiles. Similarly, because of their close retention times, it was very challenging to separate 2-methoxyphenol from 4-methoxyphenol ($C_7H_8O_2$), [1,1'-biphenyl]-4,4'-diol from 3-phenoxyphenol ($C_{12}H_{10}O_2$), naphthalen-1-ol from naphthalen-2-ol ($C_{10}H_8O$), 2-benzylphenol from 4-benzylphenol ($C_{13}H_{12}O$), and bis (2-hydroxyphenyl) methane (2,2'-methylenediphenol) from 2-[(4-hydroxyphenyl) methyl] phenol ($C_{13}H_{12}O_2$). Though these species could be identified, sometimes two distinct peaks were not apparent at all HABs i.e., at certain heights the peaks were not well resolved to enable precise integration. However, 2-benzylphenol and 4-benzylphenol ($C_{13}H_{12}O$), bis (2-hydroxyphenyl) methane (2,2'-methylenediphenol) and 2-[(4-hydroxyphenyl) methyl] phenol ($C_{13}H_{12}O_2$) were well separated in the 2D GC-MS chromatogram. To quantify these species, supplemental techniques based on other detection principles would be necessary, for instance, the synchrotron-based photoelectron photo ion coincidence (SVUV-PEPICO) spectroscopy. In addition to these issues, there were about 13 intense peaks which could not be identified using our MS systems, however could be integrated at all HABs to see their evolution with respect to the flame height. The dissociation/fragmentation patterns corresponding to these signals were not distinct. Hence, as per the NIST-MS 11 database several matches/possibilities with very low probabilities for the match were proposed. In some other cases, isomers could not be distinguished as the dissociation/fragmentation patterns were similar and sometimes the proposed matches were not even close to the structures anticipated. Since the analytical standards for some species of interest do not exist, their identification is ambiguous as there is no reference for comparison in the NIST database. In some instances, the signal to noise ratio was also insufficient for accurate identification.

Table 4. 2 and Figure 4. 3 show that the detected oxygenated aromatics possess different functionalities such as: alcohol, ether, carbonyl (aldehyde and ketone), ester, and acid. The number of aromatics belonging to a particular functional group were counted and are summarized in Figure 4. 4. Alcohols and ethers are predominant (36 and 32 species, respectively) functionalities amongst these species. The abundance of ethers could perhaps be related to the structure of anisole i.e., an aromatic ether. Interestingly, 15 out of 32 ethers are cyclic ethers (O atom in the cycle) whereas anisole itself is not a cyclic ether which indicates the existence of different mechanisms for the formation of ethers from anisole. The abundance of alcohols (36 species) underlines that the conversion of the aromatic ether as a fuel to alcoholic products is an important process under the studied conditions.

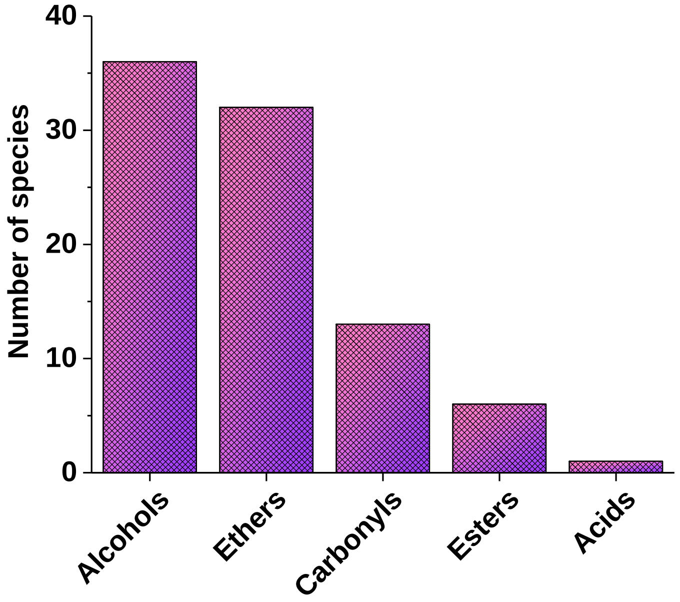

Figure 4. 4 : Number of oxygenated aromatics with different functional groups. Carbonyls include aldehydes and ketones. Species containing two identical functional groups is counted once, e.g. dibenzo-p-dioxin ($C_{12}H_8O_2$) with two ether groups. Some species were counted twice if they contained two different functional groups, e.g. 2-dibenzofuranol consists of an ether and an alcohol functional group and so is counted twice. Thus, the total number presented is greater than that for Table 4. 2.

4.1.3. Experimental indications of the formation kinetics of oxygenated aromatics

Different models were developed for the pyrolysis and combustion of anisole in the literature, such as Roy and Askari model in 2022 [241], Chen et al. model in 2022 [56], Mergulhão et al. model in 2021 [121], Büttgen et al. model in 2020 [120], CRECK model in 2020 [242] , Yuan et al. model in 2019 [53], Wagnon et al. model in 2018 [123], Nowakowska et al. model in 2014 [48]. Some of these models include oxygenated aromatics [48,53,56,242]. In Figure 4. 3, the species highlighted by bold font/bonds were the ones that are considered in the models in the literature (one might say "*a drop in the sea*"). About ten one-ring and nine two-ring oxygenated aromatics have been considered in the literature models [48,53,56,242]. However, only one out of thirteen three-ring species is considered in these models. The detection of oxygenated aromatics in the present study thus opens a very important perspective for the combustion community for the further development of kinetic models for this lignin-based biofuel. In the following text, some possible formation routes leading to the formation of oxygenated aromatics based on the current knowledge in the literature and on the present experimental indications is presented. A pictorial representation of these pathways for certain relevant oxygenated aromatics from anisole are presented in Figure 4. 5.

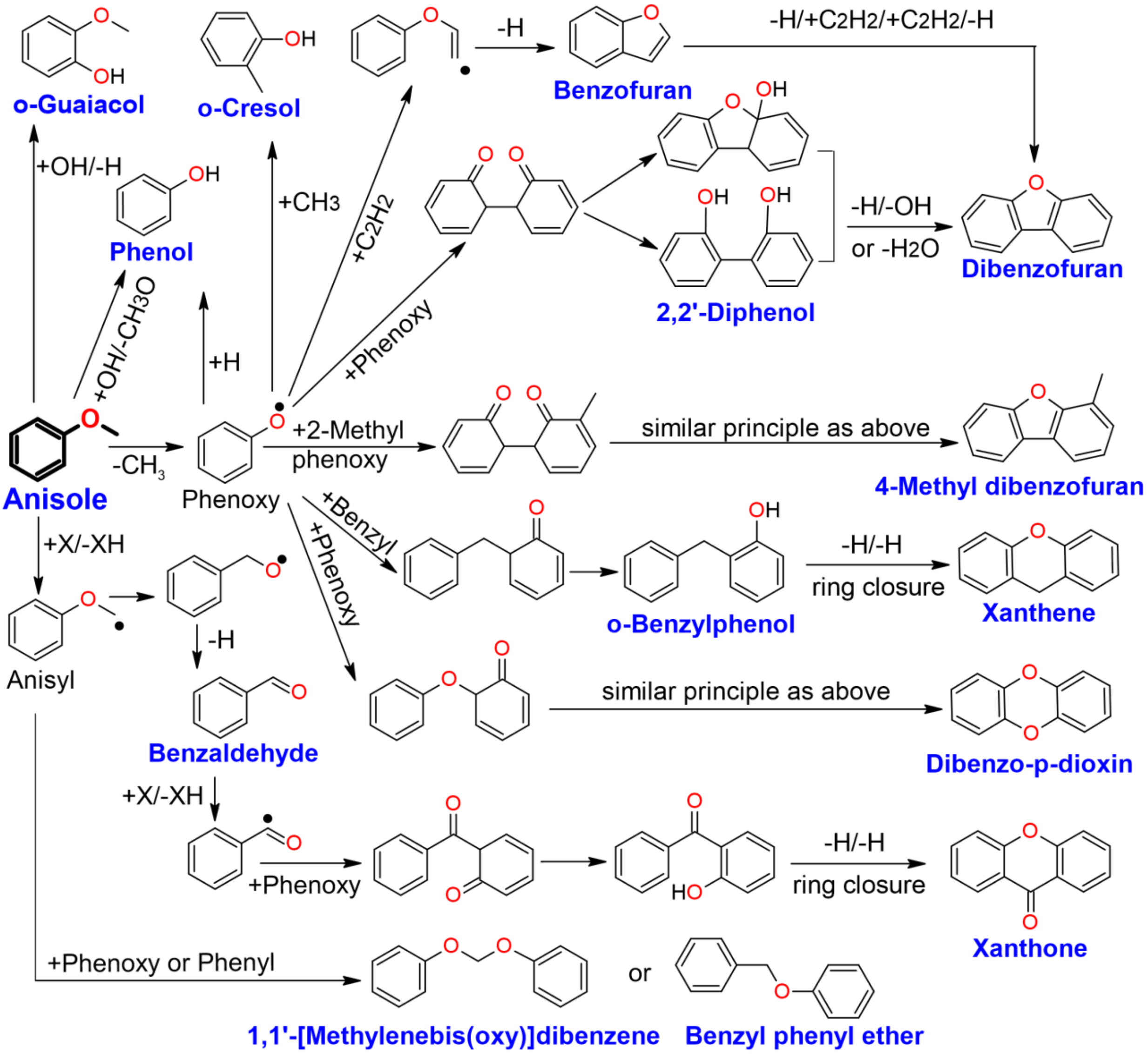

Figure 4. 5 : Some possible formation routes leading to the formation of some relevant oxygenated aromatics. Stable species with their names were experimentally identified in the present work.

As mentioned earlier, the aromatics with the alcohol functional group were the most abundant amongst the identified species. This indicates that addition of the OH radicals on the benzene ring (of anisole or of the subsequent products) followed by the subsequent C–H or C–C β-scissions could be one of the possible mechanisms contributing to the formation of these species. Figure 4. 5 presents some examples of this mechanism for the formation of m-guaiacol and phenol from anisole [51]. A second possible mechanism leading to the formation alcoholic aromatics is the tautomerization of aromatic ketones to aromatic alcohols, where the ketones could be produced from the combination of the phenoxy (C_6H_5O) radical with other aromatic radicals. Figure 4. 5 also presents examples of this mechanism for the formation 2,2′-diphenol and o-benzylphenol. The O–CH_3 bond in the methoxy group of anisole has a very low bond dissociation energy (63.2 kcal/mol), owing to which its unimolecular scission to yield phenoxy (C_6H_5O) and methyl (CH_3) radicals is strongly favored, especially under fuel-rich conditions [51]. Phenoxy is a resonance stabilized radical, that may react to form different oxygenated aromatics. For instance, they could recombine with H atoms to contribute to the formation of phenol, react with the CH_3 radical to form o-cresol [48] and with C_2H_2 to form benzofuran [53,158] that may enlarge via H-abstraction and C_2H_2 addition reactions to produce dibenzofuran (a three-ring OPAH) [158]. The phenoxy radicals themselves may also undergo self-recombination reactions followed by subsequent intramolecular rearrangements which may adequately elucidate the formation pathway to produce dibenzofuran [53,243]. 2,2’-Diphenol, an intermediate species in this pathway, was experimentally identified in the present work. A similar principle can be applied for the formation 4-methyl dibenzofuran, but from the recombination of phenoxy and 2-methyl phenoxy radicals. The self-recombination of the phenoxy radical and its combination with the benzyl radical can lead to the formation of dibenzo-p-dioxin [243] and xanthene, respectively. Anisole itself may undergo H-atom abstraction on the methoxy group by a H-atom, methyl radicals in order to yield the anisyl ($C_6H_5OCH_2$) radical. This anisyl radical can isomerize to the benzoxyl ($C_6H_5CH_2O$) radical via the *ipso* rearrangement and then undergo the β-scission reaction to yield benzaldehyde [48]. The experimental detection of xanthone suggests a possible participation of benzaldehyde in the formation OPAHs through the recombination of its radical with other aromatic radicals such as the phenoxy radicals. Furthermore, the detection of 1,1'-[methylenebis(oxy)]dibenzene and benzyl phenyl ether indicates the recombination of anisyl radical with the phenoxy and phenyl radicals, respectively. Future studies focusing on the comprehensive development of a kinetic model for anisole will have to include and test these suggested formation pathways.

It must be noted that the reaction pathways for OPAHs cited in the previous paragraphs are limited to anisole as their precursor. However, other formation routes, for instance, pathways involving PAHs cannot be excluded. Formation of OPAHs from classical PAHs could also be relevant. For example, the formation of dibenzofuran from biphenyl could also be possible [158]. However, this contribution could be considered to be less significant as compared to the direct formation pathways via anisole as none of the OPAHs were observed in detectable amounts in flame F1 (no anisole). Thus, straight-thinking implies that the formation of OPAHs detected in the anisole doped flame is mainly directed by the presence of anisole.

Nevertheless, there could be some oxygenated aromatics that could be formed because of interaction between the chemistry of anisole and iso-octane. The experimentally-detected species indicated this possibility that is exemplarily summarized in a schematic representation in Figure 4. 6.

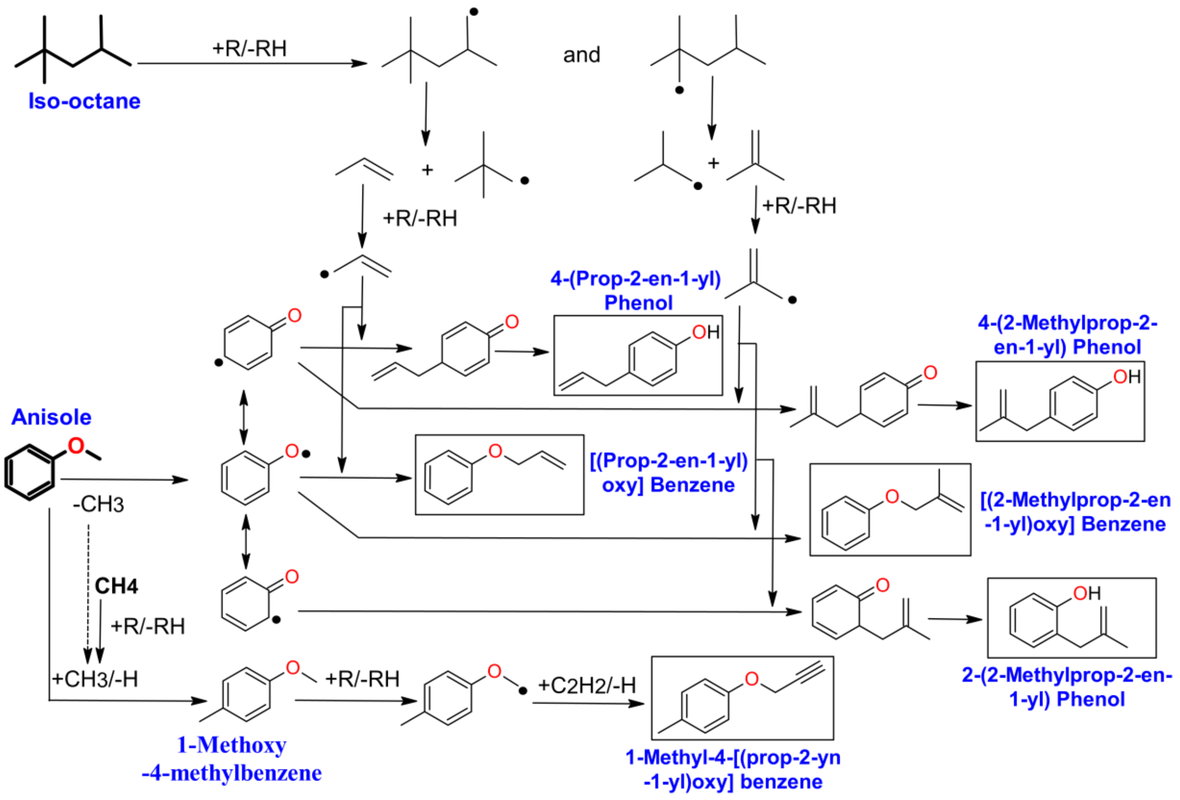

Figure 4. 6 : Some possible formation routes leading to the formation of some other relevant oxygenated aromatics considering the smaller species formed via iso-octane. Stable species with their names were experimentally identified in the present work. Species enclosed in rectangles are involved in discussions of iso-octane/methane contribution. Here R: H, OH, etc.

For instance, iso-octane can undergo H-abstraction to produce iso-octyl radicals. Depending on the site of H-abstraction, these radicals could further decompose and lead to the formation of propenyl and isobutenyl radicals. These radicals could intervene with the consumption steps of phenoxy radicals. For example, the isobutenyl radical could attack either on the oxygen atom or the ortho position or the para position of the phenoxy radical followed by isomerization to produce [(2-methylprop-2-en-1-yl)oxy] benzene, 2-(2-methylprop-2-en-1-yl) phenol, and 4-(2-methylprop-2-en-1-yl) phenol. All these oxygenated aromatics were detected in the present study which could evidence this mechanism. Similarly, the propenyl radical could attack the phenoxy radical to produce [(prop-2-en-1-yl)oxy] benzene, 2-(prop-2-en-1-yl) phenol, and 4-(prop-2-en-1-yl) phenol, respectively. The former and the latter were experimentally observed in this study. Furthermore, the detection of 1-methyl-4-[(prop-2-yn-1-yl)oxy] benzene confirms the participation of C_1 and C_2 species. The ipso-addition of CH_3 (a radical produced by the three fuels) on anisole leads to the formation of 1-methoxy-4-methylbenzene (also experimentally detected) that can react to yield 1-methyl-4-[(prop-2-yn-1-yl)oxy] benzene via H-abstraction and C_2H_2 recombination. C_2H_2 here could be produced from either of the three fuels in the mixture via different pathways. It must be noted that the reactions proposed do not constitute a complete mechanism but are mere possibilities based on the qualitative analysis of the species that were experimentally identified in this work. More species and more pathways could certainly exist.

In addition to providing experimental indications on the formation kinetics of OPAHs, accurate identification of species can also lead to quantification of species. The results presented in Section 4.1 highlight the importance of recognizing and addressing the formation mechanism of OPAHs. Detailed quantitative flame structure measurements also provide good tests for chemical kinetic mechanisms and are possible only after their accurate identification. However, it must be noted that it was certainly not feasible to quantify all the identified species in the current study. These species were present in a very complex mixture (with PAHs and other non-oxygenated aromatics as well) with diverse range of concentrations i.e., from thousands of ppm to a few ppb. It was certainly not doable to span such a broad range of concentrations for all species in a single GC injection. This is why the identification process was a result of the analysis of several chromatograms at different HABs performed using different split ratios. By increasing the split ratio in the GC method, we could resolve and identify the species that were present in abundant amounts i.e., several ppm. However, as the split ratio was increased, peaks corresponding to aromatics present in ppt amounts consequently disappeared. Though splitless injections helped to recover the information lost in the split injections, species present in abundant amounts and possessing close retention times transformed into an unresolved mixture. On the contrary, some peaks though identified due to high split injections, were not well-resolved in low split injections. Splitless injections were chosen as a compromise between having enough signal for most of the peaks that could be integrated and at the same time resolving the complex mixtures as much as possible to acquire the maximum amount of data for quantitative measurements (GC Scion). In the subsequent sections, studies on the influence of the operating conditions on the mole fraction evolution of these species have been presented. Section 4.2 presents a study on the influence of the equivalence ratio on the evolution of the mole fraction of species in flames containing 10% anisole in the total fuel mixture and Section 4.3 presents a study on the influence of the amount of anisole in flames possessing a fixed equivalence ratio.

4.2. Study of the influence of EQUIVALENCE RATIO with a constant amount of anisole

The previous section emphasizes on the qualitative analysis and features several oxygenated aromatics that were observed in anisole flames. In this section, mole fraction profiles of different chemical species (reactants, products, lighter hydrocarbons, aromatics, oxygenated aromatics) are presented as a function of HAB, using the GC setups and the methodology discussed in Chapter 2. Here, a comparison study amongst three flames characterized with three different equivalence ratios i.e., 1.70, 1.82 and 1.90 is presented to investigate how a change in the equivalence ratio would influence the formation of stable gas-phase chemical species in iso-octane/CH_4/anisole flames where the amount of anisole in the total fuel is always constant (10%). The summary of flame conditions chosen for this series has been summarized in Table 4. 3 and real photographs of the flames with the same camera settings have been shown in Figure 4. 7.

Table 4. 3 : Summary of the flame conditions studied to study the effect of an increase in the equivalence ratio when the amount of anisole in the total fuel is constant. Here L_n =normal liters per minute.

Flame	*Biofuel (%)*	*Gaseous flow rates (L_n/min)*						*Equivalence ratio*	*C/O*
		Biofuel	C_8H_{18}	CH_4	O_2	N_2	Total		
F4	Anisole (10)	0.097	0.14	0.729	2.387	6.50	9.85	**1.70**	0.52
F2	Anisole (10)	0.102	0.15	0.766	2.338	6.50	9.85	**1.82**	0.55
F5	Anisole (10)	0.105	0.15	0.788	2.308	6.50	9.85	**1.90**	0.58

Flame F4 is a slightly leaner flame with an equivalence ratio of 1.70. Flames F2 and F5 are slightly richer flames with an equivalence ratio of 1.82 and 1.90 respectively. As can be seen in the figure, the yellowish color of the flame increases with increasing equivalence ratio.

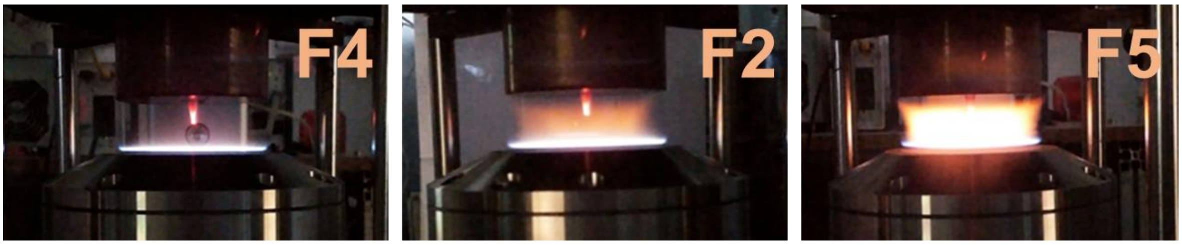

Figure 4. 7 : Photographs of premixed iso-octane/CH4/anisole/ O2/N2 flames: F4 (10% anisole, ϕ=1.70), F2 (10% anisole, ϕ=1.82), and F3 (10% anisole, ϕ=1.90) presenting their visual aspect (with the same camera settings).

4.2.1. Major species and temperature profiles

Figure 4. 8 presents the comparison of the consumption of the three fuels (anisole, iso-octane, and methane) and the oxidant (oxygen). The figure also presents the mole fraction profiles of the major end products observed for the three flames like carbon monoxide (CO) and carbon dioxide (CO_2). Peak mole fraction values for nitrogen and hydrogen are listed in Table A. 3 in the Appendices. Water has not been measured in this study. As shown in the figure, flame F4 with an equivalence ratio of 1.70 is much closer to the burner whereas flame F5 with an equivalence ratio of 1.90 is far away from the burner. The observation concerning the shift in the position of the flames is consistent with what is expected as the laminar burning velocity for a given fuel is higher at near stoichiometric conditions and gradually decreases near fuel-rich conditions [244].

The presence of iso-octane and anisole in the flame is no longer detectable from about 3 mm above the burner. Meanwhile, some methane always persists even at higher HABs. Since these flames are rich, there is no noticeable residual mole fraction of oxygen remaining in the burnt zone for all three flames, signifying that oxygen is completely consumed.

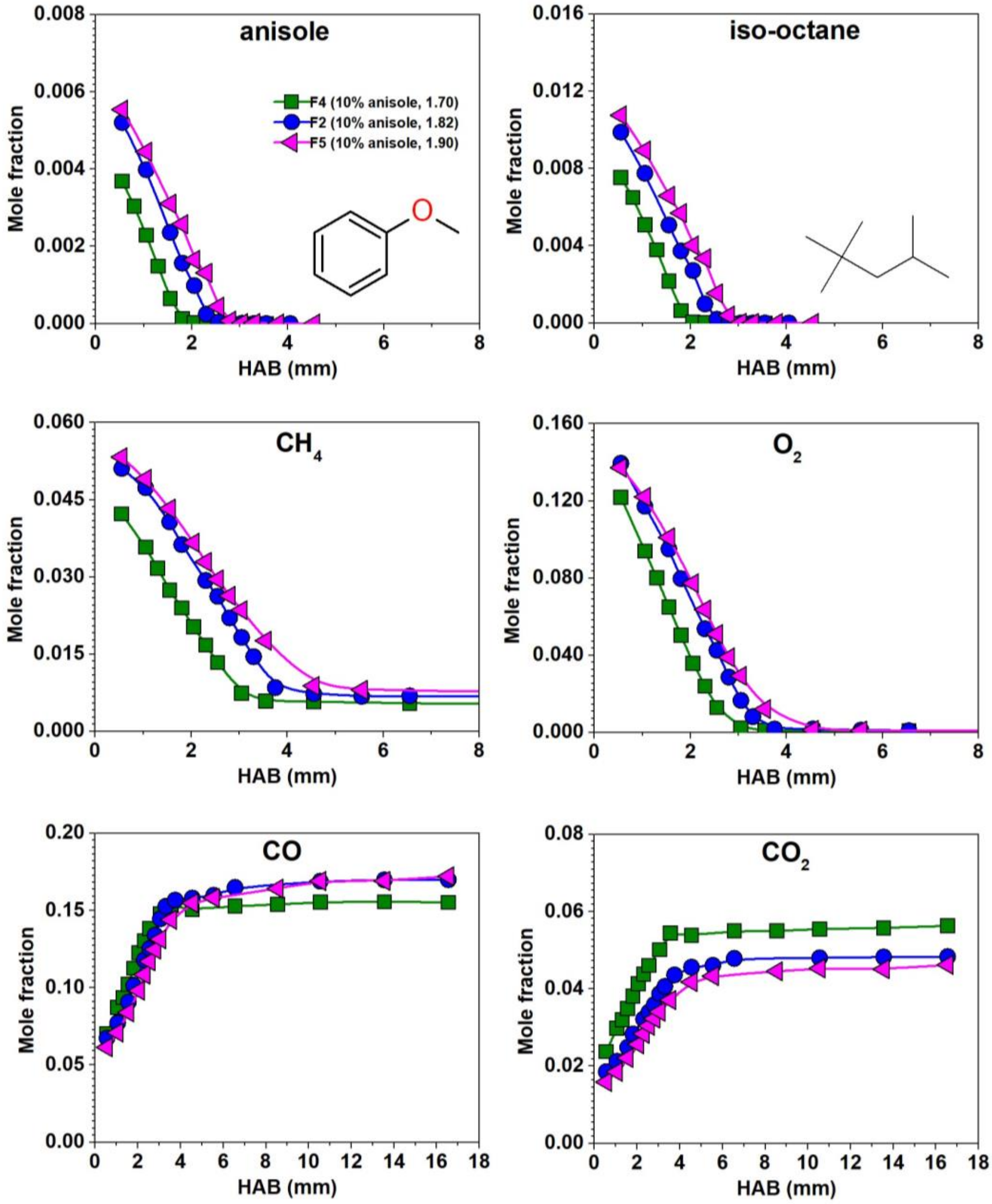

Figure 4. 8 : Comparison of the experimentally determined mole fraction profiles for the reactants and major end products formed in flames F4 (10% anisole, ϕ=1.70), F2 (10% anisole, ϕ=1.82), and F5 (10% anisole, ϕ=1.90). Experimental results have been connected by a thin line to guide the eye.

In general, if we observe each of these flames individually, it is evident that we have more CO than CO_2 in these flames. This is characteristic of rich flames. These equivalence ratios are far from the stoichiometric conditions leading to incomplete oxidation process which can explain why there is more CO than CO_2. For instance, in F5, the mole fraction of CO is around 0.164 whereas the mole fraction of CO_2 is around 0.045 in the plateau region. These significant peak mole fraction values for CO and CO_2 persist in the burnt gas zone. However, the ratio of the amount of CO/CO_2 is much elevated in F5 (about 3.6) in comparison to F4 (about 2.8).

This is somewhat anticipated as it is normal to have more CO_2 in F4 than in F5 as the former is a leaner flame with respect to F5 and thus possesses more oxygen to convert CO to CO_2.

Figure 4. 9 shows the temperature profiles obtained for the three flames in the presence and absence of the probe. Plots (a), (b) and (c) present the temperature profiles with and without the nozzle for flames F4, F2, and F5 respectively.

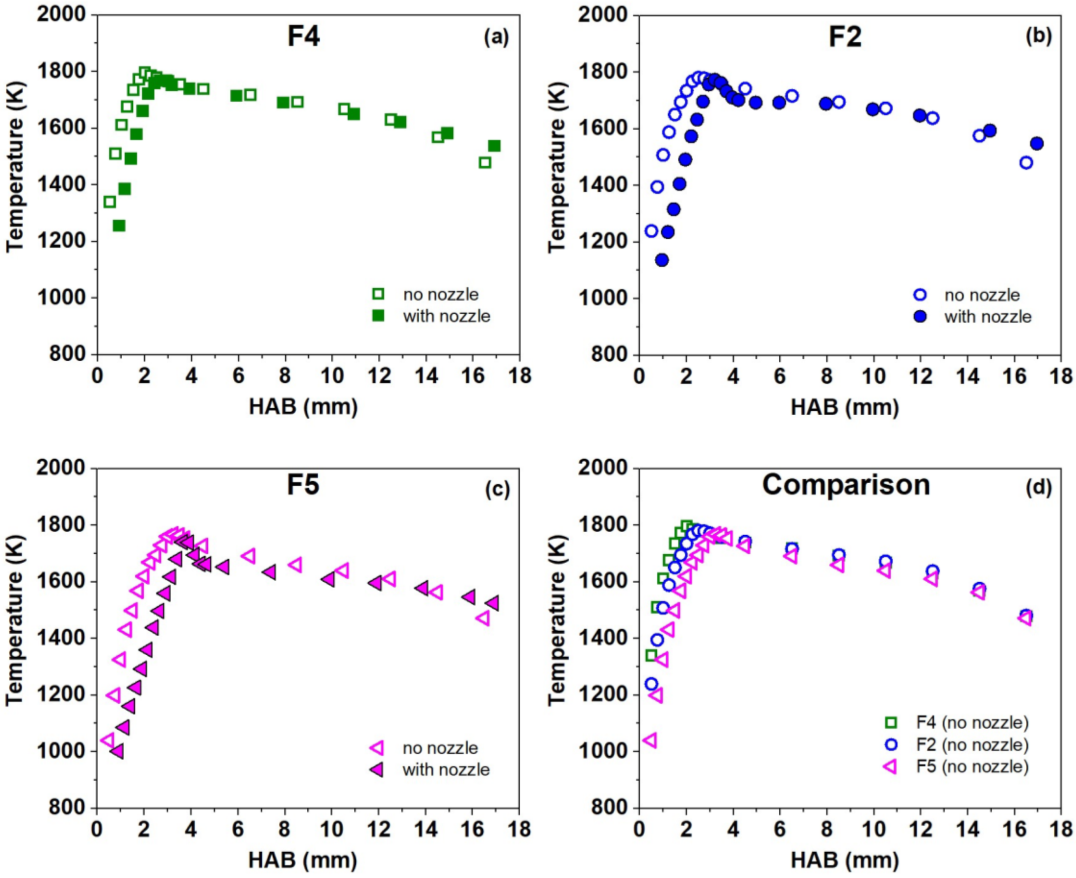

Figure 4. 9 : Experimentally determined temperature profiles obtained using the thermocouple method in the presence and the absence of the nozzle for the three flames F4 (10% anisole, ϕ=1.70), F2 (10% anisole, ϕ=1.82), and F5 (10% anisole, ϕ=1.90)

These plots indicate that the presence of the nozzle causes a shift in the temperature profile towards the burnt gas zone. It is clear that the position of the gradient has experienced a shift in all the flames in the presence of the nozzle. Meanwhile, the nozzle's presence in the flame does not significantly perturb the temperature in the burnt gas. Plot (d) presents a comparison of the three temperature profiles without the nozzle. As indicated again by the temperature profiles, flame F4 is much closer to the burner surface whereas flame F5 is much further away. If each of the temperature profiles are observed individually, it can be noticed that the lowest temperatures measured vary between ~1000-1200 K close to the surface of the burner whereas the maximum temperatures measured are around 1700-1800 K in the burnt gas zone (HAB > 2 mm) and decrease to about 1500-1600 K for the three flames near the stabilization plate.

4.2.2. Intermediate species (C_1-C_5)

Around twenty-seven C_1-C_5 intermediate species are detected and quantified in these flames with their mole fractions as a function of HAB. They are listed below:

- **C1** species – HCHO (formaldehyde), CH_3OH (methanol)
- **C2** species – C_2H_6 (ethane), C_2H_4 (ethylene), C_2H_2 (acetylene), CH_3CHO (acetaldehyde)
- **C3** species – C_3H_8 (propane), C_3H_6 (propene), aC_3H_4 (allene), pC_3H_4 (propyne), C_2H_5CHO (propanal), C_2H_3CHO (acrolein), CH_3COCH_3 (acetone),
- **C4** species – C_4H_{10} (isobutane), iC_4H_8 (isobutene), C_4H_4 (vinyl acetylene), $1C_4H_8$ (1-butene), c-$2C_4H_8$ (*cis*-2-butene), t-$2C_4H_8$ (*trans*-2-butene), 1,$3C_4H_6$ (1,3-butadiene), C_4H_4 (1-butyne), C_4H_6O (methyl vinyl ketone), C_4H_4O (furan)
- **C5** species – C_5H_{10} (2-pentene), C_5H_6O (2-methyl furan), cC_5H_6 (cyclopentadiene), C_5H_6 (2-methyl -1-buten-3-yne), C_5H_8 (1,3-pentadiene)

Out of the different intermediate species listed above, selected important small soot precursors are presented and discussed in the following text. Peak mole fraction values for other species are listed in Table A. 3 in the Appendices. As quoted in the literature [61,245,246], reactions of hydrocarbon species from C_2 to C_5 could contribute significantly to the formation of the first aromatic ring. Some typical reactions widely accepted in the literature showing how small hydrocarbons lead to the formation of the first aromatic ring are presented in Figure 4. 10. Small unsaturated hydrocarbons, such as C_2H_2, also participate in the growth of PAHs particularly via the HACA (H-abstraction-C_2H_2-addition) [247]. Therefore, these species deserve to be examined here.

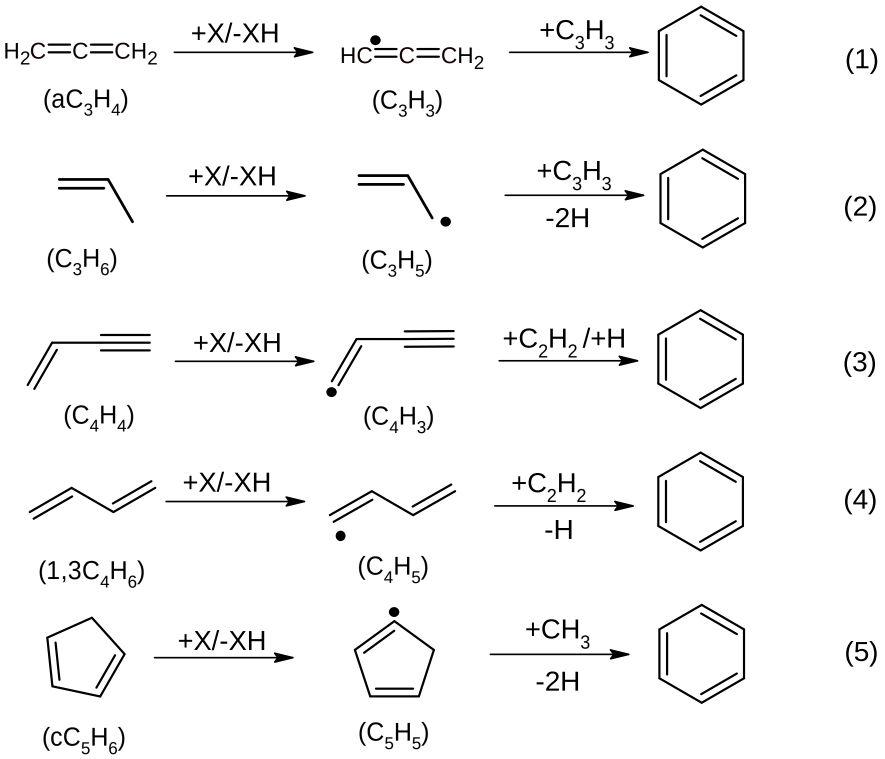

Figure 4. 10: Schematic diagrams of important reactions that form single-ring aromatic hydrocarbons from aliphatic hydrocarbons; extracted and adapted from [248].

Figure 4. 11 presents the evolution of the mole fraction of some C_2-C_5 aliphatic hydrocarbons: acetylene (C_2H_2), ethylene (C_2H_4), propene (C_3H_6) and allene (aC_3H_4) as a function of the HAB for the three flames. The mole fraction of acetylene (C_2H_2) largely predominates under these conditions making it the most abundant not only among C_2 species but also among all intermediates. As mentioned earlier, acetylene (C_2H_2) is a very important soot precursor in a variety of hydrocarbon flames, as it leads to the formation of benzene and other aromatic compounds. As shown in Figure 4. 11, the maximum mole fraction value of acetylene increases as the equivalence ratio increases. Its value is about 9310 ppm (2.5 mm) in F4 which increases to a value of 12800 ppm (3.3 mm) in F2 and to 13900 ppm (3.5 mm) in F5. Nevertheless, there is a slight shift in the profile towards the burnt gas zone with the increase in the equivalence ratio which is true for other species as well. Unlike ethylene which is completely consumed after 6 mm regardless of the different flame conditions, acetylene maintains a high mole fraction even in the burnt gas zone in the three flames.

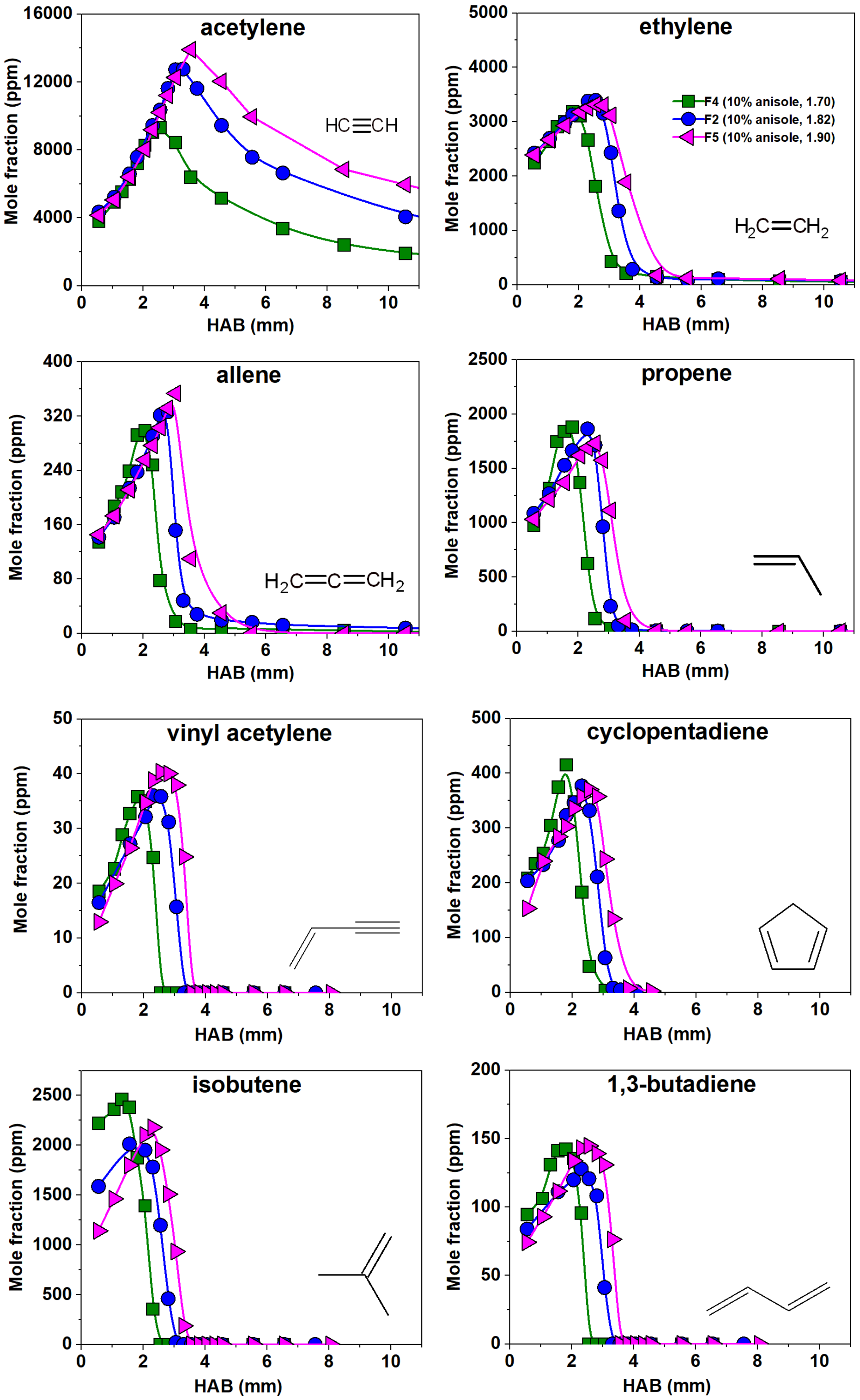

Figure 4. 11 : Comparison of the experimentally determined mole fraction profiles for some selected C2-C5 formed in flames F4 (10% anisole, ϕ=1.70), F2 (10% anisole, ϕ=1.82), and F5 (10% anisole, ϕ=1.90). Experimental results have been connected by a thin line to guide the eye.

The maximum mole fraction of acetylene is attained after ethylene, which is fully consistent with the subsequent C2 reaction sequence widely accepted in the literature [61].

Ethylene is slightly more abundant in F2/F5 (~3400 ppm) in comparison to F4 (~3180 ppm). It can be observed that the amounts of C_3 species are lower when compared to the mole fractions of the C_2 species. The mole fraction of propene is higher than that of allene. The latter species persists (a few ppm) in the flame and never completely disappear even in the burnt gas zone. While the peak mole fraction of allene increases slightly with increasing equivalence ratio, that of propene is somewhat not affected. Figure 4. 11 also presents some of the important C_4 species, i.e., isobutene (iC_4H_8), 1,3-butadiene ($1{,}3C_4H_6$), and vinyl acetylene (C_4H_4), and a C_5 species, i.e. cyclopentadiene. Isobutene is one of the four detected C_4H_8 isomers. The branched structure of iso-octane (fuel) favors the formation of isobutene making it the most abundant butene isomer in the studied flames. A similar observation was also reported by Bakali et al. in their investigation on premixed flames of iso-octane [249]. The maximum mole fraction of isobutene in flame F4 is about 2460 ppm whereas its slightly less (by a factor of 1.2) in F2 and F5 (~2000 ppm). Vinyl acetylene increases by 11% from flame F2/F4 to F5. Cyclopentadiene on the other hand decreased by 10% from flame F4 to flame F2/F5.

4.2.3. Non-oxygenated aromatics and PAHs

Several aromatic species (up to three rings) were detected and quantified in anisole flames which constitute a major part of this thesis. Using the GC-MS systems (1D and 2D), we also detected four-ring PAHs, e.g. pyrene and fluoranthene, but the GC Scion setup used for quantification could not detect them because of the upper limit of column oven temperature. As detailed in Chapter 2, though the seven columns in the GC Scion possess different maximum allowed temperatures, they are all placed in the same oven. The maximum oven temperature is then limited to 180°C, not sufficiently high for allowing elution of the heavy PAHs (above four rings) from the column used for measuring aromatics (SCION-17 MS). This is the reason why PAHs like pyrene and fluoranthene though identified using the GC-MS systems where no temperature limitations are present, could not be quantified in this study using GC Scion.

Benzene and toluene are amongst the first non-oxygenated aromatics that were produced in these flames and are conventionally believed to have the potential to participate and contribute to the formation of larger aromatics [61]. Figure 4. 12 presents a schematic representation of how species like benzene and toluene can contribute to the formation of a two-ring aromatic species, i.e. naphthalene.

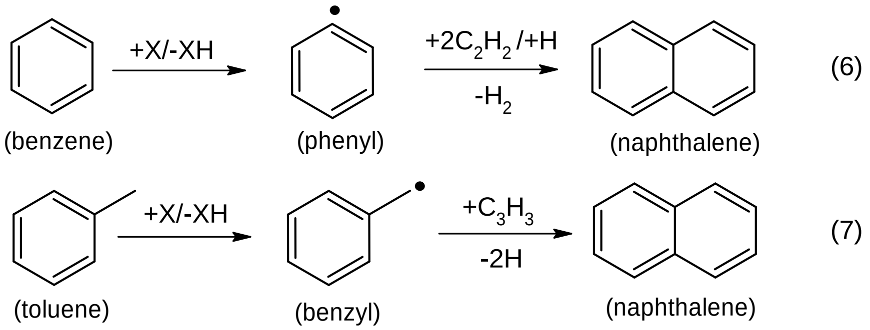

Figure 4. 12: Schematic diagrams of important reactions that form two-ring aromatic hydrocarbons from aliphatic hydrocarbons; extracted from [248].

Figure 4. 13 and Figure 4. 14 present the mole fraction profiles for non-oxygenated aromatics in the three flames respectively. Benzene and toluene are important intermediate species in these flames where the former is more abundantly produced than the latter. Figure 4. 13 presents a comparison of their mole fraction profiles. It is noticeable that the production of these aromatics increases very progressively as the equivalence ratio increases from 1.70 to 1.90. The maximum mole fraction of benzene generated is around 827 ppm (HAB=2 mm) in F4, 825 ppm (HAB=2.3 mm) in F2 and about 907 ppm (HAB=2.8 mm) in F5. There is no difference in the amount of benzene generated in F4 and F2 despite an increase in the equivalence ratio which solely leads to a shift of the profile towards the burnt gas zone. In each of these flames, the amount of benzene produced is always 12 times more the amount of toluene produced. The relationship between the production of benzene and toluene in flames, where benzene production is consistently 12 times greater than that of toluene, can be attributed to the chemical reactions occurring within the flame environment. Benzene can be produced through a series of radical reactions involving the combination and rearrangement of smaller hydrocarbon radicals. Toluene, on the other hand, can be formed from the combination of phenyl and methyl radicals. If we compare amongst the three flames (F4, F2 and F5), the trend followed by toluene is similar to that of benzene. The maximum mole fraction value of toluene is nearly 68 ppm in F4 (HAB=2 mm) and F2 (HAB=2.5 mm). Like benzene, the amount of toluene produced is unaffected by an increase of the equivalence ratio in this range. However, this amount slightly increases by nearly 12% to a value of 76 ppm in F5 (HAB=2.8 mm).

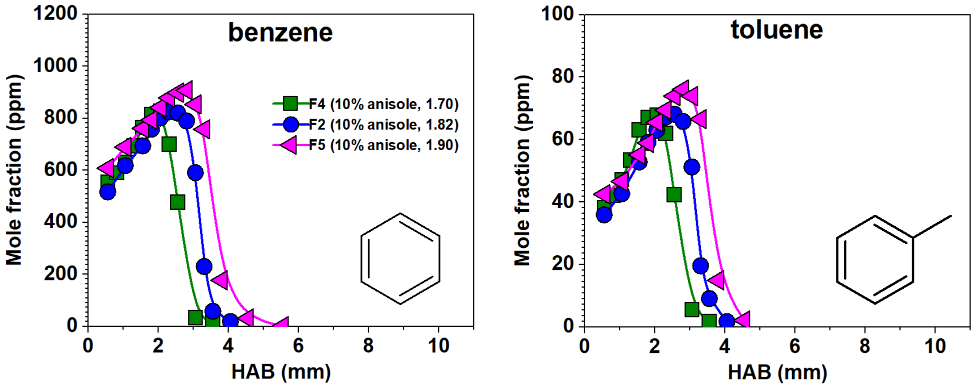

Figure 4. 13 : Comparison of the experimentally determined mole fraction profiles for benzene and toluene formed in flames F4 (10% anisole, ϕ=1.70), F2 (10% anisole, ϕ=1.82), and F5 (10% anisole, ϕ=1.90). Experimental results have been connected by a thin line to guide the eye.

Several PAHs were observed and quantified in anisole flames. PAHs are important species as they are the potential precursors of soot [58]. Comparison of the experimental results for some PAHs such as naphthalene, fluorene, acenaphthylene, acenaphthene, phenanthrene, and anthracene in the flames F1, F2 and F3 are summarized in Figure 4. 14. It is worth mentioning that these species are very challenging to identify and quantify using the conventional GCs as they are present in very low concentrations in flames. PAHs presented in Figure 4. 14 were calibrated individually to retrieve their absolute concentrations using the methodology based on their vapor pressures (described in Chapter 2). Naphthalene is in general the most abundant two-ring non-oxygenated aromatics produced in anisole flames. Besides naphthalene, indene, another two-ring PAH, was also detected in high amounts (refer to Table A. 3 in the Appendices.

As seen in this figure, the mole fraction profiles of the PAHs are sensitive to the equivalence ratio. They seem to attain their maximum mole fractions much later than the aliphatics presented in Section 4.2.2. In general, the least quantities of PAHs can be observed in flame F4 with an equivalence ratio of 1.70. This is logical as it is most fuel deficient flame out of the three flames due to which PAH formation might be suppressed. For example, the maximum mole fraction of naphthalene in F4 is nearly 4 ppm and increases by 50% to a value of about 6 ppm in F2 and F5. Likewise, amount of fluorene in F4 is around 120 ppb that doubles to nearly 270 ppb and 280 ppb in flames F2 and F5 respectively. Acenaphthene shows a similar trend with a concentration of 53 ppb in F4 and then increases by 50% to nearly 80 ppb in F2 and F5. Meanwhile, there is about 250 ppb of acenaphthylene in F4 whose formation is promoted as the equivalence ratio progressively increases, i.e., nearly 560 ppb (a factor of 2.4) and 780 ppb (a factor of 3.1) in F2 and F5 respectively. Anthracene also follows a similar trend. The concentrations of phenanthrene and anthracene are similar in flames F4 and F5. However, the amount of phenanthrene (85 ppb) produced in flame F2 is nearly 2.5 times more than the amount of anthracene (33 ppb) produced, for which we have not yet found a reason.

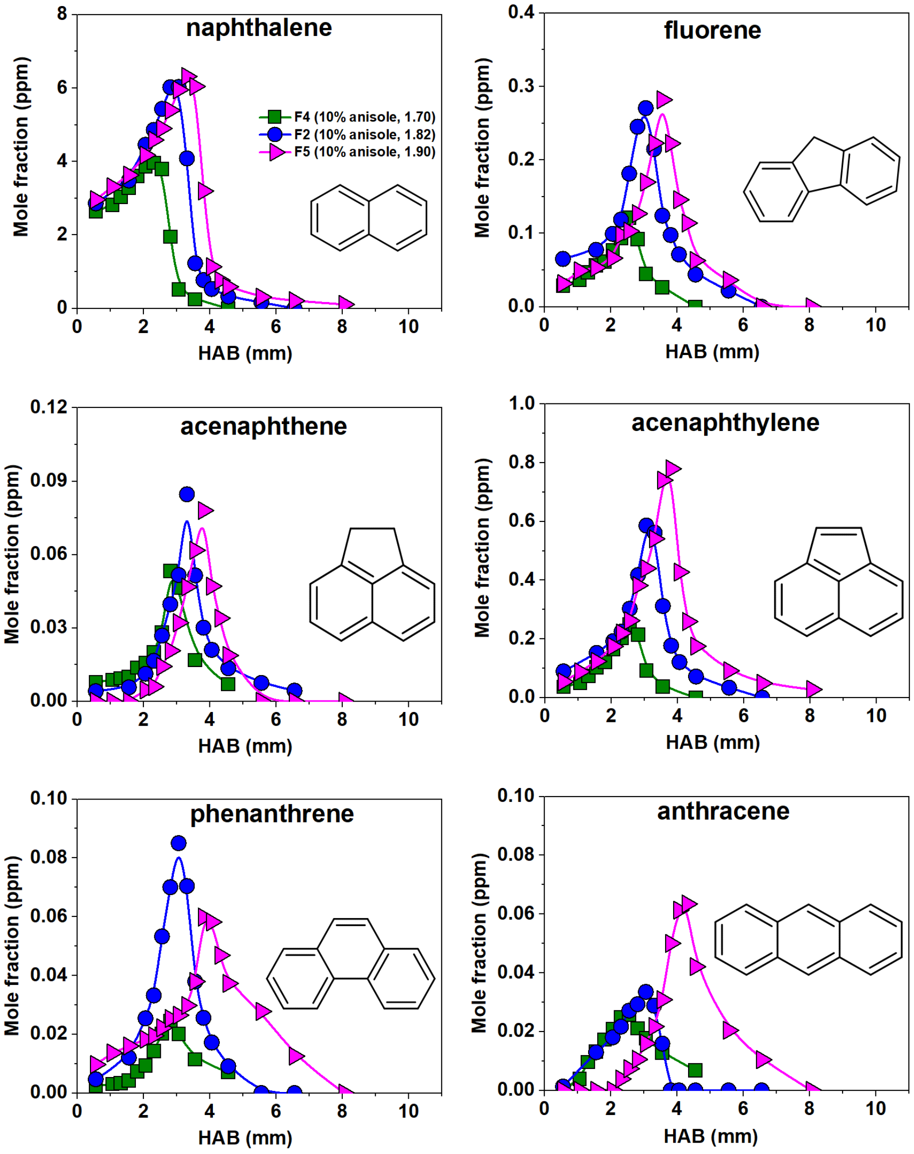

Figure 4. 14: Comparison of the experimentally determined mole fraction profiles for some selected PAHs formed in flames F4 (10% anisole, ϕ=1.70), F2 (10% anisole, ϕ=1.82), and F5 (10% anisole, ϕ=1.90). Experimental results have been connected by a thin line to guide the eye.

Figure 4. 15 presents a graphical presentation for the peak mole fraction of different non-oxygenated aromatics (from one- to three-rings) with adjacent benzene rings. It may be noted that as the number of benzene rings in the species increase, the concentration of the species reduces by two orders of magnitude. Though styrene, indene, and acenaphthylene somewhat do not belong to the group (i.e., increasing adjacent benzene rings), however, they are included in the figure for a global overview on such species. The amount of benzene produced in these

flames ranges in the order of hundreds of ppm (×10^{-4}) whereas species like naphthalene (two adjacent benzene rings) are produced in the order of tens of ppm (×10^{-6}). Meanwhile, phenanthrene and anthracene (three adjacent benzene rings) were found to be present in quantities less than a ppm or ppb levels (×10^{-8}). Owing to the custom-built GC setup with the SPT system, it was possible to quantify species which were present in very low concentrations (in ppb levels). As shown in the figure, the evolution in the peak mole fraction of the species with respect to the number of adjacent benzene rings present in their structures seems to be similar for the three equivalence ratios.

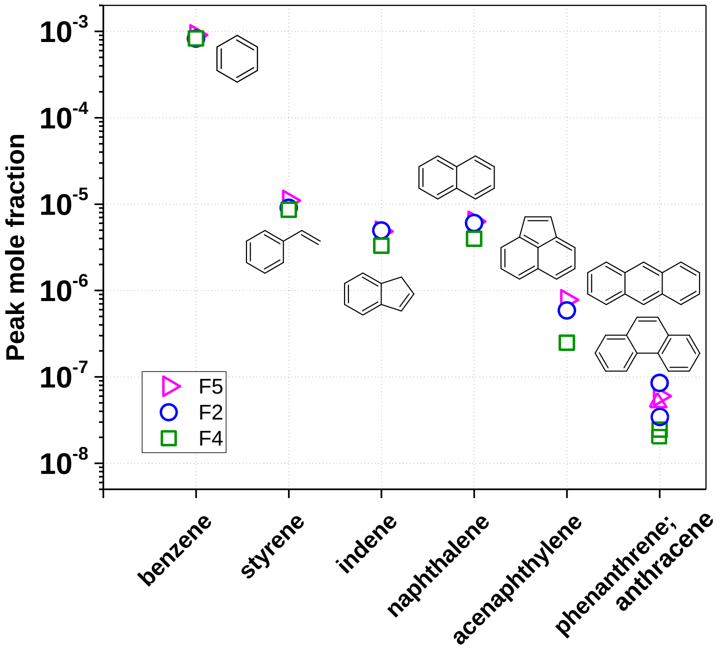

Figure 4. 15 : Peak mole fractions for selected one- to three-ring non-oxygenated aromatics quantified in flames F4 (10% anisole, ϕ=1.70), F2 (10% anisole, ϕ=1.82), and F5 (10% anisole, ϕ=1.90).

4.2.4. Oxygenated aromatics and OPAHs

Like PAHs, several OPAHs (one, two and three rings) were identified and quantified in anisole flames. They are presented in Figure 4. 16, Figure 4. 17, and Figure 4. 18 respectively. Figure 4. 16 presents some of the important oxygenated monoaromatics that were identified and quantified in these flames. As mentioned earlier, anisole can readily undergo the O-CH_3 bond dissociation because of its very low bond dissociation energy to form the phenoxy radical. The implication of the phenoxy radical in the combustion chemistry of anisole gives rise to a whole new set of stable intermediates. The recombination reactions of phenoxy with other radicals can compete with its unimolecular decomposition reaction to produce cyclopentadiene. Amongst the recombination reactions, those with the CH_3 and H radicals are the most important ones. This can lead to the formation of cresols and phenol as the products. Some possible formation pathways of oxygenated aromatics are previously presented in Section 4.1.3.

As presented in Figure 4. 16, phenol, benzaldehyde, and o/p-cresols are some of the major oxygenated aromatics that were detected in anisole flames. Amongst these species, phenol and o-cresol are the most abundant oxygenates. Though the hydroxyl functional group is the most commonly encountered functionality in OPAHs in anisole flames, the oxygen atom can also be present in the form of carbonyls, esters, ethers and carboxylic acid functional groups. Again, even amongst the one ring oxygenates, a diverse range of concentrations is possible. Phenol, benzaldehyde and cresols are present in the order of hundreds of ppm while species like phenyl acetate are only a few ppm. The amount of these species is slightly sensitive to the equivalence ratio. It can be seen that their formation is somewhat promoted in the leaner flame. The amount of phenol in F2 and F5 is similar i.e., 436 and 442 ppm respectively. Meanwhile, it increases by nearly 10% in flame F4 (477 ppm). Out of the two cresols, o-cresol is always the most abundant isomer and its formation is promoted in F4. The amount of o- and p-cresol is reduced by nearly 21% and 18% respectively with an increase in the equivalence ratio from 1.70 to 1.90.

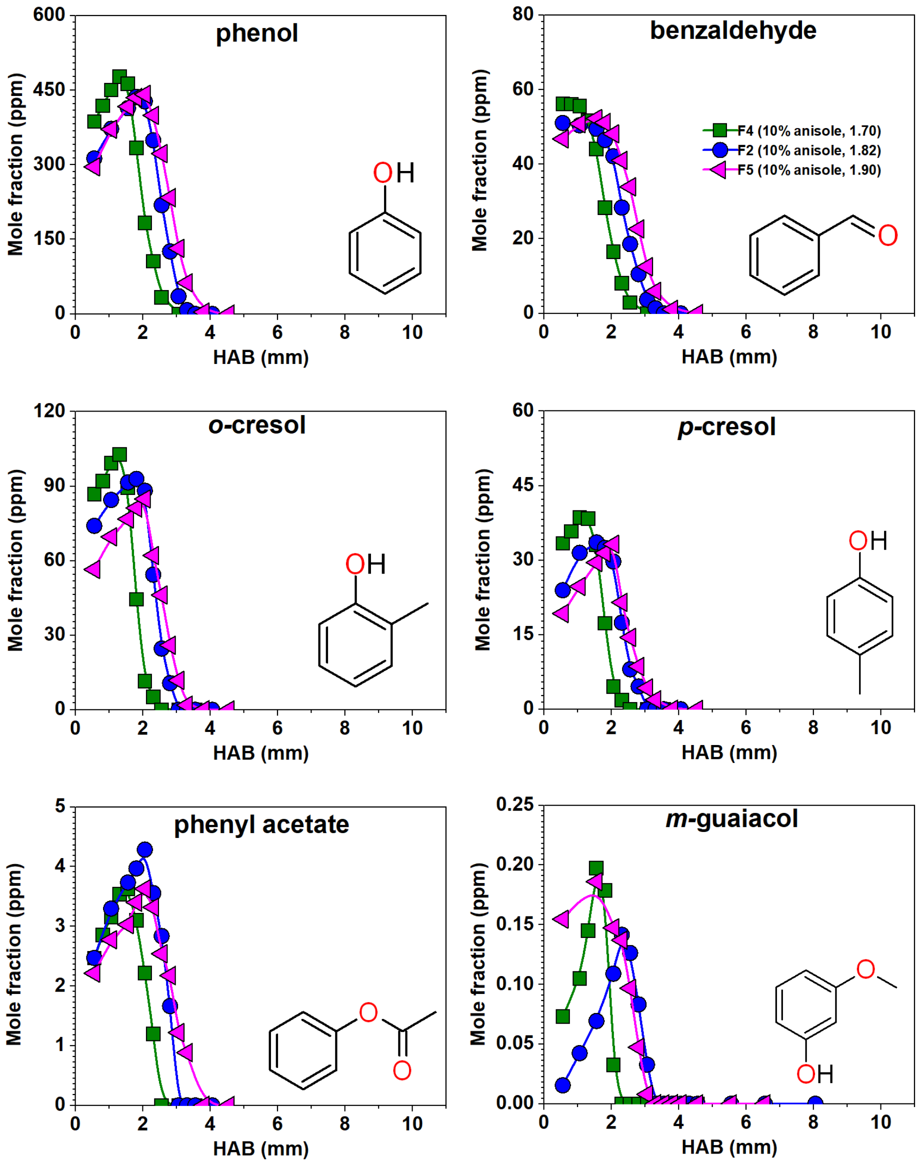

Figure 4. 16 : Comparison of the experimentally determined mole fraction profiles for some selected monoaromatic oxygenates formed in flames F4 (10% anisole, ϕ=1.70), F2 (10% anisole, ϕ=1.82), and F5 (10% anisole, ϕ=1.90). Experimental results have been connected by a thin line to guide the eye.

The quantified two- and three-ring OPAHs are presented in Figure 4. 17 and Figure 4. 18 respectively. Several benzofurans, simple and substituted indanones, xanthenes, xanthones, and dioxin like species produced in anisole flames are quantified. Some of these species (dibenzofuran, xanthene and xanthone) have been calibrated directly for quantification while the response factors for the remaining species were estimated on the basis of the species that were calibrated directly. The amounts of these OPAHs can range from a few ppm to a few ppb. Even though the percentage of anisole in the total fuel mixture is constant in these flames, differences in the equivalence ratio seem to be influencing the peak mole fraction of OPAHs. The first general trend is that this influence is much more pronounced for these species than for oxygenated monoaromatics. The second general trend is that the formation of some OPAHs is somewhat promoted in the leaner flames (F4 and F2 *vs* F5), contrary to the trend observed for PAHs (compare Section 4.2.3).

Benzofuran is the most abundant two ring OPAH produced in anisole flames (Figure 4. 17). The maximum mole fraction value of benzofuran in flames F4 and F2 is nearly 4.4 ppm and about 5.2 ppm in F5. Unlike phenol and cresols, the amount of benzofuran produced increases by nearly 21% when equivalence ratio is increased from 1.70 to 1.90. Other OPAHs like 2,3-dihydrobenzofuran, 2-ethyl benzofuran, 1-methylinden-2-one, 1-indanone, xanthene, dibenzofuran, and fluorenol presented in the figures also seem to be sensitive to a change in the equivalence ratio and show a suppression in their formation as the equivalence ratio increases. Interestingly, the maximum mole fraction for xanthone is the highest in F2. This species contains two O-atoms and the behavior followed (unlike other OPAHs discussed previously) suggests that more than one pathway may lead to its formation. A fundamental reasoning or the mechanism involved behind this trend needs to be inspected and will be considered for future perspectives by performing simulations using existing models in the literature.

As can be seen in the figures, some two-ring OPAHs (like 1-indanone and 2,3-dihydrobenzofuran) and three-ring OPAHs (like dibenzofuran, xanthene and fluorenol) start to form really close to the burner. As discussed previously, even the lowest temperatures range between 1000-1200 K for these flames. This implies that the reactions start happening near the burner surface which leads to the formation of these species even at very low HABs. As discussed in section 4.1.3, self-combination of the phenoxy radicals or the combination of phenoxy radical with other aromatic radicals can readily form two- and three-ring OPAHs. The premixed mixture (fuels, oxygen, nitrogen) injections were performed without flame to verify if there were any impurities in the fuel itself. It was seen that none of these OPAHs were present in injections from the premixed mixture in the absence of a flame. This made us certain that the OPAHs which start to form really early are formed in the flame and are not impurities present beforehand in the fuel mixture.

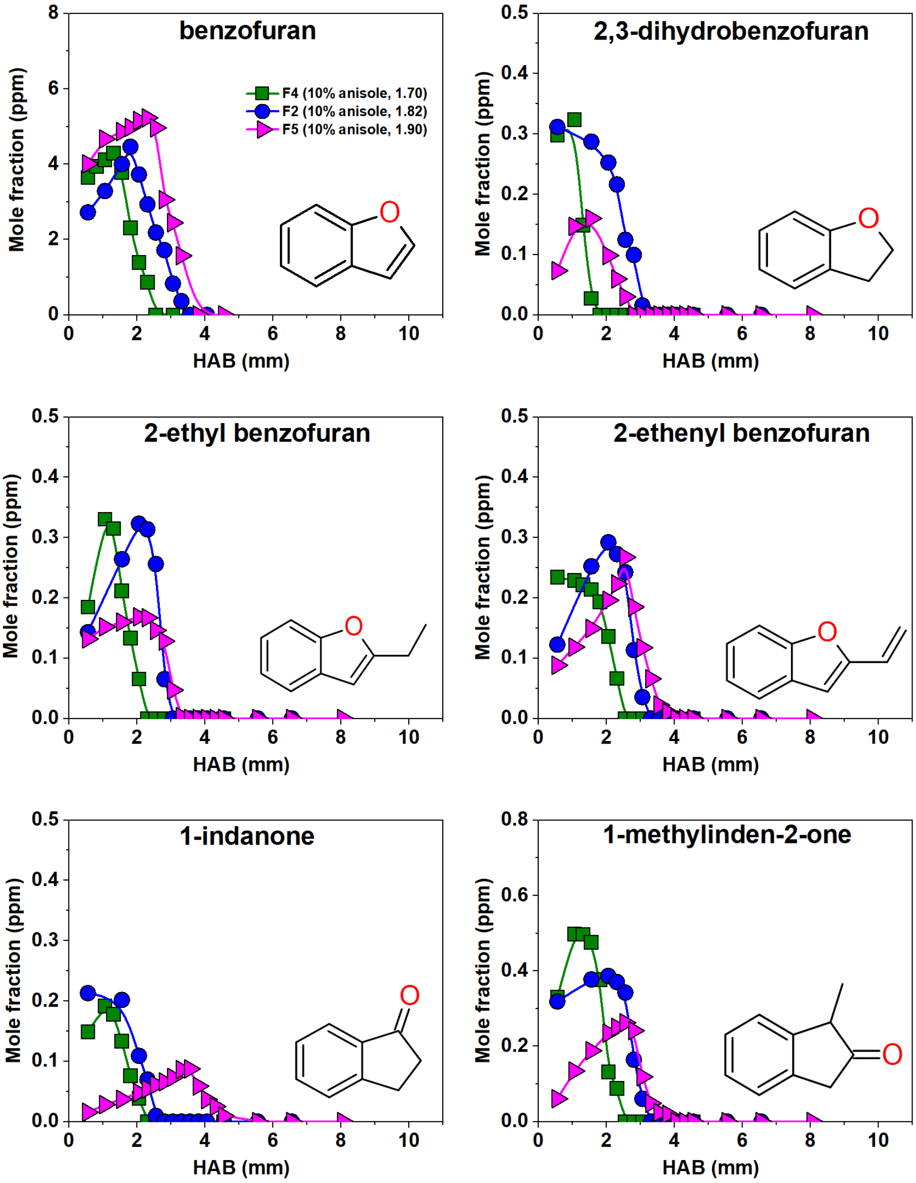

Figure 4. 17 : Comparison of the experimentally determined mole fraction profiles for some selected two-ring OPAHs formed in flames F4 (10% anisole, ϕ=1.70), F2 (10% anisole, ϕ=1.82), and F5 (10% anisole, ϕ=1.90). Experimental results have been connected by a thin line to guide the eye.

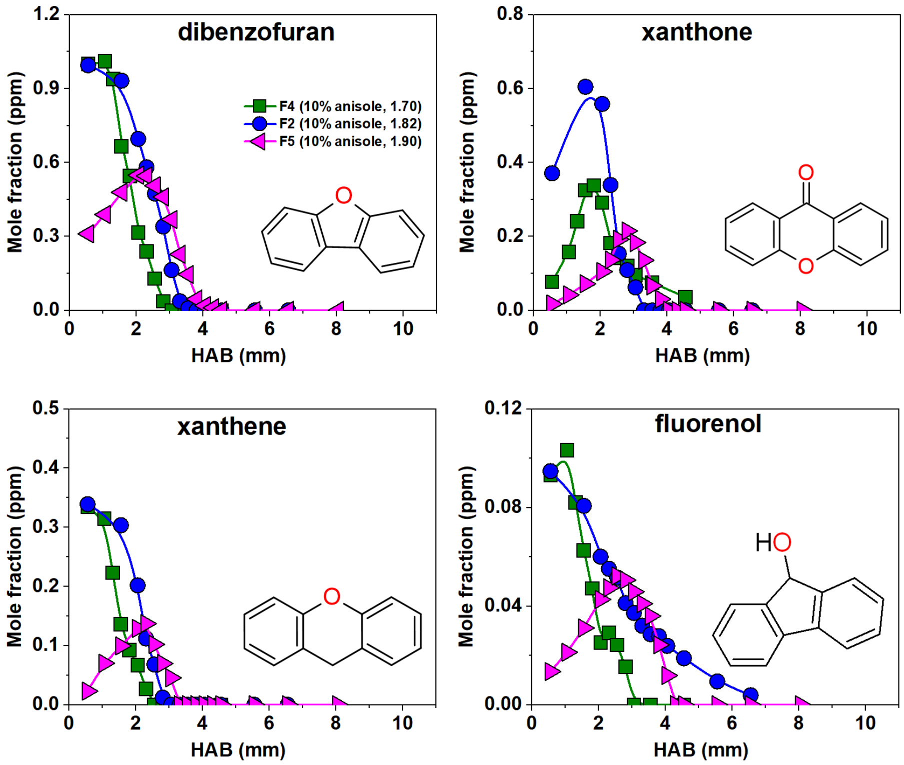

Figure 4. 18: Comparison of the experimentally determined mole fraction profiles for some selected three-ring OPAHs formed in flames F4 (10% anisole, ϕ=1.70), F2 (10% anisole, ϕ=1.82), and F5 (10% anisole, ϕ=1.90). Experimental results have been connected by a thin line to guide the eye.

If compared to non-oxygenated aromatics, it is interesting to note that, in general, oxygenated aromatics attain their peak mole fractions before those of PAHs as presented in Figure 4. 19. The bar graph representation on the right represents the sum of the peak mole fractions of species (non-oxygenated and oxygenated) with the same number of rings. The plot on the left indicates that the profiles of oxygenated aromatics are comparatively closer to the burner with respect to the non-oxygenated aromatics which suggests that these species are produced before the non-oxygenated ones. It is interesting to note that the number of rings for non-oxygenated species increase with HAB, indicating that one-ring species are formed prior to two- and three-thing species. However, this is not the case for oxygenated aromatics. Three-ring OPAHs appear to form as soon as one-ring oxygenates are formed. A comparison of the sum of the peak mole fractions of one-, two-, and three-ring aromatics on the right suggests that non-oxygenated aromatics are produced in higher amounts than oxygenated aromatics as far as one- and two-ring aromatics are concerned. However, it can be seen that three-ring OPAHs are almost as abundant as the three-ring PAHs in terms of their amounts.

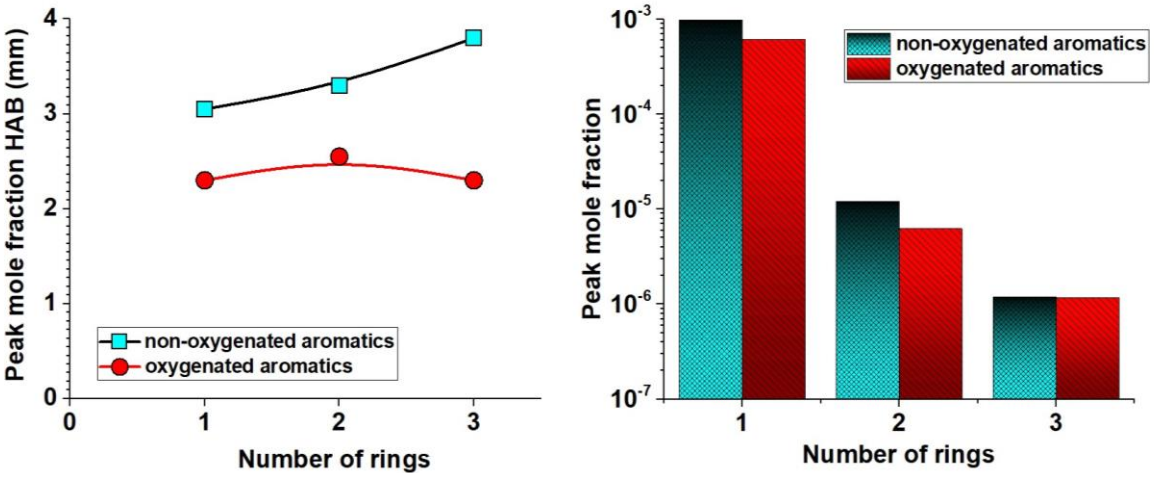

Figure 4. 19 : Comparison of the oxygenated and non-oxygenated aromatics in flame F5 (10% anisole, ϕ=1.90). The results from the flame F5 are selected for this comparison as it has the best spatial resolution. Left panel represents HABs corresponding to the sum of the peak mole fractions for one-, two-, and three-ring aromatics, respectively; Right panel represents the sum of the peak mole fractions for one-, two-, and three-ring aromatics, respectively.

4.3. Study of the influence of the ANISOLE AMOUNT at constant equivalence ratio

In this section, a study on how the presence of anisole and its amount would influence the flame structure at a given fixed equivalence ratio of 1.82 is presented. The summary of flame conditions chosen for this purpose has been summarized in Table 4. 4 and real photographs of the flames with the same camera settings are shown in Figure 4. 20.

Table 4. 4 : Summary of the flame conditions studied to study the effect of anisole. Here L_n =normal liters per minute.

Flame	*Biofuel (%)*	*Gaseous flow rates (L_n/min)*						*Equivalence ratio*	*C/O*
		Biofuel	C_8H_{18}	CH_4	O_2	N_2	Total		
F1	**-**	**-**	0.18	0.925	2.25	6.50	9.85	1.82	0.52
F2	**Anisole (10)**	**0.102**	0.15	0.766	2.338	6.50	9.85	1.82	0.55
F3	**Anisole (15)**	**0.147**	0.13	0.696	2.377	6.50	9.85	1.82	0.57

Flame F1 had no biofuel i.e., no anisole and thus acts as a reference flame that only consists of iso-octane/CH_4/O_2/N_2. Flames F2 and F3 consisted of anisole/iso-octane/CH_4/O_2/N_2 where the former had 10% whereas the latter had 15% anisole in the total fuel mixture respectively. This section is particularly devoted to the investigation of the different chemical species (reactants, products, lighter hydrocarbons, aromatics, oxygenated aromatics) and how their mole fraction profiles evolved with respect to the HAB.

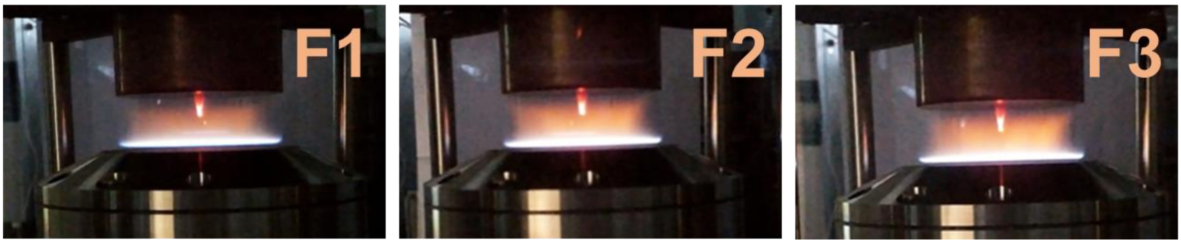

Figure 4. 20: Photographs of premixed iso-octane/ CH_4/anisole/ O_2/N_2 flames: F1 (0% anisole, ϕ=1.82), F2 (10% anisole, ϕ=1.82), and F3 (15% anisole, ϕ=1.82) presenting their visual aspect (with the same camera settings).

4.3.1. Major species and temperature profiles

Figure 4. 21 presents the comparison of the consumption of the reactants (anisole, iso-octane, methane, and oxygen) and the major end products (CO_2 and CO). Anisole and iso-octane are no longer detectable after about 3 mm above the burner whereas there is always some methane (about 5800 ppm) that persists even at higher HABs. The difference between the experimental onset and the expected theoretical concentrations for the fuels in the fresh unburnt zone can be attributed to their different reactivities close to the surface of the burner. There is no noticeable residual mole fraction of oxygen remaining in the burnt zone. It is evident that there is more CO than CO_2 in these flames. For instance, in F3, the mole fraction of CO is around 0.17 whereas the mole fraction of CO_2 is around 0. 05 in the plateau region. These significant maximum mole fraction values for CO and CO_2 persist in the burnt gas zone. The equivalence ratio of 1.82 is far from the stoichiometric conditions leading to incomplete combustion. Moreover, if we observe amongst different flames, the amount of CO and CO_2 produced is in the order: F3>F2>F1. Though the equivalence ratio is constant for the three

flames, their C/O ratios increase with increasing the added anisole amount which explains the increase for CO and CO_2. Interestingly, despite the difference in their C/H ratios (0.340, 0.407, and 0.438 for F1, F2, and F3, respectively), the added anisole amount does not significantly influence the amount of hydrogen produced (refer to Table A. 3 in the Appendices).

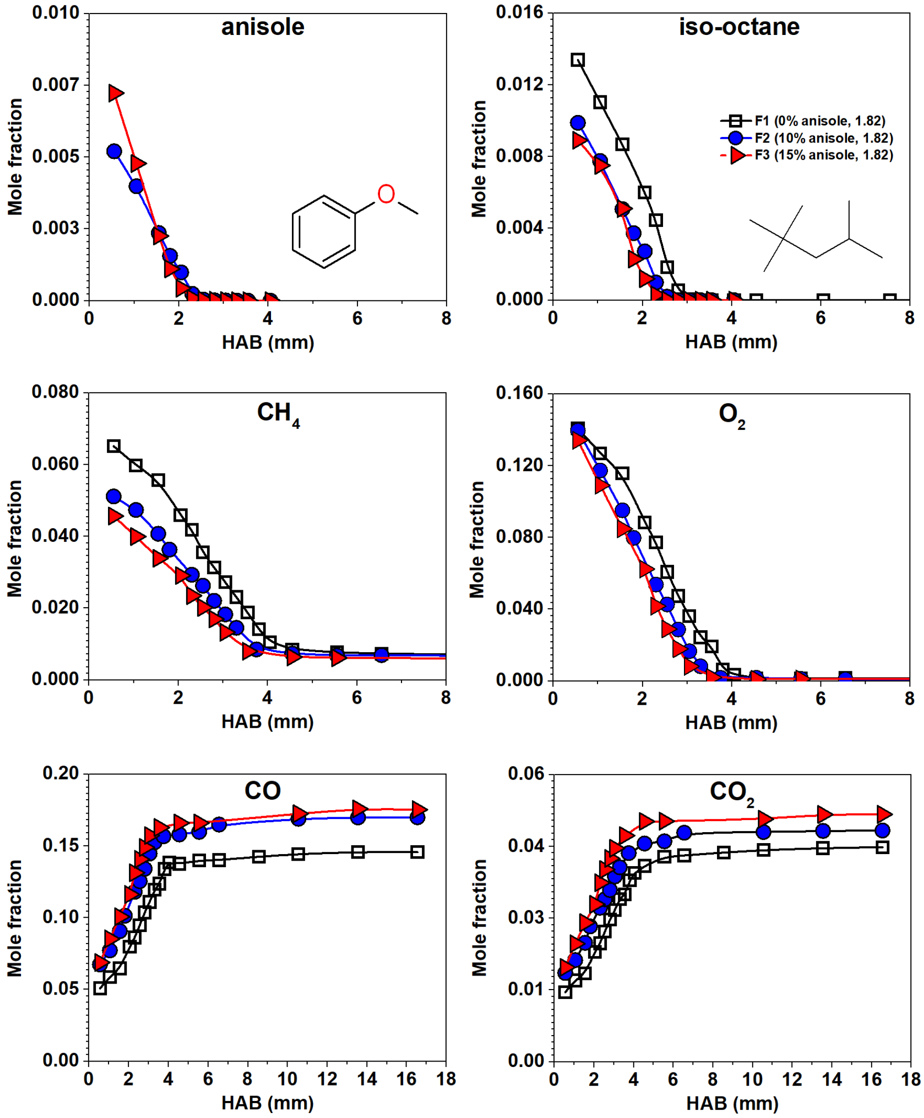

Figure 4. 21 : Comparison of the experimentally determined mole fraction profiles for the reactants and the major end products formed in flames F1 (0% anisole, ϕ=1.82), F2 (10% anisole, ϕ=1.82), and F3 (15% anisole, ϕ=1.82). Experimental results have been connected by a thin line to guide the eye.

Figure 4. 22 shows the temperature profiles obtained for the three flames in the presence and absence of the probe. It can be noticed that the presence of the nozzle causes a shift of the gradient in the temperature profile towards the burnt gas zone. However, nozzle's presence in the flame does not significantly perturb the temperature in the plateau region. The lowest temperatures measured very between ~1000-1200 K close to the burner and the maximum

temperatures measured are around 1700-1800 K in the burnt gas zone (HAB = 3-4 mm). and are quite similar for the three flames.

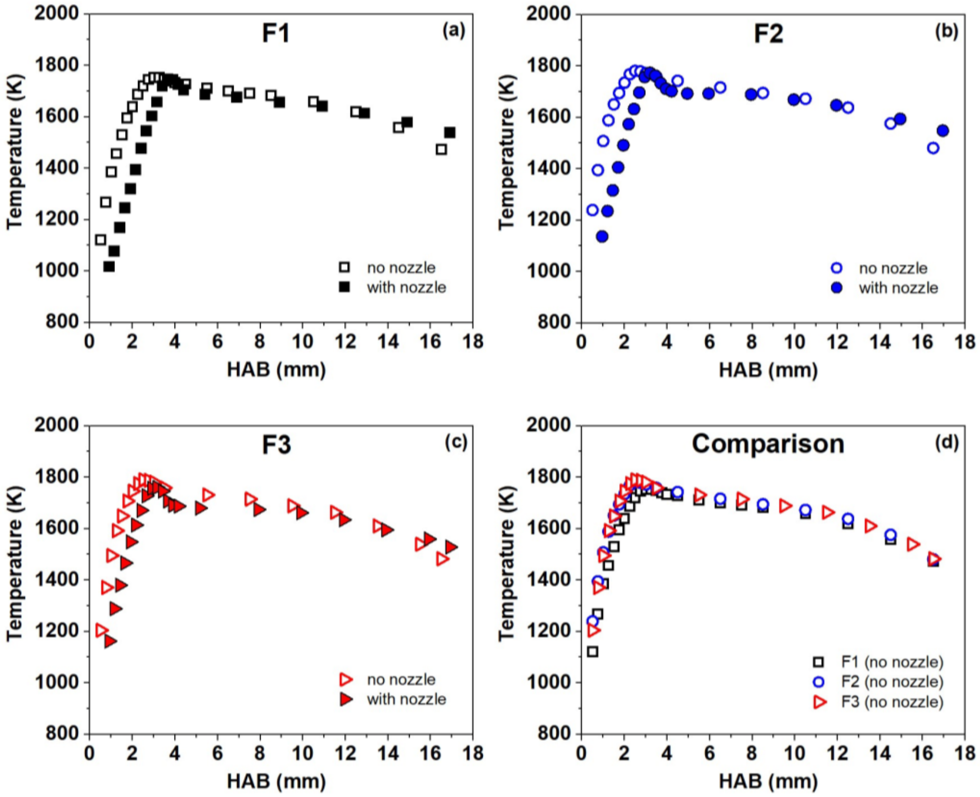

Figure 4. 22 : Experimentally determined temperature profiles obtained using the thermocouple method in the presence and the absence of the nozzle for the 3 flames

4.3.2. Intermediate species (C_1-C_5)

Twenty-seven intermediate species (C_1-C_5) are detected and quantified in these flames. They are listed below:

- **C1** species – HCHO (formaldehyde), CH_3OH (methanol)
- **C2** species – C_2H_6 (ethane), C_2H_4 (ethylene), C_2H_2 (acetylene), CH_3CHO (acetaldehyde)
- **C3** species – C_3H_8 (propane), C_3H_6 (propene), aC_3H_4 (allene), pC_3H_4 (propyne), C_2H_5CHO (propanal), C_2H_3CHO (acrolein), CH_3COCH_3 (acetone),
- **C4** species – C_4H_{10} (isobutane), iC_4H_8 (isobutene), C_4H_4 (vinyl acetylene), 1C_4H_8 (1-butene), c-2C_4H_8 (*cis*-2-butene), t-2C_4H_8 (*trans*-2-butene), 1,3C_4H_6 (1,3-butadiene), C_4H_4 (1-butyne), C_4H_6O (methyl vinyl ketone), C_4H_4O (furan)
- **C5** species – C_5H_{10} (2-pentene), C_5H_6O (2-methyl furan), cC_5H_6 (cyclopentadiene), C_5H_6 (2-methyl -1-buten-3-yne), C_5H_8 (1,3-pentadiene)

Mole fraction profiles for some relevant stable intermediate species have been presented in the text whereas peak mole fraction for others are listed in Table A. 3 in the Appendices. Figure 4. 23 presents the evolution of the mole fraction acetylene (C_2H_2), ethylene (C_2H_4), allene (aC_3H_4), propene (C_3H_6), vinyl acetylene (C_4H_4), 1,3-butadiene ($1,3C_4H_6$), isobutene (iC_4H_8), and cyclopentadiene (cC_5H_6) as a function of the HAB for the three flames. These are some of the most abundant species produced in these flames overall. They are also believed to participate in the formation of the first aromatic ring as well as their growth to form PAHs as discussed previously in Section 4.2.2. For instance, the mole fraction of acetylene (C_2H_2) largely predominates under these conditions. As discussed previously, it is an important soot precursor in a variety of hydrocarbon flames, as it leads to the formation of benzene and other aromatic compounds, thus contributing to the first step involved in the formation of soot. It can however be noticed that the presence and the amount of anisole does not really influence the amount of acetylene produced if we compare the three profiles for three flames. Nevertheless, there is a slight shift in its mole fraction profile with the addition of anisole which is true for other species as well. Other species in the figure are completely consumed regardless of the different flame conditions, unlike acetylene which maintains a high mole fraction even in the burnt gas zone in the three flames. The maximum mole fraction of acetylene is attained after that of ethylene which is slightly more abundant in F1 (~4000 ppm) in comparison to F2 (~3390 ppm) and F3 (~3260 ppm). It can be observed that the amounts of detected C_3 species are in general lower when compared to the mole fractions of the C_2 species. Propene is the most abundant C_3 species with a mole fraction of about 2000 ppm in F1, 1870 ppm in F2, and 1730 ppm in F3. Like acetylene, the maximum mole fraction of allene does not depend significantly to the added anisole amount.

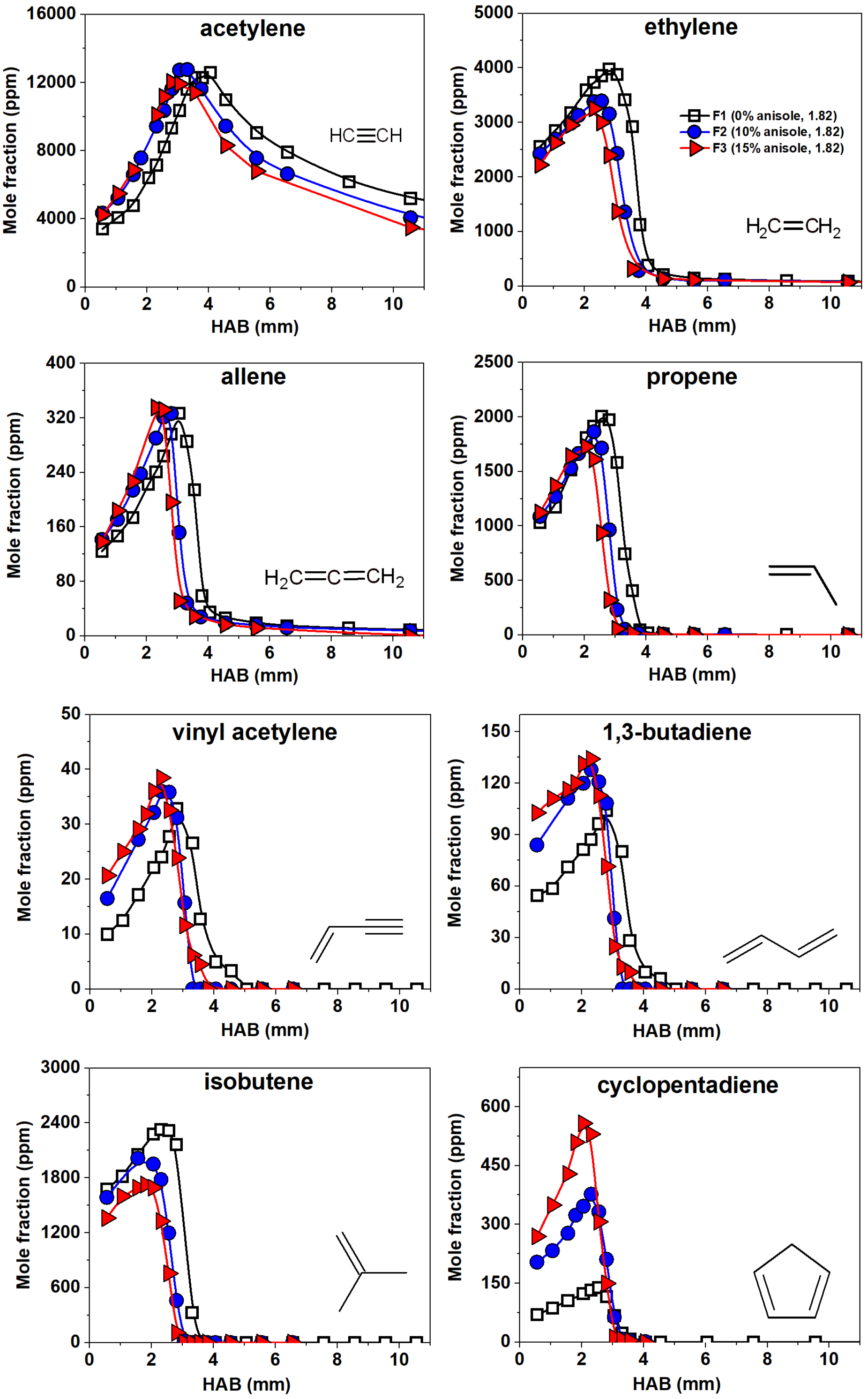

Figure 4. 23 : Comparison of the experimentally determined mole fraction profiles for C2-C3 species formed in flames F1 (0% anisole, $\phi=1.82$), F2 (10% anisole, $\phi=1.82$), and F3 (15% anisole, $\phi=1.82$). Experimental results have been connected by a thin line to guide the eye.

The different C_4 isomers are present in a diverse range of concentrations. The branched structure of iso-octane favors the formation of isobutene making it the main butene isomer in these flames [249]. In the presence of anisole, the maximum mole fraction value for isobutene is reduced. It is about 2330 ppm in F1 (no anisole) and is reduced to a value of about 2000 ppm and 1730 ppm in flames F2 (10% anisole) and F3 (15% anisole) respectively. There is a reduction of 25% of isobutene. This reduction could be attributed to the decrease in iso-octane when adding anisole. On the other hand, the formation of species like vinyl acetylene and 1,3-butadiene is enhanced in the presence of anisole. Similarly, the peak mole fraction value of 1,3-butadiene increases from a value of 96 ppm in F1 to about 135 ppm in F3. The maximum mole fraction value of vinyl acetylene also increases in the presence of anisole even though the effect is not as pronounced as for the other species. Cyclopentadiene formation is more significantly enhanced in the presence of anisole. The peak mole fraction of cyclopentadiene is about 139 ppm in F1, 377 ppm in F2 and about 560 ppm in F3. The amount of cyclopentadiene increases by four times with 15% anisole. Under flame conditions, anisole can readily via the O-CH_3 bond dissociation and decompose to phenoxy radicals which may eventually loose CO to produce the cyclopentadienyl radical. This would lead to the formation of cyclopentadiene via the H-addition reaction [250]. This reaction pathway is likely to account for the higher observed mole fractions for cyclopentadiene.

4.3.3. Non-oxygenated aromatics and PAHs

Figure 4. 24 presents some relevant reaction pathways for the formation of some selected non-oxygenated aromatics and PAHs from anisole based on some studies from the literature [51,53,240,241,250]. For example, benzene can originate from the *ipso*-addition of an H-atom at the methoxy moiety of anisole [48,240]. Secondly, H-abstraction at the CH_3 group of anisole can produce the anisyl radical. The latter may isomerize to form the benzoxyl radical that decomposes to benzene and HCO [48,53,240]. Besides these pathways, benzene can be formed from other primary products from anisole (for instance, methylcyclopentadiene). For instance, the *ipso*-addition of H-atom to phenol and benzaldehyde can also produce benzene [51].

As *ipso*-addition of H to anisole can produce benzene as discussed above, anisole may react via the *ipso*-addition of CH_3 at its methoxy group to form toluene. The barrier for this reaction is about 14.8 kcal/mol which is higher than that of benzene formation (8.17 kcal/mol) which may explain why there is more benzene than toluene in the anisole flames [240]. During the combustion of anisole in flame conditions, toluene can also be produced via the H-addition reaction of the benzyl radical and also from the recombination reaction of the phenyl radical and the methyl radical [53]. In addition to this, the *ipso*-substitution reactions of cresol and phenol might also occur to form toluene [53]. Benzene and cyclopentadiene could act as important precursors for the formation of PAHs. Benzene can undergo H-abstraction followed by phenyl radical addition to form biphenyl. Eventually, biphenyl can lead to the formation of phenanthrene via the HACA mechanism. Naphthalene can be formed by the self-combination of resonance stabilized two cyclopentadienyl radicals [250]. Naphthalene is then a source of resonance stabilized indenyl radicals, which can be involved in the subsequent formation of acenaphthylene by combination with the resonance stabilized propargyl radicals, of indene by combination with the H-atoms, and of phenanthrene by combinations with the cyclopentadienyl radicals [250].

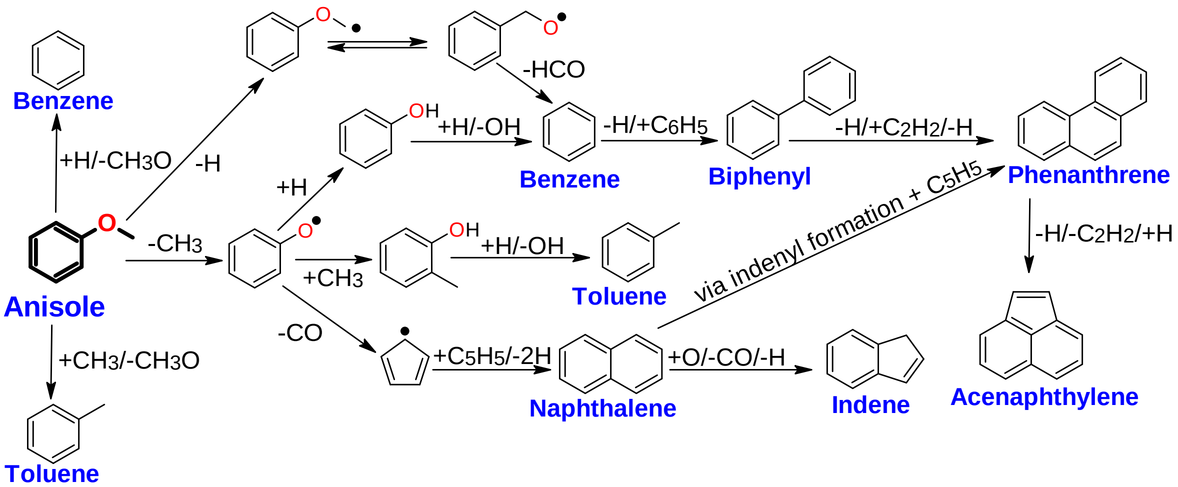

Figure 4. 24 : Some possible pathways for the formation of some selected non-oxygenated aromatics and PAHs via anisole which were experimentally identified and quantified in the present work.

Figure 4. 25 and Figure 4. 26 present a comparison of some selected mole fraction profiles of non-oxygenated aromatics (benzene and toluene) and PAHs with up to three aromatic rings respectively.

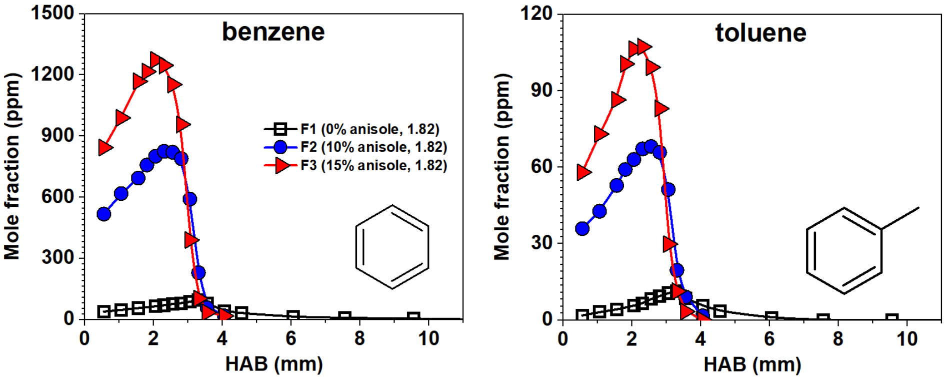

Figure 4. 25 : Comparison of the experimentally determined mole fraction profiles for benzene and toluene formed in flames F1 (0% anisole, ϕ=1.82), F2 (10% anisole, ϕ=1.82), and F3 (15% anisole, ϕ=1.82). Experimental results have been connected by a thin line to guide the eye.

Figure 4. 25 presents a comparison of the mole fraction profiles of benzene and toluene in the three flames F1, F2, and F3. The maximum mole fraction of benzene is around 95 ppm

(HAB=3.3 mm) in F1 and increases by a factor of 8.6 to a value of 825 ppm (HAB=2.5 mm) in F2 and by a factor of 13.4 (HAB=2 mm) to a value of about 1270 ppm in F3. The amount of benzene increases by nearly 13 times with the presence of 15% anisole. Evolution of the mole fraction profiles presented in the figure indicate an early formation of this first aromatic ring occurs in the order F3>F2>F1. As discussed in the previous section, the presence of anisole does not influence the smaller aliphatic species significantly. This indicates that the formation of benzene from anisole may not solely involve the usual mechanism based on C_2 and C_3 species (e.g., C_3H_3+C_3H_3), but it is also formed via more direct pathways from anisole.

It is clearly noticeable from Figure 4. 25 that the production of these aromatics is considerably enhanced in the presence of anisole. Like benzene, there is a remarked increase in the peak mole fraction of toluene as we go from F1 to F3. Also, if we compare the amount of these two species in one flame at a given time, the amount of benzene is around 8.4 times the amount of toluene in F1 and is around 12 times more than the amount of toluene in F2 and F3. The maximum mole fraction of toluene is about 11 ppm (HAB=3.3 mm) in F1, 68 ppm in F2 (HAB=2.5 mm), and around 106 ppm (HAB=2 mm) in F3. It increases by a factor of 10 in the presence of 15% anisole. Figure 4. 26 presents the comparison of the mole fraction profiles for some selected PAHs such as naphthalene, fluorene, acenaphthylene, acenaphthene, and phenanthrene for flames F1, F2 and F3. Peak mole fractions of other PAHs like substituted naphthalenes, biphenyl etc. are listed in Table A. 3 in the Appendices.

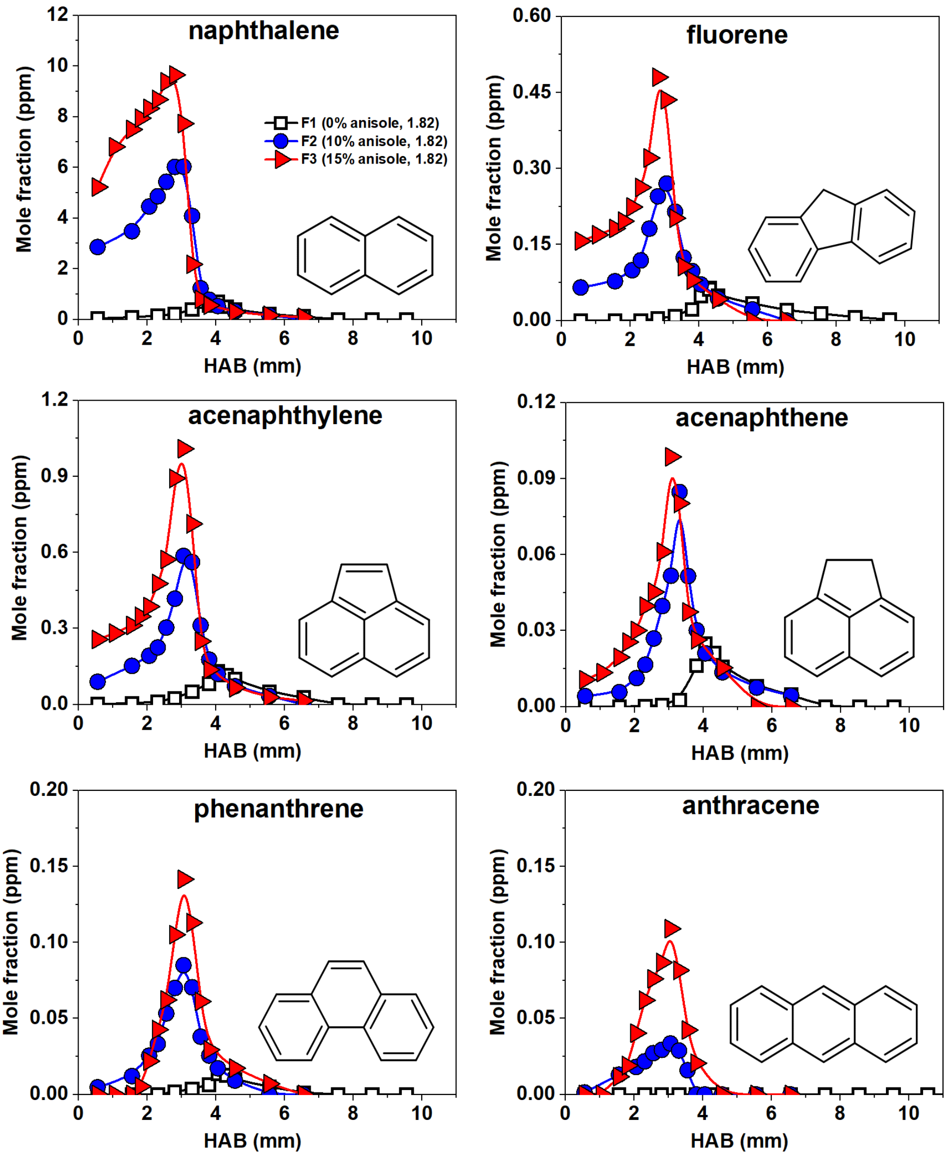

Figure 4. 26 : Comparison of the experimentally determined mole fraction profiles for selected PAHs formed in flames F1 (0% anisole, ϕ=1.82), F2 (10% anisole, ϕ=1.82), and F3 (15% anisole, ϕ=1.82). Experimental results have been connected by a thin line to guide the eye.

As seen in this figure, the peak mole fraction for all PAHs monotonically increases with the addition of anisole. This comparison reinforces the role played by anisole in the production of PAHs as well. Indene (refer to Table A. 3 in the Appendices) and naphthalene are the most abundant PAHs formed in these flames. There is about 0.7 ppm of naphthalene in F1 which increases to a value of 6 ppm in F2 and eventually 10 ppm in F3. This signifies that the presence of 15% anisole increases the amount of naphthalene by 14 times. Since the formation of cyclopentadienyl radicals is enhanced during the combustion of anisole, naphthalene production can be promoted from the self-combination reactions of cyclopentadienyl radical via the $C_{10}H_9$ intermediates besides the conventional pathways [251]. Naphthalene could also be produced via reactions from benzene and toluene whose formation enhanced in the presence of anisole (see Figure 4. 25). Other PAHs are present in smaller amounts as compared to naphthalene (even lesser than 1 ppm). If we see the general trend, acenaphthylene is the most abundant three-ring PAH followed by fluorene. The maximum mole fraction of acenaphthylene in F1 is about 0.13 ppm which increases to a value of 0.58 ppm in F2 and eventually to 1 ppm in F3. Likewise, the maximum mole fraction of fluorene in F1 is about 0.06 ppm which increases to a value of 0.27 ppm in F2 and eventually to 0.48 ppm in F3. Acenaphthylene and fluorene increase by a factor of 7.7 and 8 in the presence of 15% anisole. Similarly, maximum mole fraction of acenaphthene in F1 is about 0.02 ppm which increases to a value of 0.08 ppm in F2 and eventually to 0.1 ppm in F3. Phenanthrene and anthracene also show a similar trend, however, there is slightly more phenanthrene than anthracene in the anisole flames. Phenanthrene increases by 11% in the presence of 15% anisole.

Figure 4. 27 presents the peak mole fractions of different non-oxygenated aromatics with one-, two-, and three-rings. As shown in the figure, the overall trend followed amongst the different species is similar to what was observed earlier in Section 4.2.3. The quantity of the species is decreasing as the number of adjacent benzene rings is increasing. However, it is interesting to note that though the presence of anisole is increasing the peak mole fraction of these species to a somewhat similar extent.

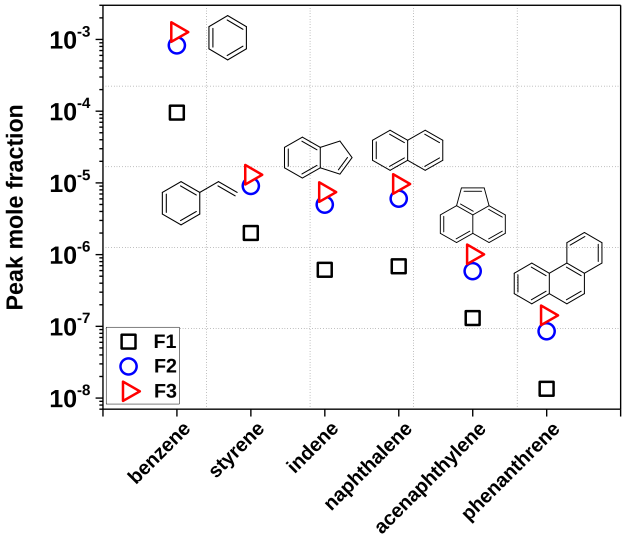

Figure 4. 27 : Peak mole fractions for selected one- to three-ring non-oxygenated aromatics quantified in flames F1 (0% anisole, ϕ=1.82), F2 (10% anisole, ϕ=1.82), and F3 (15% anisole, ϕ=1.82).

4.3.4. Oxygenated aromatics and OPAHs

Besides monoaromatics, dozens of larger oxygenated aromatics up to three rings were identified in this work as discussed in Section 4.1. Together with the identification step, several oxygenated aromatics were quantified in absolute concentrations. Note that no oxygenated aromatics were detectable in the flame F1 (0% anisole), confirming that the detected oxygenated aromatics are mainly produced via reactions from anisole.

Figure 4. 28 presents mole fraction profiles for phenol, benzaldehyde, o/p-cresols, phenyl acetate and m-guaiacol. The amount of these oxygenates increases as the percentage of anisole in the flame is increased. In general, phenol is the most abundant aromatic oxygenate present in anisole flames. The maximum mole fraction value of phenol is about 436 ppm in F2 which increases to a value of about 750 ppm in F3. The amount of phenol has increased by a factor of about 1.7 times with a 5% increase in anisole from F2 to F3. As discussed in Section 4.1.3, phenol can be produced from *ipso*-addition of OH at the methoxy moiety of anisole or via the recombination of H-atom with the phenoxy radical that is formed from dissociation of the weak O-CH_3 bond, which explains why the formation of phenol strongly depends on the added anisole. The maximum mole fraction value of benzaldehyde is about 50 ppm in F2 which increases to a value of about 85 ppm in F3. Like phenol, the amount of benzaldehyde has also increased by a factor of about 1.7 times with a 5% increase in anisole from F2 to F3. Apart from the O-CH_3 bond dissociation pathway, anisole can also decompose via an H-atom abstraction to form the unstable anisyl radical which may quickly isomerize to the benzoxyl radical through a bicyclic intermediate (Section 4.1.3). The β-C-H scission reaction of the benzoxyl radical may act as an important source of benzaldehyde. The H-abstraction from anisole is less favorable than the O-CH_3 dissociation or OH *ipso*-addition [51], which explains why phenol is more abundant than benzaldehyde in the system. Besides phenol and benzaldehyde, o/p-cresols were quantified in important mole fractions. Trace amounts of m-cresol were also identified but could not be quantified. Amongst the two quantified cresol isomers, o-cresol is more than two times more abundant than p-cresol. In flame F2, the maximum amount of o-cresol and p-cresol is around 93 ppm and 34 ppm respectively which increases to a value of 158 ppm and 66 ppm respectively in flame F3. They can be formed produced by methyl addition to the phenoxy radical at the ortho or para position (via a methylcyclohexadienone intermediate). Then, H-migration between the adjacent carbon atoms of the aromatic ring could help in triggering the final H-shift from the carbon to the oxygen atom to produce cresols [48].

Phenyl acetate and m-guaiacol are produced in lower amounts (see Figure 4. 28). These species are also absent in F1 and their maximum amount increases when the amount of anisole in the flame is increased from 10% to 15%. The maximum amount of phenyl acetate increases from about 4 to 6 ppm at 1.5 and 1.25 mm in F2 and F3 respectively. However, as seen in the figure, the maximum amount of m-guaiacol is close to the surface of the burner and it gradually declines as we move away from the burner. Though its quantity is much less significant (less than 1 ppm) in comparison to other monoaromatic oxygenates, it starts to form really early. The OH radicals present may directly attack anisole on its meta position to produce m-guaiacol (Section 4.1.3). It is clear from the resonance structures of anisole that the methoxy group increases the electron density over the o- and p-positions of the ring, which is why attack from radicals like OH would be easier at m-positions as compared to o- and p-positions of the ring. Together with monoaromatic oxygenates, Figure 4. 29 presents OPAHs consisting of two rings formed in these flames. Mole fraction profiles for two-ring OPAHs species namely benzofuran, 2,3-dihydrobenzofuran, 2-ethyl benzofuran, 2-ethenyl benzofuran, 1-indanone and 2-methylinden-1-one have been presented in Figure 4. 29. As mentioned earlier, none of these species were detected in flame F1. Amongst two-ring species, benzofuran is the most abundant diaromatic OPAH.

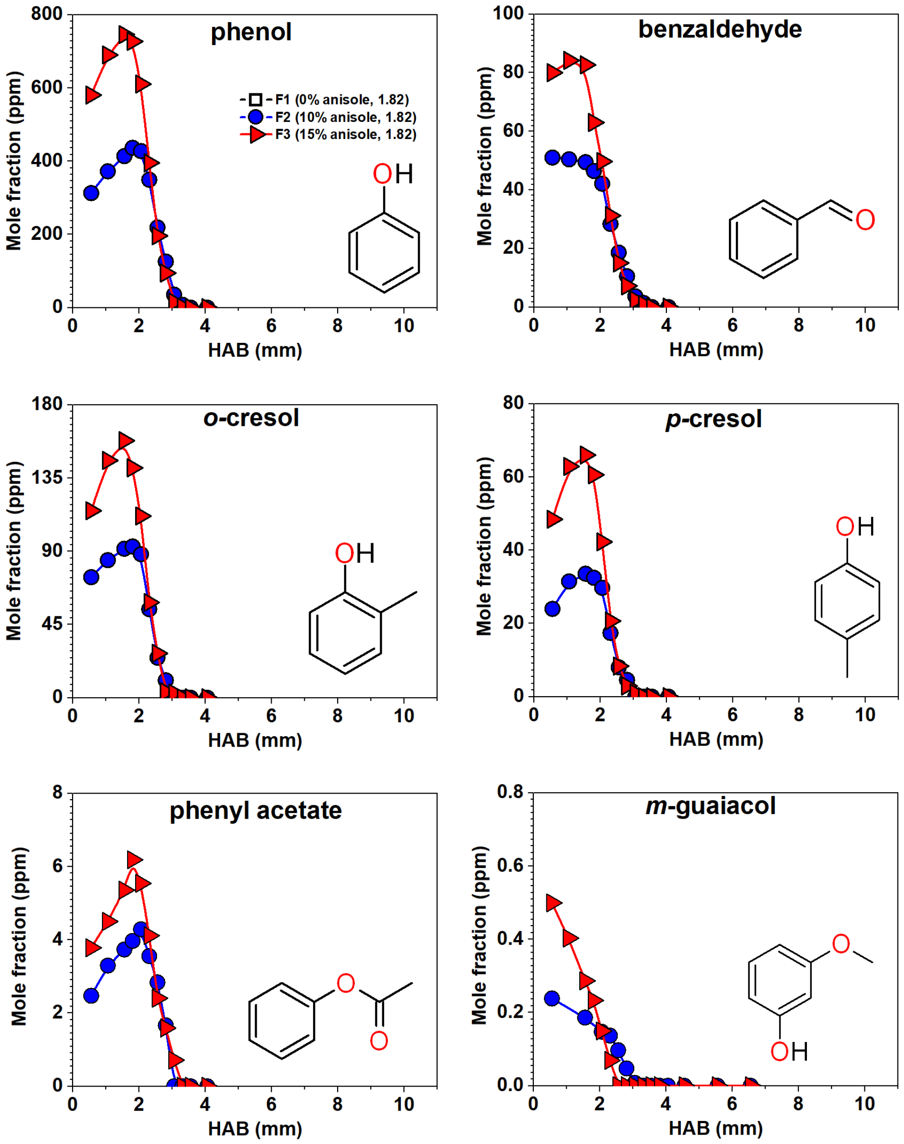

Figure 4. 28 : Comparison of the experimentally determined mole fraction profiles for monoaromatic oxygenates formed in flames F1 (0% anisole, ϕ=1.82), F2 (10% anisole, ϕ=1.82), and F3 (15% anisole, ϕ=1.82). Experimental results have been connected by a thin line to guide the eye. None of these species were present in flame F1 which is why the black points are dismissed.

As shown in Figure 4. 29, the maximum amount of benzofuran produced in the flame increases from 4.5 ppm in flame F2 to 11 ppm in flame F3. The phenoxy radical produced from anisole can react with acetylene and loose an H radical to form benzofuran. Other two-ring OPAHs are present in lesser amounts with respect to benzofuran but the comparison between different flames reinforces the fact that the formation of these species is considerably enhanced when the amount of anisole in the flame is increased.

Mole fraction profiles for 2,3-dihydrobenzofuran presented in Figure 4. 29 indicate that it starts to form prior to the formation of benzofuran. Given the proximity of its profile to the burner, it appears that it originates from reactions involving fuel decomposition. For example, the combination of anisyl and methyl radicals, subsequent hydrogen abstraction, and intramolecular cyclization within the resulting radical could yield 2,3-dihydrobenzofuran. One potential pathway for its formation could involve the abstraction of a hydrogen atom from the methyl group of o-cresol, resulting in the formation of the corresponding radical. This radical may then react with another methyl radical to generate 2-ethyl phenol. Subsequently, 2-ethyl phenol could undergo a hydrogen abstraction reaction to produce 2-ethenyl phenol, which might isomerize to yield 2,3-dihydrobenzofuran. Given the proximity of the mole fraction profile of 2,3-dihydrobenzofuran to the burner, it appears that the former pathway could be more likely than the latter for its formation. Apart from benzofuran and 2,3-dihydrobenzofuran, there are other diaromatic OPAHs like 2-ethyl benzofuran, 2-ethenyl benzofuran, 1-indanone and 2-methylinden-1-one that are present only in anisole flames and their amounts increase with the quantity of anisole in the flames.

Three-rings OPAHs namely dibenzofuran, 9H-xanthene, xanthone, and fluorenol are presented in Figure 4. 30. As mentioned before, these species are quantified for the first time in anisole flames. The general trend is like other PAHs and OPAHs, i.e., the formation of three-ring OPAHs is also evidently enhanced in the presence of anisole. If we observe a general trend, the maximum amount of most of the monoaromatics ranges from hundreds of ppm in anisole flames whereas most of the two-ring aromatic and three rings aromatic OPAHs are present in amounts less than one ppm. Dibenzofuran is the most abundant three ring OPAH. Its maximum mole fraction value was observed close to the surface of the burner and decreases until it completely disappears in the burnt zone. 9H-xanthene and fluorenol also depict similar mole fraction profiles and have their maximum concentrations close to the surface of the burner. Though they consist of three rings, they are formed even prior to the monoaromatic oxygenates. On the other hand, xanthone has a maximum mole fraction value far from the burner. In 2014, Nowakowska et al. [48] reported that trace amounts of xanthone were detected during anisole pyrolysis, however owing to its low concentration, its quantification was not feasible in their work. In this work, xanthone (less than 1 ppm) and other OPAHs (in ppb levels) were quantified. For example, there is about 0.6 ppm of xanthone in F2 and about 0.9 ppm in F3. H-abstraction from the CHO group in benzaldehyde could produce the corresponding radical which may combine with the phenoxy radical followed by an intramolecular rearrangement to produce xanthone.

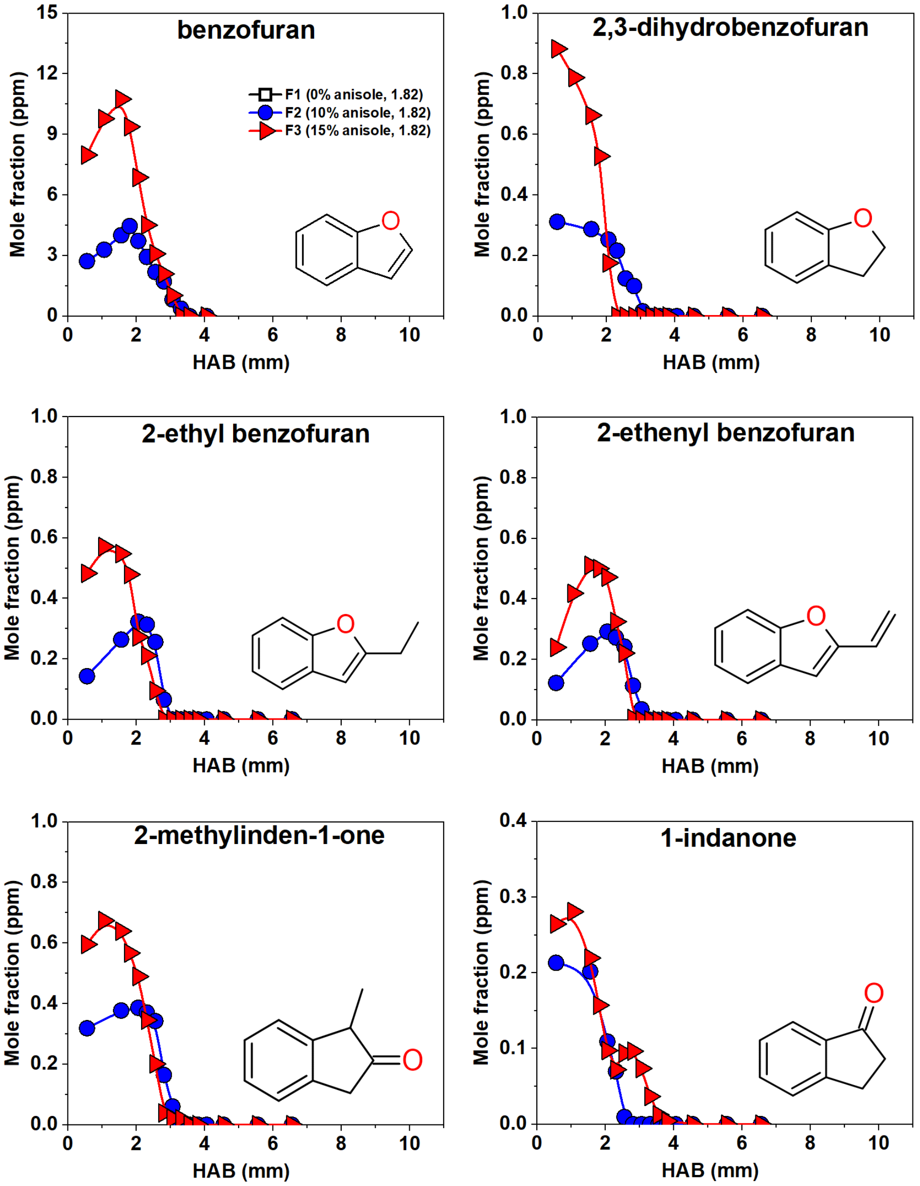

Figure 4. 29 : Comparison of the experimentally determined mole fraction profiles for two ring OPAHs formed in flames F1 (0% anisole, ϕ=1.82), F2 (10% anisole, ϕ=1.82), and F3 (15% anisole, ϕ=1.82). Experimental results have been connected by a thin line to guide the eye. None of these species were present in flame F1 which is why the black points are dismissed.

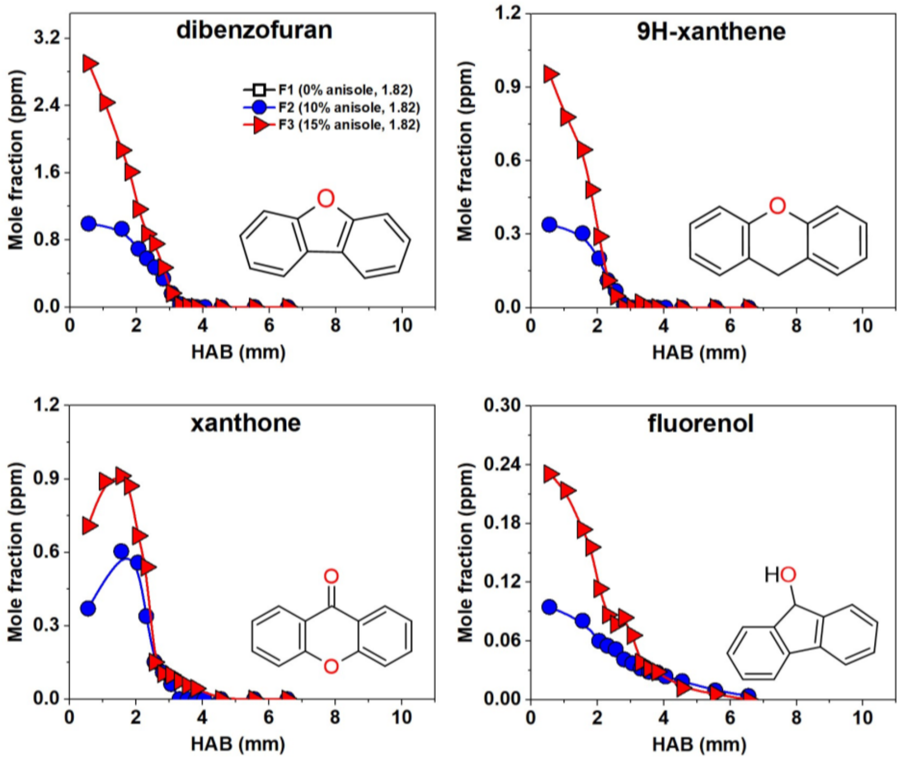

Figure 4. 30 : Comparison of the experimentally determined mole fraction profiles for three ring OPAHs formed in flames F1 (0% anisole, ϕ=1.82), F2 (10% anisole, ϕ=1.82), and F3 (15% anisole, ϕ=1.82). Experimental results have been connected by a thin line to guide the eye. None of these species were present in flame F1 which is why the black points are dismissed.

The phenoxy radicals produced via anisole could undergo self-combination reactions to form dibenzo-p-dioxin or may combine with another benzyl radical followed by an intramolecular rearrangement to form xanthene (see Section 4.1.3). It must be noted that a comparison between the oxygenated and the non-oxygenated species as performed earlier in Figure 4. 19 is not possible for this series of flames as certain OPAHs are formed really close to the burner surface. This is why the peak mole fraction values for such species cannot be retrieved.

4.4. Conclusion

This chapter presented the qualitative and quantitative results concerning the stable intermediate species formed in anisole flames with a special focus on aromatics. Section 4.1 comprised of a list of the oxygenated aromatics that were identified in this work with a brief reminder of the approach followed to do so. Analysis on the kinetic formation for some relevant oxygenated aromatics was also featured using the qualitative analysis of the experimental evidences and literature studies. Later, the subsequent sections presented the quantitative results. Section 4.2 presented the effect of change in equivalence ratio on the evolution of mole fraction profiles while the quantity of anisole was kept constant whereas Section 4.3 presented the influence of addition of anisole on the evolution of mole fraction profiles at constant equivalence ratio.

Nearly seventy-five species are quantified in this work. Results indicate that the presence of anisole shows less influence on smaller aliphatic species but significantly promotes the formation of OPAHs as well as PAHs. The formation of the phenoxy radical from anisole facilitates the formation of aromatics, several out of which are reported for the first time in this thesis. These species are hazardous to human health and their poisoning can be fatal. Diverse range of concentrations and species with a variety of functional groups were detected and quantified from a very complex mixture containing aromatics. Not just aromatics, smaller hydrocarbon species like 1-butyne, cyclopentadiene formation is also promoted which are potential precursors of higher aromatics. Comparison results indicate that the formation of OPAHs occurs prior to the formation of PAHs. Though one- and two-ring non-oxygenated species are more abundant than one- and two-ring oxygenated aromatics, the inverse is true for three-ring aromatics. It is interesting to note that oxygenated species in general constitute an important set of species produced from anisole. Increase in the number of rings of PAHs seems to happen successively with respect to the flame height, whereas the same is not true for OPAHs. Most of the OPAHs (even with three-rings) are formed very close to the burner surface.

Chapter 5. Influence of biofuel structure: comparison of anisole with ethanol and DMF

Results presented so far are limited to anisole flames. In this chapter, a comparison of anisole with other selected biofuels is presented. Experimentally observed differences in aromatics and other gaseous pollutants were reviewed and discussed. Note that the influence of these biofuels on particulate-phase pollutants will be discussed later (Chapter 6). In general, the tendency of a particular fuel to form pollutants in flames depends on its characteristics (for instance its structure) as well as the operating conditions. As mentioned in Chapter 1, ethanol has become the commercial fuel in most of the countries because of its suitable properties [252]. In addition to ethanol, DMF is another potential 2nd generation biofuel that has been a target of recent investigations [144]. Considering their potential to facilitate the transition towards a more sustainable transportation sector, substantial interest is devoted to study these biofuels (see Chapter 1). In this chapter, we have performed another study to compare anisole (emerging biofuel) with these biofuels.

Two separate cases have been chosen to showcase this comparison and are presented as two sections in this chapter. Section 5.1 comprises of a comparison study of anisole with ethanol and is featured as Case 1. Section 5.2 presents a second comparison study of anisole with DMF and is featured as Case 2. Experimental findings from results presented in these sections in conjunction with pertinent studies from the literature allowed us to explain the differences between flames with different biofuels. Sections 5.1 and 5.2 further consist of several subsections where different types of stable species have been categorized as: major reactants and products, lighter hydrocarbon intermediates, small oxygenated species, and aromatics.

5.1. Case 1: anisole and ethanol

This section presents the comparison results for Case 1, comprising flame F1 (0% biofuel, ϕ=1.82), F2 (10% anisole, ϕ=1.82) and F6 (10% ethanol, ϕ=1.82). Flame F1 has iso-octane/CH_4 and no biofuel and thus is a reference flame for this comparison study. Flame F2 is doped with 10% anisole whereas flame F6 is doped with 10% ethanol. The three flames are stabilized at an equivalence ratio of 1.82. A summary of flame conditions chosen for this comparison is presented in Table 5. 1 and their real photographs of the flames with the same camera settings is shown in Figure 5. 1.

Table 5. 1 : Summary of the flame conditions to study the effect of the structure of the biofuel for Case 1: anisole v/s ethanol; the percentage of biofuel in the total fuel mixture and the equivalence ratio are constant; Here L_n =normal liters per minute.

Flame	**Biofuel (%)**	**Gaseous flow rates (L_n/min)**						**Equivalence ratio**	**C/O**
		Biofuel	C_8H_{18}	CH_4	O_2	N_2	Total		
F1	-	-	0.18	0.925	2.25	6.50	9.85	1.82	0.52
F2	Anisole (10)	0.102	0.15	0.766	2.338	6.50	9.85	1.82	0.56
F6	Ethanol (10)	0.112	0.164	0.843	2.236	6.50	9.85	1.82	0.52

Figure 5. 1: Photographs of premixed flames: F1 (no biofuel, ϕ=1.82), F2 (10% anisole, ϕ=1.82), and F6 (10% ethanol, ϕ=1.82) presenting their visual aspect (with the same camera settings).

5.1.1. Major species

Figure 5. 2 presents the comparison of the consumption of the reactants: biofuel (anisole and ethanol), iso-octane, methane, oxygen and of the formation of two of major end products: carbon dioxide and carbon monoxide. Broadly, flames with oxygenated biofuels (F2 and F6) are closer to the burner than flame F1 where there is no biofuel. As seen in Figure 5. 2, the consumption profiles for iso-octane, methane, and oxygen are very similar for the anisole and the ethanol flame. On the contrary, for the biofuel itself, anisole appears to be consumed a little more quickly than ethanol. Also, there is an enhanced formation of CO and CO_2 in anisole flame as compared to the ethanol flame and this increase is more pronounced for CO than CO_2. These observations could be explained if we review the initial decomposition pathways for the two biofuels. As discussed earlier, anisole can readily decompose to generate the phenoxy radical because of the very low bond dissociation energy of the O-CH_3 bond (63.2 kcal/mol). This bond dissociation energy is much lower than the weakest bond in ethanol (C-C bond) for which the bond dissociation energy is nearly 87.2 kcal/mol [152]. Owing to the low energy barrier for the initial decomposition pathway in comparison to ethanol, anisole can quickly generate the phenoxy radical which may subsequently loose a CO molecule to produce the cyclopentadienyl radical [48]. This could explain why anisole is consumed much rapidly as compared to ethanol as well as why there is more CO close to the burner surface in anisole flame than the ethanol flame. These initial reaction pathways could dictate the behavior of the products close to the

surface of the burner whereas the slightly higher C/O ratio (see Table 5. 1) could explain the 20% increase in the mole fraction of CO in the burnt gas region for the anisole flame.

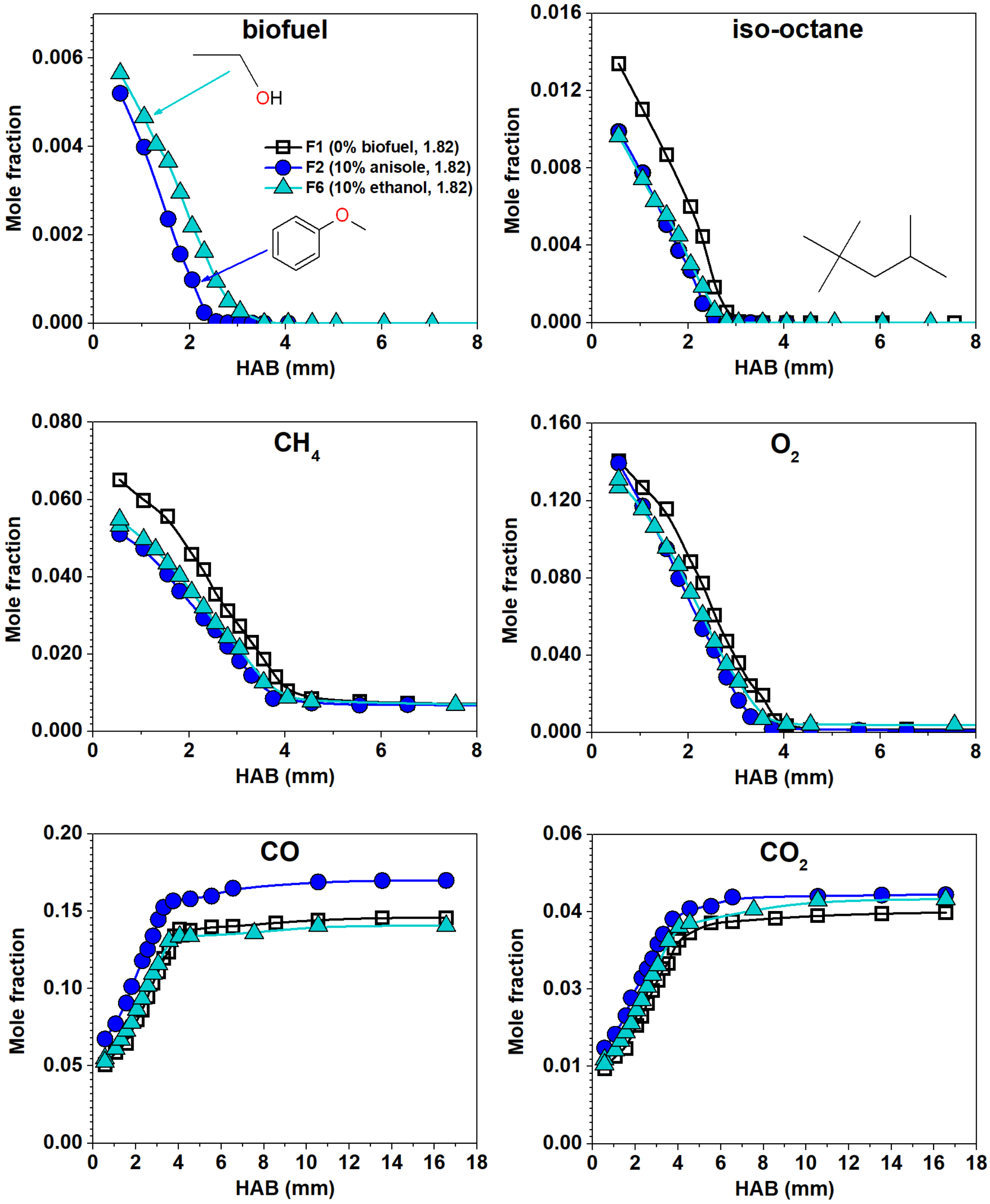

Figure 5. 2: Comparison of the consumption of the reactants and the major end products in the three flames: F1 (no biofuel, ϕ=1.82), F2 (10% anisole, ϕ=1.82), and F6 (10% ethanol, ϕ=1.82). Experimental results have been connected by a thin line to guide the eye.

5.1.2. Comparison of intermediate species: C_1-C_4

As already discussed in the Chapter 4 (Section 4.2.2), lighter hydrocarbons can act as reactants in most of the proposed aromatics formation pathways. This section is devoted to study some selected intermediates formed in these flames.

The first panel in Figure 5. 3 presents on overview of the of the peak mole fraction of some C_1-C_4 aliphatic intermediate species: acetylene (C_2H_2), ethylene (C_2H_4), propene (C_3H_6), allene (aC_3H_4), 1,3-butadiene ($1,3C_4H_6$), vinylacetylene (C_4H_4), formaldehyde (HCHO), acetaldehyde (CH_3CHO), acrolein (C_3H_4O), and acetone (CH_3COCH_3) in the form of a bar graph. The second panel in Figure 5. 3 presents the evolution of the mole fraction of some selected species amongst those presented in the first panel. Peak mole fractions of other stable intermediates formed in these flames are presented in Table A. 3 in the Appendices. The figure shows that C_1-C_3 species were detected with only slight differences between the three flames. Anisole produces nearly 16% more acetylene than produced in the ethanol flame. Ethylene formation on the other hand is lower by about 4% in anisole flame (~3260 ppm) as compared to the ethanol flame (~3390 ppm). The peak mole fraction of allene reduces by nearly 17% with the presence of ethanol with respect to the anisole flame. Two important C_4 species i.e., 1,3-butadiene (C_4H_6), and vinyl acetylene (C_4H_4) are also presented. Anisole addition promotes the formation of 1,3-butadiene by 28% and vinyl acetylene by 20%, while ethanol addition does not influence these species with respect to the reference flame. As observed from the figure and the discussion in the previous text, the formation of most of these soot precursors is suppressed in the presence of ethanol.

According to the studies performed in flame conditions, it is well known that propene (C_3H_6) can be formed via ethylene (C_2H_4), directly or through the formation of the C_2H_3 radical [61]. Acetylene (C_2H_2) is also formed via the formation of the C_2H_3 radical. Propyne (pC_3H_4) comes mainly from C_2H_2, directly or via the formation of the propargyl radical (C_3H_3). Allene (aC_3H_4) is the main product of propene decomposition via the formation of a resonantly-stabilized allyl radical (C_3H_5) [61]. Consequently, since the amount of acetylene produced is somewhat reduced in the presence of ethanol, quantities of other species that are formed via acetylene are also suppressed. It is interesting to note that though anisole is an aromatic fuel, it is promoting the formation of small aliphatic species as well. Similar effect is observed for other species like cyclopentadiene for which the peak mole fraction in the different flames is listed in Table A. 3 in the Appendices.

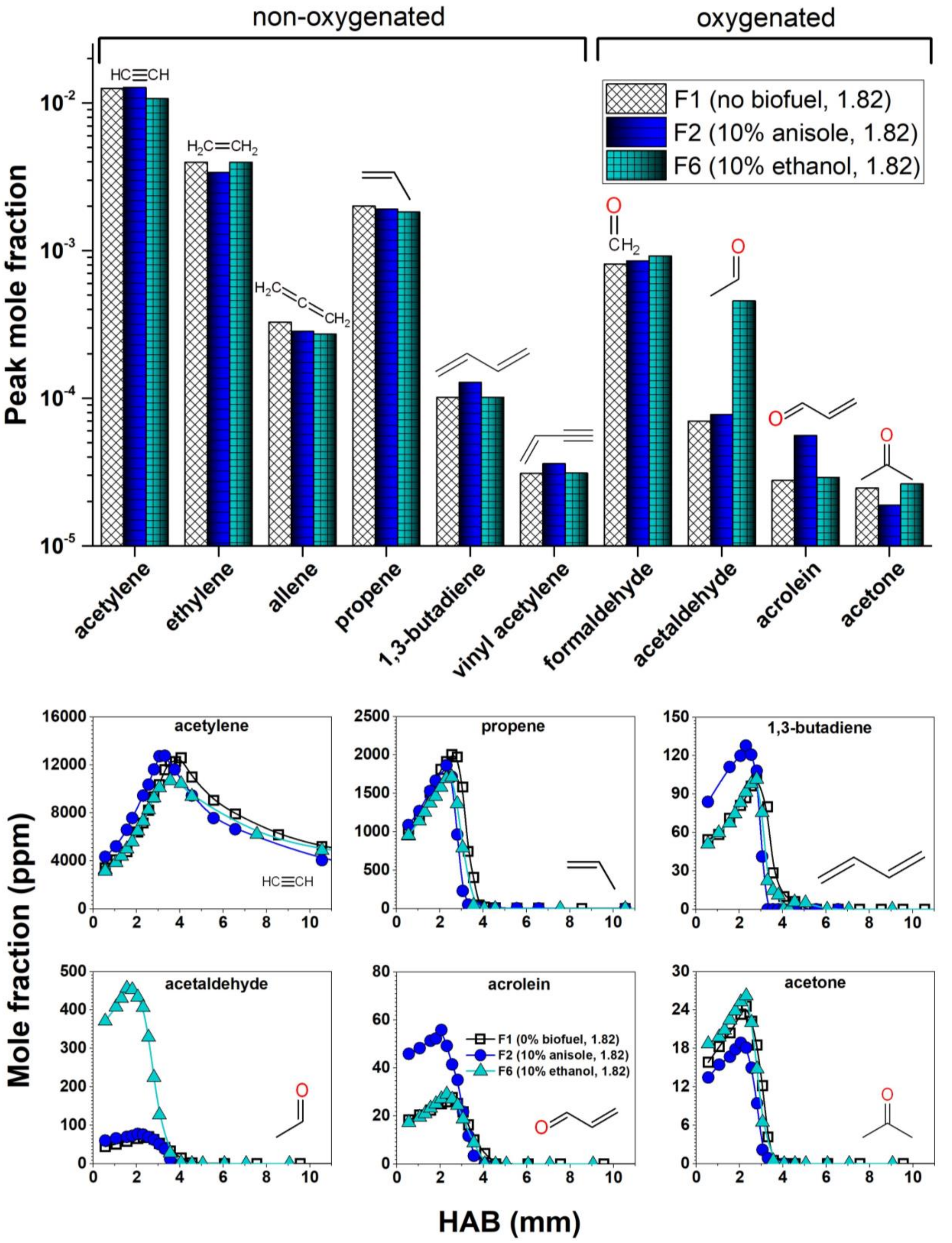

Figure 5. 3: The first panel comprises a bar graph presentation of the peak mole fractions for selected small oxygenated and non-oxygenated aliphatic species; the second panel presents a comparison of the evolution of the mole fraction profiles for the three flames: F1 (no biofuel, ϕ=1.82), F2 (10% anisole, ϕ=1.82), and F6 (10% ethanol, ϕ=1.82); In the second panel, experimental results have been connected by a thin line to guide the eye.

In addition to aliphatic hydrocarbons, some small oxygenated species were detected in these flames. Some of these species are highly toxic. Other than formaldehyde, the difference between the peak mole fractions of oxygenated species amongst ethanol and anisole flames is evident. As seen in the figure, ethanol causes a small increase the formation of formaldehyde by 14% as compared to the anisole and the reference flame. The peak mole fraction of acetaldehyde increases by a factor of more than 6 in the presence of ethanol as compared to the anisole flame. In 2006, Ergut et al. [234] performed a study on 1-D premixed fuel-rich atmospheric ethanol flames and investigated reaction pathway analysis for some dominant pathways. According to their study, hydrogen abstraction with H and OH from the ethanol molecule could lead to the formation of CH_2CH_2OH, CH_3CHOH and CH_3CH_2O and these reactions are the most dominant consumption for ethanol. The α-hydroxyethyl radical (CH_3CHOH), in turn, can react mainly by oxidation followed by the β-scission of the O–H bond to form acetaldehyde [152,253]. This pathway could explain why the amount of acetaldehyde is considerably increased in the presence of ethanol as a biofuel. Acrolein and acetone are other important oxygenated compounds that are formed in these flames even though their quantities are less significant in comparison to formaldehyde and acetaldehyde. Higher amounts (almost by a factor of 2) of acrolein produced in anisole flame, whereas its amount is somewhat similar in the ethanol and the reference flame. Anisole on the other hand reduces the formation of acetone by 30% as compared to the ethanol and the reference flame.

5.1.3. Comparison of single ring aromatics and PAHs

The first panel in Figure 5. 4 presents on overview of the of the peak mole fraction of some non-oxygenated aromatic species: benzene (C_6H_6), toluene (C_7H_8), indene (C_9H_8), naphthalene ($C_{10}H_8$), acenaphthylene ($C_{12}H_8$), acenaphthene ($C_{12}H_{10}$), and fluorene ($C_{13}H_{10}$). The second panel in Figure 5. 4 presents the evolution of the mole fraction with respect to the flame height for some selected PAHs amongst the those already presented the first panel. The plots presented in the second panel of Figure 5. 4, consist of a primary as well as a secondary vertical axis. Because of a significant difference in mole fraction between the flames, the primary axis represents the scale for flames F1 and F6 while the secondary axis solely represents the mole fraction for flame F2. From the figure, it is clearly noticeable that the production of these aromatics is considerably enhanced in anisole flame as compared to the ethanol flame. The addition of ethanol reduces slightly the mole fractions of aromatics as compared to the reference flame. The peak mole fraction of benzene increases by more than 10 times in the anisole flame as compared to the ethanol flame.

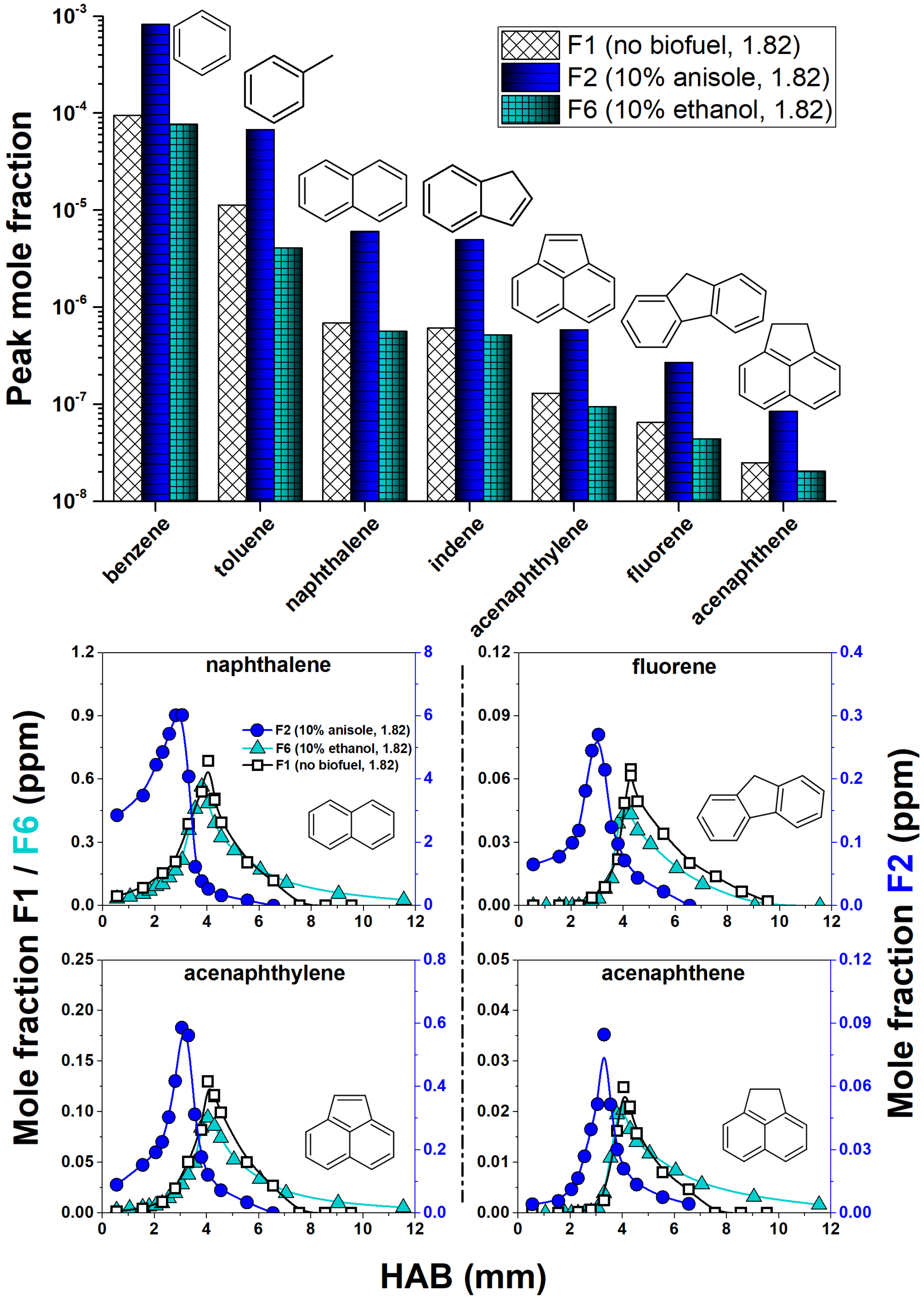

Figure 5. 4 : The first panel comprises a bar graph presentation of the peak mole fractions for non-oxygenated aromatics; the second panel presents a comparison of the evolution of the mole fraction profiles for these species in the three flames: F1 (no biofuel, ϕ=1.82), F2 (10% anisole, ϕ=1.82), and F6 (10% ethanol, ϕ=1.82); In the second panel, experimental results have been connected by a thin line to guide the eye.

Similar behavior is observed for toluene. The peak mole fraction of toluene is about 17 times more in the anisole flame (~68 ppm) than in the ethanol flame (~4 ppm). If we observe the second panel, it is worth noticing that the formation of these species in the ethanol flame and flame F1 is more gradual (3-3.3 mm) contrary to the progression in their amounts in anisole flame which is very steep and the maximum mole fraction is attained quicker at nearly 2.5 mm. Besides formation, the decomposition of these species is much rapid in the case of anisole contrary to a very gradual decay in the ethanol flame.

It is well established in the literature that there is no single reaction pathway that produces benzene in all flames [61]. Most frequently-cited formation reactions for benzene via smaller aliphatic species were outlined in Chapter 4 (Section 4.2.2). The brief survey mentioned in this section demonstrated that benzene could be formed by a wide variety of precursors. As a matter of fact, it was seen that every possible size combination (C_3 and C_3, C_4 and C_2, C_5 and C_1, and C_6) could contribute to the formation of benzene. Veritably, the fuel structure can possess a strong influence on the benzene formation mechanisms in any given flame, especially in the case of larger fuels which might decompose to a broad range of products. Thus, the dominant pathways may vary with fuel structure, composition, and the operating conditions. Assuming that the contribution of iso-octane in the formation of aromatics would be quite similar, it is relevant to study the contribution from each of the individual biofuels. During ethanol decomposition, the dominant pathways leading to benzene formation would involve lighter hydrocarbons. Together with a fraction of iso-octane replacement with ethanol and then the slightly restrained formation of these species in the presence of ethanol leads to subsequent reduced benzene formation. Several studies in the literature [47,151,154–156,253,254] have also confirmed this trend and reported that the concentration of benzene and other soot precursors decreases with an increase in the proportion of ethanol blended with different hydrocarbon fuels. On the other hand, the formation of benzene in the anisole flame does not solely involve the usual mechanism based on the lighter aliphatic species but, other possible pathways exist, especially the *ipso*-addition of an H-atom at the methoxy moiety of anisole, as previously discussed which can significantly contribute to the formation of benzene (see Chapter 4). This explains why anisole produces benzene to such a noteworthy extent as compared to ethanol. An analogous explanation can be applied for the influence of the added biofuels to toluene formation.

For PAHs as well, it is evident that the peak mole fraction values increase in anisole flame as compared to the ethanol flame. It is well recognized in the literature that larger aromatics are formed by the growth of additional benzenoid rings to the first ring formed (benzene), and not by decomposition of the fuel structure to non-aromatic/aliphatic fragments followed by synthesis of completely new rings [255]. As detailed in Chapter 4, anisole heavily promotes the formation of PAHs as the relatively slow step of creating the initial ring i.e., benzene is hastened by other possible pathways which are more favorable due to low barriers. This is not the case for ethanol flame as explained previously.

Richter and co-workers [69,256] performed a detailed study of naphthalene formation in premixed benzene flames and concluded that the cyclopentadienyl self-reaction is the main naphthalene formation pathway for benzene flames with an equivalence ratio of 1.80. As discussed previously, during the decomposition of anisole, the phenoxy radical produced can lose a CO molecule to generate cyclopentadienyl radicals. These radicals are resonantly stabilized and may undergo a self-combination reaction to form naphthalene. There is about 6 ppm in flame F2 with the presence of anisole. Anisole increases naphthalene by nearly 12 times with respect to the ethanol flame.

The peak mole fraction of acenaphthylene increases by more than 6 times in the anisole flame with respect to the ethanol flame. Other three-ring PAHs like acenaphthene and fluorene seem to present a similar behavior. After the formation of naphthalene, the fuel-independent HACA mechanism can promote further growth to form PAHs with more than two rings according to Frenklach et al. [247]. Figure 5. 5 presents an example of how species with three rings can be formed with naphthalene as a precursor.

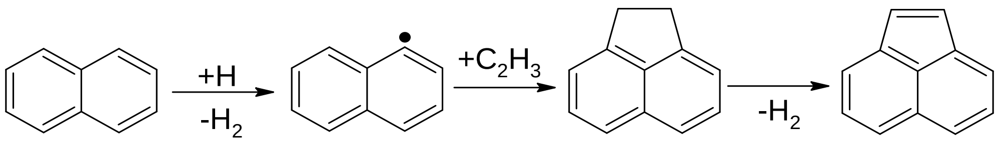

Figure 5. 5 : Reaction pathway followed to produce acenaphthene and acenaphthene via the naphthyl radical from naphthalene [257].

Since naphthalene is an important precursor of higher PAHs, it’s concentration in the flame would dictate the quantity of higher PAHs as well. Consequently, formation of other three ring PAHs is also enhanced in the presence of anisole contrary to a slight decline in their formation in the presence of ethanol. Later, addition of acetylene to an aromatic radical can lead to the formation of higher aromatics like naphthalene or PAHs with three-rings. In the ethanol flame, species like C_2H_2 (acetylene), C_3H_3 (propargyl radical), C_3H_5 (allyl radical), and C_6H_6 (benzene) are of particular importance for the formation of PAHs. The smaller aliphatic species would gradually first lead to the formation of the first ring. This way the number of steps necessary to generate the first ring and eventually PAHs would increase contrary to the flame of anisole. This could also explain the shape of the PAHs mole fraction profiles. It can be seen in Figure 5. 4 that the PAHs are formed beforehand in the anisole flame in comparison to the ethanol flame. Similarly, their decomposition is pretty slower in the ethanol flame.

Section 5.1 provides an overall comparative study between anisole and ethanol by focusing especially on soot precursors, for example acetylene, 1,3-butadiene, benzene etc. and toxic oxygenated compounds such as formaldehyde, acetaldehyde, and acrolein. Ethanol reduces the formation of soot precursors whereas anisole exerts an opposite trend by promoting their formation by significant factors. Note that we did not observe any oxygenated aromatics in ethanol doped flame, while numerous OPAHs were reported in anisole doped flames as presented in Chapter 4 previously. Needless to say, the discussion in this section is only limited to small soot precursors, toxic oxygenated species and non-oxygenated aromatic species only.

5.2. Case 2: anisole and dimethylfuran

In this section, we present a comparison study of the mole fraction profiles for two flames, i.e., flame F7 (DMF/iso-octane/CH_4/O_2/N_2) and flame F5 (anisole/iso-octane/CH_4/O_2/N_2). Both flames exhibit the same equivalence ratio of 1.90. The summary of flame conditions chosen for this purpose has been summarized in Table 5. 2 and the real photographs for these flames with the same camera settings are shown in Figure 5. 6. As can be seen from the figure, these flames were really bright and luminous.

Table 5. 2 : Summary of the flame conditions to study the effect of the structure of the biofuel for Case 2: anisole and DMF; the percentage of biofuel in the total fuel mixture and the equivalence ratio is constant. Here L_n represents normal liters per minute.

Flame	*Biofuel (%)*	*Gaseous flow rates (L_n/min)*						*Equivalence ratio*	*C/O*
		Biofuel	C_8H_{18}	CH_4	O_2	N_2	Total		
F5	Anisole (10)	0.105	0.15	0.788	2.308	6.50	9.85	1.90	0.58
F7	DMF (10)	0.106	0.156	0.801	2.291	6.50	9.85	1.90	0.57

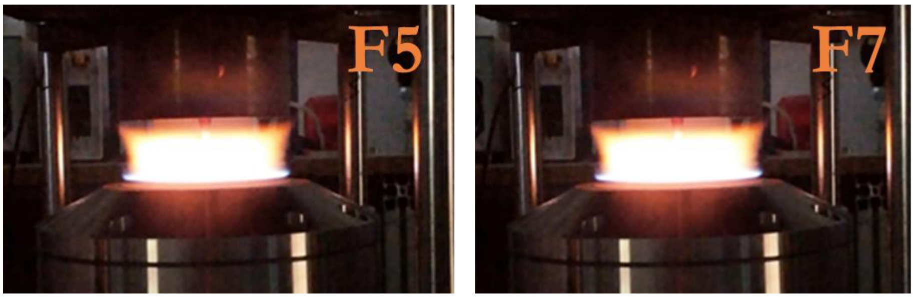

Figure 5. 6 : Photographs of premixed flames: F5 (10% anisole, ϕ=1.90), and F7 (10% DMF, ϕ=1.90) presenting their visual aspect (with the same camera settings).

5.2.1. Major species

Figure 5. 7 presents the comparison of the consumption of the reactants: biofuel (DMF and anisole), iso-octane, methane oxidant (oxygen) as well as the major end products such as CO and CO_2.

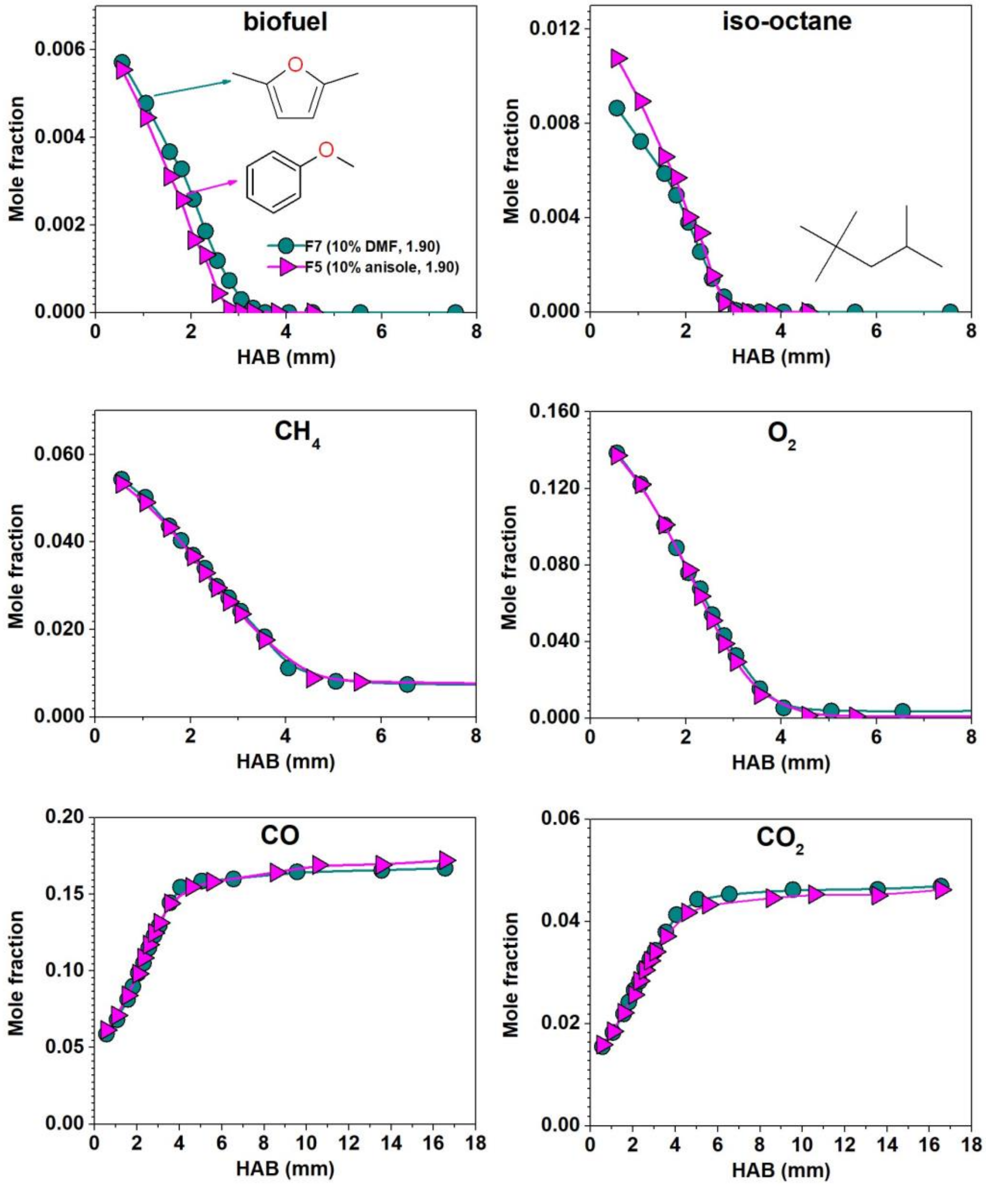

Figure 5. 7: Comparison of the evolution of the mole fraction of the reactants and principal products in flames F5 (10% anisole, ϕ=1.90), and F7 (10% DMF, ϕ=1.90). Experimental results have been connected by a thin line to guide the eye.

From the figure, it is perceivable that the consumption profiles for methane and oxygen and the formation profiles for the end products are almost indistinguishable. However, for the biofuel itself, anisole is consumed much rapidly than DMF. The lowest bond dissociation energy in case of anisole is 63.2 kcal/mol which is much lower than the lowest bond dissociation energy (C-H bond of the methyl group) in case of DMF i.e., 85.5 kcal/mol. This could explain the swift consumption of anisole with respect to DMF.

5.2.2. Comparison of species: C_2-C_5

Figure 5. 8 presents the peak mole fraction of some of the important C_2-C_5 intermediate species together with the mole fraction profiles of some selected species. Peak mole fractions other intermediate species formed in these flames are presented in listed in Table A. 3 in the Appendices. In the figure, the peak mole fraction is presented for acetylene (C_2H_2), ethylene (C_2H_4), propene (C_3H_6), allene (aC_3H_4), 1,3-butadiene ($1,3C_4H_6$), and vinyl acetylene (C_4H_4), formaldehyde (HCHO), acetaldehyde (CH_3CHO), propanal (C_3H_6O), acetone (C_3H_6O), furan (C_4H_4O) and 2-methyl furan (MF, C_5H_6O).

In general, it is intriguing to note that like major species, the mole fraction of C_2-C_3 non-oxygenated species is virtually identical between the two flames, while C_4 and oxygenated species were measured in (slightly or significantly) higher mole fraction in the DMF doped flame (Figure 5. 8). This indicates that reaction pathways forming these species could be one of the primary reactions for DMF decomposition. Exemplary discussions on the formation of these species are presented in the following text.

As demonstrated in Figure 5. 9, H-addition on DMF followed by ring opening and subsequent rearrangements of the initial adduct stabilized by resonance lead to the formation of 1,3-butadiene ($1,3C_4H_6$) and the acetyl radical (CH_3CO). H-addition reaction was found to be an important reaction class in high temperature combustion of DMF [258,259] This reaction pathway could explain why 1,3-butadiene was detected in high amounts in the DMF doped flame. 1,3-butadiene in turn can react via H-abstractions followed by C-H β scission to form vinyl acetylene. The latter can be also partially produced directly from the isomerization of DMF to hexa-3,4-dien-2-one followed by the C–C bond scission to give the CH_3CO and buta-1,2-dien-1-yl (C_4H_5, stabilized by resonance) radicals that would decompose to give hydrogen atom and vinyl acetylene by β-scission of the C–H bond [153].

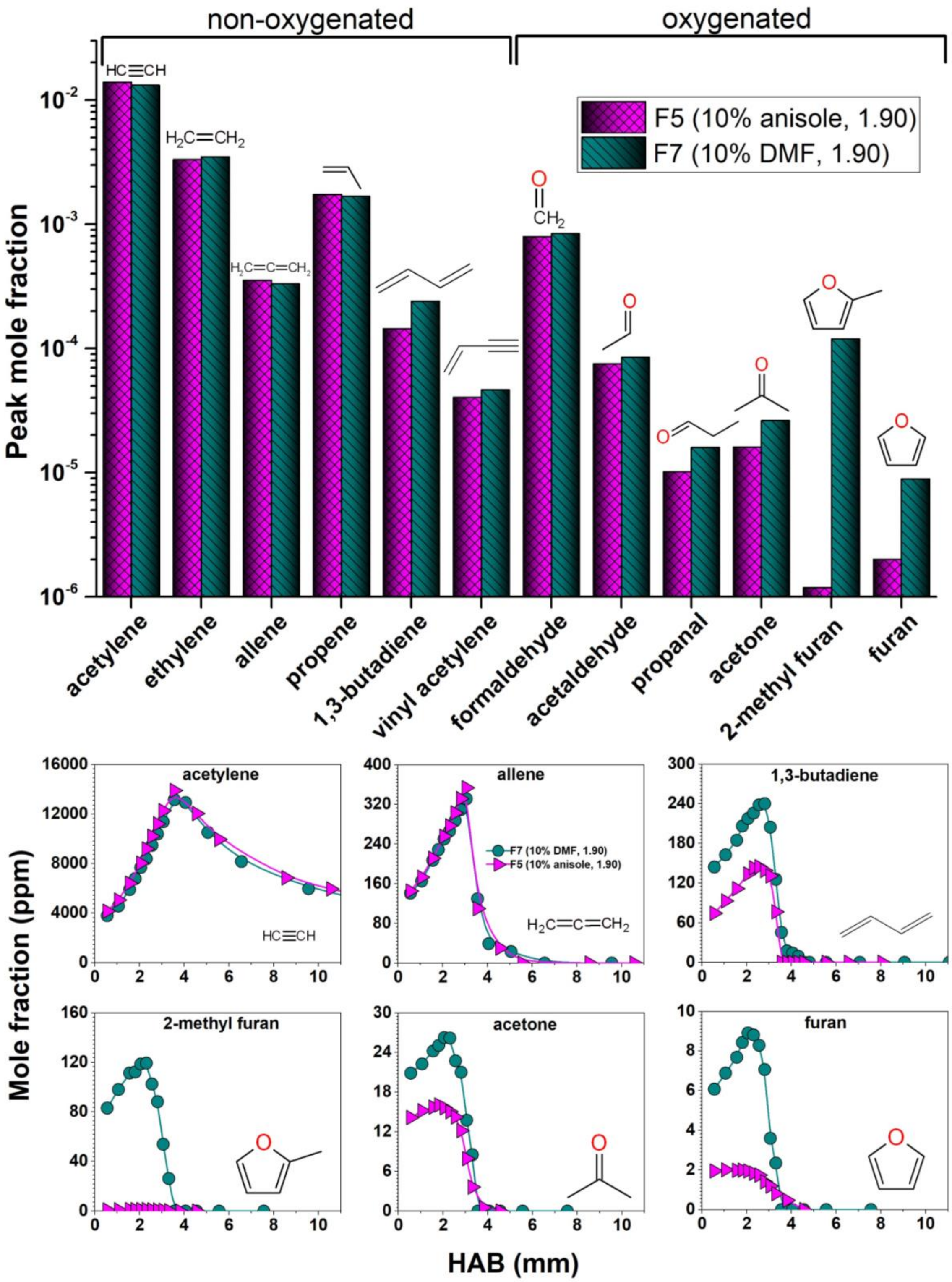

Figure 5. 8 : The first panel comprises a bar graph presentation of the peak mole fractions for selected small oxygenated and non-oxygenated aliphatic species; the second panel presents a comparison of the evolution of some selected mole fraction profiles for the two flames: F5 (10% anisole, ϕ=1.90), and F7 (10% DMF, ϕ=1.90); In the second panel, experimental results have been connected by a thin line to guide the eye.

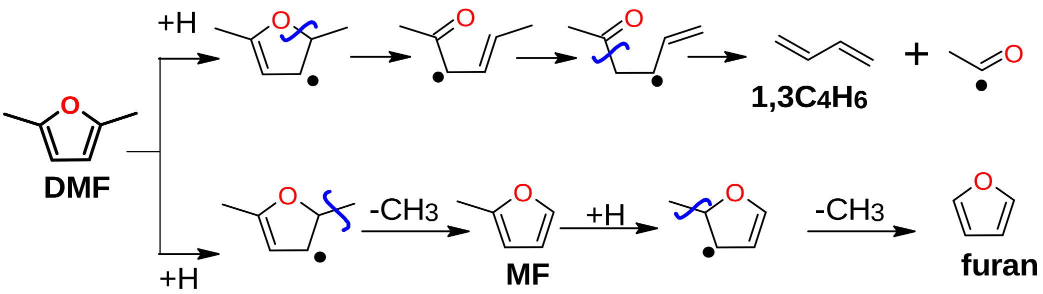

Figure 5. 9 : Addition of H atom on DMF leading to the formation of 1,3C4H6, MF, and furan, based on studies reported by Togbé et al. [258] and Sirjean et al. [259].

Apparently, the formation of small oxygenated species is slightly more enhanced in the presence of DMF than in the presence of anisole. Formaldehyde formation is marginally promoted in the DMF flame in comparison to the anisole flame. The peak mole fraction of formaldehyde in flame F5 is nearly 796 ppm and increases to a value of 850 ppm (by 6%) in flame F7. Likewise, the amount of acetaldehyde produced in flame F7 (115 ppm) is about 1.5 times more than it is produced in flame F5 (75 ppm). In the same fashion, formation of acetone and propanal is also promoted in flame F7 than in flame F5. The addition of the hydroxyl radical to a DMF molecule can generate acetaldehyde (CH_3CHO), acetylene (C_2H_2) and the CH_3CO radical. There is roundly 10 ppm of propanal and 16 ppm of acetone in F5 which increase to a value of 16 ppm and 26 ppm respectively in F7. Their amounts increase by 62% and 60% respectively in the presence of DMF.

In parallel with small oxygenated compounds, cyclic ethers such as furan and 2-methyl furan were also produced. Amongst these two, 2-methyl furan is a much more abundant species than furan for flame F7. However, the opposite is the case for flame F5. The peak mole fraction of 2-methyl furan in flame F5 is about 1.2 ppm which increases to a value of 120 ppm in flame F7. On the other hand, the amount of furan in flame F5 is nearly 2 ppm which increases to a value of 9 ppm in flame F7. As shown in Figure 5. 9, the *ipso*-addition of the hydrogen atom on DMF leads to the formation of the methyl radical and 2-methyl furan [153]. The latter leads to the formation of furan following the same reaction mechanism.

5.2.3. Comparison of aromatics

This section is devoted to the formation of aromatic species in the two flames. Figure 5. 10 and Figure 5. 11 present some selected non-oxygenated and oxygenated aromatics respectively. Figure 5. 10 presents a comparison of peak mole fraction for benzene (C_6H_6), toluene (C_7H_8) and several PAHs namely: naphthalene ($C_{10}H_8$), acenaphthylene ($C_{12}H_8$), fluorene ($C_{13}H_{10}$), acenaphthene ($C_{12}H_{10}$), phenanthrene ($C_{14}H_{10}$) and anthracene ($C_{14}H_{10}$). Figure 5. 11 presents a comparison of the peak mole fraction for phenol (C_6H_6O), benzaldehyde

(C_7H_6O) together with some selected OPAHs namely: dibenzofuran ($C_{12}H_8O$), 1-methylinden-2-one ($C_{10}H_{10}O$), ethenyl benzofuran ($C_{10}H_8O$), ethyl benzofuran ($C_{10}H_{10}O$), and 1-indanone (C_9H_8O) together with some selected mole fraction profiles. The first part of the following text is devoted to the discussion of one-ring non-oxygenated aromatics and PAHs while the second part is dedicated to the discussion on one-ring oxygenated aromatics and OPAHs.

As presented in Figure 5. 10, it can be observed that as the number of rings increase, the peak mole fraction of the species decreases. This trend is similar for both flames. One ring species like benzene and toluene are much more abundant than three-ring PAHs. The trend followed reflects that even if the number of rings is the same, their arrangement and carbon/hydrogen number in a given structure influences their amounts. For instance, acenaphthylene is more abundant than fluorene and the latter is more abundant than acenaphthene. If we compare between the two flames, it is clearly noticeable that the production of these species is considerably enhanced in the presence of anisole. Though both biofuels possess the ability to generate soot precursors in their own ways, experimental results indicate that anisole favors their formation to a greater extent than DMF because it has a higher tendency to form PAHs precursors (such as cyclopentadiene and benzene). Peak mole fraction for cyclopentadiene in the different flames are mentioned in the listed in Table A. 3 in the Appendices.

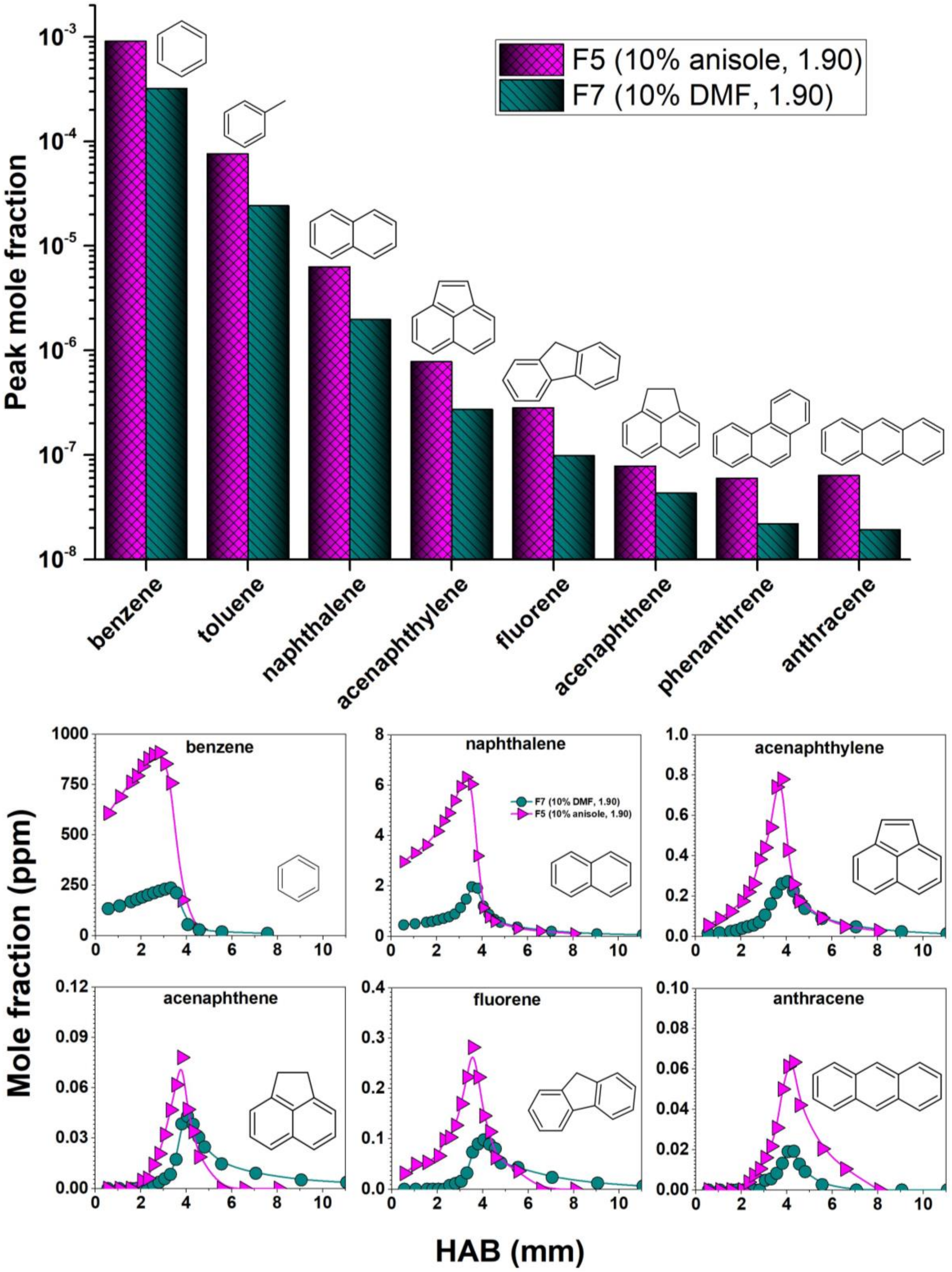

Figure 5. 10 : The first panel comprises a bar graph presentation of the peak mole fractions for non-oxygenated aromatics and PAHs; the second panel presents a comparison of the evolution of the mole fraction profiles for some selected species in the two flames: F5 (10% anisole, ϕ=1.90), and F7 (10% DMF, ϕ=1.90). Experimental results have been connected by a thin line to guide the eye.

Naphthalene is present in the range of few ppm whereas quantities of other PAHs with three rings are reduced by an order of magnitude. Naphthalene can be obtained via the combination of two resonance-stabilized cyclopentadienyl radicals [256]. In flame F7, this pathway is certainly the most probable route to form naphthalene. However, in flame F5, besides cyclopentadiene there is plenty amount of benzene which is also an efficient precursor to generate naphthalene [260]. Thus, the amount of naphthalene in flame F5 would be certainly more than in flame F7. The amount of naphthalene produced in flame F7 is about 2 ppm which increases to a value of 6.5 ppm in flame F5. The quantity is increased by more than three-fold if the biofuel used is anisole. After naphthalene, acenaphthylene is the most abundant PAH. Its amount in flame F7 is about 0.27 ppm which increases to a value of 0.80 ppm in flame F5 (by a factor of 3). Fluorene amounts to about 0.10 ppm in flame F7 and increases to about 0.30 ppm in flame F5. It is mystifying that the quantities of PAHs produced in flame F5 are more or less 3 times greater than their amounts for flame F7.

Concerning the OPAHs, one of the important precursors contributing to the formation of OPAHs is the phenoxy radical. As seen in Chapter 4, anisole can directly produce phenol via *ipso* addition of the OH radical and can also readily decompose to the phenoxy radical via scission of the O-CH_3 bond and then combine with an H radical to form phenol. Note that the phenoxy radical and phenol are important OPAH precursors as discussed in Chapter 4. DMF also possesses the ability to produce phenol in flame conditions but this process does not occur in a single step like anisole. As presented in Figure 5. 12, this ability results from the ring enlargement of a radical yielded from the ring opening of the resonance-stabilized 5-methyl-2-furanylmethyl (DMF-yl) radical. In the DMF molecule, the energy of the C–H bond in the methyl group (85.5 kcal/mol) is the lowest as compared with that of the C–H bond in the cycle (120.2 kcal/mol) and with that of the C–CH_3 bond (114.6 kcal/mol). Thus, DMF gets consumed significantly by H-abstractions by OH, H, O and CH_3, etc. on one of the adjacent methyl groups to form the resonance-stabilized 5-methyl-2-furanylmethyl (DMF-yl) radical. Due to the availability of the second lateral methyl group, this radical can favorably react via ring enlargement through several steps to generate cyclohexa-2,4-diene-1-one which would subsequently form phenoxy radical or phenol [153]. Such a route is globally called "ring opening/enlargement" reaction but numerous intramolecular rearrangements take place to lead to the final product. This could justify the amount of phenol produced in the anisole flame (~445 ppm) is much more than in the flame of DMF (~18 ppm). Phenol could also act as an important precursor of benzene in both anisole and DMF flames. However, in flame F5, there are multiple other low barrier pathways that exist to generate benzene via anisole as already discussed in Chapter 4.

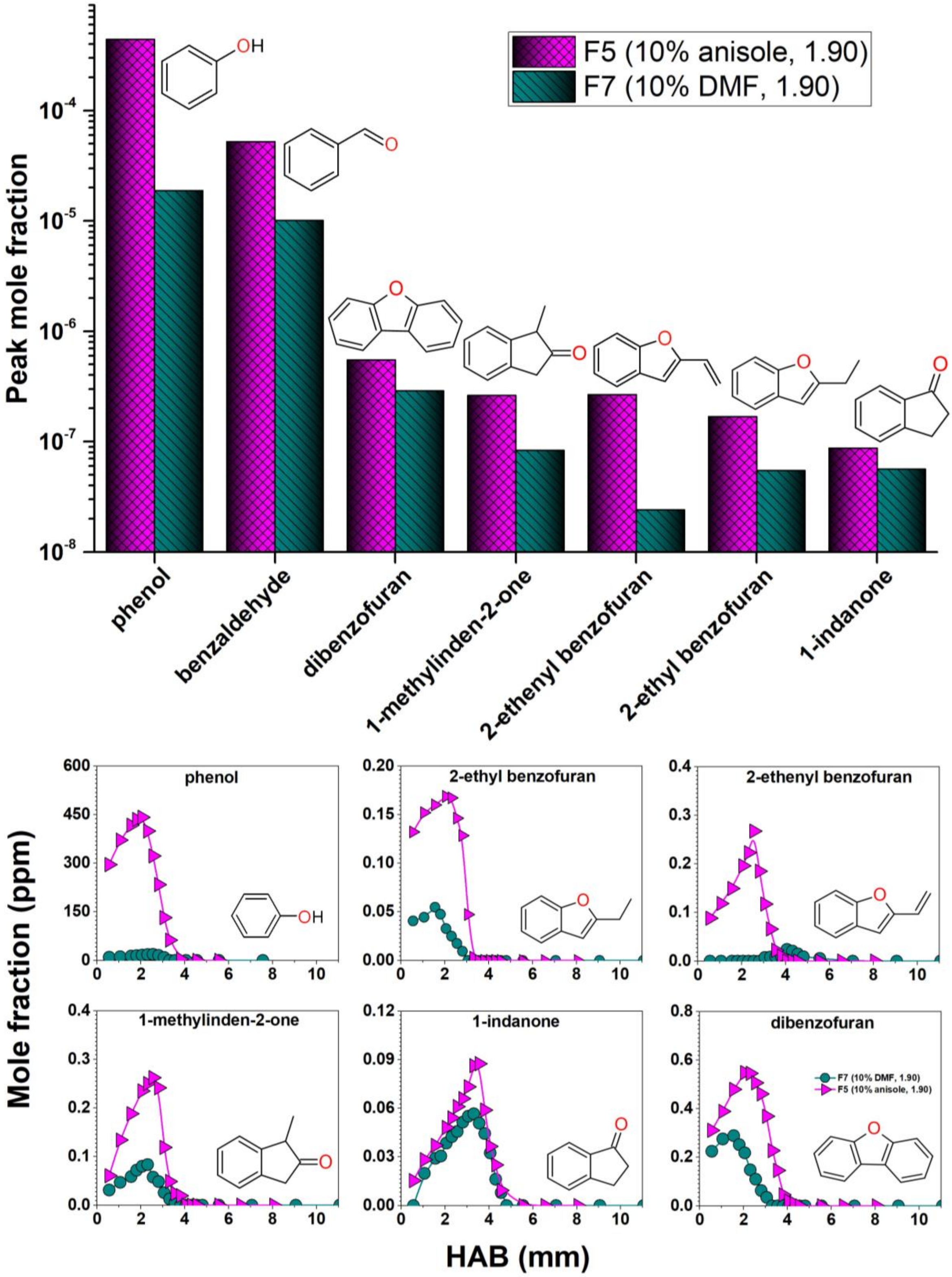

Figure 5. 11 : The first panel comprises a bar graph presentation of the peak mole fractions for oxygenated aromatics and OPAHs; the second panel presents a comparison of the evolution of the mole fraction profiles for some selected species in the two flames: F5 (10% anisole, ϕ=1.90), and F7 (10% DMF, ϕ=1.90). Experimental results have been connected by a thin line to guide the eye.

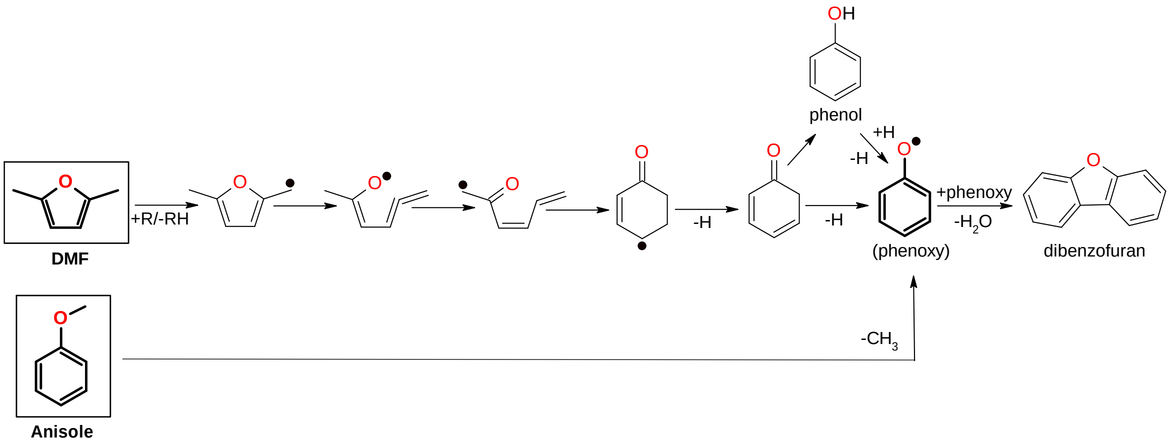

Figure 5. 12 : Reaction pathway analysis for the formation of phenoxy, phenol, and dibenzofuran via DMF and anisole from phenoxy radical as a precursor (combined information from [48,258,259]).

On the contrary, phenol acts as a main precursor for benzene in flame F7. The maximum mole fraction of benzene in flame F7 is about 237 ppm which increases to a value of 898 ppm in flame F5. There exists a factor of ~3.8 amongst the two flames for the amount of benzene. Similarly, the maximum mole fraction of toluene in flame F7 is about 22 ppm which increases to a value of 76 ppm in flame F5. Other than the discussed species, cyclopentadiene is an important precursor to form naphthalene and both the biofuels produce this species in the range of hundreds of ppm (listed in Table A. 3 in the Appendices). The resonance-stabilized 5-methyl-2-furanylmethyl (DMF-yl) radical can decompose to generate cyclopentadiene in flame F7 besides also forming phenol. In flame F5, decomposition of the phenoxy radical would act as the main reaction pathway to form cyclopentadiene. Mainly, subsequent reactions of phenol in the two flames contribute to the formation of other soot precursors such as benzene and cyclopentadiene, which eventually participate in naphthalene ($C_{10}H_8$) formation via cyclopentadienyl (C_5H_5) self-recombination. Since phenol is more abundant flame F5, these precursors are more susceptible to be produced in flame F5 than in flame F7.

In conclusion, the consumption pathways of DMF can lead to the formation of small linear compounds (C_4 species, acetaldehyde etc.), via the elimination of small molecules like (CO, C_2H_2, etc.) while metatheses followed by ring-opening and subsequent enlargement of the cycle can lead to the formation of more wide range of compounds (like phenol, benzene and cyclopentadiene). Several rearrangements and further steps are actually needed before DMF can break down to form other species. In the case of anisole, decomposition to form the phenoxy radical is the most probable step which can undergo further decomposition to form other aromatics or can undergo self-combination to form a whole range of oxygenated products as shown previously in Chapter 4. It is worth mentioning that though the phenoxy radical is susceptible to be produced via both biofuels, it is more however more easily formed from anisole than from DMF as already discussed in the previous section. A reaction pathway for the same has been presented in Figure 5. 12. This could explain why most of the OPAHs presented in Figure 5. 11 are present in higher amounts in flame F5 than in flame F7. For instance, there is about 0.3 ppb of dibenzofuran in flame F7 that increases to a value of about 0.57 ppm (almost double) in flame F5. Similarly, there is about 0.06 ppm of 2-ethyl benzofuran in flame F7 which increases to a value of about 0.165 ppm (by a factor of 2.7) in flame F5. Indanones have been detected in DMF flames for the first time in this study. The amount of 1-indanone and 1-methylinden-2-one increase by a factor of 1.5 and 3 respectively in the presence of anisole. It is also noteworthy that the number of OPAHs generated in flame F5 are much more elevated than the number of OPAHs generated in the DMF flame as were discussed previously. Though DMF is a cyclic oxygenated biofuel, its tendency to form OPAHs is less as compared to anisole as the initial fuel decomposition pathways lead to the formation of other smaller species as discussed previously.

A comparative evolution of the mole fraction of some selected abundant Oxygenated Aromatic (OA) and Non-Oxygenated Aromatic (NOA) soot precursors is presented in Figure 5. 13. It can be seen that benzene is responsible for a substantial contribution to the total sum of aromatics for both flames followed by other two and three ring species. It is interesting to note that the OA are formed and decomposed before the maximum mole fraction of benzene and other PAHs is attained. In other words, the formation and decomposition of OA occurs at lower temperatures and is quite rapid in contrast to NOAs which occurs at comparatively higher HABs. The plots give an impression that the OA in both the flames are short-lived and perish at a fast pace. NOAs on the other hand, are being formed and consumed at a much slower pace. If we compare the consumption of the NOAs amongst the two flames, they are consumed faster in flame F5 than in flame F7.

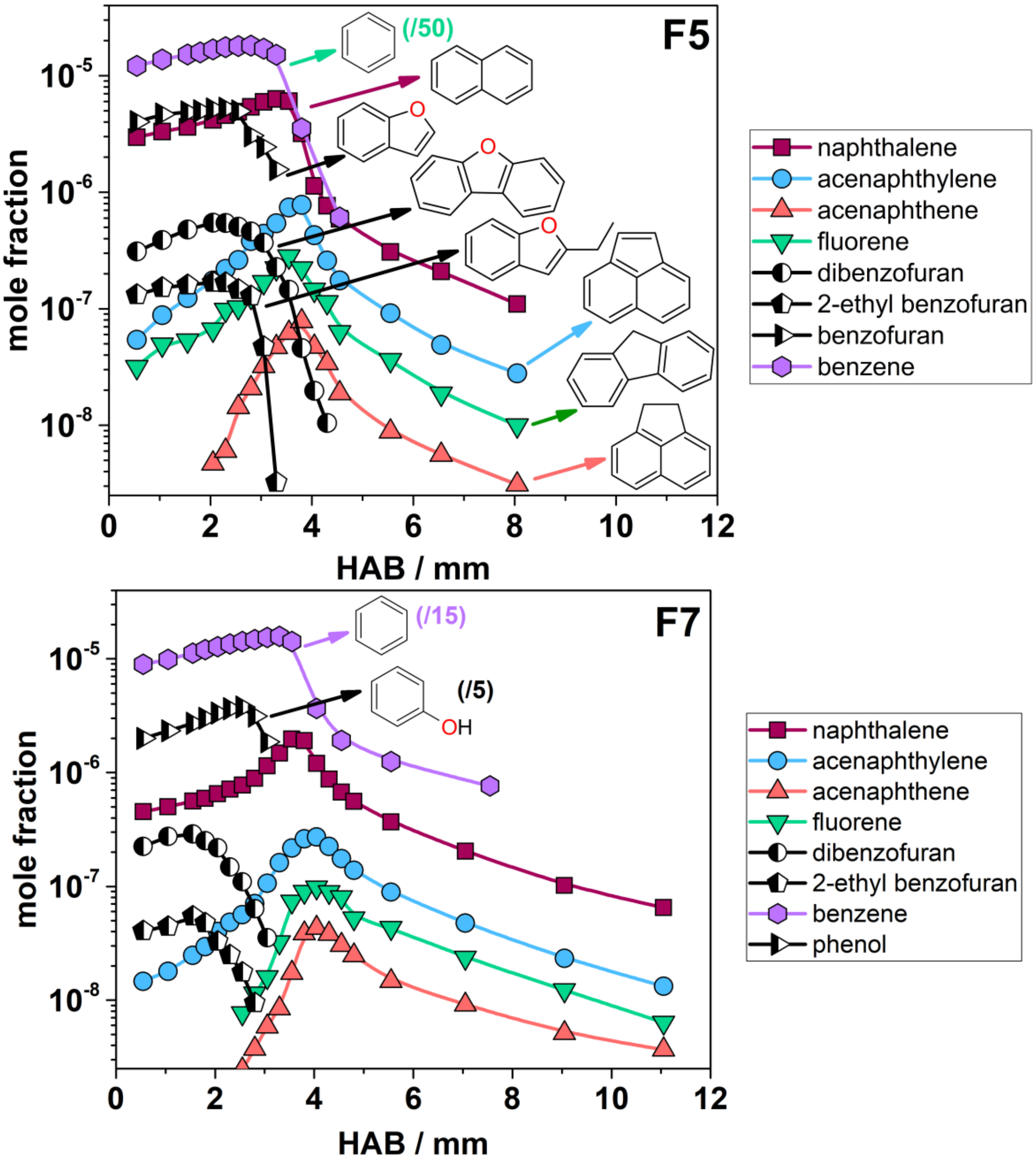

Figure 5. 13: Evolution of the mole fraction with HAB for selected OAs and NOAs for flames F5 and F7 (in log scale); the black and white symbols here represent OAs and the colored symbols represent NOAs (the numbers mentioned in the brackets are the factors by which the mole fraction has been divided to put all profiles in the scale).

5.3. Conclusion

This chapter presents a comparative study of different biofuels. In this context, two cases were studied: Case 1 involved studying a reference flame, an ethanol (10%) flame and an anisole (10%) flame whereas Case 2 comprised of an investigation on an anisole (10%) flame and a DMF (10%) flame. These case studies allowed us to evaluate the tendency of a given biofuel to form soot precursors and other pollutants. In case 1, it was observed that ethanol suppresses the formation of aromatic species in the flame meanwhile anisole promotes the formation of aromatics. However, ethanol significantly promotes the formation of toxic aldehydes (i.e., formaldehyde, acetaldehyde etc.). In case 2, findings from experimental results indicated that DMF and anisole both produce soot precursors (benzene (C_6H_6), toluene (C_7H_8) and phenol (C_6H_6O)), yet, anisole exerts a stronger effect on the formation of these species than DMF. These species can be generated from the most important routes of consumption of anisole while DMF needs to undergo multiple step reactions in order to produce these precursors. It must be noted that potential promising biofuels with an oxygen atom can behave differently and their structure plays an important role to decide their fate in a combustion environment. Comprehending the formation mechanism of Oxygenated Polycyclic Aromatic Hydrocarbons (OPAHs) is significantly more intricate compared to Polycyclic Aromatic Hydrocarbons (PAHs), primarily due to the scarcity of data available in the literature concerning OPAHs in comparison to PAHs. In contrast to OPAHs, the formation of PAHs is much better understood, largely owing to the substantial number of studies already documented in the literature. Moreover, with the presence of one or more oxygen atoms as distinct functional groups in their structures, it suggests that the formation chemistry of OPAHs could be even more complex. This complexity necessitates additional fundamental studies to comprehensively understand the mechanisms involved. One of the important precursors contributing to the formation of OPAHs is the phenoxy radical. The formation pathway of the phenoxy radical is not universal and varies with the structure of the biofuel. The following chapter focuses on the soot particles that are formed in their flames.

Chapter 6. Characterization of soot particles

So far, the influence of added biofuels on the formation of gas-phase aromatics (PAHs and OPAHs) was discussed in this study. Results from Chapter 4 and Chapter 5 demonstrate that the amount of the biofuel, the structure of the biofuel and local flame conditions influence the formation of gas phase species, particularly aromatics. In this chapter, we report the influence of the added biofuels on small soot particles that were characterized by LII and a commercial nano-SMPS. As discussed in Chapter 1, small soot particles are challenging but very important to study due to their health impacts. This chapter illustrates some early results on small sized soot particles produced in biofuel flames.

As already elaborated in Chapter 2, the LII signal is nearly proportional to the soot volume fraction (f_v). Since decades, the LII technique has been used to measure fv with high spatial resolution in fundamental as well as applied combustion experiments [64,65]. Complementary to LII, the SMPS allows to record the changes in the soot particle concentrations and size distribution. Since recently, several investigators have widely demonstrated the potential of SMPS in the context of flame investigations [203–207,209,261–263]. The experimental results presented in this chapter enable us to gain some insights on the quantity and the size of the soot particles formed in these flames. This chapter consists of two sections. Section 6.1 is devoted to the details concerning the soot dependence on the amount of anisole in the flame and Section 6.2 articulates the soot dependence on the structure of the oxygenated biofuel.

6.1. Soot dependence on the amount of anisole

This section presents a study to assess the effect of the presence of anisole and its amount on the soot particles produced in an iso-octane/CH_4/O_2/N_2 laminar premixed reference flame. This comparison permits us to highlight the main repercussions associated with the addition of anisole on the size and quantity of soot particles. The flames conditions chosen for this investigation have been summarized in Table 6. 1.

Table 6. 1 : Summary of the flame conditions established to investigate the soot dependence on the amount of anisole; L_n: normal liters per minute (anisole percentage here is a molar percentage with respect to the total fuel)

Flame	*Biofuel (%)*	*Flow rates (L_n/min)*						*Equivalence ratio*	*C/O*
		Biofuel	C_8H_{18}	CH_4	O_2	N_2	Total		
F1	-	-	0.18	0.925	2.25	6.50	9.85	1.82	0.52
F2	Anisole (10)	0.102	0.15	0.766	2.338	6.50	9.85	1.82	0.55
F3	Anisole (15)	0.147	0.13	0.696	2.377	6.50	9.85	1.82	0.57

Flame F1 has no anisole and thus acts as a reference flame that consists only of iso-octane/CH_4/O_2/N_2. Flames F2 and F3 consist of anisole/iso-octane/CH_4/O_2/N_2 where the former has 10% whereas the latter has 15% anisole. It must be noted that the other parameters like equivalence ratio, total flow, and dilution flow are kept constant. The interpretation of the experimental results concerning this series of flames is divided in two parts. The opening of the discussion is devoted to the analysis of the soot volume fraction derived via LII thereupon followed by the assessment of the Particle Size Distributions (PSDs) provided by the SMPS.

As detailed in Chapter 2, the soot absorption function, '$E(m)$' is an important parameter to measure f_v. In this work, $E(m)$ is determined by comparing the fluence curves of the flame in question to a reference flame for which the $E(m)$ is already known ($E(m)$ = 0.35) at an HAB of 16 mm [202]. Fluence curves (LII signal vs. laser fluence) represent the dependence of the incandescence signal on the laser energy density thereby providing information about the absorption efficiency of the particles or their ability to be heated which depends on $E(m)$. The measured fluence curves recorded using LII detection for flame F3 and the reference ethylene flame are reported in Figure 6. 1. After an energy threshold near 0.1 J/cm^2, the LII signal sharply increases due to the increase in the temperature acquired by the soot particles being heated. Then, the curve begins to gently bend around 0.54 J/cm^2. At higher fluence, the decrease in the LII signal in the ethylene flame can be explained by the sublimation of soot particles [182,264]. On the other hand, this decrease is not observed for flame F3 which is an indication that the sublimation temperature is not reached. As shown in Figure 6. 1, the gradient at low fluence which symbolizes the particles' ability to be heated, was slightly different for flame F3 as compared to the reference flame, which signifies a difference in the particle properties [181] supposing that the maximum temperature attained by the soot particles amongst the two flames. This difference can be compensated by taking a fluence shift (1.4) into account to replicate a similar gradient as that of the reference flame for which $E(m)$ is known (0.35). This method led us to estimate $E(m)$ = 0.25 for flame F3.

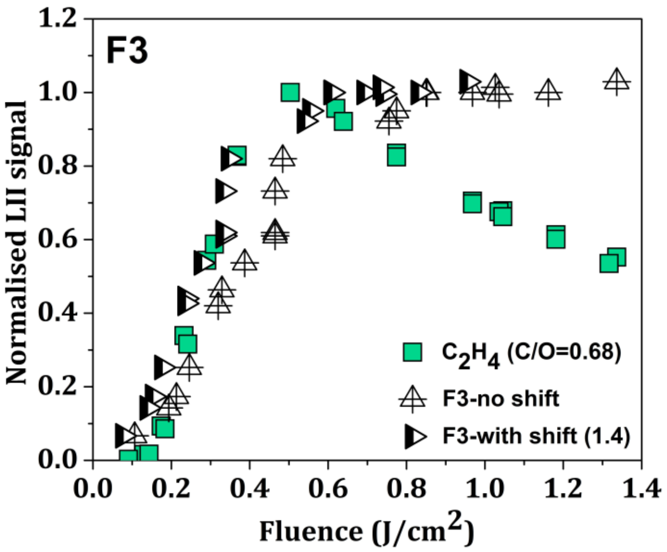

Figure 6. 1: Comparison of the fluence curves for flame F3 (15% anisole, ϕ=1.82) with and without the shift and the reference ethylene flame (C/O=0.68) at an HAB = 16 mm. The curves are normalized with respect to the highest values in each case.

Similar value of $E(m)$ was reported by Betrancourt et al. [181] for very small early soot particles in n-butane flames. Fluence curves for flames F1 and F2 could not be established because of the low signal to noise ratio. However, we assumed that the particles present in these flames must be very small (as was later confirmed by SMPS measurements) and thus would possess more or less the same value of $E(m)$. In order to calibrate the intensity profiles measured by LII, we used another calibrated ethylene flame as a reference for which f_v and the absorption function $E(m)$ were known (at HAB = 16 mm). Table 6. 2 presents the f_v (at an HAB of 16 mm) for the three flames (F1, F2 and F3) respectively. Sum of the aromatic species in the two flames is also presented. It must be noted that the sum of aromatics quoted in the table corresponds to the maximum concentrations attained by the quantified aromatic species (non-oxygenated as well as oxygenated aromatics) in these flames.

Table 6. 2 : A recapitulation of the flame conditions with the soot volume fraction (in ppt) measured by LII for each flame at an HAB = 16mm respectively

Flame	*Biofuel (%)*	*Equivalence ratio*	***Aromatics sum (ppm)***	***Soot volume fraction, f_v (ppt)***
F1	-	1.82	**~226**	**1.5**
F2	anisole (10)	1.82	**~1820**	**2.4**
F3	anisole (15)	1.82	**~2855**	**3.0**

It is worth bearing in mind that this sum only constitutes the different aromatics quantified in this study. Several identified species could unfortunately not be quantified (as detailed in Chapter 4) and consequently were not included in the sum. However, major abundant aromatics are counted in to evaluate this sum and can henceforth provide an approximate idea. Aftermaths from Table 6. 2 shows that the sum of maximum concentration for all aromatics in flame F3 (15% anisole) and flame F2 (10% anisole) is nearly 13 and 8 times more than in flame F1 (no anisole) respectively.

Quantitative measurements for f_v profiles as a function of the HAB were not possible as we were at the limit of the detection threshold [205,265]. Researchers performing quantitative f_v measurements in atmospheric premixed flames have quantified 0.01 ppb or 10 ppt [181] at the lowest which is considered as the detection limit. Since the f_v in our flames is a few ppt (at HAB=16 mm), it was not possible to trace a full profile of the f_v evolution along the flame. However, as it was within the realms of possibility, f_v at an HAB of 16 mm was determined for the three flames and is reported in Table 6. 2. Though the uncertainty close to the detection limit is high (±40%), data seems to indicate that the presence of anisole is increasing soot volume fraction at an HAB of 16 mm which is later confirmed via SMPS measurements. Recently, Cruz et al. [96] studied laminar co-flow diffusion flame of anisole and gasoline surrogate blend and suggested that the presence of anisole noticeably increased f_v by a factor of 1.6 (4.1 to 6.8 ppm)-1.8 (4.5 ppm to 9.6 ppm) depending on the HAB. They attributed this observation to the increased formation of aromatics (soot precursors) in the presence of anisole. However, it is worth mentioning that they observed ppm levels of soot in their conditions which is much more than what we observed in our conditions.

Together with the amount of soot produced, particle size distribution (PSDs) also serve to characterize the soot particles. A fine SMPS study was carried out to investigate the evolution of the size and the concentration of the soot particles to complement the LII data discussed previously for these flames. Commercial SMPS are generally limited to study particles with d_m > 10 nm. However, as discussed in Chapter 2, the SMPS used for this thesis is additionally equipped with a nano-enhancer module which allows the detection of very small particles down to $d_\mathrm{m} \approx 1.5$ nm. This way we could probe the early soot particles whose diameters lie in this range [66].

For this series of measurements (F1, F2 and F3), the differential pressure (pressure difference between the flame and the sampling line, see Chapter 2) was always kept constant to evaluate the soot dependence on the HAB in a given flame and on the amount of anisole amongst three flames. The aim was to perform sampling in a way so as to preserve the salient features of the PSDs. In particular, post-sampling coagulation results in the shift to higher d_m of the PSDs. To avoid the post-sampling coagulation processes, preliminary acquisitions were performed by decreasing the differential pressure (thereby increasing the dilution ratio) until the particle number density was sufficiently low to eliminate coagulation issues due to low dilution. To obtain unbiased data, experiments were performed during the same day and continuous attention was paid to monitor the atmospheric pressure and the differential pressure at all times during the measurements.

Multiple acquisitions were taken for a given HAB to also verify the reproducibility of each measurement. Figure 6. 2 illustrates the PSDs at different HABs for flames F1, F2 and F3 in two ways. The upper panel of the figure depicts the size distribution of particles as 2-D plots, while the lower panel presents the average of the different distributions recorded for a given HAB in a 3-D view. The y-axes present the normalized particle number density $\frac{\mathrm{d}N}{\mathrm{dlog}d_{\mathrm{m}}}$ at different HABs whereas the x-axis denotes the mobility diameter d_{m} of the particles. It is noteworthy that we chose the normalized number density $\frac{dN}{\mathrm{dlog}d_{\mathrm{m}}}$ instead of $\frac{\mathrm{d}N}{\mathrm{d}d_{\mathrm{m}}}$ to represent the concentration of particles since the former is independent of the instrument resolution and therefore is tremendously useful when comparing data amongst different instruments with different resolutions.

In addition, it must be noted that the total particle concentration presented in Figure 6. 2 given by the SMPS does not directly represent the particle concentration in the flames. The concentration number provided by the SMPS is biased by the sampling procedure and needs to be corrected by the dilution ratio, the flame-sampling line temperature difference, and the nanoparticles' transport efficiency.

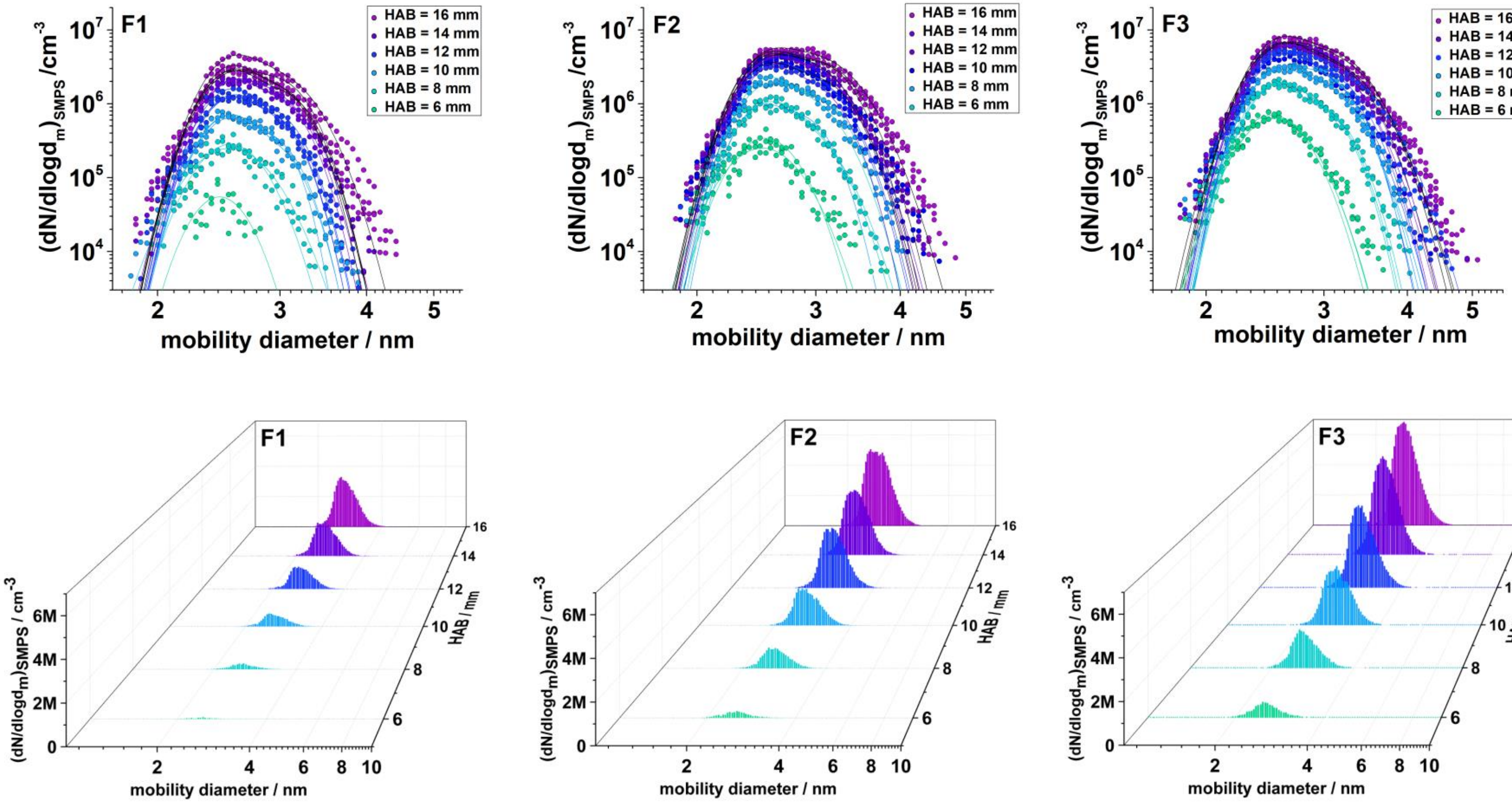

Figure 6. 2: Upper panel presents the 2-D soot PSDs (both axes in log scale) recorded for flames F1, F2 and F3 where symbols denote the measured distributions whereas the lines represent log-normal fits of the data; Lower panel depicts a 3D view of the same PSDs at different HABs (y-axis is presented in a linear scale representing the total particle number concentration in millions and the x-axis is presented in log scale) to show the variation in the soot particle number for each flame.

In particular, while the dilution and temperature corrections are assumed not to change the PSDs and therefore can be treated as proportionality factors, diffusion losses can alter the shape of the PSDs during the transport of the diluted sample: small particles are more susceptible to be lost in the line in comparison to bigger particles as they possess faster diffusion velocity. To limit these losses, the sampling system was set up in a very compact manner, and the sampling flow was maximized in order to minimize the transport time in the sampling line. The quantitative estimation of these losses is very challenging and well beyond the scope of this thesis. There are nonetheless some studies in the literature [266,267] devoted to estimate these losses experimentally, however, these estimations are validated for very specific experimental conditions and are subject to large uncertainties which is why they can be problematic to generalize. That being the case, and to avoid introducing further uncertainty in the interpretation of the measurements, we decided to investigate the raw size distributions obtained by SMPS (uncorrected). The corrections involved to recover the particle concentration is certainly an important perspective of this work and will be an objective of a future investigation.

The PSDs presented in Figure 6. 2 have been acquired using a differential pressure of 18 mbar (the same for three flames) and was kept constant at all HABs. The 3-D representation of the data clearly highlights a difference in the number of particles produced at each HAB in each flame. It can be observed that the number of particles in flame F3 are much more elevated than in flame F1. Addition of more anisole to the flame increases the number of these small soot particles (flames F2 and F3). Another noteworthy point is the size of the soot particles which ranges between 2-4 nm for these flames. These particles are very small in size, which explains the f_v in the ppt range. A predominance of particles is in this diameter range (few nanometers) refers to primary soot particles. The major uncertainty in the evaluation of particle size is related to possible deviations from a spherical shape. However, as the particles in these flames are very small, it is reasonable to approximate them as primarily spherical in shape and isolated from one another. At a first glance, the raw PSDs in these three flames appear as if they can be pronounced by a monomodal function centered around 2.6 nm on the entire height of the flame.

More insights can be revealed via a detailed mathematical examination of the variation of the distributions with flame height. In spite of what preceded, we will see further in the subsequent detailed analysis of these PSDs that there is in fact a minor second mode, symbolizing that some soot particle growth processes are nevertheless taking place in these flames. Many studies have shown that aerosol PSDs are well fitted by log-normal functions. Accordingly, shapes of PSDs in flames are frequently characterized by means of log-normal type functions in the literature [204,206]. The size spectra shown in Figure 6. 2 can be closely fitted using a lognormal distribution function:

$$f(x) = \frac{A}{xw\sqrt{2\pi}}\, exp\left(-\frac{\left(\ln \frac{x}{x_c}\right)^2}{2w^2} \right) \qquad \textit{Equation 6. 1}$$

Here,

x : Electric mobility diameter of the soot particles (nm);

x_c : Median mobility diameter of soot particles (nm);

A : Integrated area under the distribution;

w : Geometric standard deviation of the distribution.

Equation 6. 1 is used to establish a theoretical log-normal distribution function to represent the measured PSDs. To do so, measured PSDs were fit with just one or a sum of two log-normal functions, if necessary (depending on the HAB), using the OriginPro 2016 software (χ^2 tolerance < 10^{-9} to reach convergence). Figure 6. 3 presents the average of measured PSDs (represented by the black empty circles) for the three flames and the associated log-normal distributions calculated from Equation 6. 1 (represented by the fits shown as solid lines).

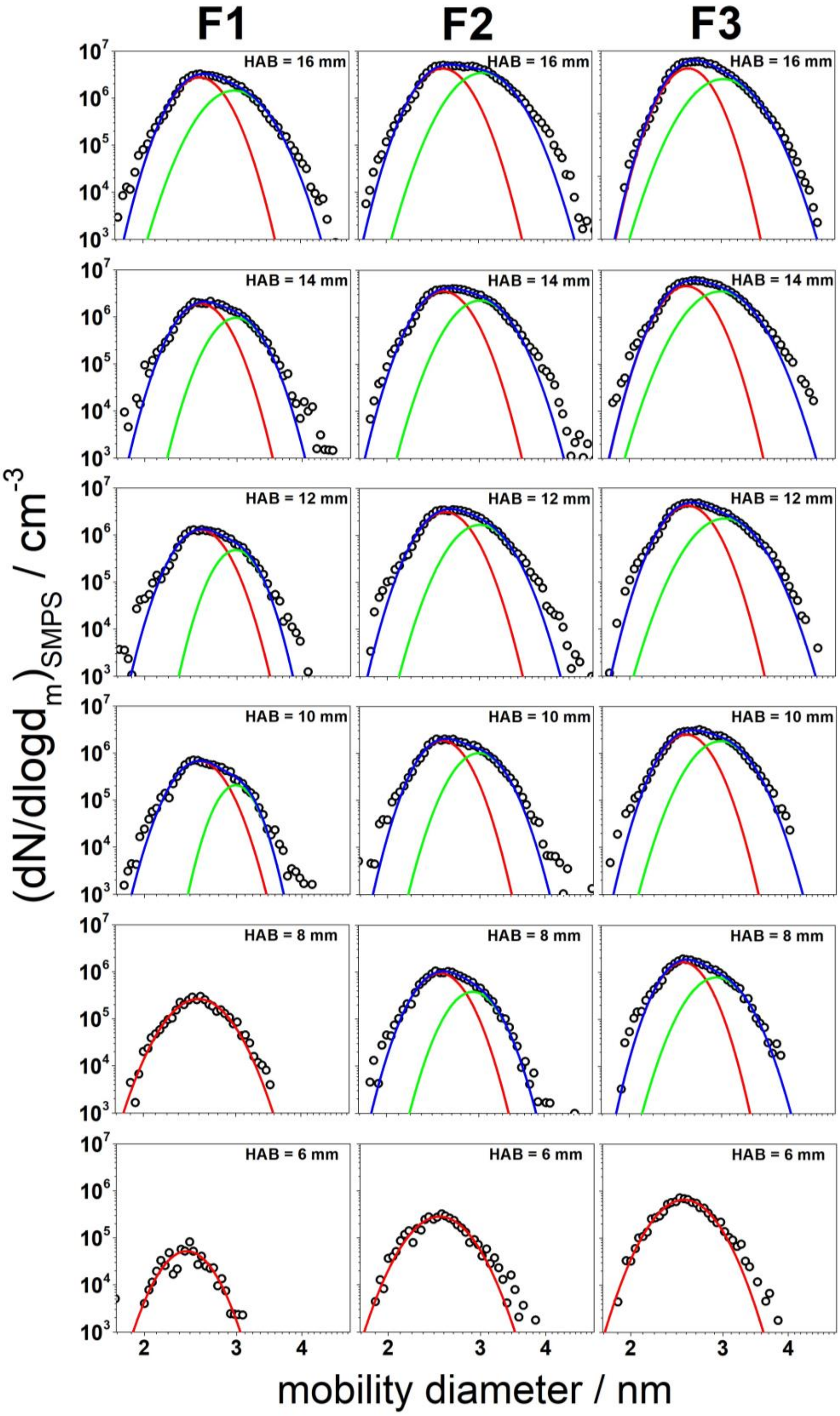

Figure 6. 3 : Evolution of the PSD as a function of HAB for flames F1, F2 and F3. Black circles represent the measured PSD whereas lines present the log-normal fits; log-normal fit for Mode-1 and Mode-2 are presented by the red and the green lines respectively whereas the blue line represents the cumulative fit.

Though each acquisition recorded was fit and analyzed individually, an average distribution per HAB is presented in Figure 6. 3 and discussed in the following text for a lucid interpretation of the data. The red and the green solid lines represent Mode-1 and Mode-2 respectively. The blue line represents the cumulative fit. As presented in Figure 6. 3, good agreement is observed between the measured and calculated curves, thereby confirming the utility of the usually accepted log-normal character for soot PSDs. In the literature, monomodal distributions are observed for incipient or primary soot particles and bimodal distributions are noticed for PSDs in rich flames [58,205,265]. As presented in Figure 6. 3, for flame F1, one log-normal function was sufficient to fit PSDs at 6 mm and 8 mm HAB, while two log-normal functions were required to fit the PSDs at higher HABs. At around 6 mm HAB, soon after the flame front, particle inception can result in the formation of nanoparticles leading to a unimodal PSD centered at about 2.5 nm (Mode-1). Starting from the HAB of 10 mm, one log-normal was not enough to replicate the measured PSD. From 10 mm onwards, a small shoulder begins to appear at slightly larger dm (~ 3 nm), for which the particle number rises with the HAB. To reach convergence of the fitting, a second log-normal referred to as Mode-2 was added to the sum. Initially, Mode-2 appears as a broadening of the curve or a tail towards larger d_m which enlarges as we go to higher HABs. It always coexists with Mode-1 and does not exist as a separate distinct mode. Mode-2 appears at earlier HABs in flames F2 and F3 as compared to flame F1, implying that soot growth processes start earlier in the presence of anisole. This bimodal distribution function persists from HAB of 10 to 16 mm in flame F1 and from HAB of 8 to 16 mm for flames F2 and F3. The particle size in Mode-2 ranges around 3 nm (also small) depending on the flame and HAB. The appearance of Mode-2 becomes clearer at higher HABs though Mode-1 is still active. Mathematically, we have an illustration that the two processes (inception and particle growth) take place simultaneously for all the three flames. Starting from lower HABs, this behavior persists even in the post-flame region suggesting a sort of equilibrium. The widths of the distributions or the geometric standard deviation (see Equation 6. 1) for Mode-1 and Mode-2 lie in the range of 0.05-0.12.

Although particles in Mode-2 gradually increase in concentration with flame height, the number of particles in Mode-1 does not decrease and in fact continues to increase with an increasing flame height. This indicates that small incipient particles do exist in the post-flame region as well. Some modeling studies in the literature [261,268] have shown that the apparent, constant particle size observed for soot particles in the post flame front region could depend on steady-state kinetics of particle inception versus consumption by coagulation to form larger particles. The fact that small particles from Mode-1 are always observed in the PSDs in Figure 6. 3, indicate that inception is somewhat a continuous process throughout the region even later in these flames. Furthermore, it seems that perchance, the early soot particles from Mode-1 are consumed by growth processes at a rate lower than the rate at which they are produced in such a way that their concentration in fact keeps increasing. This feature could be caused by an intrinsic competition between the rate at which the two processes i.e., continuous, and simultaneous inception and growth processes are taking place.

However, it is worth taking note that these interpretations are deduced via preliminary interpretation of the mathematical fits. This set of data does not allow deriving a more complete scientific understanding regarding the phenomenon involved at the current moment. Additional investigations are necessary to unravel the experimental evidence and validate these hypotheses. A complementary modeling study could possibly help derive a more complete understanding.

The resulting parameters deduced from the fit procedure i.e., the mean diameter (x_c), the integrated area (A) and the geometric standard deviation or the width of the modes (w) for both Mode-1 and Mode-2 log-normal distributions are plotted in Figure 6. 4 as function of HAB. Based on the data shown in Figure 6. 4, the median mobility diameter of the soot particles corresponding to Mode-1 remains almost constant all over the investigated conditions, at about 2.5-2.6 nm i.e., the particle diameter does not increase as a function of HAB. On the other hand, the median diameter for Mode-2 particles lies around 3 nm for the three flames.

It can be observed that x_c is almost constant in flame F1 with respect to the flame height and a rather modest or a faint slope with respect to the flame height for anisole flames. This could possibly imply very little soot growth in general for these flames. Under the hypothesis of spherical and isolated particles, and keeping in mind that the three flames were investigated using the same experimental conditions, the evolution of A is considered to be representative of the relative variation of the particle concentration in the flame. The linear relationship between the total number concentration provided by the SMPS output and the area under the distribution was verified before assuming that the integrated area is representative of the particle number concentration.

Figure 6. 4 indicates that Mode-1 continues to increase against HAB. Particles associated with this mode are more abundant in flames F2 and F3. Also, it seems that the particles in Mode-2 increase in number at a faster pace for flame F2 and flame F3 in comparison to flame F1. This shows that the soot growth processes not only begin earlier in anisole flames but are also progressing at a sped-up pace in the presence of anisole. There is a difference between the number of particles associated with the two modes in flame F1 where Mode-1 contains a greater number of particles than Mode-2. On the other hand, it is observed that the presence of 10%

anisole somewhat promotes particle growth to increase the number of particles in Mode-2 and the presence of 15% anisole favors this increase to such an extent that the number of particles in Mode-2 surpasses the number of particles in Mode-1. Particle number density grows about more than twofold times between flame F1 and flame F3 (at HAB of 16 mm). It is interesting to note that these observations are actually coherent with the LII data. Mode-2 starts with smaller widths in flame F1 contrary to anisole flames.

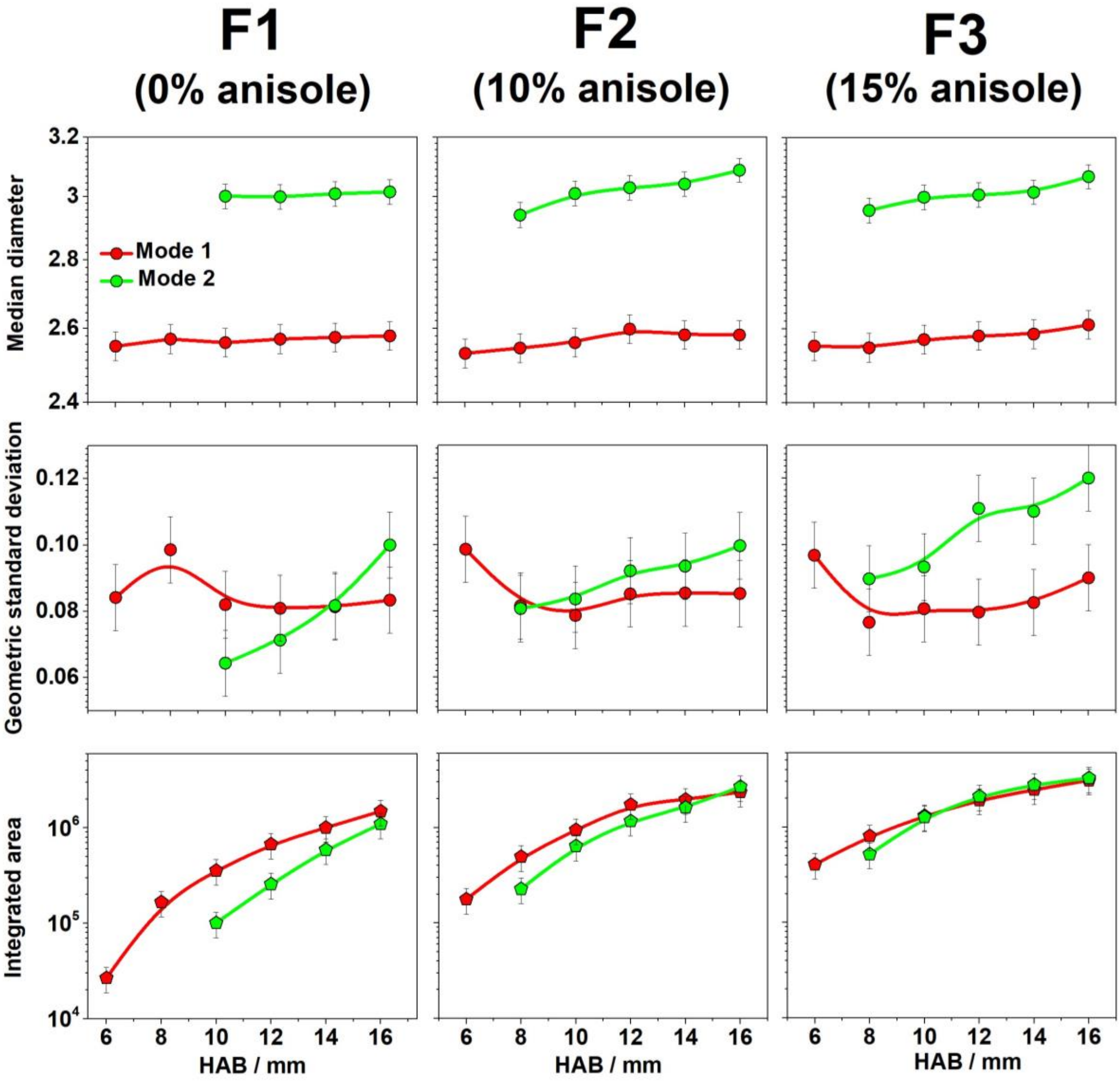

Figure 6. 4 : Evolution of x_c (first row), w (second row) and A (third row) of the two lognormal fits characterized as Mode 1 and Mode 2 with respect to the flame HAB for the three flames.

Figure 6. 5 compares *A* (total area under the distribution) for the three flames. The figure clearly indicates as mentioned before that the number of small-sized particles increases in the presence of anisole even though the particle growth processes seem limited in these flames. As seen from LII, the amount of soot increases in the presence of anisole. It is interesting to note

that the enhanced amount of soot produced in the presence of anisole is coming from small-sized soot particles. Increase in soot amount due to small-sized soot particles implies large number concentrations of soot particles.

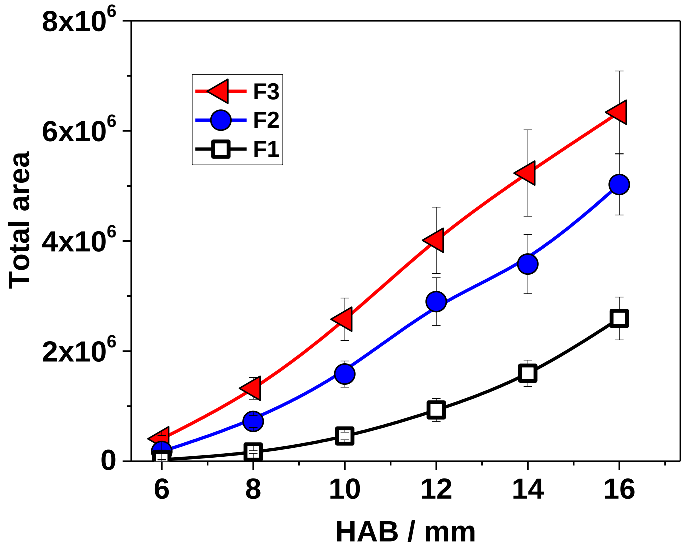

Figure 6. 5 : Comparison of the total area under the distribution (in millions) for the three flames with respect to the HAB.

6.2. Soot dependence on the type of biofuel: anisole and DMF

In the previous section, three different flames were investigated to study the soot dependence on the amount of anisole present in the flames. Experimental results indicated that the presence of anisole not only enhances the f_v but also promotes the number of small soot particles produced. This section presents another study to assess the soot dependence on the structure of the biofuel. In this context, two flames with different biofuel additives, i.e., anisole (10%) and DMF (10%) are studied. This comparison permits us to inspect the influence of two structurally different oxygenated biofuel additives on the f_v and the PSDs of soot particles. The flame conditions chosen for this investigation have been summarized in Table 6. 3.

Table 6. 3 : Summary of the flame conditions to study the soot dependence on the structure of the biofuel i.e., anisole and DMF; L_n: normal liters per minute (biofuel percentage here is a molar percentage with respect to the total fuel)

Flame	*Biofuel (%)*	*Gaseous flow rates (L_n/min)*						*Equivalence ratio*	*C/O*
		Biofuel	C_8H_{18}	CH_4	O_2	N_2	Total		
F5	anisole (10)	0.105	0.150	0.788	2.308	6.500	9.850	1.90	0.58
F7	DMF (10)	0.106	0.156	0.801	2.291	6.500	9.850	1.90	0.57

It must be noted that other parameters such as the dilution, total flow and the equivalence ratio are constant. A detailed comparison of the important soot precursors and other gaseous species produced in the two flames has been detailed in Chapter 5. As stated previously, the soot particles formed in these flames are also characterized via LII and SMPS. Following the interpretation of the LII data, a detailed analysis of the SMPS data is performed. The analytical protocol followed for the determination of the f_v profiles was detailed in Chapter 2. As discussed earlier, the LII technique is not a straightforward quantitative technique and only allows access to relative values of incandescence signals characteristic of the evolution of the f_v in flames.

$E(m)$ is again determined by comparing the fluence curves of the flame in question to a reference flame for which the $E(m)$ was known ($E(m)$ = 0.35) at an HAB of 16 mm as mentioned earlier in section 6.1. The measured fluence curves for flame F5 and F7 together with the reference ethylene flame are reported in Figure 6. 6. As shown in the figure, the gradient at low fluence which represents the particles' ability to be heated, was exactly the same for flame F5 and the reference flame. This implies that the particles in the two flames possess similar absorption properties i.e., similar optical properties. Thus, we used the same value of $E(m)$ for flame F5 as the reference flame i.e., 0.35. On the other hand, the gradient for flame F7 is not the same as the reference flame and necessitates a shift. The difference is compensated by incorporating a fluence shift to replicate a similar gradient as that of the reference flame. This method led us to estimate $E(m)$ = 0.29 for flame F7.

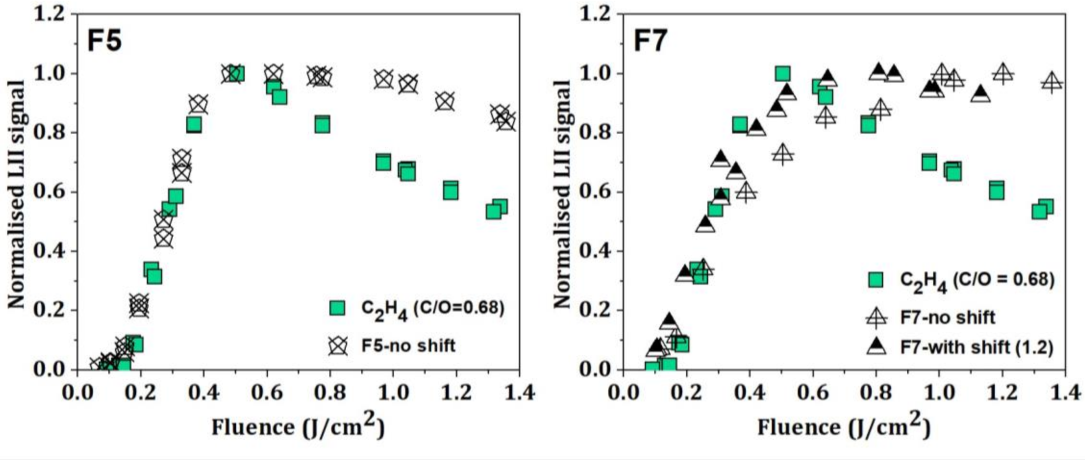

Figure 6. 6: Comparison of the fluence curves for flame F5 and flame F7 together with that of the reference ethylene flame (C/O=0.68). The curves are normalized with respect to the highest values in each case.

Calibration of the LII signals was carried out in the same way as for flames F1, F2 and F3. The uncertainty associated with these measurements is around ±20%. It was not feasible to acquire a complete f_v profile for flames F1, F2 and F3 because of the inadequate signal-to-noise ratio. However, flames F5 and F7 possess a higher equivalence ratio of 1.90, which enabled us to trace the evolution of the f_v with respect to the HAB. Table 6. 4 presents the maximum f_v and a recapitulation of the maximum amount of the aromatic species and that were reported for flame F5 and flame F7 respectively. The sum of aromatic species mentioned in the table encompasses the peak mole fractions of the most abundant aromatics (oxygenated as well as non-oxygenated aromatic species) present in the two flames that were quantified in this study (details in Chapter 5). Likewise, the f_v reported for the two flames is the maximum value retrieved at an HAB of 18 mm. Figure 6. 7 presents the evolution of the acenaphthylene (the most abundant three ring-aromatic in these flames) in parallel with the evolution of the f_v for flames F5 and F7 respectively. The acenaphthylene profile has been shifted towards the burner to consider the nozzle effect by using the difference in the temperature profiles between with and without the nozzle.

Table 6. 4 : Recapitulation of the flame conditions, sum of the maximum mole fraction of the aromatics (oxygenated and non-oxygenated aromatic species) and the maximum f_v (at HAB = 18 mm) obtained for the two flames respectively

Flame	Biofuel (%)	Equivalence ratio	**Aromatics sum (ppm)**	**f_v (ppt)**
F5	Anisole (10)	1.90	**~1870**	**182**
F7	DMF (10)	1.90	**~542**	**45**

The primary y-axis denotes the mole fraction of acenaphthylene (in ppm) whereas the secondary y-axis serves to present the f_v (in ppt). Although already discussed in Chapter 5, it is worth mentioning here that there was no difference in the amounts of smaller aliphatic species (like acetylene, propene and propyne) amongst the two flames which are also considered to play an important role in the soot formation process. Thus, the difference in the amount of soot produced is expected to be due to the difference in the quantity of aromatic species in the two flames. This observation also supports that aromatic compounds are more crucial species in the soot nucleation process than the aliphatic species.

This is why only the evolution of the sum of the aromatic species is presented in Table 6. 4 as their amount differs amongst the two flames which could justify the difference in the amount of soot produced. As demonstrated in the figure, the onset of soot formation commences close to the depletion process of acenaphthylene. This figure notably shows that the formation of aromatics and soot is more in flame F5 than in flame F7. Data presented in Table 6. 4 and Figure 6. 7 indicates that the maximum amount of soot produced in flame F5 is nearly four times more than in flame F7. This observation is in accordance with the amount of aromatic species formed in these flames.

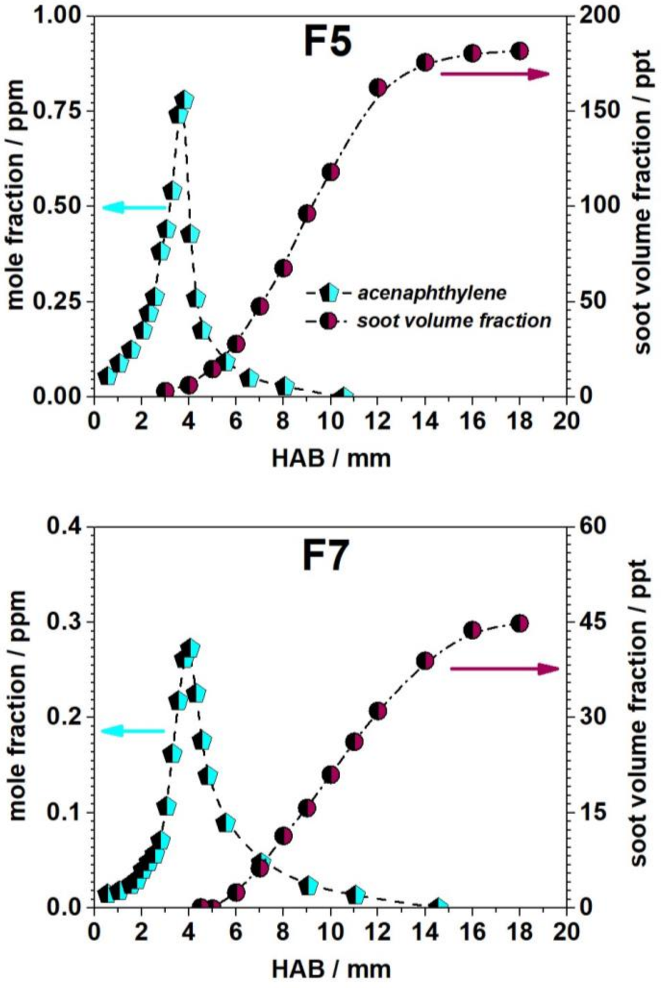

Figure 6. 7 : Evolution of the aromatics (oxygenated and non-oxygenated aromatics; primary y-axis) and the f_v (secondary y-axis) with respect to the flame height for flame F5 and flame F7.

As shown in Table 6. 4, the quantity of aromatics in flame F5 ranges in thousands of ppm whereas their amount in flame F7 lies in the range of hundreds of ppm which accounts to a difference by an order of magnitude. In absolute terms, the maximum mole fraction of aromatics in flame F5 is nearly ~3.4 times more than their maximum mole fraction in flame F7. A strong increase of the f_v with flame height appears following the decomposition of the aromatic species which increases exponentially initially but then gradually becomes constant. Also, the initial increase of the f_v in flame F5 is much steeper than in flame F7. This signifies that the rate at which the amount of soot is increasing with respect to the flame height, is higher in F5 than in F7. Figure 6. 8 presents normalized peak mole fractions for some selected non-oxygenated and oxygenated species and soot volume fraction in the two flames. It presents a global overview of the evolution of the slope at which aromatics and soot increase in F5 with respect to F7. It is noteworthy that the slope for benzene and PAHs is somewhat similar unlike the case for phenol and dibenzofuran. The increase for phenol is more abrupt in comparison to non-oxygenated species and the slope at which soot is increasing is closer to that of the non-oxygenated species.

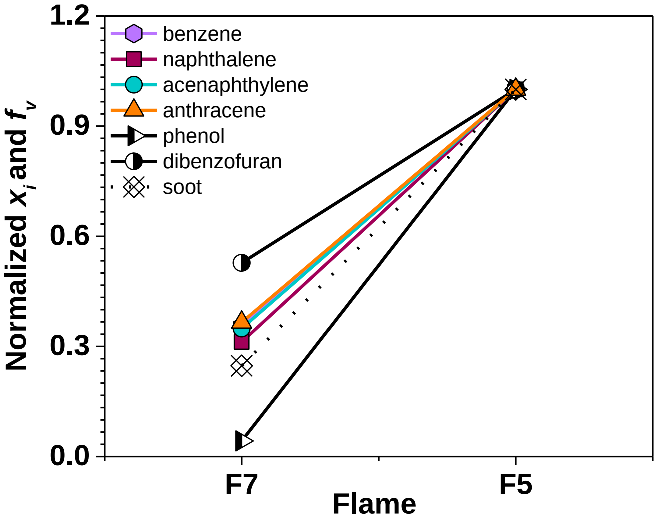

Figure 6. 8: Normalized peak mole fraction values attained by benzene, phenol, PAHs, and OPAHs (selected species) and the soot volume fraction in flames F5 and F7 respectively.

In addition to the axial f_v profiles, we also investigated the dependence of f_v on the equivalence ratio (biofuel amount constant). As first proposed by Musick et al. [269] in 1996 and then used by Melton et al. [270,271] in 1998 and 2000, the effect of equivalence ratio on f_v can be analyzed using the empirical formula:

$$f_v^{max} = A_i \phi^{n_i} \qquad \text{Equation 6. 2}$$

Here, f_v^{max} represents the maximum soot volume fraction, ϕ is the equivalence ratio and A_i and n_i are the correlation parameters. The sensitivity of the f_v^{max} to equivalence ratio is represented by the parameter n_i. Melton et al. [271] reported a value of n_i = 13 for their soot measurements in atmospheric methane sooting flames where particles underwent growth processes. Figure 6. 9 represents the evolution of the f_v^{max} with respect to ϕ for two series of flames with 10% anisole and 10% DMF. f_v^{max} was measured in all flames at an HAB of 16 mm. It is worth mentioning that other parameters like total flow and dilution were always constant. LII signals were converted to absolute f_v^{max} in the same way as discussed previously. Experimentally determined measurements were then fit using linear regressions using

Equation 6. 2 However, this empirical law did not apply over the complete range of investigation. Thus, we split the evolution of the f_v into two zones. In general,

- a first zone between ϕ=1.86 and ϕ=1.92 for anisole flames and between ϕ=1.88 and ϕ=1.96 for DMF flames was observed; where we notice a very significant increase in the f_v with ϕ (sensitivity factor of 88). This is where the inception process predominates.
- and a second zone between ϕ=1.92 and ϕ=2 for anisole flames and between ϕ=1.96 and ϕ=2.04 for DMF flames where the soot growth process predominates, with a lower sensitivity towards ϕ.

Each of these zones were fit individually. Whatever the area considered, the value obtained is however greater than that determined by Melton et al. at atmospheric pressure. Figure 6. 9 shows that the f_v^{max} for flame F5 is always greater than flame F7 and this difference is more pronounced when the equivalence ratio ranges between 1.86 to 1.92.

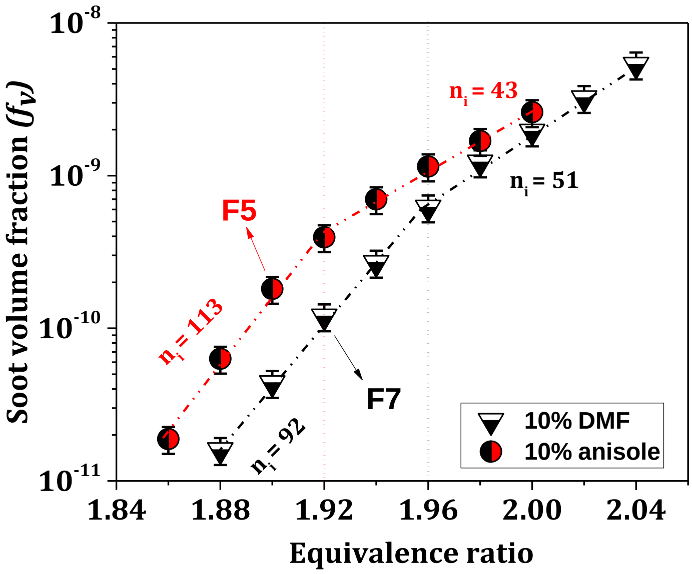

Figure 6. 9 : Evolution of f_v (in log scale) with respect to the equivalence ratio for two series of flames containing 10% anisole and 10% DMF respectively; Symbols represent experimentally measured values (at HAB = 16mm) whereas the dashed lines represent the fits performed to retrieve the unknown parameters.

This difference decreases as we approach very high equivalence ratios beyond 1.96. In general, as shown in the figure, there is a remarkable increase in the f_v in the initial phase for each series of flames until ϕ=1.92. The sensitivity factor describing the dependence is greater for anisole (113) than for DMF (92) in the first zone. After an equivalence ratio of 1.92, the increase in the f_v for the anisole flame series is less pre-eminent and the trend becomes less significant than at lower equivalence ratios. On the other hand, the increase in the f_v for the

DMF flame series increases notably even at higher equivalence ratios. This analysis shows that the conditions for F5 and F7 studies in this work for aromatics and soot lie in a range where the soot inception process are predominating the soot growth processes.

In parallel to the LII measurements, PSDs were also determined for the two flames via the SMPS. It must be noted that the f_v in flame F5 is 4 times higher than in flame F7 (at HAB = 18 mm). In order to compare the PSDs of two different flames, it is essential that they are determined using the same dilution ratio i.e., by using the same differential pressure as we are not correcting for the dilution ratio at this stage of analysis. Since the f_v in one flame is much higher than the other, it is not feasible to generalize and apply the same differential pressure to determine the PSDs for both flames. It was found that the differential pressure to run smooth PSDs measurements was nearly 14 and 12 mbar for flames F5 and flame F7 respectively. The raw PSDs obtained for the two flames are presented in Figure 6. 10. It must be noted that these size distributions cannot be compared to one another as they have not been determined in similar conditions, but need to be investigated to gain further insights rather independently. In other words, the two flames cannot be compared directly. A minimum of three acquisitions were taken at several HABs to verify the reproducibility of the measurements. More information concerning the soot growth along the flame can be revealed via a comprehensive analysis of the variation of the soot size distributions with flame height in the same way as presented for the other flames in the previous section.

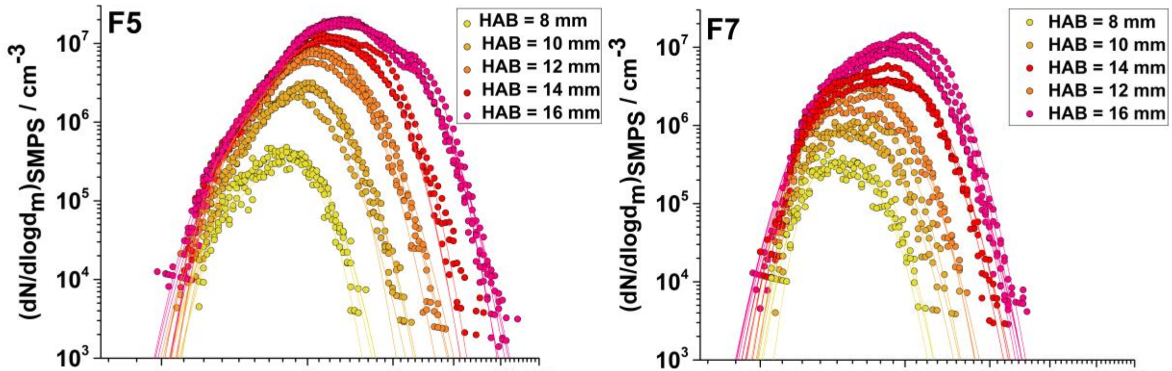

Figure 6. 10: Soot PSDs (log scale) recorded for flames F5 and F7 where colored symbols denote the raw measured distributions whereas the lines represent cumulative log-normal fits for each acquisition.

To do so, Equation 6. 1 was again used to frame a theoretical log-normal distribution function to replicate the measured PSDs as discussed previously. Thus, measured PSDs were closely fit with one or a combination of two or three log-normal functions if necessary (depending on the HAB). In this manner, the onset of bimodality in the size distribution was estimated from the residual analysis of these fits.

Figure 6. 11 presents the measured PSDs (the black empty circles) and the associated log-normal functions from Equation 6. 1 (solid lines) for flames F5 and flame F7. Red, green, and pink solid lines represent Mode-1, Mode-2 and Mode-3 respectively. Though each recorded acquisition was fit and analyzed individually (as presented in Figure 6. 10), an average distribution per HAB is presented in the figure and discussed in the following text for a lucid interpretation of the data. It must be noted that the PSDs for the two flames are determined with different dilutions which is why the soot particle number as well as the areas under the distributions cannot be compared as these parameters are sensitive to the dilution ratio. However, there are still some conclusions that can be drawn from Figure 6. 11.

As shown in the figure, the size of the particles in the flames is very small with $d_{\mathrm{m}} < 10$ nm. Mode-1 could present formation of incipient particles and Mode-2 probably consists of small soot agglomerates which evolve to larger diameters for both flames. The distributions exhibit a characteristic evolution from the inception mode to a bimodal distribution at higher HABs. However, if we see the evolution of the modes in flame F5, one log-normal function was not sufficient even at an HAB of 7 mm and thus at least two log-normal functions were always required to fit the PSDs at all flame heights. At higher HABs, i.e., at about 10 mm, three log-normal functions were used to make a fit that could best describe the raw PSDs. It is not usual to use more than two modes to describe the best cumulative fit.

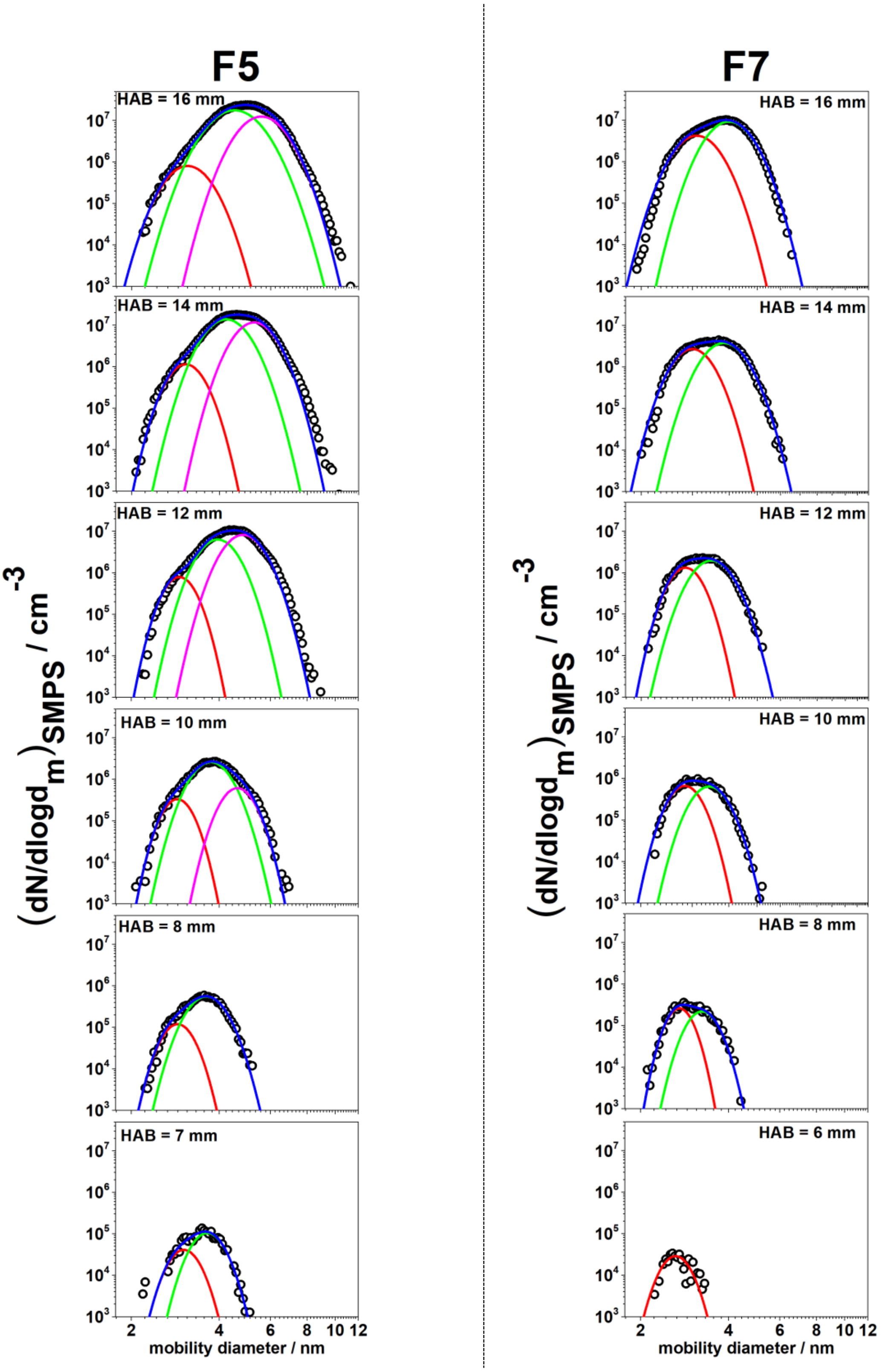

Figure 6. 11 : Evolution of the PSD as a function of HAB for flames F5 and F7. Black circles represent the measured PSD whereas lines present the log-normal fits; log-normal fit for Mode-1, Mode-2 and Mode-3 are presented by the red, green, and pink lines respectively whereas the blue line represents the combined cumulative fit.

To be able to perform the comparison with LII, the differential pressure was kept constant at all HABs in F5. It might very well be that Mode-3 emerged due to post-coagulation of Mode-2 as the dilution ratio was constantly fixed. In order to verify if Mode-3 was indeed real or an artifact, we increased the dilution ratio (i.e., lowered the differential pressure) at constant HAB. It was seen that Mode-3 became indistinct with progressive increase in dilution indicating that it was perhaps due to post-sampling coagulation. Nevertheless, since measurements were performed using constant dilution, PSDs were not ideal in this specific case because of the reasons just discussed. As a consequence, three modes were primordial to fit the experimentally measured PSDs.

In flame F5, there is a greater number of particles in Mode-2 since the onset of soot formation. This could indicate that the early soot particles are quickly undergoing the growth processes to form particles with slightly larger diameters thereby being consumed in the process. Though incipient particles collide and coagulate to form larger sized particles, they do not seem to completely disappear even at the highest probe position employed. Mode-2 is always accompanied with Mode-1 even though its intensity is always greater than the latter and is constantly increasing with HAB.

On the other hand, for flame F7, Mode-1 dominates at lower HABs. The unimodal distribution can be attributed to a burst in the particle inception related to the rise and the fall of the PAHs. Later, incipient soot particles could grow and initiate the development of Mode-2. After the onset of bimodality at HAB of 8 mm, Mode-2 increases gradually, becomes equivalent to Mode-1, and finally surpasses it. However, it seems that there is persistent inception and constant bimodality occurring at the same time. As also observed for flame F5, Mode-1 never disappears in flame F7 as well. The onset of bimodality however starts earlier in flame F5 in contrast to flame F7. This indicates that the soot growth processes if involved, started earlier in flame F5 as compared in flame F7. At HAB of 16 mm, the ratio of the number of particles in Mode-2/Mode-1 is greater in flame F5 than in flame F7.

Figure 6. 12 presents an evolution of the median diameters associated with the different modes with respect to the flame height for flame F5 and flame F7 respectively. It must be noted that the particles present in these flames are also very small with most particles having diameters less than ~5-6 nm. The median diameters corresponding to Mode-1 in this case are slightly higher than what was found for other flames (F1, F2 and F3). The median diameter for Mode-1 in F5 is ~ 3 nm whereas the median diameter for Mode-1 in F7 is not constant at a given value. It starts with ~2.6 nm at early HABs and increases slightly until ~3.15 nm at 16 mm. For soot particles belonging to Mode-2, there is a continuous increase in their median diameters with respect to the flame height in both flames. This increase is more important in

flame F5 and is rather gradual in flame F7 signifying that growth to larger particle diameters is probably more rapid in F5. The median diameter of particles associated to Mode-3 is also increasing with a similar tendency. Mode-3 is however not present in flame F7.

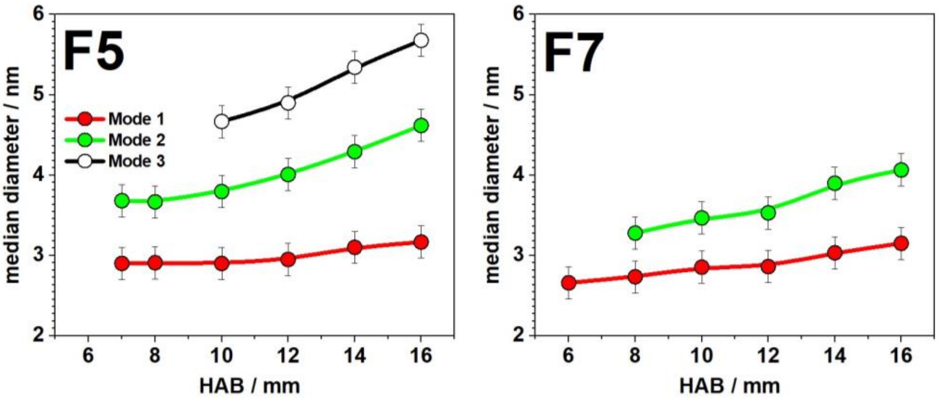

Figure 6. 12: Evolution of the median diameter of Mode-1, Mode-2, and Mode-3 with respect to the flame height for flames F5 and F7.

It must be noted that widths and areas of the modes cannot be compared between F5 and F7 as they were performed using different dilutions. However, they can be studied independently. Figure 6. 13 presents the evolution of the widths and the areas associated with the different modes with respect to HAB for flame F5. In theory, it is expected that a larger number of particles in Mode-1 would imply a higher collision frequency, that should credibly lead to larger particles. The continuous upswing of the width of Mode-2 in F5 indicates a likelihood of formation of soot aggregates. As a result of the competition of small particles generated by inception and those consumed via growth in F5, Mode-1 has smaller values of the geometric standard deviation indicating that the inception becomes less dominant than growth process at higher HABs in F5.

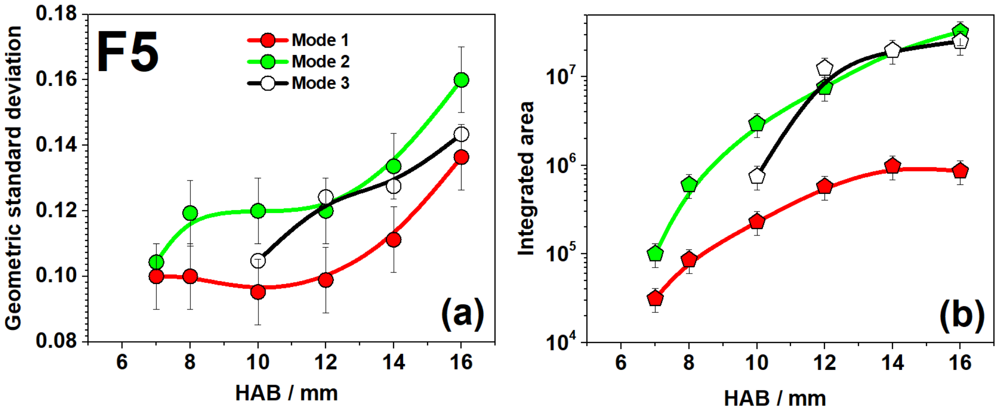

Figure 6. 13: Evolution of the widths and the integrated areas associated with the modes for flame F5.

Figure 6. 14 presents the evolution of the widths and the areas associated with the different modes with respect to HAB for flame F7. The areas under the two modes are in accordance with the increase of their widths. At HAB=6 mm, inception processes dominate and from HAB=8mm onwards, growth processes also come into picture. The number of particles associated with both modes continue to increase as HAB increases. It is interesting to note that the particles in Mode-2 are always more than particles in Mode-1 at a given HAB. As the HAB increases, the difference in the particle number in the two modes also increases indicating that growth processes somewhat start to dominate.

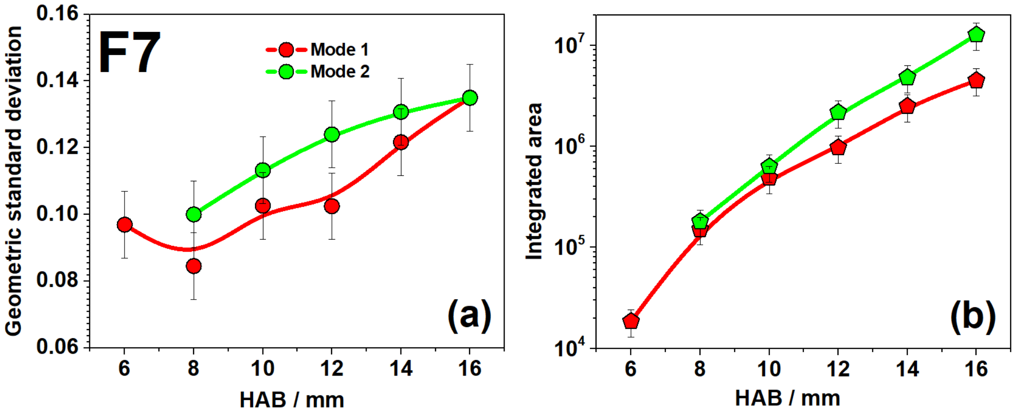

Figure 6. 14: Evolution of the widths and the integrated areas associated with the modes for flame F7.

6.3. Conclusion and perspectives

This chapter presents the experimental results and their subsequent analysis concerning the soot particle measurements using LII and SMPS. Soot volume fraction f_v profiles for flames F1, F2 and F3 could not be traced as we were at the threshold of the detection limit, however, at least one value of f_v (at HAB of 16 mm) was determined. For flames F5 and F7, we obtained full f_v profiles with respect to the flame height. Nevertheless, in terms of the f_v determined for the flames of investigation (i.e., ppt levels of soot), these flames could be considered as very slightly sooting. The f_v profiles were complemented with PSD measurements to get more insights about the size and the number density of the particles formed in these flames. In general, very small soot particles were observed in our flames of investigation with the median of the mobility diameter d_m consistently smaller than 5 nm. Understanding the formation of very small soot particles is not straightforward, however this study provides encouraging results and opens several new perspectives.

Experimental results indicated that anisole enhances soot formation by increasing the concentration of the early soot particles. It also produces more soot than DMF in similar conditions. Bimodal PSDs were observed in the flames possibly indicating particle inception followed by growth processes to form larger particles. f_v dependence on the equivalence ratio suggests that in the chosen conditions, though both soot inception and growth take place simultaneously, the former is dominant for flames F5 and F7. In general, it was observed that growth processes were limited and the size of the particles ranged over a few nanometers. This study provides a rich database for soot modeling. The interpretation discussed in the text relies solely on the analysis of the experimental results obtained using the two techniques. Additional investigations and soot modeling are necessary to derive a complete understanding of the mechanism involved in these flames.

Concerning the PSDs, the discussion in this chapter is limited to the raw SMPS output. Correction of the raw data and determination of the absolute number concentration of particles from the flames is an important perspective of this work. To evaluate the difference in the real number concentration and the SMPS output, we determined the f_v from the PSDs obtained using SMPS, and compared it with the f_v obtained using LII. Figure 6. 15 presents a correlation plot of the f_v determined using the two techniques. As seen in the figure, the correlation between the two techniques is not linear. LII relies on the ability of the particles to get heated whereas the SMPS relies on the ability of a particle to traverse an electric field which is fundamentally related to the particle size. The difference in the nature of the two techniques certainly implies the need of a systematic study to establish facts and reach new conclusions for their correlation. The final concentration number provided by the SMPS is biased by the sampling procedure as the PSDs are sensitive to the dilution ratio and need to undergo some corrections for the same. Another important phenomenon is the possibility of losing particles in the sampling line. Even after substantial dilution, because of the small size and high concentrations of soot particles, it is possible that aerosol processes may distort the measurements during transport of the diluted sample: diffusion and coagulation being the dominant processes of concern. The small particles are more susceptible to be lost in the line in comparison to the bigger particles as smaller soot particles have faster diffusion speeds. This implies that the loss of small particles during measurements is consequential and must be corrected. Diffusion losses of soot particles occurs when the particles collide with and stick to the surface of the sampling line due to the Van der Waals forces, electrostatic forces or via surface tensions. The quantitative estimation of the soot particles losses via diffusion during their transport in the line is challenging and very well beyond the scope of this thesis. Real quantification of the absolute number is a challenging step and this correction would be the following step to derive a more comprehensive understanding of the data.

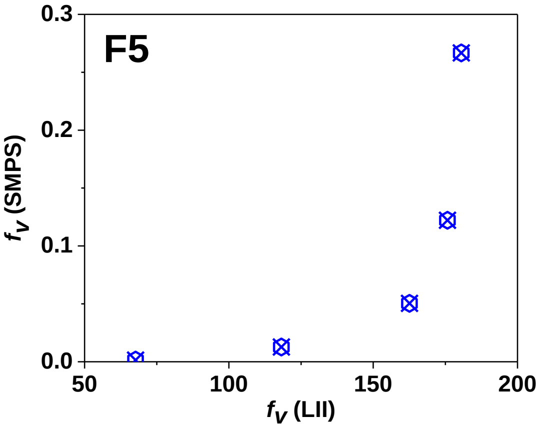

Figure 6. 15 : Correlation of the f_v determined by LII and SMPS.

General conclusion and perspectives

Though the transition to decarbonize the current energy system is happening, it is certainly not fast enough for the renewables and nuclear to keep up with the growing energy demand. Particularly for the transport sector, the introduction of biofuels is considered as one of the most promising options to attain decarbonization. Transport fuels are now subjected to blending mandates with alternative fuels to achieve ambitious emission targets and reduce our dependency on fossil fuels. In this context, lignin-based biofuels are infrastructure-compatible liquid transportation fuels which can fulfil such mandates as they are identical to the petroleum-based fuels that they are designed to replace. Due to the presence of a large portion of aromatic rings with oxygen functionalities in lignin, OPAHs are expected to constitute a large family of undesirable pollutants from the combustion of biomass and lignin-based biofuels. Studies focusing on the formation of OPAHs, its link with PAHs and soot from the combustion of lignin-based biofuels are very scarce in the literature. However, to achieve safe integration of these biofuels into our energy system, studies on OPAHs emissions and the size of soot particles generated during their combustion processes are amongst essential aspects. This information is somewhat crucial for decoding their impact on the environment.

In this context, the main objective of this thesis work was (1) to detect and quantify the different oxygenated aromatics as well as the associated PAHs, and (2) to evaluate the size of the soot particles from biofuels oxidation in flame conditions. In this study, anisole was employed as the simplest model compound to represent lignin-based biofuels. A comparison with other biofuels, DMF (a potential new 2nd generation cellulose-based biofuel) and ethanol (already in commercial use), has been also performed. In this report, we have presented experimental results on different intermediate species especially non-oxygenated and oxygenated aromatics in anisole/iso-octane/CH_4/O_2/N_2 atmospheric laminar flat premixed flames. Overall, seven flames were stabilized. Out of the seven flames, the first flame was a reference flame and did not contain any biofuel. The remaining flames were stabilized with the biofuel, out of which four flames contained anisole and two flames were stabilized using DMF and ethanol. All these flames were stabilized in slightly sooting conditions to study the aromatics and the primary soot particles. Different series of flames were categorized to study the influence of the biofuel amount, the equivalence ratio and the biofuel structure on the formation of aromatics. In general, the identification of species was carried out using 1-D and 2-D GC-MS setups and species were quantified using 1-D GC-TCD-FID and 1-D GC-SPT-TCD-FID setups. The analytical system used in this work enables us to identify nearly 100 oxygenated aromatic species produced in anisole flames. Numerous species amongst these have been identified for the first time in this work. A comprehensive approach based on different split injections was used to resolve the complex mixture including non-oxygenated aromatics to perform an exhaustive identification of species. These species highlighted the significant implication of the phenoxy radical, a primary radical produced in the early stages during the combustion chemistry of lignin-based fuels like anisole. So far, only a few out of the identified oxygenated aromatics are included in the current kinetic mechanisms which implies that the available mechanisms are still incomplete. In order to build trustworthy kinetic models, it is necessary to take these species into account as their absence in the current models can play a significant role in the overall behavior of the models. None of the oxygenated aromatics were observed in the reference flame without anisole which confirmed the contribution of anisole. Nearly 80 intermediate species were overall quantified in this work. Calibration of absolute concentrations was performed using commercial standard mixtures for smaller species and using the vapor pressure method for heavier aromatics. For the remaining species, the response factors were estimated. It was interesting to note that anisole had lesser impact on the formation of smaller intermediate species but greatly affected the formation of non-oxygenated as well as oxygenated aromatics, especially OPAHs and PAHs. Anisole is susceptible to produce the phenoxy radical by losing the methyl group and this phenoxy radical can undergo self-combination or combination reactions with other aromatic radicals to produce different types of oxygenated aromatics. It was observed that not only the amount of anisole in the fuel, the equivalence ratio of the flame also plays a role in the formation of oxygenated aromatics. This study provides an experimental database to develop and validate chemical kinetic mechanisms. The comparison between the OPAHs and PAHs in a given flame indicates that the OPAHs (up to three rings) are formed and decomposed before the peak mole fractions of PAHs are attained.

In addition to the effect exerted by the anisole amount and the equivalence ratio, two other flames containing ethanol and DMF were also compared with anisole flames. As expected, no oxygenated aromatics were observed for the ethanol flame and other aromatics species' formation was reduced in comparison to anisole. However, small oxygenated species like acetaldehyde and acetone significantly increased in the presence of ethanol with respect to the anisole flame. On comparison with the DMF flame, it was found that the formation of small oxygenated species like formaldehyde, acetaldehyde, propanal, and acetone increased in the DMF in comparison to the anisole flame. On the contrary, though DMF produces some oxygenated aromatics, the potential of anisole in producing oxygenated aromatics is much more significant in comparison to DMF.

Together with the study of the gas phase aromatics, primary soot particles were also characterized using LII and SMPS. The soot particles measured in the studied flames are smaller than 10 nm. It was observed that at constant equivalence ratio, anisole increases the number of small soot particles formed in these flames. These particles are referred to as primary soot particles on account of their small size. It was observed that the soot inception processes start at early HABs in the anisole flames as compared to the reference flame. Also soot growth processes overall were very limited in these flames. At higher equivalence ratio of 1.90, anisole produced more soot than DMF in similar conditions. It was observed that though the growth processes were limited, they occurred at a faster pace in anisole flame in comparison to the DMF flame. Together with the measurement of oxygenated aromatics and soot particles, determination of the temperature profile in this work was carried out using an experimental protocol which was validated in this thesis for laminar premixed flames by comparison with other techniques like LIF-NO. We have shown that the implementation of the extrapolation method, requiring the use of 4 thermocouples of different diameters, allowed very simple calibration of the radiative losses.

Though this work did shed some light on the oxygenated aromatics and the size of soot particles in these flames, there is still a lot to be explored. Though several oxygenated aromatics were identified and quantified in this work, some signals could not be identified. Additionally, several OPAHs with three or more oxygen atoms though identified in this work are not reported in the thesis report as more specific studies are needed to analyze and confirm their identification. A thorough and complete kinetic model being currently developed at our laboratory will be improvised to include the identified oxygenated aromatics and would be tested with the experimental database. Only stable gas phase species have been studied in this work and certainly more sophisticated spectroscopic techniques (like the Electron Paramagnetic Resonance, EPR) are necessary to study other aromatic radicals formed in these flames to gain some deeper insights. Some work on the use of EPR is already underway to perform PAHs analysis in laminar diffusion flames [272]. Though aromatic species and soot formation studies are carried out independently in this work, it is still too early to answer the scientific question concerning whether the OPAHs play a role in the formation of soot particles which is why complimentary studies would be certainly necessary to understand the mechanism involved. It would be interesting to perform a pyrolysis study on anisole in other reactors to confirm if the oxygen in OPAHs is coming from the oxidant or the fuel itself. The study on small sized soot particles in this work provides a rich experimental database for soot modelling to understand better the mechanism involved. The particle size distributions presented in this work were not corrected for the dilution ratio and the diffusion losses (biases linked to the analysis methods used) and constitute an important perspective of this work.

Finally, it is important not to lose sight of the fact that this work aims to improve the quality of the environment in which future generations will live. All the knowledge accumulated in this work finds an ideal application for example in the characterization of the environmental impact of new fuels, and in particular for those based on mixtures of hydrocarbons with lignin-based biofuels which are an important center of attention in the domain of combustion kinetics. In a socio-economic context, which is still struggling to make a transition towards lesser environmental impact from human activities, still relies largely on combustion to guarantee a large part of basic services, which is why the capacity to predict and effectively characterize the formation of toxic pollutants is fundamental to developing more efficient and less polluting transport systems.

References

[1] Johnsson F, Kjärstad J, Rootzén J. The threat to climate change mitigation posed by the abundance of fossil fuels. Clim Policy 2019;19:258–74. https://doi.org/10.1080/14693062.2018.1483885.

[2] Zhang X, Zhang M, Zhang H, Jiang Z, Liu C, Cai W. A review on energy, environment and economic assessment in remanufacturing based on life cycle assessment method. J Clean Prod 2020;255:120160. https://doi.org/10.1016/j.jclepro.2020.120160.

[3] IEA (2022), World Energy Outlook 2022, IEA, Paris https://www.iea.org/reports/world-energy-outlook-2022, License: CC BY 4.0 (report); CC BY NC SA 4.0 (Annex A). IEA n.d.

[4] Abdel-Shafy HI, Mansour MSM. A review on polycyclic aromatic hydrocarbons: Source, environmental impact, effect on human health and remediation. Egypt J Pet 2016;25:107–23. https://doi.org/10.1016/j.ejpe.2015.03.011.

[5] IEA (2021), The role of critical minerals in clean energy transitions, iea, paris https://www.iea.org/reports/the-role-of-critical-minerals-in-clean-energy-transitions, license: cc by 4.0. IEA n.d. https://www.iea.org/reports/the-role-of-critical-minerals-in-clean-energy-transitions/executive-summary.

[6] Cox B, Innis S, Kunz NC, Steen J. The mining industry as a net beneficiary of a global tax on carbon emissions. Commun Earth Environ 2022;3:1–8. https://doi.org/10.1038/s43247-022-00346-4.

[7] Ritchie H, Rosado P, Roser M. Emissions by sector. Our World Data 2023.

[8] Gray N, McDonagh S, O'Shea R, Smyth B, Murphy JD. Decarbonising ships, planes and trucks: An analysis of suitable low-carbon fuels for the maritime, aviation and haulage sectors. Adv Appl Energy 2021;1:100008. https://doi.org/10.1016/j.adapen.2021.100008.

[9] Kohse-Höinghaus K. Combustion in the future: The importance of chemistry. Proc Combust Inst 2021;38:1–56. https://doi.org/10.1016/j.proci.2020.06.375.

[10] Battin-Leclerc F, Delort N, Meziane I, Herbinet O, Sang Y, Li Y. Possible use as biofuels of monoaromatic oxygenates produced by lignin catalytic conversion: A review. Catal Today 2023;408:150–67. https://doi.org/10.1016/j.cattod.2022.06.006.

[11] Kohse-Höinghaus K, Oßwald P, Cool TA, Kasper T, Hansen N, Qi F, et al. Biofuel combustion chemistry: from ethanol to biodiesel. Angew Chem Int Ed 2010;49:3572–97. https://doi.org/10.1002/anie.200905335.

[12] Jeswani H, Chilvers A, Azapagic A. Environmental sustainability of biofuels: a review. Proc R Soc Math Phys Eng Sci 2020;476:20200351. https://doi.org/10.1098/rspa.2020.0351.

[13] Bae C, Kim J. Alternative fuels for internal combustion engines. Proc Combust Inst 2017;36:3389–413. https://doi.org/10.1016/j.proci.2016.09.009.

[14] Fayyazbakhsh A, Pirouzfar V. Comprehensive overview on diesel additives to reduce emissions, enhance fuel properties and improve engine performance. Renew Sustain Energy Rev 2017;74:891–901. https://doi.org/10.1016/j.rser.2017.03.046.

[15] Shih CF, Zhang T, Li J, Bai C. Powering the future with liquid sunshine. Joule 2018;2:1925–49. https://doi.org/10.1016/j.joule.2018.08.016.

[16] Hirani AH, Javed N, Asif M, Basu SK, Kumar A. A review on first- and second-generation biofuel productions. In: Kumar A, Ogita S, Yau Y-Y, editors. Biofuels Greenh. Gas Mitig.

Glob. Warm. Gener. Biofuels Role Biotechnol., New Delhi: Springer India; 2018, p. 141–54. https://doi.org/10.1007/978-81-322-3763-1_8.

[17] Sims REH, Mabee W, Saddler JN, Taylor M. An overview of second generation biofuel technologies. Bioresour Technol 2010;101:1570–80. https://doi.org/10.1016/j.biortech.2009.11.046.

[18] Timilsina GR, Cheng JJ. Advanced biofuel technologies : status and barriers. The World Bank; 2010. https://doi.org/10.1596/1813-9450-5411.

[19] Xu L, Wang Y, Liu D. Effects of oxygenated biofuel additives on soot formation: A comprehensive review of laboratory-scale studies. Fuel 2022;313:122635. https://doi.org/10.1016/j.fuel.2021.122635.

[20] Kozak M, Merkisz J. Oxygenated diesel fuels and their effect on pm emissions. Appl Sci 2022;12:7709. https://doi.org/10.3390/app12157709.

[21] Guan C, Cheung CS, Li X, Huang Z. Effects of oxygenated fuels on the particle-phase compounds emitted from a diesel engine. Atmospheric Pollut Res 2017;8:209–20. https://doi.org/10.1016/j.apr.2016.08.005.

[22] Lapuerta M, Oliva F, Agudelo JR, Boehman AL. Role of dimethyl ether in incipient soot formation in premixed ethylene flames. Combust Flame 2012;159:844–53. https://doi.org/10.1016/j.combustflame.2011.09.003.

[23] Sirignano M, Conturso M, Magno A, Di lorio S, Mancaruso E, Vaglieco BM, et al. Evidence of sub-10 nm particles emitted from a small-size diesel engine. Exp Therm Fluid Sci 2018;95:60–4. https://doi.org/10.1016/j.expthermflusci.2018.01.031.

[24] Lapuerta M, Martos FJ, Herreros JM. Effect of engine operating conditions on the size of primary particles composing diesel soot agglomerates. J Aerosol Sci 2007;38:455–66. https://doi.org/10.1016/j.jaerosci.2007.02.001.

[25] Lapuerta M, Armas O, Rodríguez-Fernández J. Effect of biodiesel fuels on diesel engine emissions. Prog Energy Combust Sci 2008;34:198–223. https://doi.org/10.1016/j.pecs.2007.07.001.

[26] Chen B, Kruse S, Schmid R, Cai L, Hansen N, Pitsch H. Oxygenated PAH formation chemistry investigation in anisole jet stirred reactor oxidation by a thermodynamic approach. Energy Fuels 2021;35:1535–45. https://doi.org/10.1021/acs.energyfuels.0c03829.

[27] Lundstedt S, White PA, Lemieux CL, Lynes KD, Lambert IB, Öberg L, et al. Sources, fate, and toxic hazards of oxygenated polycyclic aromatic hydrocarbons (PAHs) at PAH-contaminated sites. Ambio 2007;36:475–85.

[28] Xiao L, Hu S, Han H, Ren Q, He L, Jiang L, et al. An insight into the OPAHs and SPAHs formation mechanisms during alkaline lignin pyrolysis at different temperatures. J Anal Appl Pyrolysis 2021;156:105104. https://doi.org/10.1016/j.jaap.2021.105104.

[29] Kanaly R, Harayama S. Biodegradation of high molecular weight polycyclic aromatic hydrocarbons by bacteria. J Bacteriol 2000;182:2059–67. https://doi.org/10.1128/JB.182.8.2059-2067.2000.

[30] Raquel S, Natalia G, Luis Fernando B, Maria Carmen M. Biodegradation of high-molecular-weight polycyclic aromatic hydrocarbons by a wood-degrading consortium at low temperatures. FEMS Microbiol Ecol 2013;83:438–49. https://doi.org/10.1111/1574-6941.12006.

[31] Kochany J, Maguire RJ. Abiotic transformations of polynuclear aromatic hydrocarbons and polynuclear aromatic nitrogen heterocycles in aquatic environments. Sci Total Environ 1994;144:17–31. https://doi.org/10.1016/0048-9697(94)90424-3.

[32] Cerniglia CE. Fungal metabolism of polycyclic aromatic hydrocarbons: past, present and future applications in bioremediation. J Ind Microbiol Biotechnol 1997;19:324–33. https://doi.org/10.1038/sj.jim.2900459.

[33] Lampi M, Gurska J, McDonald K, Xie F, Huang X-D, Dixon DG, et al. Photoinduced toxicity of polycyclic aromatic hydrocarbons to Daphnia magna: Ultraviolet-mediated effects and the toxicity of polycyclic aromatic hydrocarbon photoproducts. Environ Toxicol Chem SETAC 2006;25:1079–87. https://doi.org/10.1897/05-276R.1.

[34] Yu H. Environmental carcinogenic polycyclic aromatic hydrocarbons: photochemistry and phototoxicity. J Environ Sci Health Part C Environ Carcinog Ecotoxicol Rev 2002;20:10.1081/GNC-120016203. https://doi.org/10.1081/GNC-120016203.

[35] Walgraeve C, Demeestere K, Dewulf J, Zimmermann R, Van Langenhove H. Oxygenated polycyclic aromatic hydrocarbons in atmospheric particulate matter: Molecular characterization and occurrence. Atmos Environ 2010;44:1831–46. https://doi.org/10.1016/j.atmosenv.2009.12.004.

[36] Hartnik T, Norli HR, Eggen T, Breedveld GD. Bioassay-directed identification of toxic organic compounds in creosote-contaminated groundwater. Chemosphere 2007;66:435–43. https://doi.org/10.1016/j.chemosphere.2006.06.031.

[37] Bamforth SM, Singleton I. Bioremediation of polycyclic aromatic hydrocarbons: current knowledge and future directions. J Chem Technol Biotechnol 2005;80:723–36. https://doi.org/10.1002/jctb.1276.

[38] Shen G, Tao S, Wang W, Yang Y, Ding J, Xue M, et al. Emission of oxygenated polycyclic aromatic hydrocarbons from indoor solid fuel combustion. Environ Sci Technol 2011;45:3459–65. https://doi.org/10.1021/es104364t.

[39] Vicente E, Vicente A, Bandowe B, Alves C. Particulate phase emission of parent polycyclic aromatic hydrocarbons (PAHs) and their derivatives (alkyl-PAHs, oxygenated-PAHs, azaarenes and nitrated PAHs) from manually and automatically fired combustion appliances. Air Qual Atmosphere Health 2015;9. https://doi.org/10.1007/s11869-015-0364-1.

[40] Nyström R, Sadiktsis I, Ahmed TM, Westerholm R, Koegler JH, Blomberg A, et al. Physical and chemical properties of RME biodiesel exhaust particles without engine modifications. Fuel 2016;186:261–9. https://doi.org/10.1016/j.fuel.2016.08.062.

[41] Ahmed TM, Bergvall C, Westerholm R. Emissions of particulate associated oxygenated and native polycyclic aromatic hydrocarbons from vehicles powered by ethanol/gasoline fuel blends. Fuel 2018;214:381–5. https://doi.org/10.1016/j.fuel.2017.11.059.

[42] Li X, Zheng Y, Guan C, Cheung CS, Huang Z. Effect of biodiesel on PAH, OPAH, and NPAH emissions from a direct injection diesel engine. Environ Sci Pollut Res 2018;25:34131–8. https://doi.org/10.1007/s11356-018-3382-3.

[43] Lara S, Villanueva F, Cabañas B, Sagrario S, Aranda I, Soriano JA, et al. Determination of policyclic aromatic compounds, (PAH, nitro-PAH and oxy-PAH) in soot collected from a diesel engine operating with different fuels. Sci Total Environ 2023;900:165755. https://doi.org/10.1016/j.scitotenv.2023.165755.

[44] Allen JO, Dookeran NM, Taghizadeh K, Lafleur AL, Smith KA, Sarofim AF. Measurement of oxygenated polycyclic aromatic hydrocarbons associated with a size-segregated urban aerosol. Environ Sci Technol 1997;31:2064–70. https://doi.org/10.1021/es960894g.

[45] Albinet A, Leoz-Garziandia E, Budzinski H, Villenave E, Jaffrezo J-L. Nitrated and oxygenated derivatives of polycyclic aromatic hydrocarbons in the ambient air of two French alpine valleys Part 2: Particle size distribution. Atmos Environ 2008;42:55–64. https://doi.org/10.1016/j.atmosenv.2007.10.008.

[46] Ahmed TM, Bergvall C, Westerholm R. Emissions of particulate associated oxygenated and native polycyclic aromatic hydrocarbons from vehicles powered by ethanol/gasoline fuel blends. Fuel 2018;214:381–5. https://doi.org/10.1016/j.fuel.2017.11.059.

[47] Therrien RJ, Ergut A, Levendis YA, Richter H, Howard JB, Carlson JB. Investigation of critical equivalence ratio and chemical speciation in flames of ethylbenzene–ethanol blends. Combust Flame 2010;157:296–312. https://doi.org/10.1016/j.combustflame.2009.07.023.

[48] Nowakowska M, Herbinet O, Dufour A, Glaude P-A. Detailed kinetic study of anisole pyrolysis and oxidation to understand tar formation during biomass combustion and gasification. Combust Flame 2014;161:1474–88. https://doi.org/10.1016/j.combustflame.2013.11.024.

[49] Pelucchi M, Faravelli T, Frassoldati A, Ranzi E, SriBala G, Marin GB, et al. Experimental and kinetic modeling study of pyrolysis and combustion of anisole. Chem Eng Trans 2018;65:127–32. https://doi.org/10.3303/CET1865022.

[50] Nowakowska M, Herbinet O, Dufour A, Glaude PA. Kinetic study of the pyrolysis and oxidation of guaiacol. J Phys Chem A 2018;122:7894–909. https://doi.org/10.1021/acs.jpca.8b06301.

[51] Bierkandt T, Hemberger P, Oßwald P, Krüger D, Köhler M, Kasper T. Flame structure of laminar premixed anisole flames investigated by photoionization mass spectrometry and photoelectron spectroscopy. Proc Combust Inst 2019;37:1579–87. https://doi.org/10.1016/j.proci.2018.07.037.

[52] Yerrayya A, Natarajan U, Vinu R. Fast pyrolysis of guaiacol to simple phenols: Experiments, theory and kinetic model. Chem Eng Sci 2019;207:619–30. https://doi.org/10.1016/j.ces.2019.06.025.

[53] Yuan W, Li T, Li Y, Zeng M, Zhang Y, Zou J, et al. Experimental and kinetic modeling investigation on anisole pyrolysis: Implications on phenoxy and cyclopentadienyl chemistry. Combust Flame 2019;201:187–99. https://doi.org/10.1016/j.combustflame.2018.12.028.

[54] Namysl S, Pelucchi M, Pratali Maffei L, Herbinet O, Stagni A, Faravelli T, et al. Experimental and modeling study of benzaldehyde oxidation. Combust Flame 2020;211:124–32. https://doi.org/10.1016/j.combustflame.2019.09.024.

[55] Kim Y, Etz BD, Fioroni GM, Hays CK, St. John PC, Messerly RA, et al. Investigation of structural effects of aromatic compounds on sooting tendency with mechanistic insight into ethylphenol isomers. Proc Combust Inst 2021;38:1143–51. https://doi.org/10.1016/j.proci.2020.06.321.

[56] Chen B, Hellmuth M, Faller S, May L, Liu P, Cai L, et al. Exploring the combustion chemistry of anisole in laminar counterflow diffusion-flames under oxy-fuel conditions. Combust Flame 2022;243:111929. https://doi.org/10.1016/j.combustflame.2021.111929.

[57] Wang T, Yalamanchi KK, Bai X, Liu S, Li Y, Qu B, et al. Computational thermochemistry of oxygenated polycyclic aromatic hydrocarbons and relevant radicals. Combust Flame 2023;247:112484. https://doi.org/10.1016/j.combustflame.2022.112484.

[58] Michelsen HA, Colket MB, Bengtsson P-E, D’Anna A, Desgroux P, Haynes BS, et al. A review of terminology used to describe soot formation and evolution under combustion

and pyrolytic conditions. ACS Nano 2020;14:12470–90. https://doi.org/10.1021/acsnano.0c06226.

[59] Frenklach M. Reaction mechanism of soot formation in flames. Phys Chem Chem Phys 2002;4:2028–37. https://doi.org/10.1039/B110045A.

[60] Frenklach M, Mebel AM. On the mechanism of soot nucleation. Phys Chem Chem Phys 2020;22:5314–31. https://doi.org/10.1039/D0CP00116C.

[61] McEnally CS, Pfefferle LD, Atakan B, Kohse-Höinghaus K. Studies of aromatic hydrocarbon formation mechanisms in flames: Progress towards closing the fuel gap. Prog Energy Combust Sci 2006;32:247–94. https://doi.org/10.1016/j.pecs.2005.11.003.

[62] D'Anna A. Combustion-formed nanoparticles. Proc Combust Inst 2009;32:593–613. https://doi.org/10.1016/j.proci.2008.09.005.

[63] Wang H. Formation of nascent soot and other condensed-phase materials in flames. Proc Combust Inst 2011;33:41–67. https://doi.org/10.1016/j.proci.2010.09.009.

[64] Desgroux P, Mercier X, Thomson KA. Study of the formation of soot and its precursors in flames using optical diagnostics. Proc Combust Inst 2013;34:1713–38. https://doi.org/10.1016/j.proci.2012.09.004.

[65] Michelsen HA. Probing soot formation, chemical and physical evolution, and oxidation: A review of in situ diagnostic techniques and needs. Proc Combust Inst 2017;36:717–35. https://doi.org/10.1016/j.proci.2016.08.027.

[66] Martin JW, Salamanca M, Kraft M. Soot inception: Carbonaceous nanoparticle formation in flames. Prog Energy Combust Sci 2022;88:100956. https://doi.org/10.1016/j.pecs.2021.100956.

[67] Thomson MJ. Modeling soot formation in flames and reactors: Recent progress and current challenges. Proc Combust Inst 2023;39:805–23. https://doi.org/10.1016/j.proci.2022.07.263.

[68] Kittelson D, Kraft M. Particle formation and models. Encycl. Automot. Eng., John Wiley & Sons, Ltd; 2014, p. 1–23. https://doi.org/10.1002/9781118354179.auto161.

[69] Richter H, Howard JB. Formation of polycyclic aromatic hydrocarbons and their growth to soot—a review of chemical reaction pathways. Prog Energy Combust Sci 2000;26:565–608. https://doi.org/10.1016/S0360-1285(00)00009-5.

[70] Hansen N, Cool TA, Westmoreland PR, Kohse-Höinghaus K. Recent contributions of flame-sampling molecular-beam mass spectrometry to a fundamental understanding of combustion chemistry. Prog Energy Combust Sci 2009;35:168–91. https://doi.org/10.1016/j.pecs.2008.10.001.

[71] Li Y, Qi F. Recent applications of synchrotron vuv photoionization mass spectrometry: insight into combustion chemistry. Acc Chem Res 2010;43:68–78. https://doi.org/10.1021/ar900130b.

[72] Wang Y, Chung SH. Soot formation in laminar counterflow flames. Prog Energy Combust Sci 2019;74:152–238. https://doi.org/10.1016/j.pecs.2019.05.003.

[73] Ni T, Gupta SB, Santoro RJ. Suppression of soot formation in ethene laminar diffusion flames by chemical additives. Symp Int Combust 1994;25:585–92. https://doi.org/10.1016/S0082-0784(06)80689-2.

[74] Rubino L, Thomson MJ. The effect of oxygenated additives on soot precursor formation in a counterflow diffusion flame. Warrendale, PA: SAE International; 1999. https://doi.org/10.4271/1999-01-3589.

[75] Curran HJ, Fisher EM, Glaude P-A, Marinov NM, Pitz WJ, Westbrook CK, et al. Detailed chemical kinetic modeling of diesel combustion with oxygenated fuels. Warrendale, PA: SAE International; 2001. https://doi.org/10.4271/2001-01-0653.

[76] Hoon Song K, Nag P, Litzinger TA, Haworth DC. Effects of oxygenated additives on aromatic species in fuel-rich, premixed ethane combustion: a modeling study. Combust Flame 2003;135:341–9. https://doi.org/10.1016/S0010-2180(03)00180-9.

[77] Sinha A, Thomson MJ. The chemical structures of opposed flow diffusion flames of C3 oxygenated hydrocarbons (isopropanol, dimethoxy methane, and dimethyl carbonate) and their mixtures. Combust Flame 2004;136:548–56. https://doi.org/10.1016/j.combustflame.2003.12.011.

[78] Wu J, Song KH, Litzinger T, Lee S-Y, Santoro R, Linevsky M, et al. Reduction of PAH and soot in premixed ethylene–air flames by addition of ethanol. Combust Flame 2006;144:675–87. https://doi.org/10.1016/j.combustflame.2005.08.036.

[79] Chen G, Yu W, Fu J, Mo J, Huang Z, Yang J, et al. Experimental and modeling study of the effects of adding oxygenated fuels to premixed n-heptane flames. Combust Flame 2012;159:2324–35. https://doi.org/10.1016/j.combustflame.2012.02.020.

[80] Sirignano M, Salamanca M, D'Anna A. The role of dimethyl ether as substituent to ethylene on particulate formation in premixed and counter-flow diffusion flames. Fuel 2014;126:256–62. https://doi.org/10.1016/j.fuel.2014.02.039.

[81] Zheng Z, Wang X, Yue L, Liu H, Yao M. Effects of six-carbon alcohols, ethers and ketones with chain or ring molecular structures on diesel low temperature combustion. Energy Convers Manag 2016;124:480–91. https://doi.org/10.1016/j.enconman.2016.07.057.

[82] Park W, Park S, Reitz RD, Kurtz E. The effect of oxygenated fuel properties on diesel spray combustion and soot formation. Combust Flame 2017;180:276–83. https://doi.org/10.1016/j.combustflame.2016.02.026.

[83] Song J, Zello V, Boehman AL, Waller FJ. Comparison of the impact of intake oxygen enrichment and fuel oxygenation on diesel combustion and emissions. Energy Fuels 2004;18:1282–90. https://doi.org/10.1021/ef034103p.

[84] Boot M, Frijters P, Luijten C, Somers B, Baert R, Donkerbroek A, et al. Cyclic oxygenates: a new class of second-generation biofuels for diesel engines? Energy Fuels 2009;23:1808–17. https://doi.org/10.1021/ef8003637.

[85] Cheng Z, Xing L, Zeng M, Dong W, Zhang F, Qi F, et al. Experimental and kinetic modeling study of 2,5-dimethylfuran pyrolysis at various pressures. Combust Flame 2014;161:2496–511. https://doi.org/10.1016/j.combustflame.2014.03.022.

[86] Sirignano M, Conturso M, D'Anna A. Effect of furans on particle formation in diffusion flames: An experimental and modeling study. Proc Combust Inst 2015;35:525–32. https://doi.org/10.1016/j.proci.2014.05.062.

[87] Alexandrino K, Millera Á, Bilbao R, Alzueta MU. Novel aspects in the pyrolysis and oxidation of 2,5-dimethylfuran. Proc Combust Inst 2015;35:1717–25. https://doi.org/10.1016/j.proci.2014.06.002.

[88] Viteri F, Baena C, Millera Á, Bilbao R, Alzueta MU. Formation of polycyclic aromatic hydrocarbons in the pyrolysis of 2-methylfuran at different reaction temperatures. Combust Sci Technol 2016;188:611–22. https://doi.org/10.1080/00102202.2016.1138827.

[89] Conturso M, Sirignano M, D'Anna A. Effect of furanic biofuels on particles formation in premixed ethylene–air flames: An experimental study. Fuel 2016;175:137–45. https://doi.org/10.1016/j.fuel.2016.02.038.

[90] Alexandrino K, Salvo P, Millera Á, Bilbao R, Alzueta MU. Influence of the temperature and 2,5-dimethylfuran concentration on its sooting tendency. Combust Sci Technol 2016;188:651–66. https://doi.org/10.1080/00102202.2016.1138828.

[91] Liu H, Zhang P, Liu X, Chen B, Geng C, Li B, et al. Laser diagnostics and chemical kinetic analysis of PAHs and soot in co-flow partially premixed flames using diesel surrogate and oxygenated additives of n-butanol and DMF. Combust Flame 2018;188:129–41. https://doi.org/10.1016/j.combustflame.2017.09.025.

[92] Alexandrino K, Baena C, Millera Á, Bilbao R, Alzueta MU. 2-methylfuran pyrolysis: Gas-phase modelling and soot formation. Combust Flame 2018;188:376–87. https://doi.org/10.1016/j.combustflame.2017.10.017.

[93] Xiong G, Xie J, Chen L, Wang W, Zhou L. Sooting tendency of n-heptane/anisole blends in laminar counter-flow flames with oxygen enrichment. Fuel 2019;255:115820. https://doi.org/10.1016/j.fuel.2019.115820.

[94] Etz BD, Fioroni GM, Messerly RA, Rahimi MJ, St. John PC, Robichaud DJ, et al. Elucidating the chemical pathways responsible for the sooting tendency of 1 and 2-phenylethanol. Proc Combust Inst 2021;38:1327–34. https://doi.org/10.1016/j.proci.2020.06.072.

[95] Wang W, Zhang Z, Shi D, Huang Y, Zhou L. Study of soot formations in co-flow laminar diffusion flames of n-heptane and oxygenated aromatic biofuels from atmospheric condition to 2.3 bar. Fuel 2021;297:120753. https://doi.org/10.1016/j.fuel.2021.120753.

[96] Cruz JJ, Escudero F, Verdugo I, Rivera P, Gutiérrez-Cáceres N, Yon J, et al. Sooting propensity and maturity of gasoline/anisole blends in a laminar coflow diffusion flame. Fuel 2023;345:128091. https://doi.org/10.1016/j.fuel.2023.128091.

[97] Gogoi B, Raj A, Alrefaai MM, Stephen S, Anjana T, Pillai V, et al. Effects of 2,5-dimethylfuran addition to diesel on soot nanostructures and reactivity. Fuel 2015;159:766–75. https://doi.org/10.1016/j.fuel.2015.07.038.

[98] Russo C, D'Anna A, Ciajolo A, Sirignano M. Analysis of the chemical features of particles generated from ethylene and ethylene/2,5 dimethyl furan flames. Combust Flame 2016;167:268–73. https://doi.org/10.1016/j.combustflame.2016.02.003.

[99] Guerrero Peña GDJ, Hammid YA, Raj A, Stephen S, Anjana T, Balasubramanian V. On the characteristics and reactivity of soot particles from ethanol-gasoline and 2,5-dimethylfuran-gasoline blends. Fuel 2018;222:42–55. https://doi.org/10.1016/j.fuel.2018.02.147.

[100] Alexandrino K, Millera Á, Bilbao R, Alzueta MU. Reactivity and physicochemical properties of the soot produced in the pyrolysis of 2,5-dimethylfuran and 2-methylfuran. Energy Fuels 2019;33:9851–8. https://doi.org/10.1021/acs.energyfuels.9b01760.

[101] Jiang B, Wang P, Liu D. Effects of magnetic fields on morphology and nanostructure evolution of incipient soot particles from n-heptane/2,5-dimethylfuran inverse diffusion flames. J Therm Sci 2020;29:820–39. https://doi.org/10.1007/s11630-020-1262-x.

[102] Jiang B, Jia P, Liu D. Comparative study on soot characteristics of non-swirling and swirling inverse diffusion iso-octane flames with biofuel 2,5-dimethylfuran addition. J Energy Inst 2020;93:2108–23. https://doi.org/10.1016/j.joei.2020.05.006.

[103] Chu H, Ya Y, Nie X, Zhou Y, Hu J, Dong S, et al. Effects of ethanol and 2, 5-dimethylfuran addition on the morphology and nanostructure evolution of soot in gasoline primary reference fuel-air coflow diffusion flames. Fuel 2020;281:118711. https://doi.org/10.1016/j.fuel.2020.118711.

[104]Zhang C, Wu Y, Liu B, Wang Z, Zhou L. Investigation of soot particles morphology and size distribution produced in a n-heptane/anisole laminar diffusion flame based on TEM images. Combust Flame 2022;244:112234. https://doi.org/10.1016/j.combustflame.2022.112234.

[105]Conturso M, Sirignano M, D'Anna A. Effect of 2,5-dimethylfuran doping on particle size distributions measured in premixed ethylene/air flames. Proc Combust Inst 2017;36:985–92. https://doi.org/10.1016/j.proci.2016.06.048.

[106]Xiong G, Boot M, Zhou L, Reijnders J, De Goey P. Soot particle size distribution measurements in laminar diffusion flames of n-heptane with oxygenated aromatic fuel additives by time-resolved laser-induced incandescence. Energy Fuels 2018;32:11511–8. https://doi.org/10.1021/acs.energyfuels.8b02012.

[107]McCormick RL, Ratcliff MA, Christensen E, Fouts L, Luecke J, Chupka GM, et al. Properties of oxygenates found in upgraded biomass pyrolysis oil as components of spark and compression ignition engine fuels. Energy Fuels 2015;29:2453–61. https://doi.org/10.1021/ef502893g.

[108]Custodis VBF, Hemberger P, Ma Z, van Bokhoven JA. Mechanism of fast pyrolysis of lignin: studying model compounds. J Phys Chem B 2014;118:8524–31. https://doi.org/10.1021/jp5036579.

[109]Britt PF, Buchanan AC, Cooney MJ, Martineau DR. Flash vacuum pyrolysis of methoxy-substituted lignin model compounds. J Org Chem 2000;65:1376–89. https://doi.org/10.1021/jo991479k.

[110]Lu X, Gu X. A review on lignin pyrolysis: pyrolytic behavior, mechanism, and relevant upgrading for improving process efficiency. Biotechnol Biofuels Bioprod 2022;15:106. https://doi.org/10.1186/s13068-022-02203-0.

[111] Cozzani V, Lucchesi A, Stoppato G, Maschio G. A new method to determine the composition of biomass by thermogravimetric analysis. Can J Chem Eng 1997;75:127–33. https://doi.org/10.1002/cjce.5450750120.

[112] Chiaramonti D, Buffi M, Palmisano P, Redaelli S. Lignin-based advanced biofuels: a novel route towards aviation fuels. Chem Eng Trans 2016;50:109–14. https://doi.org/10.3303/CET1650019.

[113] Christensen E, Fioroni GM, Kim S, Fouts L, Gjersing E, Paton RS, et al. Experimental and theoretical study of oxidative stability of alkylated furans used as gasoline blend components. Fuel 2018;212:576–85. https://doi.org/10.1016/j.fuel.2017.10.066.

[114] Gschwend D, Soltic P, Wokaun A, Vogel F. Review and performance evaluation of fifty alternative liquid fuels for spark-ignition engines. Energy Fuels 2019;33:2186–96. https://doi.org/10.1021/acs.energyfuels.8b02910.

[115] Singerman GM. Novel anisole mixture and gasoline containing the same. US4312636A, 1982.

[116] McCormick RL, Fioroni G, Fouts L, Christensen E, Yanowitz J, Polikarpov E, et al. Selection criteria and screening of potential biomass-derived streams as fuel blendstocks for advanced spark-ignition engines. SAE Int J Fuels Lubr 2017;10:442–60. https://doi.org/10.4271/2017-01-0868.

[117] Lin C-Y, Lin MC. Thermal decomposition of methyl phenyl ether in shock waves: the kinetics of phenoxy radical reactions. J Phys Chem 1986;90:425–31. https://doi.org/10.1021/j100275a014.

[118] Hemings EB, Bozzano G, Dente M, Ranzi E. Detailed kinetics of the pyrolysis and oxidation of anisole. Chem Eng Trans 2011;24:61–6. https://doi.org/10.3303/CET1124011.

[119] Herzler J, Fikri M, Schulz C. Ignition delay time study of aromatic lif tracers in a wide temperature and pressure range, Int Colloq Dyn Explos React Syst ICDERS Boston MA; 2017.

[120] Büttgen RD, Tian M, Fenard Y, Minwegen H, Boot MD, Heufer KA. An experimental, theoretical and kinetic modelling study on the reactivity of a lignin model compound anisole under engine-relevant conditions. Fuel 2020;269:117190. https://doi.org/10.1016/j.fuel.2020.117190.

[121] Mergulhão CS, Carstensen H-H, Song H, Wagnon SW, Pitz WJ, Vanhove G. Probing the antiknock effect of anisole through an ignition, speciation and modeling study of its blends with isooctane. Proc Combust Inst 2020. https://doi.org/10.1016/j.proci.2020.08.013.

[122] Wu Y, Rossow B, Modica V, Yu X, Wu L, Grisch F. Laminar flame speed of lignocellulosic biomass-derived oxygenates and blends of gasoline/oxygenates. Fuel 2017;202:572–82. https://doi.org/10.1016/j.fuel.2017.04.085.

[123] Wagnon SW, Thion S, Nilsson EJK, Mehl M, Serinyel Z, Zhang K, et al. Experimental and modeling studies of a biofuel surrogate compound: laminar burning velocities and jet-stirred reactor measurements of anisole. Combust Flame 2018;189:325–36. https://doi.org/10.1016/j.combustflame.2017.10.020.

[124] Zare S, Roy S, El Maadi A, Askari O. An investigation on laminar burning speed and flame structure of anisole-air mixture. Fuel 2019;244:120–31. https://doi.org/10.1016/j.fuel.2019.01.149.

[125] Zabeti S, Aghsaee M, Fikri M, Welz O, Schulz C. Optical properties and pyrolysis of shock-heated gas-phase anisole. Proc Combust Inst 2017;36:4525–32. https://doi.org/10.1016/j.proci.2016.06.156.

[126] Arends IWCE, Louw R, Mulder P. Kinetic study of the thermolysis of anisole in a hydrogen atmosphere. J Phys Chem 1993;97:7914–25. https://doi.org/10.1021/j100132a020.

[127] Pecullan M, Brezinsky K, Glassman I. Pyrolysis and oxidation of anisole near 1000 k. J Phys Chem A 1997;101:3305–16. https://doi.org/10.1021/jp963203b.

[128] Platonov VV, Proskuryakov VA, Ryl'tsova SV, Popova YuN. Homogeneous pyrolysis of anisole. Russ J Appl Chem 2001;74:1047–52. https://doi.org/10.1023/A:1013076330586.

[129] Friderichsen AV, Shin E-J, Evans RJ, Nimlos MR, Dayton DC, Ellison GB. The pyrolysis of anisole (C6H5OCH3) using a hyperthermal nozzle. Fuel 2001;80:1747–55. https://doi.org/10.1016/S0016-2361(01)00059-X.

[130] Scheer AM, Mukarakate C, Robichaud DJ, Ellison GB, Nimlos MR. Radical chemistry in the thermal decomposition of anisole and deuterated anisoles: an investigation of aromatic growth. J Phys Chem A 2010;114:9043–56. https://doi.org/10.1021/jp102046p.

[131] Mackie JC, Doolan KR, Nelson PF. Kinetics of the thermal decomposition of methoxybenzene (anisole). J Phys Chem 1989;93:664–70. https://doi.org/10.1021/j100339a033.

[132] Zhang Y, Jiao A, Li Y, Liu P, Yang G, Zhan R, et al. Chemical effects of anisole and toluene addition to n-heptane on PAH characteristics in laminar premixed flames by LIF

measurement and kinetic model. Fuel 2021;303:121255. https://doi.org/10.1016/j.fuel.2021.121255.

[133]Schlosberg RH, Szajowski PF, Dupre GD, Danik JA, Kurs A, Ashe TR, et al. Pyrolysis studies of organic oxygenates: 3. High temperature rearrangement of aryl alkyl ethers. Fuel 1983;62:690–4. https://doi.org/10.1016/0016-2361(83)90308-3.

[134]Klein MT, Virk PS. Model pathways in lignin thermolysis. 1. Phenethyl phenyl ether. Ind Eng Chem Fundam 1983;22:35–45. https://doi.org/10.1021/i100009a007.

[135]Lawson JR, Klein MT. Influence of water on guaiacol pyrolysis. Ind Eng Chem Fundam 1985;24:203–8. https://doi.org/10.1021/i100018a012.

[136]Pera C, Knop V. Methodology to define gasoline surrogates dedicated to auto-ignition in engines. Fuel 2012;96:59–69. https://doi.org/10.1016/j.fuel.2012.01.008.

[137]Masurier J-B, Foucher F, Dayma G, Dagaut P. Investigation of iso-octane combustion in a homogeneous charge compression ignition engine seeded by ozone, nitric oxide and nitrogen dioxide. Proc Combust Inst 2015;35:3125–32. https://doi.org/10.1016/j.proci.2014.05.060.

[138]Lu X, Han D, Huang Z. Fuel design and management for the control of advanced compression-ignition combustion modes. Prog Energy Combust Sci 2011;37:741–83. https://doi.org/10.1016/j.pecs.2011.03.003.

[139]Zhang C, Hui X, Lin Y, Sung C-J. Recent development in studies of alternative jet fuel combustion: Progress, challenges, and opportunities. Renew Sustain Energy Rev 2016;54:120–38. https://doi.org/10.1016/j.rser.2015.09.056.

[140]Dooley S, Won SH, Heyne J, Farouk TI, Ju Y, Dryer FL, et al. The experimental evaluation of a methodology for surrogate fuel formulation to emulate gas phase combustion kinetic phenomena. Combust Flame 2012;159:1444–66. https://doi.org/10.1016/j.combustflame.2011.11.002.

[141] Wang H, Zhu C, Li D, Liu Q, Tan J, Wang C, et al. Recent advances in catalytic conversion of biomass to 5-hydroxymethylfurfural and 2, 5-dimethylfuran. Renew Sustain Energy Rev 2019;103:227–47. https://doi.org/10.1016/j.rser.2018.12.010.

[142]Tran L-S, Carstensen H-H, Lamoureux N, Foo KK, Gosselin S, El Bakali A, et al. Exploring the flame chemistry of c5 tetrahydrofuranic biofuels: tetrahydrofurfuryl alcohol and 2-methyltetrahydrofuran. Energy Fuels 2021;35:18699–715. https://doi.org/10.1021/acs.energyfuels.1c01949.

[143]Tran L-S, Verdicchio M, Monge F, Martin RC, Bounaceeur R, Sirjean B, et al. An experimental and modeling study of the combustion of tetrahydrofuran. Combust Flame 2015;162:1899–918. https://doi.org/10.1016/j.combustflame.2014.12.010.

[144]Hoang AT, Nižetić S, Ölçer AI. 2,5-Dimethylfuran (DMF) as a promising biofuel for the spark ignition engine application: A comparative analysis and review. Fuel 2021;285:119140. https://doi.org/10.1016/j.fuel.2020.119140.

[145]Tuan Hoang A, Viet Pham V. 2-Methylfuran (MF) as a potential biofuel: A thorough review on the production pathway from biomass, combustion progress, and application in engines. Renew Sustain Energy Rev 2021;148:111265. https://doi.org/10.1016/j.rser.2021.111265.

[146]Qian Y, Zhu L, Wang Y, Lu X. Recent progress in the development of biofuel 2,5-dimethylfuran. Renew Sustain Energy Rev 2015;41:633–46. https://doi.org/10.1016/j.rser.2014.08.085.

[147]Román-Leshkov Y, Barrett CJ, Liu ZY, Dumesic JA. Production of dimethylfuran for liquid fuels from biomass-derived carbohydrates. Nature 2007;447:982–5. https://doi.org/10.1038/nature05923.

[148]Saha B, Abu-Omar MM. Current technologies, economics, and perspectives for 2,5-dimethylfuran production from biomass-derived intermediates. ChemSusChem 2015;8:1133–42. https://doi.org/10.1002/cssc.201403329.

[149]Xu N, Gong J, Huang Z. Review on the production methods and fundamental combustion characteristics of furan derivatives. Renew Sustain Energy Rev 2016;54:1189–211. https://doi.org/10.1016/j.rser.2015.10.118.

[150]Tran L-S, Herbinet O, Carstensen H-H, Battin-Leclerc F. Chemical kinetics of cyclic ethers in combustion. Prog Energy Combust Sci 2022;92:101019. https://doi.org/10.1016/j.pecs.2022.101019.

[151] Korobeinichev OP, Yakimov SA, Knyazkov DA, Bolshova TA, Shmakov AG, Yang J, et al. A study of low-pressure premixed ethylene flame with and without ethanol using photoionization mass spectrometry and modeling. Proc Combust Inst 2011;33:569–76. https://doi.org/10.1016/j.proci.2010.07.066.

[152]Tran L-S, Glaude P-A, Fournet R, Battin-Leclerc F. Experimental and modeling study of premixed laminar flames of ethanol and methane. Energy Fuels 2013;27:2226–45. https://doi.org/10.1021/ef301628x.

[153]Tran LS. Étude de la formation de polluants lors de la combustion de carburants oxygénés. These de doctorat. Université de Lorraine, 2013.

[154]Dias V, Katshiatshia HM, Jeanmart H. The influence of ethanol addition on a rich premixed benzene flame at low pressure. Combust Flame 2014;161:2297–304. https://doi.org/10.1016/j.combustflame.2014.03.005.

[155]Wang Q, Saldinger JC, Elvati P, Violi A. Insights on the effect of ethanol on the formation of aromatics. Fuel 2020;264:116773. https://doi.org/10.1016/j.fuel.2019.116773.

[156]Matti Maricq M. Soot formation in ethanol/gasoline fuel blend diffusion flames. Combust Flame 2012;159:170–80. https://doi.org/10.1016/j.combustflame.2011.07.010.

[157]Salamanca M, Sirignano M, Commodo M, Minutolo P, D'Anna A. The effect of ethanol on the particle size distributions in ethylene premixed flames. Exp Therm Fluid Sci 2012;43:71–5. https://doi.org/10.1016/j.expthermflusci.2012.04.006.

[158]Shi X, Wang Q, Violi A. Chemical pathways for the formation of benzofuran and dibenzofuran in combustion. Combust Flame 2020;212:216–33. https://doi.org/10.1016/j.combustflame.2019.10.008.

[159]Salamanca M, Sirignano M, D'Anna A. Particulate formation in premixed and counter-flow diffusion ethylene/ethanol flames. Energy Fuels 2012;26:6144–52. https://doi.org/10.1021/ef301081q.

[160]Aizawa T, Nishigai H, Kondo K, Yamaguchi T, Nerva J-G, Genzale C, et al. Transmission electron microscopy of soot particles directly sampled in diesel spray flame - a comparison between us#2 and biodiesel soot. SAE Int J Fuels Lubr 2012;5:665–73.

[161] Taylor AMKP. Science review of internal combustion engines. Energy Policy 2008;36:4657–67. https://doi.org/10.1016/j.enpol.2008.09.001.

[162]Dutcher DD, Stolzenburg MR, Thompson SL, Medrano JM, Gross DS, Kittelson DB, et al. Emissions from ethanol-gasoline blends: a single particle perspective. Atmosphere 2011;2:182–200. https://doi.org/10.3390/atmos2020182.

[163]Michelsen HA, Schulz C, Smallwood GJ, Will S. Laser-induced incandescence: Particulate diagnostics for combustion, atmospheric, and industrial applications. Prog Energy Combust Sci 2015;51:2–48. https://doi.org/10.1016/j.pecs.2015.07.001.

[164]Betrancourt C. Experimental study of soot formation in laminar premixed flames of fuels of interest for automobile and aeronautics : a focus on the soot nucleation process. These de doctorat. Lille 1, 2017.

[165]Tran L-S, Carstensen H-H, Foo KK, Lamoureux N, Gosselin S, Gasnot L, et al. Experimental and modeling study of the high-temperature combustion chemistry of tetrahydrofurfuryl alcohol. Proc Combust Inst 2021;38:631–40. https://doi.org/10.1016/j.proci.2020.07.057.

[166]FLUIDAT® on the Net, mass flow and physical properties calculations n.d. https://www.fluidat.com/default.asp (accessed November 2, 2023).

[167]Jiang L, Zhou G, Huo J, Gu C, Chen X. Experimental study on hydrodynamic instability characteristics of N2-diluted n-C4H10/air flat flames. Flow Turbul Combust 2022;108:1–23. https://doi.org/10.1007/s10494-021-00303-9.

[168]Osborn AG, Douslin DR. Vapor pressures and derived enthalpies of vaporization for some condensed-ring hydrocarbons. J Chem Eng Data 1975;20:229–31. https://doi.org/10.1021/je60066a022.

[169]Monte MJS, Pinto SP, Lobo Ferreira AIMC, Amaral LMPF, Freitas VLS, Ribeiro da Silva MDMC. Fluorene: An extended experimental thermodynamic study. J Chem Thermodyn 2012;45:53–8. https://doi.org/10.1016/j.jct.2011.09.006.

[170]Verevkin SP. Vapor pressure measurements on fluorene and methyl-fluorenes. Fluid Phase Equilibria 2004;225:145–52. https://doi.org/10.1016/j.fluid.2004.08.037.

[171] Monte MJS, Santos LMNBF, Sousa CAD, Fulem M. Vapor pressures of solid and liquid xanthene and phenoxathiin from effusion and static studies. J Chem Eng Data 2008;53:1922–6. https://doi.org/10.1021/je800333q.

[172]Monte MJS, Sousa CAD, Fonseca JMS, Santos LMNBF. Thermodynamic study on the sublimation of anthracene-like compounds. J Chem Eng Data 2010;55:5264–70. https://doi.org/10.1021/je100850z.

[173]Goldfarb JL, Suuberg EM. Vapor pressures and enthalpies of sublimation of ten polycyclic aromatic hydrocarbons determined via the knudsen effusion method. J Chem Eng Data 2008;53:670–6. https://doi.org/10.1021/je7005133.

[174]Rordorf BF, Sarna LP, Webster GRB, Safe SH, Safe LM, Lenoir D, et al. Vapor pressure measurements on halogenated dibenzo-p-dioxins and dibenzofurans. An extended data set for a correlation method. Chemosphere 1990;20:1603–9. https://doi.org/10.1016/0045-6535(90)90319-O.

[175]Giarracca L. Impact of lignocellulosic biofuels on NOx formation in premixed laminar flames. These de doctorat. Université de Lille (2018-2021), 2018.

[176]Wartel M, Pauwels J-F, Desgroux P, Mercier X. Pyrene measurements in sooting low pressure methane flames by jet-cooled laser-induced fluorescence. J Phys Chem A 2011;115:14153–62. https://doi.org/10.1021/jp206970t.

[177] Hansen PC, Eckert CA. An improved transpiration method for the measurement of very low vapor pressures. J Chem Eng Data 1986;31:1–3. https://doi.org/10.1021/je00043a001.

[178]Chirico RD, Gammon BE, Knipmeyer SE, Nguyen A, Strube MM, Tsonopoulos C, et al. The thermodynamic properties of dibenzofuran. J Chem Thermodyn 1990;22:1075–96. https://doi.org/10.1016/0021-9614(90)90157-L.

[179]Li X-W, Shibata E, Kasai E, Nakamura T. Vapour pressure determination for dibenzo-p-dioxin, dibenzofuran, octachlorodibenzo-p-dioxin and octachlorodibenzofuran using a knudsen effusion method. Mater Trans - MATER TRANS 2002;43:2903–7. https://doi.org/10.2320/matertrans.43.2903.

[180]Van Geem KM, Pyl SP, Reyniers M-F, Vercammen J, Beens J, Marin GB. On-line analysis of complex hydrocarbon mixtures using comprehensive two-dimensional gas chromatography. J Chromatogr A 2010;1217:6623–33. https://doi.org/10.1016/j.chroma.2010.04.006.

[181]Betrancourt C, Mercier X, Liu F, Desgroux P. Quantitative measurement of volume fraction profiles of soot of different maturities in premixed flames by extinction-calibrated laser-induced incandescence. Appl Phys B 2019;125:16. https://doi.org/10.1007/s00340-018-7127-2.

[182]Mouton T, Mercier X, Wartel M, Lamoureux N, Desgroux P. Laser-induced incandescence technique to identify soot nucleation and very small particles in low-pressure methane flames. Appl Phys B 2013;112:369–79. https://doi.org/10.1007/s00340-013-5446-x.

[183]Melton LA. Soot diagnostics based on laser heating. Appl Opt 1984;23:2201–8. https://doi.org/10.1364/AO.23.002201.

[184]Eckbreth AC. Effects of laser-modulated particulate incandescence on Raman scattering diagnostics. J Appl Phys 2008;48:4473–9. https://doi.org/10.1063/1.323458.

[185]Delhay J, Desgroux P, Therssen E, Bladh H, Bengtsson P-E, Hönen H, et al. Soot volume fraction measurements in aero-engine exhausts using extinction-calibrated backward laser-induced incandescence. Appl Phys B 2009;95:825–38. https://doi.org/10.1007/s00340-009-3534-8.

[186]Lemaire R, Therssen E, Desgroux P. Effect of ethanol addition in gasoline and gasoline–surrogate on soot formation in turbulent spray flames. Fuel 2010;89:3952–9. https://doi.org/10.1016/j.fuel.2010.06.031.

[187]Michelsen HA, Liu F, Kock BF, Bladh H, Boiarciuc A, Charwath M, et al. Modeling laser-induced incandescence of soot: a summary and comparison of LII models. Appl Phys B 2007;87:503–21. https://doi.org/10.1007/s00340-007-2619-5.

[188]Schulz C, Kock BF, Hofmann M, Michelsen H, Will S, Bougie B, et al. Laser-induced incandescence: recent trends and current questions. Appl Phys B 2006;83:333–54. https://doi.org/10.1007/s00340-006-2260-8.

[189]Snelling DR, Liu F, Smallwood GJ, Gülder ÖL. Determination of the soot absorption function and thermal accommodation coefficient using low-fluence LII in a laminar coflow ethylene diffusion flame. Combust Flame 2004;136:180–90. https://doi.org/10.1016/j.combustflame.2003.09.013.

[190]Melton LA. Soot diagnostics based on laser heating. Appl Opt 1984;23:2201–8. https://doi.org/10.1364/AO.23.002201.

[191]Kirchhoff G. Ueber das Verhältniss zwischen dem Emissionsvermögen und dem Absorptionsvermögen der Körper für Wärme und Licht. Ann Phys 1860;185:275–301. https://doi.org/10.1002/andp.18601850205.

[192]Dalzell WH, Sarofim AF. Optical constants of soot and their application to heat-flux calculations. J Heat Transf 1969;91:100–4. https://doi.org/10.1115/1.3580063.

[193]Chang H, Charalampopoulos TT. Determination of the wavelength dependence of refractive indices of flame soot. Proc R Soc Lond Ser Math Phys Sci 1997;430:577–91. https://doi.org/10.1098/rspa.1990.0107.

[194]HABIB ZG, Vervisch P. On the refractive index of soot at flame temperature. Combust Sci Technol 1988;59:261–74. https://doi.org/10.1080/00102208808947100.

[195]Lee SC, Tien CL. Optical constants of soot in hydrocarbon flames. Symp Int Combust 1981;18:1159–66. https://doi.org/10.1016/S0082-0784(81)80120-8.

[196]Krishnan SS, Lin K-C, Faeth GM. Extinction and scattering properties of soot emitted from buoyant turbulent diffusion flames. J Heat Transf 2000;123:331–9. https://doi.org/10.1115/1.1350823.

[197]Yon J, Lemaire R, Therssen E, Desgroux P, Coppalle A, Ren K. Examination of wavelength dependent soot optical properties of diesel and diesel/rapeseed methyl ester mixture by extinction spectra analysis and LII measurements. Appl Phys B 2011;104:253–71. https://doi.org/10.1007/s00340-011-4416-4.

[198]Maffi S, De Iuliis S, Cignoli F, Zizak G. Investigation on thermal accommodation coefficient and soot absorption function with two-color Tire-LII technique in rich premixed flames. Appl Phys B Lasers Opt 2011;104:357–66. https://doi.org/10.1007/s00340-011-4536-x.

[199]Michelsen HA. Understanding and predicting the temporal response of laser-induced incandescence from carbonaceous particles. J Chem Phys 2003;118:7012–45. https://doi.org/10.1063/1.1559483.

[200]Schoemaecker Moreau C, Therssen E, Mercier X, Pauwels JF, Desgroux P. Two-color laser-induced incandescence and cavity ring-down spectroscopy for sensitive and quantitative imaging of soot and PAHs in flames. Appl Phys B Lasers Opt 2004;78:485–92. https://doi.org/10.1007/s00340-003-1370-9.

[201]Mannazhi M, Török S, Gao J, Bengtsson P-E. Soot maturity studies in methane-air diffusion flames at elevated pressures using laser-induced incandescence. Proc Combust Inst 2021;38:1217–24. https://doi.org/10.1016/j.proci.2020.07.127.

[202]Desgroux P, Lamoureux N, Faccinetto A. Combining performances of LII and absorption for in-situ measuring volume fraction of 2-4 nm diameter soot particles. Curr Prep n.d.

[203]Zhao B, Yang Z, Wang J, Johnston MV, Wang H. Analysis of soot nanoparticles in a laminar premixed ethylene flame by scanning mobility particle sizer. Aerosol Sci Technol 2003;37:611–20. https://doi.org/10.1080/02786820300908.

[204]Maricq MM, Harris SJ, Szente JJ. Soot size distributions in rich premixed ethylene flames. Combust Flame 2003;132:328–42. https://doi.org/10.1016/S0010-2180(02)00502-3.

[205]Betrancourt C, Aubagnac-Karkar D, Mercier X, El-Bakali A, Desgroux P. Experimental and numerical investigation of the transition from non sooting to sooting premixed n-butane flames, encompassing the nucleation flame conditions. Combust Flame 2022;243:112172. https://doi.org/10.1016/j.combustflame.2022.112172.

[206]Commodo M, De Falco G, Bruno A, Borriello C, Minutolo P, D'Anna A. Physicochemical evolution of nascent soot particles in a laminar premixed flame: from nucleation to early growth. Combust Flame 2015;162:3854–63. https://doi.org/10.1016/j.combustflame.2015.07.022.

[207]Camacho J, Liu C, Gu C, Lin H, Huang Z, Tang Q, et al. Mobility size and mass of nascent soot particles in a benchmark premixed ethylene flame. Combust Flame 2015;162:3810–22. https://doi.org/10.1016/j.combustflame.2015.07.018.

[208]Abid AD, Camacho J, Sheen DA, Wang H. Evolution of Soot Particle Size Distribution Function in Burner-Stabilized Stagnation n-Dodecane–Oxygen–Argon Flames. Energy Fuels 2009;23:4286–94. https://doi.org/10.1021/ef900324e.

[209]Stirn R, Baquet TG, Kanjarkar S, Meier W, Geigle KP, Grotheer HH, et al. Comparison of Particle Size Measurements with Laser-Induced Incandescence, Mass Spectroscopy, and Scanning Mobility Particle Sizing in a Laminar Premixed Ethylene/Air Flame. Combust Sci Technol 2009;181:329–49. https://doi.org/10.1080/00102200802483498.

[210]Tang Q, Cai R, You X, Jiang J. Nascent soot particle size distributions down to 1nm from a laminar premixed burner-stabilized stagnation ethylene flame. Proc Combust Inst 2017;36:993–1000. https://doi.org/10.1016/j.proci.2016.08.085.

[211]Stolzenburg MR, McMurry PH. An ultrafine aerosol condensation nucleus counter. Aerosol Sci Technol 1991;14:48–65. https://doi.org/10.1080/02786829108959470.

[212]Magnusson L-E, Koropchak JA, Anisimov MP, Poznjakovskiy VM, de la Mora JF. Correlations for vapor nucleating critical embryo parameters. J Phys Chem Ref Data 2003;32:1387–410. https://doi.org/10.1063/1.1555590.

[213]Iida K, Stolzenburg MR, McMurry PH. Effect of working fluid on sub-2 nm particle detection with a laminar flow ultrafine condensation particle counter. Aerosol Sci Technol 2009;43:81–96. https://doi.org/10.1080/02786820802488194.

[214]Cecere D, Sgro LA, Basile G, D'Alessio A, D'Anna A, Minutolo P. Evidence and characterization of nanoparticles produced in nonsooting premixed flames. Combust Sci Technol 2002;174:377–98. https://doi.org/10.1080/00102200215079.

[215]Shaddix CR. Correcting thermocouple measurements for radiation loss: A critical review. American Society of Mechanical Engineers, New York, NY (US); 1999.

[216]Kiefer J, Ewart P. Laser diagnostics and minor species detection in combustion using resonant four-wave mixing. Prog Energy Combust Sci 2011;37:525–64. https://doi.org/10.1016/j.pecs.2010.11.001.

[217]Kaiser SA, Frank JH, Long MB. Use of Rayleigh imaging and ray tracing to correct for beam-steering effects in turbulent flames. Appl Opt 2005;44:6557–64. https://doi.org/10.1364/AO.44.006557.

[218]Hindasageri V, Vedula RP, Prabhu SV. Thermocouple error correction for measuring the flame temperature with determination of emissivity and heat transfer coefficient. Rev Sci Instrum 2023;84:024902. https://doi.org/10.1063/1.4790471.

[219]Jiménez S. Relevance of heat conduction in the correction and interpretation of high temperature, fine wire thermocouple measurements. Combust Flame 2022;240:112022. https://doi.org/10.1016/j.combustflame.2022.112022.

[220]Heitor MV, Moreira ALN. Thermocouples and sample probes for combustion studies. Prog Energy Combust Sci 1993;19:259–78. https://doi.org/10.1016/0360-1285(93)90017-9.

[221]Yon J, Cruz JJ, Escudero F, Morán J, Liu F, Fuentes A. Revealing soot maturity based on multi-wavelength absorption/emission measurements in laminar axisymmetric coflow ethylene diffusion flames. Combust Flame 2021;227:147–61. https://doi.org/10.1016/j.combustflame.2020.12.049.

[222]Attya AM, Whitelaw JH. Velocity, temperature and species concentrations in unconfined kerosene spray flames. Am Soc Mech Eng Pap U S 1981;81-WA/HT-47.

[223]Blevins LG, Pitts WM. Modeling of bare and aspirated thermocouples in compartment fires. Fire Saf J 1999;33:239–59. https://doi.org/10.1016/S0379-7112(99)00034-X.

[224]Gilbert M, Lobdell JH. Resistance-thermometer measurements in'a low-pressure flame. Symp Int Combust 1953;4:285–94. https://doi.org/10.1016/S0082-0784(53)80037-8.

[225]Brohez S, Delvosalle C, Marlair G. A two-thermocouples probe for radiation corrections of measured temperatures in compartment fires. Fire Saf J 2004;39:399–411. https://doi.org/10.1016/j.firesaf.2004.03.002.

[226]Lemaire R, Menanteau S. Assessment of radiation correction methods for bare bead thermocouples in a combustion environment. Int J Therm Sci 2017;122:186–200. https://doi.org/10.1016/j.ijthermalsci.2017.08.014.

[227]McEnally CS, Köylü ÜÖ, Pfefferle LD, Rosner DE. Soot volume fraction and temperature measurements in laminar nonpremixed flames using thermocouples. Combust Flame 1997;109:701–20. https://doi.org/10.1016/S0010-2180(97)00054-0.

[228]Nichols EL. On the Temperature of the Acetylene Flame. Phys Rev Ser I 1900;10:234–52. https://doi.org/10.1103/PhysRevSeriesI.10.234.

[229]Daniels GE. Measurement of gas temperature and the radiation compensating thermocouple. J Appl Meteorol Climatol 1968;7:1026–35. https://doi.org/10.1175/1520-0450(1968)007<1026:MOGTAT>2.0.CO;2.

[230]Bradley D, Matthews KJ. Measurement of High Gas Temperatures with Fine Wire Thermocouples. J Mech Eng Sci 1968;10:299–305. https://doi.org/10.1243/JMES_JOUR_1968_010_048_02.

[231]Elias J, Faccinetto A, Batut S, Carrivain O, Sirignano M, D'Anna A, et al. Thermocouple-based thermometry for laminar sooting flames: Implementation of a fast and simple methodology. Int J Therm Sci 2023;184:107973. https://doi.org/10.1016/j.ijthermalsci.2022.107973.

[232]Hayhurst AN, Kittelson DB. Heat and mass transfer considerations in the use of electrically heated thermocouples of iridium versus an iridiumrhodium alloy in atmospheric pressure flames. Combust Flame 1977;28:301–17. https://doi.org/10.1016/0010-2180(77)90036-0.

[233]Pitts WM, Braun E, Peacock RD, Mitler HE, Johnsson EL, Reneke PA, et al. Temperature uncertainties for bare-bead and aspirated thermocouple measurements in fire environments. ASTM Spec Tech Publ 2003;1427:3–15.

[234]Ergut A, Levendis Y. An investigation on thermocouple-based temperature measurements in sooting flames, American Society of Mechanical Engineers Digital Collection; 2008, p. 397–403. https://doi.org/10.1115/IMECE2005-82332.

[235]Daily JW. Laser induced fluorescence spectroscopy in flames. Prog Energy Combust Sci 1997;23:133–99. https://doi.org/10.1016/S0360-1285(97)00008-7.

[236]Betrancourt C, Liu F, Desgroux P, Mercier X, Faccinetto A, Salamanca M, et al. Investigation of the size of the incandescent incipient soot particles in premixed sooting and nucleation flames of n-butane using lii, him, and 1 nm-smps. Aerosol Sci Technol 2017;51:916.

[237]Foo KK, Lamoureux N, Cessou A, Lacour C, Desgroux P. The accuracy and precision of multi-line NO-LIF thermometry in a wide range of pressures and temperatures. J Quant Spectrosc Radiat Transf 2020;255:107257. https://doi.org/10.1016/j.jqsrt.2020.107257.

[238]Lamoureux N, Desgroux P. In Situ Laser-Induced Fluorescence and Ex Situ Cavity Ring-Down Spectroscopy Applied to NO Measurement in Flames: Microprobe Perturbation and Absolute Quantification. Energy Fuels 2021;35:7107–20. https://doi.org/10.1021/acs.energyfuels.0c03806.

[239]Cieplik MK, Epema OJ, Louw R. Thermal hydrogenolysis of dibenzo-p-dioxin and dibenzofuran. Eur J Org Chem 2002;2002:2792–9. https://doi.org/10.1002/1099-0690(200208)2002:16<2792::AID-EJOC2792>3.0.CO;2-H.

[240]Zhang T, Bhattarai C, Son Y, Samburova V, Khlystov A, Varganov SA. Reaction mechanisms of anisole pyrolysis at different temperatures: experimental and theoretical studies. Energy Fuels 2021;35:9994–10008. https://doi.org/10.1021/acs.energyfuels.1c00858.

[241]Roy S, Askari O. Detailed kinetics for anisole oxidation under various range of operating conditions. Fuel 2022;325:124907. https://doi.org/10.1016/j.fuel.2022.124907.

[242]CRECK modeling group: Anisole model. C1-C16 HT mechanism (Version 2003, March 2020). n.d. http://creckmodeling.chem.polimi.it/menu-kinetics/menu-kinetics-detailed-mechanisms/107-category-kinetic-mechanisms/402-mechanisms-1911-tot-ht n.d.

[243]Wiater I, Born JGP, Louw R. Products, rates, and mechanism of the gas-phase condensation of phenoxy radicals between 500-840 k. Eur J Org Chem 2000;2000:921–8. https://doi.org/10.1002/(SICI)1099-0690(200003)2000:6<921::AID-EJOC921>3.0.CO;2-P.

[244]Farrell JT, Johnston RJ, Androulakis IP. Molecular structure effects on laminar burning velocities at elevated temperature and pressure. Warrendale, PA: SAE International; 2004. https://doi.org/10.4271/2004-01-2936.

[245]Cole JA, Bittner JD, Longwell JP, Howard JB. Formation mechanisms of aromatic compounds in aliphatic flames. Combust Flame 1984;56:51–70. https://doi.org/10.1016/0010-2180(84)90005-1.

[246]Kholghy MR, Veshkini A, Thomson MJ. The core–shell internal nanostructure of soot – A criterion to model soot maturity. Carbon 2016;100:508–36. https://doi.org/10.1016/j.carbon.2016.01.022.

[247]Wang H, Frenklach M. Calculations of rate coefficients for the chemically activated reactions of acetylene with vinylic and aromatic radicals. J Phys Chem 1994;98:11465–89. https://doi.org/10.1021/j100095a033.

[248]McEnally CS, Pfefferle LD, Atakan B, Kohse-Höinghaus K. Studies of aromatic hydrocarbon formation mechanisms in flames: Progress towards closing the fuel gap. Prog Energy Combust Sci 2006;32:247–94. https://doi.org/10.1016/j.pecs.2005.11.003.

[249]Bakali AE, Deflau J-L, Vovelle C. Experimental study of 1 atmosphere, rich, premixed n-heptane and iso-octane flames. Combust Sci Technol 1998;140:69–91. https://doi.org/10.1080/00102209808915768.

[250]Tran LS, Sirjean B, Glaude P-A, Fournet R, Battin-Leclerc F. Influence of substituted furans on the formation of Polycyclic Aromatic Hydrocarbons in flames. Proc Combust Inst 2015;35:1735. https://doi.org/10.1016/j.proci.2014.06.137.

[251]Long AE, Merchant SS, Vandeputte AG, Carstensen H-H, Vervust AJ, Marin GB, et al. Pressure dependent kinetic analysis of pathways to naphthalene from cyclopentadienyl recombination. Combust Flame 2018;187:247–56. https://doi.org/10.1016/j.combustflame.2017.09.008.

[252]von Blottnitz H, Curran MA. A review of assessments conducted on bio-ethanol as a transportation fuel from a net energy, greenhouse gas, and environmental life cycle perspective. J Clean Prod 2007;15:607–19. https://doi.org/10.1016/j.jclepro.2006.03.002.

[253]Ergut A, Granata S, Jordan J, Carlson J, Howard JB, Richter H, et al. PAH formation in one-dimensional premixed fuel-rich atmospheric pressure ethylbenzene and ethyl alcohol flames. Combust Flame 2006;144:757–72. https://doi.org/10.1016/j.combustflame.2005.07.019.

[254]Dagaut P, Togbé C. Experimental and modeling study of the kinetics of oxidation of ethanol–gasoline surrogate mixtures (e85 surrogate) in a jet-stirred reactor. Energy Fuels 2008;22:3499–505. https://doi.org/10.1021/ef800214a.

[255]Jin H, Yuan W, Li W, Yang J, Zhou Z, Zhao L, et al. Combustion chemistry of aromatic hydrocarbons. Prog Energy Combust Sci 2023;96:101076. https://doi.org/10.1016/j.pecs.2023.101076.

[256]Richter H, Benish TG, Mazyar OA, Green WH, Howard JB. Formation of polycyclic aromatic hydrocarbons and their radicals in a nearly sooting premixed benzene flame. Proc Combust Inst 2000;28:2609–18. https://doi.org/10.1016/S0082-0784(00)80679-7.

[257]Levey ZD, Laws BA, Sundar SP, Nauta K, Kable SH, da Silva G, et al. PAH growth in flames and space: formation of the phenalenyl radical. J Phys Chem A 2022;126:101–8. https://doi.org/10.1021/acs.jpca.1c08310.

[258]Togbé C, Tran L-S, Liu D, Felsmann D, Oßwald P, Glaude P-A, et al. Combustion chemistry and flame structure of furan group biofuels using molecular-beam mass spectrometry and gas chromatography – Part III: 2,5-Dimethylfuran. Combust Flame 2014;161:780–97. https://doi.org/10.1016/j.combustflame.2013.05.026.

[259]Sirjean B, Fournet R. Theoretical study of the reaction 2,5-dimethylfuran+H→products. Proc Combust Inst 2013;34:241–9. https://doi.org/10.1016/j.proci.2012.05.027.

[260]Mebel AM, Landera A, Kaiser RI. Formation mechanisms of naphthalene and indene: from the interstellar medium to combustion flames. J Phys Chem A 2017;121:901–26. https://doi.org/10.1021/acs.jpca.6b09735.

[261]Zhao B, Yang Z, Johnston MV, Wang H, Wexler AS, Balthasar M, et al. Measurement and numerical simulation of soot particle size distribution functions in a laminar premixed ethylene-oxygen-argon flame. Combust Flame 2003;133:173–88. https://doi.org/10.1016/S0010-2180(02)00574-6.

[262]Sgro LA, Barone AC, Commodo M, D'Alessio A, De Filippo A, Lanzuolo G, et al. Measurement of nanoparticles of organic carbon in non-sooting flame conditions. Proc Combust Inst 2009;32:689–96. https://doi.org/10.1016/j.proci.2008.06.216.

[263]Frenzel I, Krause H, Trimis D. Study on the influence of ethanol and butanol addition on soot formation in iso-octane flames. Energy Procedia 2017;120:721–8. https://doi.org/10.1016/j.egypro.2017.07.203.

[264]Ni T, Pinson JA, Gupta S, Santoro RJ. Two-dimensional imaging of soot volume fraction by the use of laser-induced incandescence. Appl Opt 1995;34:7083–91. https://doi.org/10.1364/AO.34.007083.

[265]Do H-Q, Faccinetto A, Tran L-S, Desgroux P, Gasnot L, El Bakali A, et al. Hydrogen as a fuel additive in laminar premixed methane flames: Impact on the nucleation and growth of soot particles. Fuel 2022;315:123125. https://doi.org/10.1016/j.fuel.2021.123125.

[266]Chen D-R, Pui DYH, Hummes D, Fissan H, Quant FR, Sem GJ. Design and evaluation of a nanometer aerosol differential mobility analyzer (Nano-DMA). J Aerosol Sci 1998;29:497–509. https://doi.org/10.1016/S0021-8502(97)10018-0.

[267]Birmili W, Stratmann F, Wiedensohler A, Covert D, Russell LM, Berg O. Determination of differential mobility analyzer transfer functions using identical instruments in series. Aerosol Sci Technol 1997;27:215–23. https://doi.org/10.1080/02786829708965468.

[268]Appel J, Bockhorn H, Wulkow M. A detailed numerical study of the evolution of soot particle size distributions in laminar premixed flames. Chemosphere 2001;42:635–45. https://doi.org/10.1016/S0045-6535(00)00237-X.

[269]Musick M, Van Tiggelen PJ, Vandooren J. Experimental study of the structure of several fuel-rich premixed flames of methane, oxygen, and argon. Combust Flame 1996;105:433–50. https://doi.org/10.1016/0010-2180(95)00228-6.

[270]Melton TR, Inal F, Senkan SM. The effects of equivalence ratio on the formation of polycyclic aromatic hydrocarbons and soot in premixed ethane flames. Combust Flame 2000;121:671–8. https://doi.org/10.1016/S0010-2180(99)00180-7.

[271]Melton TR, Vincitore AM, Senkan SM. The effects of equivalence ratio on the formation of polycyclic aromatic hydrocarbons and soot in premixed methane flames. Symp Int Combust 1998;27:1631–7. https://doi.org/10.1016/S0082-0784(98)80001-5.

[272]Elias J. Mise en évidence et caractérisation des espèces chimiques à l'origine de la nucléation des particules de suie dans les flammes. These de doctorat. Université de Lille (2019-22), 2022.

Appendices

Table A. 1 : Summary of the analysis conditions optimized for the 1-D GC-SPT-TCD-FID referred to as "GC Scion" in the text.

		Injectors	
		Channel 1 (Split/Splitless)	
Split event table	Time (min)	Split state	Split ratio
	Initial	ON	10
Heater (setpoint)		ON (220°C)	
		Channel 2 (Mini Gas Splitter)	
Split event table	Time (min)	Split state	Split ratio
	Initial	ON	60
		Channel 3 (SPT)	
Heater		ON	
Temperature program		Step (°C)	Time (min)
		-50	5.80
		200	14.80
		Total time	20.60
		Column oven zone	
Temperature program	Rate (°/C)	Step (°C)	Time (min)
	Initial	50	15.00
	8	190	12.50
	Total time		45.00
		Columns	
Channel 1		Hayesep Q Molsieve 13X	
Channel 2		Scion-1 Scion-Al_2O_3/Na_2SO_4	
Channel 3		Scion-17MS	
		Detectors	
		Channel 1 (TCD)	
Electronics		ON	
Heater (setpoint)		ON (175°C)	
Filament temperature limit		390°C	
Filament temperature		300°C	
		Channel 2 and Channel 3 (FIDs)	
Electronics		ON	
Heater		300°C	
Make up (Nitrogen) flow		20 mL/min	
Hydrogen flow		30 mL/min	
Air flow		300 mL/min	

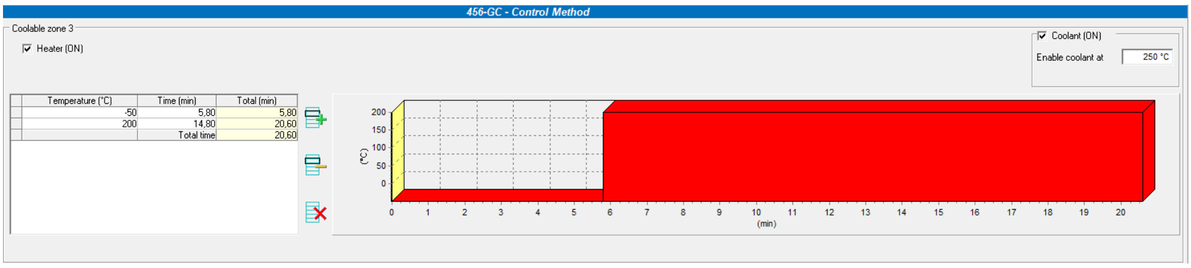

456-GC - Control Method

Coolable zone 3

☑ Heater (ON)

☑ Coolant (ON)

Enable coolant at 250 °C

Temperature (°C)	Time (min)	Total (min)
-50	5,80	5,80
200	14,80	20,60
	Total time	20,60

Figure A. 1 : Temperature program used for the SPT in Channel 3 in GC Scion.

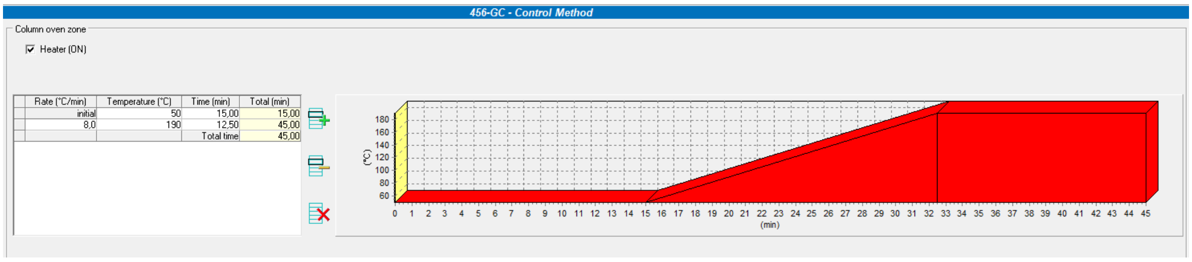

456-GC - Control Method

Column oven zone

☑ Heater (ON)

Rate (°C/min)	Temperature (°C)	Time (min)	Total (min)
initial	50	15,00	15,00
8,0	190	12,50	45,00
		Total time	45,00

Figure A. 2 : Temperature program used for all columns in different channels in GC Scion.

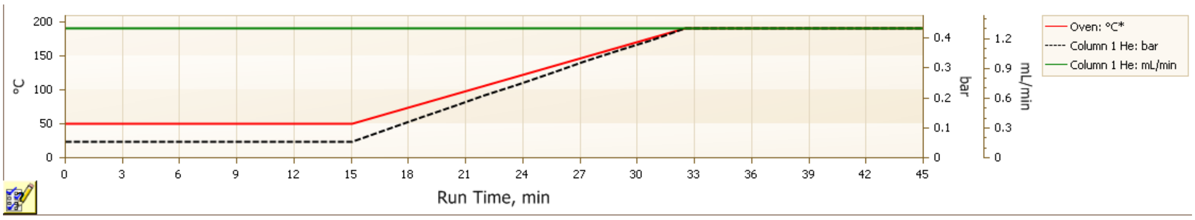

Figure A. 3 : Temperature program used for 1-D GC-MS; it was kept similar to GC Scion in order to carry out a comparison of the chromatograms to identify the peaks.

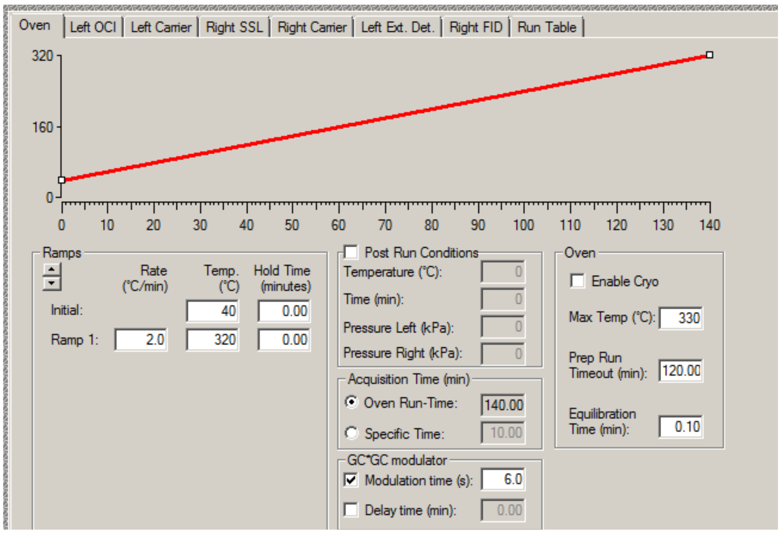

Ramps

	Rate (°C/min)	Temp. (°C)	Hold Time (minutes)
Initial:		40	0.00
Ramp 1:	2.0	320	0.00

☐ Post Run Conditions
Temperature (°C): 0
Time (min): 0
Pressure Left (kPa): 0
Pressure Right (kPa): 0

Acquisition Time (min)
● Oven Run-Time: 140.00
○ Specific Time: 10.00

GC*GC modulator
☑ Modulation time (s): 6.0
☐ Delay time (min): 0.00

Oven
☐ Enable Cryo
Max Temp (°C): 330
Prep Run Timeout (min): 120.00
Equilibration Time (min): 0.10

Figure A. 4 : Temperature program used for the 2D-GC Thermo Fischer Scientific at the Laboratory for Chemical Technology at the University of Ghent.

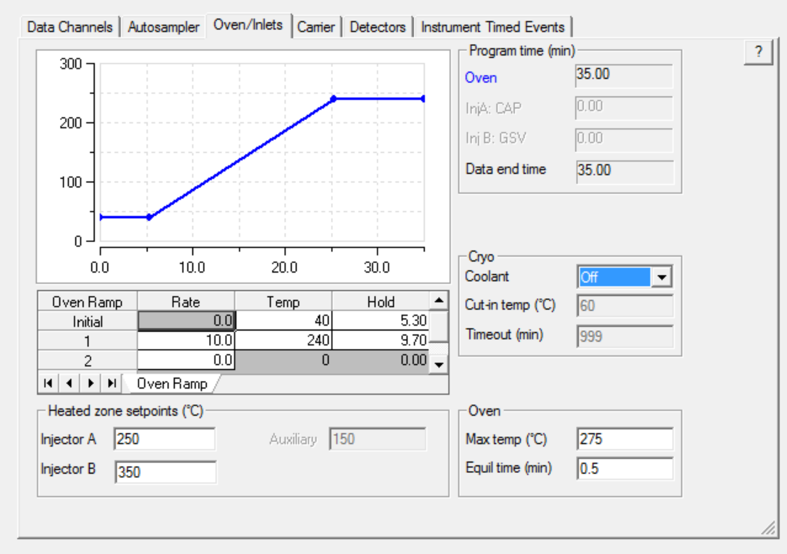

Oven Ramp	Rate	Temp	Hold
Initial	0.0	40	5.30
1	10.0	240	9.70
2	0.0	0	0.00

Program time (min)
Oven 35.00
InjA: CAP 0.00
Inj B: GSV 0.00
Data end time 35.00

Cryo
Coolant Off
Cut-in temp (°C) 60
Timeout (min) 999

Heated zone setpoints (°C)
Injector A 250
Injector B 350
Auxiliary 150

Oven
Max temp (°C) 275
Equil time (min) 0.5

Figure A. 5 : Temperature program used for the 1-D GC-TCD-FID referred to as "GC Perkin" in the text.

Table A. 2 : List of the non-oxygenated aromatics and PAHs that were identified in this work in anisole flames.

N°	Molar mass (g/mol)	Formula	Name	Structure
1.	78.11	C_6H_6	Benzene	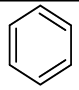
2.	92.14	C_7H_8	Toluene	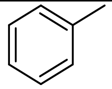
3.	104.15	C_8H_8	Ethenyl benzene	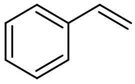
4.	116.16	C_9H_8	Indene	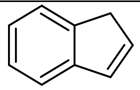
5.	126.15	$C_{10}H_6$	1,4-Diethynylbenzene	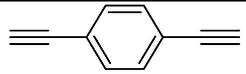
6.	128.17	$C_{10}H_8$	Naphthalene	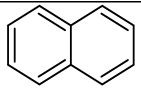
7.	142.20	$C_{11}H_{10}$	1-Methyl naphthalene	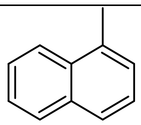
8.	142.20	$C_{11}H_{10}$	2-Methyl naphthalene	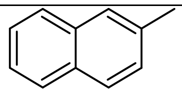
9.	152.20	$C_{12}H_8$	Biphenylene	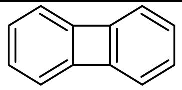
10.	152.20	$C_{12}H_8$	Acenaphthylene	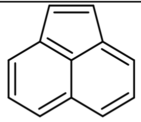
11.	154.21	$C_{12}H_{10}$	Acenaphthene	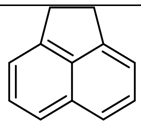
12.	154.21	$C_{12}H_{10}$	Biphenyl	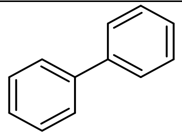
13.	154.21	$C_{12}H_{10}$	2-Ethenyl naphthalene	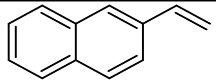
14.	156.22	$C_{12}H_{12}$	2-Ethyl naphthalene	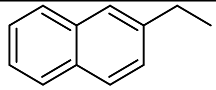
15.	166.22	$C_{13}H_{10}$	Fluorene	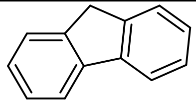

16.	166.21	$C_{13}H_{10}$	1H-Phenalene	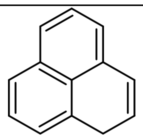
17.	168.23	$C_{13}H_{12}$	1,1'-Methylenedibenzene	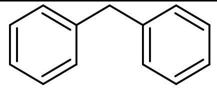
18.	178.23	$C_{14}H_{10}$	Anthracene	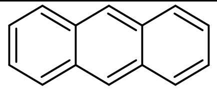
19.	178.23	$C_{14}H_{10}$	Phenanthrene	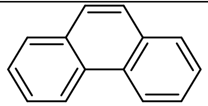
20.	202.25	$C_{16}H_{10}$	Fluoranthene	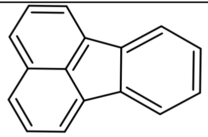
21.	206.28	$C_{16}H_{14}$	Pyrene	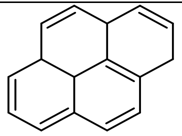

Table A. 3 : A recapitulation of the different species (in the order of increasing molar mass) that were quantified using different GC setups with their respective peak mole fractions in the different flames investigated in this work. Superscript "p" and "s" refer to the GCs using which they were quantified where "p" implies GC Perkin and "s" implies GC Scion; the hyphen "-" implies that the species was not detected in the flame. For the reactants, the peak mole fraction presented is the value close to the burner surface whereas for the major end products, the peak mole fraction is the value in the plateau region.

N°	**Name**	**Formula**	**Molar mass (g/mol)**	**Structure**	**Calibration**	**F1**	**F2**	**F3**	**F4**	**F5**	**F6**	**F7**
1.	Hydrogen	H_2	2.01	H−H	Direct^{p}	1.24E-01	1.22E-01	1.17E-01	1.06E-01	1.26E-01	1.18E-01	1.22E-01
2.	Methane	CH_4	16.04	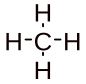 $H-\overset{H}{\underset{H}{C}}-H$	Direct^{p,s}	6.51E-02	5.19E-02	4.56E-02	4.23E-02	5.33E-02	5.49E-02	5.43E-02
3.	Acetylene	C_2H_2	26.04	HC≡CH	Direct^{p,s}	1.26E-02	1.28E-02	1.20E-02	9.31E-03	1.39E-02	1.07E-02	1.32E-02
4.	Nitrogen	N_2	28.01	N≡N	Direct^{p,s}	6.11E-01	6.05E-01	5.95E-01	5.93E-01	5.95E-01	5.93E-01	5.91E-01
5.	Carbon monoxide	CO	28.01	C≡O	Direct^{p,s}	1.46E-01	1.70E-01	1.76E-01	1.56E-01	1.72E-01	1.41E-01	1.67E-01
6.	Ethylene	C_2H_4	28.05	$H_2C=CH_2$	Direct^{p,s}	3.98E-03	3.39E-03	3.26E-03	3.18E-03	3.32E-03	3.98E-03	3.48E-03
7.	Formaldehyde	HCHO	30.03	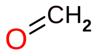	Estimated^{p}	8.09E-04	8.53E-04	8.54E-04	7.96E-04	7.96E-04	9.21E-04	8.55E-04
8.	Ethane	C_2H_6	30.07	H_3C-CH_3	Direct^{p,s}	1.46E-03	1.43E-03	1.34E-03	1.42E-03	1.32E-03	1.27E-03	1.20E-03
9.	Oxygen	O_2	31.99	O=O	Direct^{p,s}	1.41E-01	1.40E-01	1.34E-01	1.22E-01	1.37E-01	1.31E-01	1.39E-01
10.	Methanol	CH_3OH	32.04	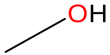	Estimated^{p}	4.08E-05	3.83E-05	3.77E-05	4.05E-05	3.16E-05	4.61E-05	4.52E-05
11.	Allene	aC_3H_4	40.06	$H_2C=C=CH_2$	Estimated^{p,s}	3.01E-04	3.27E-04	3.35E-04	2.99E-04	3.54E-04	2.72E-04	4.17E-04
12.	Propyne	pC_3H_4	40.06	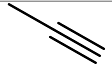	Direct^{p,s}	5.15E-04	4.88E-04	4.79E-04	4.16E-04	4.97E-04	3.78E-04	7.01E-04
13.	Propene	C_3H_6	42.08	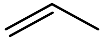	Direct^{p,s}	2.01E-03	1.87E-03	1.73E-03	1.88E-03	1.73E-03	1.71E-03	1.68E-03
14.	Carbon dioxide	CO_2	44.01	O=C=O	Direct^{p,s}	4.48E-02	4.83E-02	5.17E-02	5.63E-02	4.62E-02	4.74E-02	4.69E-02
15.	Acetaldehyde	CH_3CHO	44.05	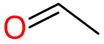	Estimated^{p}	7.00E-05	7.74E-05	9.08E-05	8.06E-05	7.53E-05	4.57E-04	2.33E-05
16.	Propane	C_3H_8	44.09		Direct^{p,s}	3.20E-05	2.48E-05	2.18E-05	2.55E-05	2.39E-05	2.87E-05	4.96E-05
17.	Ethanol	C_2H_5OH	46.06	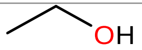	Direct^{p}	1.90E-04	2.31E-04	2.93E-04	1.61E-04	3.42E-04	5.65E-03	2.82E-04

18.	Vinylacetylene	C_4H_4	52.07	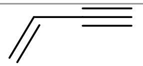	Direct[s]	3.09E-05	3.60E-05	3.85E-05	3.58E-05	4.04E-05	3.11E-05	4.63E-05
19.	1,3-Butadiene	C_4H_6	54.09	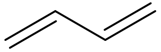	Direct[s]	1.01E-04	1.28E-04	1.34E-04	1.42E-04	1.45E-04	1.02E-04	2.40E-04
20.	2-Propenal	C_2H_3CHO	56.02	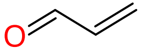	Estimated[p]	1.24E-05	5.58E-05	7.43E-05	5.76E-05	5.01E-05	2.91E-05	4.96E-05
21.	1-Butene	C_4H_8	56.10	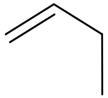	Direct[s]	1.40E-04	1.21E-04	1.16E-04	1.53E-04	1.46E-04	1.26E-04	1.38E-04
22.	Trans-2-butene	C_4H_8	56.10	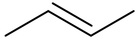	Direct[s]	9.99E-06	8.70E-06	8.43E-06	1.07E-05	9.69E-06	1.02E-05	1.14E-05
23.	Cis-2-butene	C_4H_8	56.10	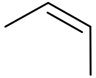	Direct[s]	6.19E-06	7.28E-06	6.96E-06	8.43E-06	5.19E-06	8.55E-06	9.12E-06
24.	Isobutene	C_4H_8	56.10	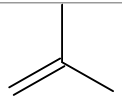	Direct[s]	2.62E-03	2.01E-03	1.73E-03	2.46E-03	2.18E-03	2.39E-03	1.86E-03
25.	1-Butyne	C_4H_6	54.10	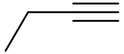	Direct[s]	7.52E-05	1.37E-04	1.67E-04	1.32E-04	1.63E-04	6.88E-05	1.70E-04
26.	Propanal	C_2H_5CHO	58.04	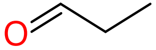	Estimated[p]	1.28E-05	1.09E-05	1.15E-05	1.16E-05	1.01E-05	1.54E-05	1.59E-05
27.	Acetone	CH_3COCH_3	58.07	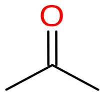	Estimated[p]	2.46E-05	1.89E-05	1.88E-05	2.11E-05	1.60E-05	2.62E-05	2.63E-05
28.	Isobutane	iC_4H_{10}	58.12	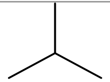	Estimated[p]	1.46E-05	1.22E-05	1.33E-05	1.40E-05	1.19E-05	1.17E-05	1.66E-05
29.	2-Methyl-1-buten-3-yne	C_5H_6	66.10	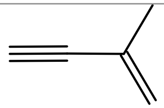	Estimated[p]	3.00E-06	4.54E-06	5.72E-06	4.52E-06	5.16E-06	2.31E-06	5.35E-06
30.	Cyclopentadiene	cC_5H_6	66.1	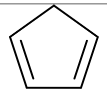	Estimated[p]	1.39E-04	3.77E-04	5.58E-04	4.15E-04	3.70E-04	1.19E-04	2.92E-04
31.	Furan	C_4H_4O	68.07	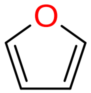	Estimated[p]	-	1.91E-06	3.21E-06	2.09E-06	2.01E-06	-	8.91E-06

32.	1,3-Pentadiene	C_5H_8	68.11	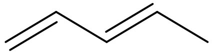	Estimated[p]	5.37E-05	6.71E-05	7.34E-05	7.19E-05	6.25E-05	4.91E-05	6.51E-05
33.	Methacrolein	C_4H_6O	70.09	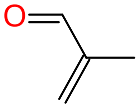	Estimated[p]	2.95E-05	1.01E-06	1.13E-06	2.08E-06	1.92E-06	2.97E-05	2.05E-05
34.	1-Pentene	C_5H_{10}	70.13	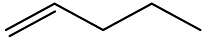	Direct[s]	9.92E-05	7.38E-05	8.18E-05	1.01E-04	7.89E-05	9.08E-05	6.65E-05
35.	2-Pentene	C_5H_{10}	70.13	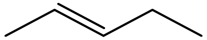	Estimated[p]	3.88E-06	4.55E-06	5.09E-06	4.44E-06	4.33E-06	2.98E-06	7.81E-06
36.	Benzene	C_6H_6	78.11	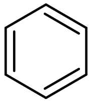	Direct[p,s]	9.53E-05	8.25E-04	1.27E-03	9.07E-04	9.07E-04	7.70E-05	3.21E-04
37.	1-Methyl-1,3-cyclopentadiene	C_6H_8	80.13	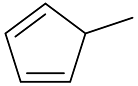	Estimated[p]	5.25E-06	1.44E-04	3.35E-04	1.69E-04	1.69E-04	-	2.02E-05
38.	Methyl vinyl ketone	C_4H_6O	81.40	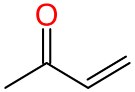	Estimated[p]	-	2.68E-06	3.83E-06	3.18E-06	1.92E-06	-	4.85E-05
39.	2-Methyl furan	C_5H_6O	82.1	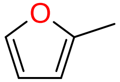	Estimated[p]	-	1.81E-06	2.13E-06	2.08E-06	1.19E-06	-	1.19E-04
40.	Toluene	C_7H_8	92.14	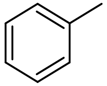	Direct[p,s]	1.13E-05	6.81E-05	1.07E-04	6.79E-05	7.61E-05	4.09E-06	2.42E-05
41.	Phenol	C_6H_6O	94.11	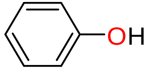	Estimated[p]	-		7.45E-04	4.77E-04	4.42E-04	-	1.88E-05
42.	Dimethyl furan	C_6H_8O	96.13	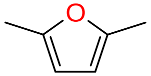	Direct[p,s]	-	-	-	-	-	-	5.71E-03
43.	4,4-Dimethyl-2-pentene (E/Z)	C_7H_{14}	98.19	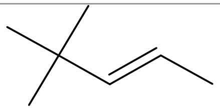	Estimated[p]	5.91E-05	4.05E-05	4.38E-05	4.91E-05	4.20E-05	4.65E-05	2.90E-05
44.	2,4-Dimethyl-2-pentene	C_7H_{14}	98.18	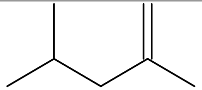	Estimated[p]	6.21E-05	4.80E-05	4.91E-05	5.37E-05	4.67E-05	4.74E-05	4.61E-05

45.	2,4-Dimethyl-1-pentene	C_7H_{14}	98.18	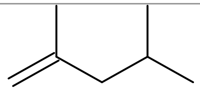	Estimated^{p}	3.75E-05	2.77E-05	2.94E-05	3.25E-05	2.92E-05	2.91E-05	2.40E-05
46.	Benzaldehyde	C_7H_6O	106.12	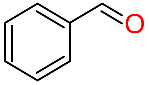	Estimated^{p}	-	5.10E-05	8.42E-05	5.62E-05	5.23E-05	-	1.01E-05
47.	Anisole	C_7H_8O	108.14	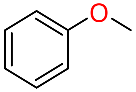	Direct^{p,s}	-	5.20E-03	7.23E-03	3.69E-03	5.54E-03	-	-
48.	o-Cresol	C_7H_8O	108.14	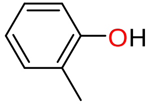	Estimated^{p}	-	9.29E-05	1.08E-05	1.03E-04	8.49E-05	-	-
49.	p-Cresol	C_7H_8O	108.14	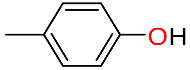	Estimated^{p}	-	3.36E-05	6.60E-05	3.86E-05	3.32E-05	-	-
50.	Iso-octane	C_8H_{18}	114.23	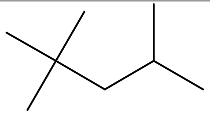	Direct^{p,s}	1.34E-02	9.88E-03	8.91E-03	7.52E-03	1.08E-02	9.64E-03	8.64E-03
51.	Indene	C_9H_8	116.16	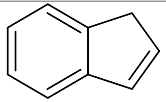	Estimated^{s}	6.12E-07	4.96E-06	7.44E-06	3.30E-06	4.85E-06	5.18E-07	1.58E-06
52.	Benzofuran	C_8H_6O	118.10	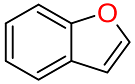	Estimated^{p}	-	4.46E-06	1.08E-05	4.30E-06	5.23E-06	-	-
53.	2,3-Dihydro benzofuran	C_8H_8O	120.15	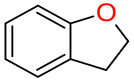	Estimated^{s}	-	3.12E-07	8.83E-07	3.24E-07	1.60E-07	-	-
54.	3-Hydroxy benzaldehyde	$C_7H_6O_2$	122.12	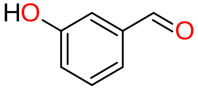	Estimated^{s}	-	2.28E-07	3.88E-07	3.23E-07	1.90E-07	-	1.14E-07
55.	m-Guaiacol	$C_7H_8O_2$	124.14	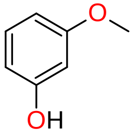	Estimated^{s}	-	1.86E-07	4.99E-07	1.97E-07	1.42E-07	-	-

56.	Naphthalene	$C_{10}H_8$	128.17	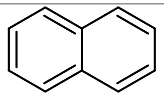	Direct[s]	6.87E-07	6.03E-06	9.65E-06	3.97E-06	6.31E-06	5.65E-07	1.97E-06
57.	1-Indanone	C_9H_8O	132.16	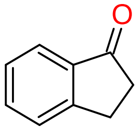	Estimated[s]	-	2.13E-07	2.81E-07	1.92E-07	8.75E-08	-	5.67E-08
58.	2-Coumaranone	$C_8H_6O_2$	134.13	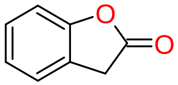	Estimated[s]	-	1.31E-07	2.40E-07	2.03E-08	6.21E-08	-	-
59.	Phenyl acetate	$C_8H_8O_2$	136.15	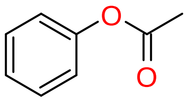	Estimated[p]	-	3.75E-06	5.41E-06	3.17E-06	3.17E-06	-	-
60.	1-Methyl naphthalene	$C_{11}H_{10}$	142.2	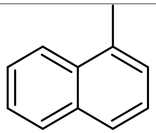	Estimated[s]	1.40E-07	6.94E-07	8.99E-07	4.90E-07	6.76E-07	9.40E-08	1.74E-07
61.	2-Methyl naphthalene	$C_{11}H_{10}$	142.20	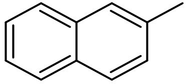	Estimated[s]	8.05E-08	5.56E-07	8.17E-07	3.63E-07	6.09E-07	7.46E-08	1.27E-07
62.	1-Methyl-1,3-dihydro-2*H*-inden-2-one	$C_{10}H_8O$	144.17	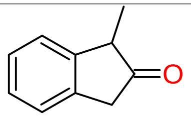	Estimated[s]	-	3.86E-07	6.74E-07	4.97E-07	2.62E-07	-	8.36E-08
63.	2-Ethenyl benzofuran	$C_{10}H_8O$	144.17	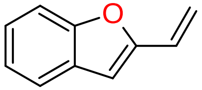	Estimated[s]	-	2.92E-07	5.11E-07	2.35E-07	2.67E-07	-	2.41E-08
64.	2-Ethyl benzofuran	$C_{10}H_{10}O$	146.18	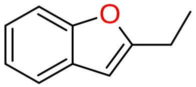	Estimated[s]	-	3.23E-07	5.72E-07	3.30E-07	1.69E-07	-	5.47E-08
65.	Acenaphthylene	$C_{12}H_8$	152.19	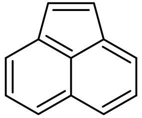	Direct[s]	1.30E-07	5.86E-07	1.01E-06	2.49E-07	7.80E-07	9.42E-08	2.72E-07

66.	Acenaphthene	$C_{12}H_{10}$	154.21	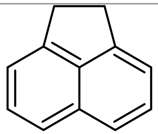	Direct^{s}	2.48E-08	8.47E-08	9.86E-08	5.33E-08	7.80E-08	2.04E-08	4.30E-08
67.	Biphenyl	$C_{12}H_{10}$	154.21	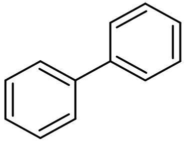	Estimated^{s}	3.94E-08	3.89E-07	5.66E-07	2.38E-07	3.23E-07	2.83E-08	2.32E-07
68.	Fluorene	$C_{13}H_{10}$	166.22	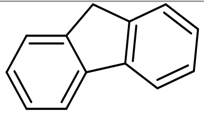	Direct^{s}	6.46E-08	2.70E-07	4.80E-07	1.22E-07	2.82E-07	4.40E-08	9.81E-08
69.	Dibenzofuran	$C_{12}H_8O$	168.19	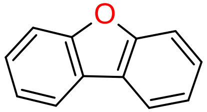	Direct^{s}	-	9.95E-07	2.90E-06	1.01E-06	5.48E-07	-	2.89E-07
70.	Phenanthrene	$C_{14}H_{10}$	178.23	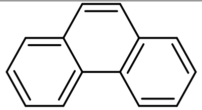	Direct^{s}	1.34E-08	8.50E-08	1.42E-07	2.45E-08	5.99E-08	5.78E-09	2.19E-08
71.	Anthracene	$C_{14}H_{10}$	178.23	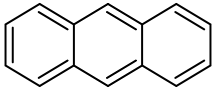	Direct^{s}	9.11E-09	3.35E-08	1.09E-07	2.57E-08	6.34E-08	7.86E-09	1.93E-08
72.	9H-Xanthene	$C_{13}H_{10}O$	182.21	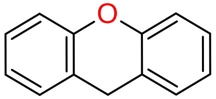	Direct^{s}	-	3.39E-07	9.54E-07	3.34E-07	1.37E-07	-	-
73.	6H-Dibenzo[b,d]pyran	$C_{13}H_{10}O$	182.22	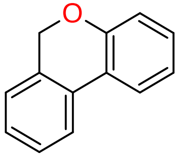	Estimated^{s}	-	3.23E-07	3.90E-07	2.51E-07	1.12E-07	-	-
74.	Fluorenol	$C_{13}H_{10}O$	182.22	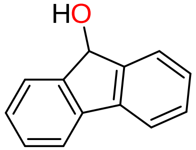	Estimated^{s}	-	9.48E-08	2.31E-07	1.03E-07	5.23E-08	-	3.39E-08

75.	Dibenzo-p-dioxin	$C_{12}H_8O_2$	184.19	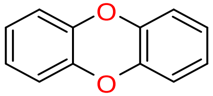	Estimated[s]	-	1.83E-08	3.11E-08	4.78E-09	5.63E-09	-	-
76.	[1,1"-Biphenyl]-2,2"-diol	$C_{12}H_{10}O_2$	186.20	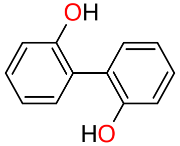	Estimated[s]	-	5.69E-07	4.66E-07	4.22E-07	1.79E-07	-	6.57E-08
77.	Benzyl phenyl ether	$C_{13}H_{12}O$	184.23	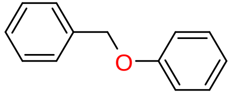	Estimated[s]	-	5.12E-08	6.96E-08	1.36E-08	5.53E-08	-	-
78.	Xanthone	$C_{13}H_8O_2$	196.19	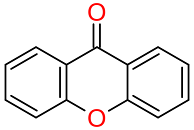	Direct[s]	-	6.05E-07	9.13E-07	3.38E-07	2.15E-07	-	-